UNIVERSITY OF CALIFORNIA, SAN DIEGO

Dynamic Response of Monolithic and Laminate/Particulate Reactive Mixtures

A dissertation submitted in partial satisfaction of the requirements for the degree Doctor of Philosophy

in

Materials Science and Engineering

by

Chung-Ting Wei

Committee in charge:

>Professor Marc A. Meyers, Chair
>Professor David J. Benson
>Professor Prabhakar R. Bandaru
>Professor Richard K. Herz
>Professor Vitali F. Nesterenko

2011

The dissertation of Chung-Ting Wei is approved, and it is acceptable in quality and form for publication on microfilm and electronically:

_____

_____

_____

_____
                                                                                          Chair

University of California, San Diego

2011

iii

DEDICATION

Lovingly dedicated to my family. Without the support and encouragement from them, I would never have this opportunity to study abroad and finish my PhD research.

TABLE OF CONTENTS

LIST OF FIGURES

LIST OF TABLES

ACKNOWLEDGEMENTS

I would like to acknowledge Professor Marc A. Meyers for his support as the chair of my committee and the advisor of my PhD research. I would also like to acknowledge Profs. Nesterenko, Thadhani, Weihs, and Benson for their generous helps in many ways. Without them, my research cannot be done. Their invaluable help is gratefully appreciated.

Chapters 3 and 4, in part, has been published or is being currently prepared for submissions as the following papers: Laser Shock-Induced Spalling and Fragmentation in Vanadium, 2010, H. Jarmakani, B. Maddox, C. T. Wei, D. Kalantar, M. A. Meyers, Acta Materialia; Reaction in Ni–Al Laminates by Laser-Shock Compression and Spalling, 2011, C. T. Wei, B. R. Maddox, A. K. Stover, T. P. Weihs, V. F. Nesterenko, M. A. Meyers, Acta Materialia; Effects of Geometry and Intermetallic Bonding on the Mechanical Response, Spalling, and Fragmentation of Ni-Al Laminates, 2011, E. Vitali, C. T. Wei, D. J. Benson, M. A. Meyers, Acta Meterialia; Response of Ni/Al Laminates to Laser-Driven Compression, C. T. Wei, V. F. Nesterenko, T. P. Weihs, B. Remington, S. -H. Park, M. A. Meyers, Acta Materialia, submitted; Quasi-static and Dynamic Response of Explosively Consolidated Metal-Aluminum Powder Mixtures, C. T. Wei, E. Vitali, D. J. Benson, F. Jiang, K. S. Vecchio, N. N. Thadhani, M. A. Meyers, Acta Materialia, to be submitted. The dissertation author was the primary author or co-author of these papers.

VITA

<u>**2007-2011**</u>   Doctor of Philosophy, Materials Science and Engineering, University of California, San Diego

<u>**2006- 2007**</u>   Process support engineer in PDC (Process Diagnostic & Correction) group of TSMC account of Applied Materials Inc. in Taiwan (AMAT)

<u>**2005-2006**</u>   Military duty in Taiwan

<u>**2002-2004**</u>   Master, Materials Science and Engineering, National Tsing Hua University

<u>**2002**</u>   Bachelor, Materials Science and Engineering, National Tsing Hua University

PUBLICATIONS

"**Laser Compression and Fragmentation of Metals**", M. A. Meyers, H. Jarmakani, B. Y. Cao, C. T. Wei, B. A. Remington, E. M. Bringa, B. Maddox,D. Kalantar, D. Eder, A. Koniges, DYMAT Proc., pp. 999-1006, 2009.

"**Laser Shock Compression and Spalling of Reactive Ni-Al Laminate Composites**", C. T. Wei, B. R. Maddox, T. P. Weihs, A. K. Stover, V. F. Nesterenko, and M. A. Meyers, APS Conf. Proc., pp. 305-308, 2009.

"**Explosive Compactions of Intermetallic-forming Powder Mixtures for Fabricating Structural Energetic Materials",** S. W. Du, B. Aydelotte, D. Fondse, C.-T. Wei, F. Jiang, E. Herbold, K. Vecchio, M. A. Meyers, and N. N. Thadhani, APS Conf. Proc., p. 498, 2009.

"**Laser-Shock Induced Spalling and Fragmentation in Vanadium**", H. Jarmakani, B. R. Maddox, C. T. Wei, D. Kalantar, and M. A. Meyers, Acta Materialia, Vol. 58, pp. 4604-4628, 2010.

"**Reaction in Ni-Al Laminates by Laser-shock Compression and Spalling**", C. T. Wei, B. R. Maddox, T. P. Weihs, A. K. Stover, V. F. Nesterenko, and M. A. Meyers, Acta Materialia, Vol. 59, pp. 5276-5287, 2011.

"**Effects of Geometry and Intermetallic Bonding on the Mechanical Response, Spalling, and Fragmentation of Ni-Al Laminates**", E. Vitali, C. T. Wei, D. J. Benson, M. A. Meyers, Acta Meterialia, Vol. 59, pp. 5869-5880, 2011.

"**Quasi-static and Dynamic Response of Explosively Consolidated Metal-Aluminum Powder Mixtures**", C. T. Wei, E. Vitali, D. J. Benson, F. Jiang, K. S. Vecchio, N. N. Thadhani, M. A. Meyers, Acta Meterialia, to be submitted.

"**Response of Ni/Al Laminates to Laser-Driven Compression**" C. T. Wei, V. F. Nesterenko, T. P. Weihs, B. Remington, H. -S. Park, M. A. Meyers, Acta Meterialia, to be submitted.

INTERNATIONAL CONFERENCE

Poster: "Laser Shock and Spall of Reactive Ni-Al Laminate Composites" Research Expo 2008, University of California, San Diego.

Poster: "Mechanical and Computational Investigation of Ni-Al Laminates in Laser-Shock Compression and Spalling" Research Expo 2010, University of California, San Diego.

Presentation: "Reaction of Ni-Al Laminate Composites by Laser Shock Compression and Spalling" C.T. Wei, B. Maddox, T.P. Weihs, V. F. Nesterenko, M.A. Meyers, The 2009 TMS Annual Meeting, San Francisco.

Presentation: "Laser Shock Compression and Spalling of Reactive Ni-Al Laminate Composites", C. T. Wei, B. R. Maddox, T. P. Weihs, A. K. Stover, V. F. Nesterenko, and M. A. Meyers, 2009, 16th APS Topical Conference on Shock Compression of Condensed at Tennessee.

Presentation: "Laser Shock Compression and Spalling of Reactive Ni-Al Laminate Composites", C. T. Wei, B. R. Maddox, T. P. Weihs, A. K. Stover, V. F. Nesterenko, and M. A. Meyers, The 2009 Fall Materials Research Society Annual Meeting, Boston.

Presentation: " Mechanical and Computational Investigation of Ni-Al Laminates in Laser-Shock Compression and Spalling", C.T. Wei, M.A. Meyers, B. Maddox, T.P. Weihs, A.K. Stover, V. Efrem, D.J. Benson, The 2009 TMS Annual Meeting, Seattle.

Presentation: " Quasi-Static and Dynamic Response of Explosively Consolidated Reactive Mixtures", Chung-Ting Wei, Marc A. Meyers, David J. Benson, Efrem Vitali, F. Jiang, Kenneth S. Vecchio, Naresh N. Thadahani, The 2011 TMS Annual Meeting, San Diego.

FIELD OF STUDY

Major Field: Materials Science and Engineering

ABSTRACT OF THE DISSERTATION

Dynamic Response of Monolithic and Laminate/Particulate Reactive Mixtures

by

Chung-Ting Wei

Doctor of Philosophy in Materials Science and Engineering

University of California, San Diego, 2011

Professor Marc A. Meyers, Chair

Two dynamic compression methods were applied to a monolithic metal and reactive mixtures to investigate their responses:

(a) Dynamic experiments using a split Hopkinson pressure bar were applied to reactive mixtures densified by explosive consolidation in order to establish their mechanical response and failure mechanisms.

(b) Laser compression and release, which can impart high stresses, up to hundreds GPa, in times of nanoseconds and fractions thereof, was applied to establish the spalling strength of vanadium and the reaction threshold for Ni/Al laminates.

The spallation and fragmentation exhibited by recovered mono- and poly-crystalline vanadium prove that the laser intensities and crystal structure play important roles in determining spall strength, fragmentation, and microstructural processes.

Densified reactive mixtures with different microstructures (Ni, Mo, W, Nb and Ta with Al) were subjected to the quasi-static and dynamic strain rates. Two distinct failure mechanisms, axial splitting and shear failure, were observed in the recovered specimens. Axial splitting occurred when the bonding between the powders was poor; shear failure was primarily associated with extensive deformation of continuous Ta and Nb phases. Finite element simulations provided valuable information in interpreting the experimental results and predicting failure mechanisms akin to those observed.

Ni/Al laminates were subjected to laser compression. The strain rates varied from 10^5 to 10^8 s^{-1}, and the initial stress varied from 30 to ~300 GPa. It is found the thickness of the lamellar and the interlaminar bonding strength are the two critical factors in determining mechanical failure. The intermetallic reaction leading to Ni_3Al and NiAl were produced by the laser energies and laser pulse durations in direct laser shock experiments. Laser-driven compression was also applied to study the high temperature synthesis in nano-scale Ni/Al laminates with bilayer thickness 54 nm. Intermetallic phases, NiAl and $NiAl_3$, were found on the plasma stagnated laminates. However, the self-propagating high temperature synthesis (SHS) did not self-sustain in the micro-scale laminate because of the short duration of the pulse.

Chapter 1.

Introduction:

In this study, the responses of different types of materials, including mono- and poly-crystalline pure element (vanadium), powder consolidated aluminum base reactive mixtures and Ni-Al reactive composites in laminar micro-structure, were examined mechanically, or chemically, or both aspects under a quasi-static, dynamic, or extreme (by laser) loading condition. There were three primary purposes which we endeavored to achieve by investigating those materials with varying approaches: (1) To understand the mechanical responses of the mono-crystalline material (BCC vanadium) and the Ni/Al composite with the laminar micro-structure under the laser shock loading condition; (2) To investigate the dynamic fracture mechanisms corresponding to different geometries, micro-structures and interfacial bonding strength of composite materials (Ni/Al laminates and powder consolidated Al base mixtures); (3) To specify the self-sustaining high temperature reaction of the Ni/Al laminates using the laser shock approaches.

The principle of the combustion synthesis and the self-sustaining high temperature reaction are revealed in Chapter 2. The basic mechanical properties and strengthening mechanism are also briefly introduced in this chapter. The reaction mechanisms of SHS, shock-induced and shock-assisted reactions are also addressed in Chapter 2. In Chapter 3, the experimental techniques including sample preparations, mechanical tests, laser shock experiments, the post analysis tools and the computational methodologies are shown and explained.

Chapter 4 presents the experimental results and discussion. The study of mono-
and poly-crystalline vanadium irradiated by high intensity laser shock provided general
information of materials under extreme loading conditions in Section 4.1. The recovered
vanadium samples were characterized using metrology such as SEM, VISAR and
HYADES in order to understand the principle of mechanical properties of the typical
body-centered cubic (BCC) metal under an extremely high strain rate using direct laser
shock loading.

Section 4.2 describes how the powder consolidated cylinders were produced using
an explosive double-tube shock consolidation process with five binary combinations,
Ni+Al, Nb+Al, Ta+Al, Mo+Al, W+Al. These consolidated powder mixtures, compacted
with different particle morphologies, sizes and components, were subjected to the
uniaxial compression and the split Hopkinson bar dynamic tests. These tests provided a
valuable understanding of the mechanical properties tailored by micro-structures. Using
Al base reactive mixtures with different inclusions provided systematic information to
obtain the optimum solution for manipulating reactive powder mixtures in order to apply
them to further commercial uses and metallurgical processes.

In order to investigate the chemical and mechanical properties of Ni/Al reactive
laminates subjected to high energy laser irradiations, the Ni/Al laminates were produced
with micro- (5 and 30 µm) and nano-scale bilayer thicknesses (54 nm), using the
accumulative cold-roll bonding and magnetron physical vapor deposition processes
respectively. Section 4.3 describes how these laminates were subjected to high intensity
laser irradiations at Lawrence Livermore National Laboratory and the OMEGA laser
facility at the University of Rochester. The following analysis using XRD, SEM, TEM,

OM, and EDX was conducted on as-produced and recovered samples for characterizing chemical reactions, fracture mechanisms, and the interactions between laser shock-wave pressures and laminates. Moreover, quasi-static tensile tests were also employed for obtaining comparable quasi-static mechanical properties. The computational methodologies, RAVEN and HYADES, were also used to investigate the failure mechanism corresponding to the geometries and interfacial bonding strength. It should be noted that the reactive laminates with nano- or micro-scale bilayer have been studied broadly in order to make use of the fast exothermic reaction and to understand the mechanism of the reaction in different materials for nearly two decades [1, 2]. Weihs *et al.* found that the SHS reactions of nano-scale reactive laminates were controlled by the bilayer thickness and the premixing layer [3, 4]. It was shown that the reactions of nano-laminates with thicker premixing layers were retarded or prohibited due to the decrease of the temperature gradient, and the decrease of the diffusion gradient [3-5]. There were also a numerous amount of studies of reactive nano-laminates using the combustion synthesis [6], the laser-energy initiation [1] and the electrical ignition method [2]. However, it was rare to see studies of chemical reactions on cold rolled micro-laminates, which had a relatively strong mechanical strength and a potential for using in military applications and construction materials.

Chapter 2.

Background

2.1 Combustion synthesis (Self-sustaining high temperature synthesis)

Combustion synthesis, which utilizes the exothermic heat of reactive materials in order to produce new materials or commercial products, was studied for decades [7-14]. The reaction mechanism was to produce a significant amount of releasing heat and sustain the self-propagating high temperature reactions. This mechanism was also named the self-sustaining high temperature synthesis (SHS) [12].

Nickel/Aluminum base composites are one of the promising reactive materials being used in many commercial applications such as welds [15-18], constructions, and aerospace [15]. This binary metallic composite was known as one of the reactive materials for SHS reaction [16-18]. The reactive materials in terms of candidates for the combustion synthesis have many different combinations, such as Ti+C, Ti+Si, Mo+2B [11, 12], Ni+Al [16, 17] (in nano-scale), Ti+C+Ni+Mo [9, 10], TiB_2+SiC [14], which have high releasing energies from the exothermic reactions [7, 19, 20]. The exotherm contributes a large amount of thermal heat that results in sequential reactions in reactive materials. Exothermic reactions generate intermetallic compounds and strengthen the internal bonding between different elements [8, 19, 20] in the reactive materials. In fact, many of the advantages of reactive materials are achieved by utilizing exothermic reactions and its big variety of compositions [6-25], which have potentialities for commercial uses.

The attractive factors of utilizing the reactive materials and SHS reactions are the reaction speed and the strong exotherms. Vecchio et al. [21] found that for a reactive material, the reaction speed can reach $10^7 \sim 10^9$ times faster than a diffusion controlled reaction. The combustion synthesis was first used to weld rail tracks in 1899, utilizing the thermite reaction discovered in 1893 by the German chemist Hans Goldschimdt. The general principle of using reactive material to weld and fix the railroad was to utilize the reduction process and the intensive exothermic heat to melt and generate the iron filling into the broken area. By using this thermite process, people were able to fix the rail track on-site in a couple minutes. The exothermic chemical reaction can be written as: $Fe_2O_3 + Al \rightarrow 2Fe + Al_2O_3 + Heat$ (see Figure 1) [22]. The exothermic heat incorporated a drastic temperature increase that was very intense, which can melt the iron fixing the broken tracks.
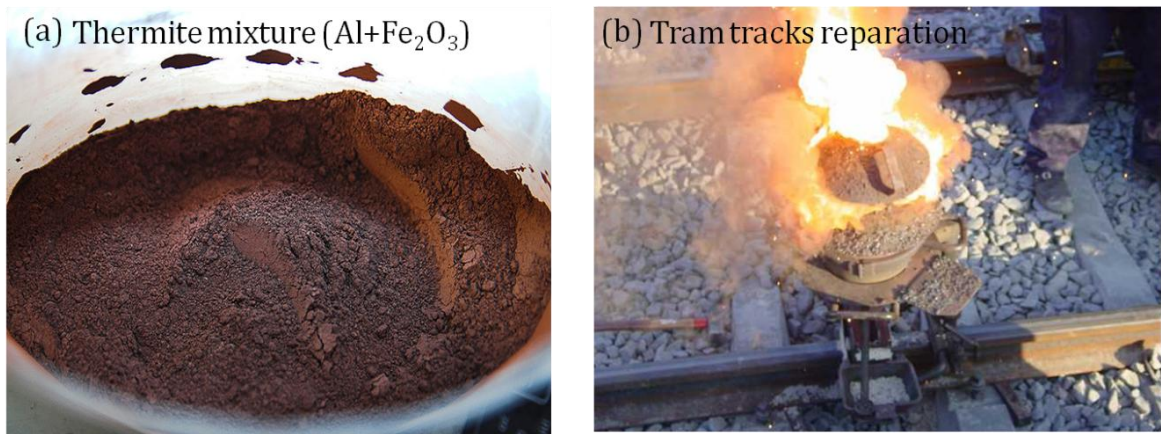
Figure 1: Thermite reaction: Fe2O3+Al→2Fe+Al2O3+Heat: (a) thermite mixture; (b) thermite reaction applied for reparation of rail track [22].

Figure 2. shows a commercial application (Figure 2 (a)) and an experimental result (Figure 2 (b)) of the SHS reaction. Figure 2 (a) shows the commercial use of welding a copper heat sink on a high operating temperature device [16, 24]. The SHS/DC disks of TiC in Figure 2 (b) shows the self-propagating high-temperature synthesis compacted and hot-pressed titanium carbides from left to right, corresponding to the evolution from the ignition to the reaction propagation using combustion synthesis [6]. The SHS reaction in the combustion synthesis can be utilized to produce high melting temperature, high strength and hardness compounds such titanium alloys, and ceramics [9-14].
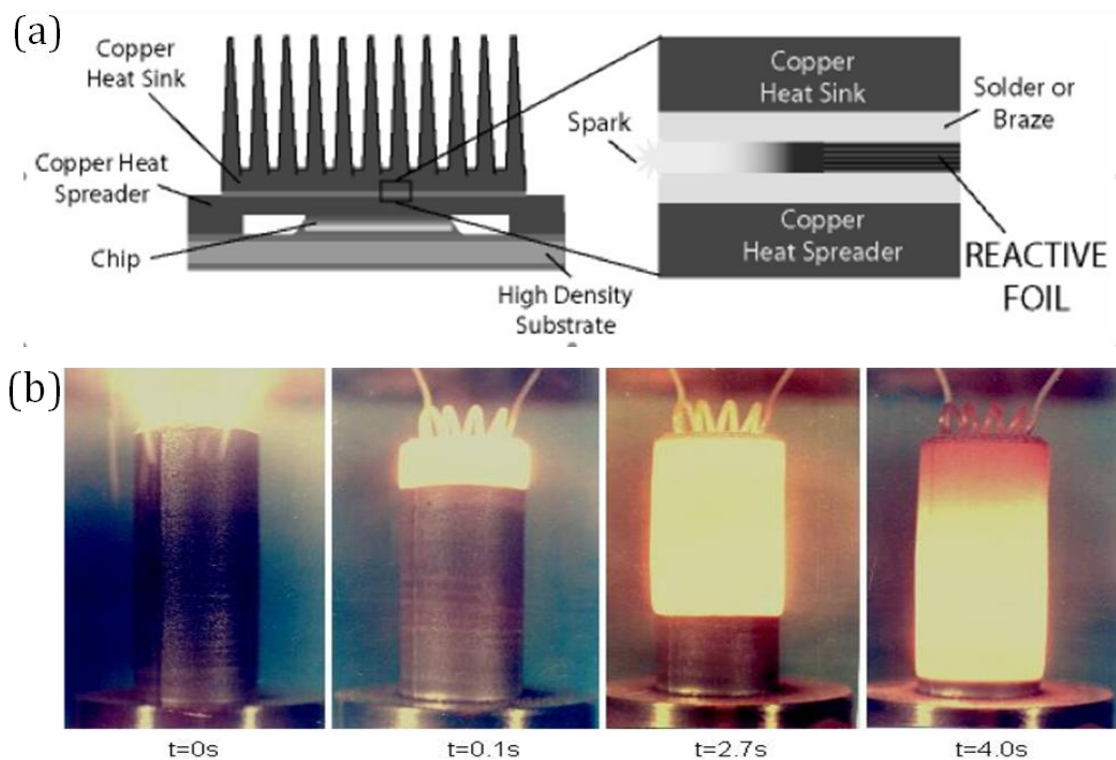
Figure 2: Self-propagating High-temperature Synthesis: (a) using SHS for soldering copper heat sink onto a high operating temperature chip [16]; (b) the SHS experimental result [6].

Recently, the reactive materials were also used in military applications [26. 27]. Figure 3 shows the scheme of the reactive materials enhanced warhead. It was proved that by using reactive materials, the lethal radius was increased to more than 2 times of traditional warheads. The anti-missile system can also be improved by using reactive materials to enhance its interception radii. These different applications proved that reactive materials are promising candidates for many fields.
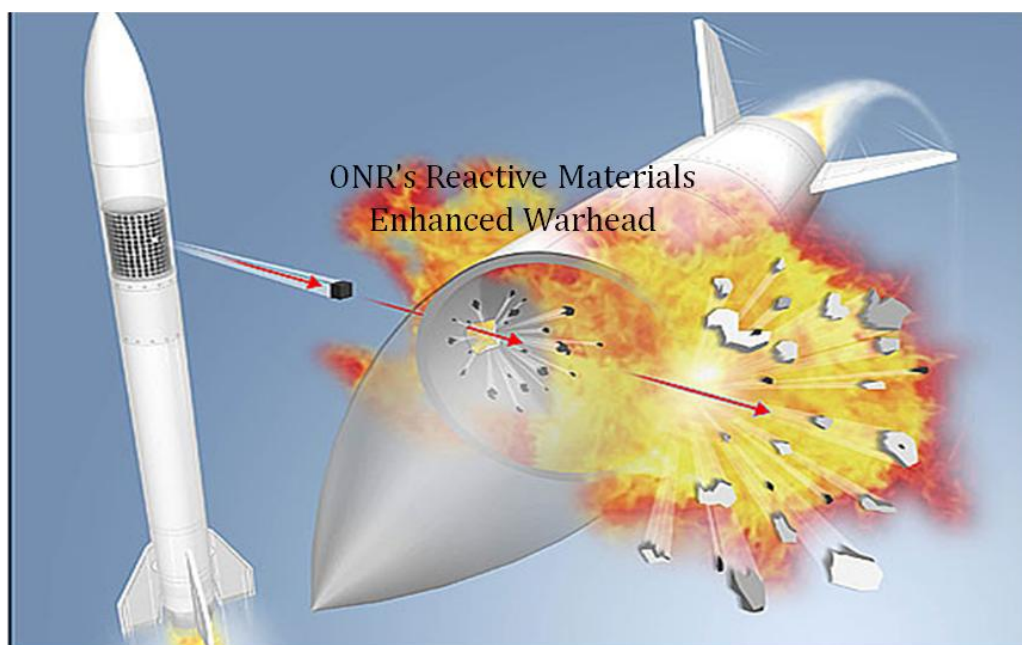
Figure 3: Reactive materials enhanced warhead: using the exothermic reaction from the reactive materials to enhance explosions and increase the lethal radius [26, 27].

It is worth having a brief introduction of the historical evaluation of the dynamic synthesis of reactive materials. In 1956, the Russian scientist, Ryabinin, and American scientists, Decarli *et al.*, first attempted to produce diamonds [8, 23] by explosively compressing graphite. It was the first ever approach of using the dynamic compression

for synthesizing new materials in history. Due to this innovative discovery, scientists were dedicated to search for other possibilities of synthesizing new materials or finding more commercial usages using dynamic methods [6, 7, 15-20]. Well-known commercial applications of the dynamic compressing (or shock) synthesis are the shock synthesis of high melting ceramics such as TiB_2 [11, 12] and TiC [7], and the self-propagating high-temperature synthesis (SHS) used to weld and solder parts [16-18], or generate new compounds [6, 7].

2.2 Mechanical and chemical properties

In this study, the materials used in preparing initial samples and characterizing the corresponding properties were reactive. The reactivity played important roles for whether determining the properties of the as-prepared sample or predicting the characters of the recovered samples. Mechanical and chemical properties of reactive materials and single elemental materials are quite different and going to be clarified in the following sections.

2.2.1 Young's modulus

Young's modulus represents elastic properties of materials. The linear portion of a stress-strain curve shows that a material is stretched or constrained as a tension or compression occurs (see Figure 4). This elastic property was experimentally demonstrated by Robert Hooke in 1678 [28]. The elastic stress-strain behavior can be easily presented in a mathematical form called Young's modulus or the elastic modulus (E),

$$E = \frac{\sigma}{\varepsilon},$$ <div style="float:right">Eqn. (1)</div>

where E is the Young's modulus, σ is an applied stress (engineering stress), and ε is the normal strain. This elastic property can be altered by porosities, cracks, and inclusions in the materials.
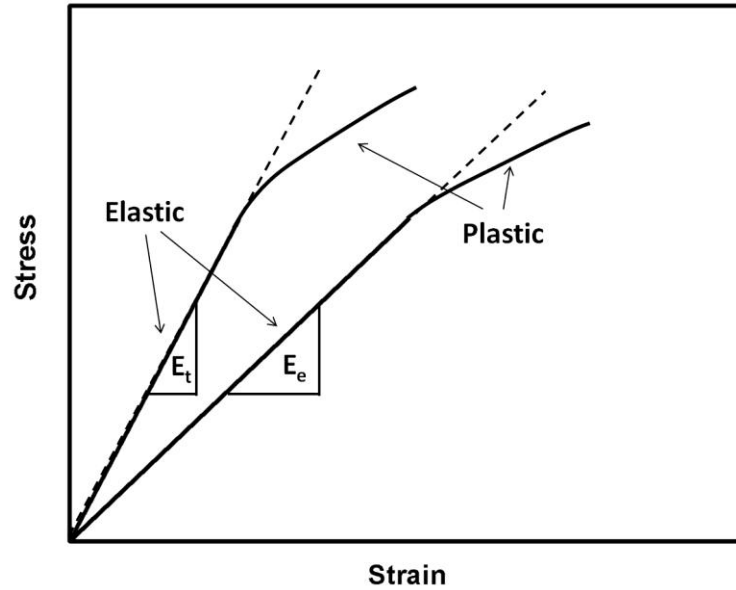
Figure 4: Stress vs. strain curves (for metals).

For instance, materials with a sufficient amount of porosities such as ceramics have a distinct elastic modulus from fully dense bulks. Wachtman [29] and MacKenzie [30] characterized this by the mathematical expression,

$$E = E_o(1 - f_1 p + f_2 p^2),$$ <div style="float:right">Eqn. (2)</div>

where f_1 and f_2 are equal to 1.9 and 0.9 for spherical voids, and p is the porosity. If the material is compacted with several constituents, the law of mixtures can be applied,

$$E = E_A(1 - f_B) + E_B f_B \ ,$$
<div align="right">Eqn. (3)</div>

here E_A and E_B are the Young's modulus of mixtures, and f_B is the fraction of the component B.

The pre-existing cracks also play an important role in the elastic behavior of materials. O'Connell and Budiansky proposed an estimation [31] to explain this phenomenon:

$$\frac{E}{E_o} = 1 - \frac{16(10 - 3v)(1 - v^2)}{45(2 - v)} f_s$$
<div align="right">Eqn. (4)</div>

where *fs* is defined as the volume fraction of cracks (the number of cracks per unit volume, N, multiplied by the cube of the mean crack radius, a^3) and *v* is Poisson's ration of materials. This demonstrated the effect of the cracks on the elastic behavior of materials.

2.2.2 Yield stress

Yield stress/flow stress represents the critical stress, which allowed materials to start deforming plastically. This irreversible plastic deformation is due to the glide planes slide, dislocation movement, void accumulation, etc. Based on different manufacturing processes, materials with similar compositions may have different yield stresses (see Figure 5). AISI 1040 steels have different flow stresses due to many factors such as crystal sizes, different phases, or dispersions. Based on different quenching and tempering processes, the phases and grain sizes of the steel are manipulated, thus altering the mechanical properties by the manufacturing processes of the steel. Parabolic work-hardening curves are clearly shown in the stress-strain plot following the elastic stress-

strain curves in Figure 5. This work hardening behavior can be written as follows (Ludwik-Hollomon equation):

$$\sigma = \sigma_o + K\varepsilon^n \ ,$$

Eqn. (5)

where σ_o is the yield stress, K is a constant, and the exponent n is the material constant.
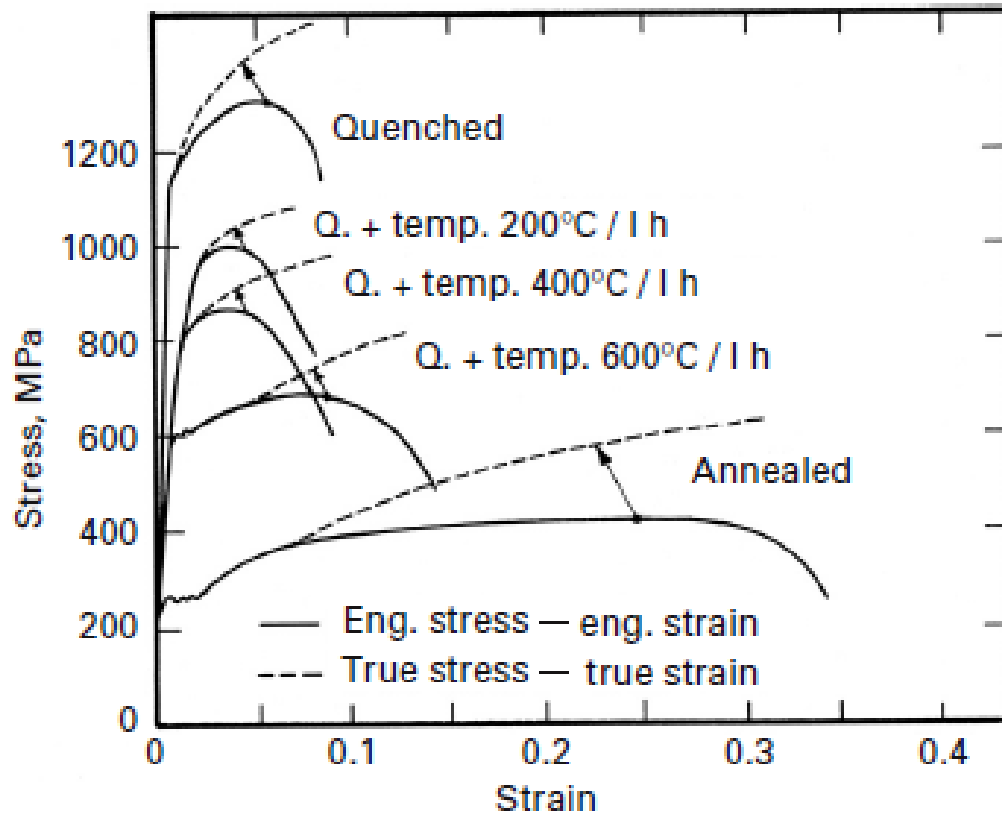
Figure 5: Stress-strain curves for AISI 1040 steel subjected to different heat treatments [28].

Other than the intrinsic factors of materials mentioned above, the test environments can also play an important role. Strain rates and temperatures are often

considered as factors influencing plastic behaviors. The stress-strain constitutive equation incorporating strain rate and thermal activity effects is called the Johnson-Cook equation:

$$\sigma = (\sigma_0 + K\varepsilon^n)(1 + C \ln \frac{\dot{\varepsilon}}{\dot{\varepsilon}_0})\left[1 - \left(\frac{T - T_r}{T_m - T_r}\right)^m\right],$$
Eqn. (6)

where the *K, n,* and *m* are material parameters, T_r and T_m are the reference temperature and melting temperature respectively, and $\dot{\varepsilon}_0$ is the reference strain rate. This equation was commonly used to predict large-scale deformations. Nevertheless the constitutive equations incorporating microstructural elements such as grain sizes, dislocation interactions and dynamics are also used to provide stress-strain behavior computationally. The Zerilli-Armstrong equation [32] is one of these constitutive equations. The basic idea behind this equation is to develop a computational method to represent the mechanical responses of materials from low to high temperatures and from low strain rates ($\sim 10^{-5}$ s^{-1}) to extremely high strain rates ($\sim 10^9$ s^{-1}).

2.2.3 Strain rate dependence of the mechanical response

A high strain rate test applied on the material can present a totally distinct stress-strain behavior compared to a low strain rate test. Strain rate sensitivities can vary wildly depending on materials [33]. Figure 6 shows nano-crystalline Ni tested under a range of strain rates form 3×10^{-4} to 3×10^{-1} s^{-1}. The yield stress increases as the applied strain rate increases [34]. A quantitative estimation for characterizing this strain rate dependence of different composites is the strain rate sensitivity parameter *m*, defined as Eqn. (7):

$$m = \frac{\partial \ln \tau}{\partial \ln \dot{\varepsilon}}$$
<div align="right">Eqn. (7)</div>

where τ is the yield stress, and $\dot{\varepsilon}$ is the strain rate. It is commonly seen that materials with small grains have a higher strain rate sensitivity value due to grain boundary (GB) deformation mechanisms such as grain boundary migration, grain boundary sliding, or dislocation nucleation [33-35]. The strain rate sensitivity can be altered by external properties of materials such as dimensions of grains (see Figure 7), porosities, or inclusions in the materials.
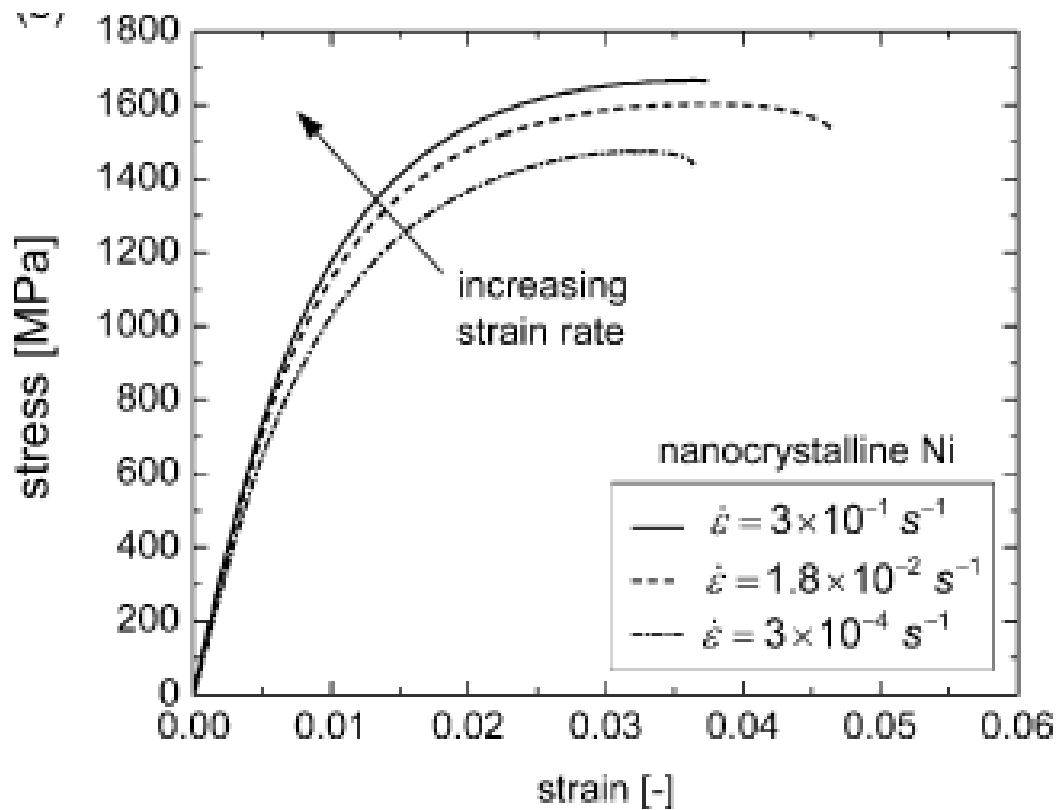
Figure 6: Nanocrystalline Ni was tested using different tensile strains: 3×10^{-4}, 3×10^{-2}, 3×10^{-1} s^{-1} [34].
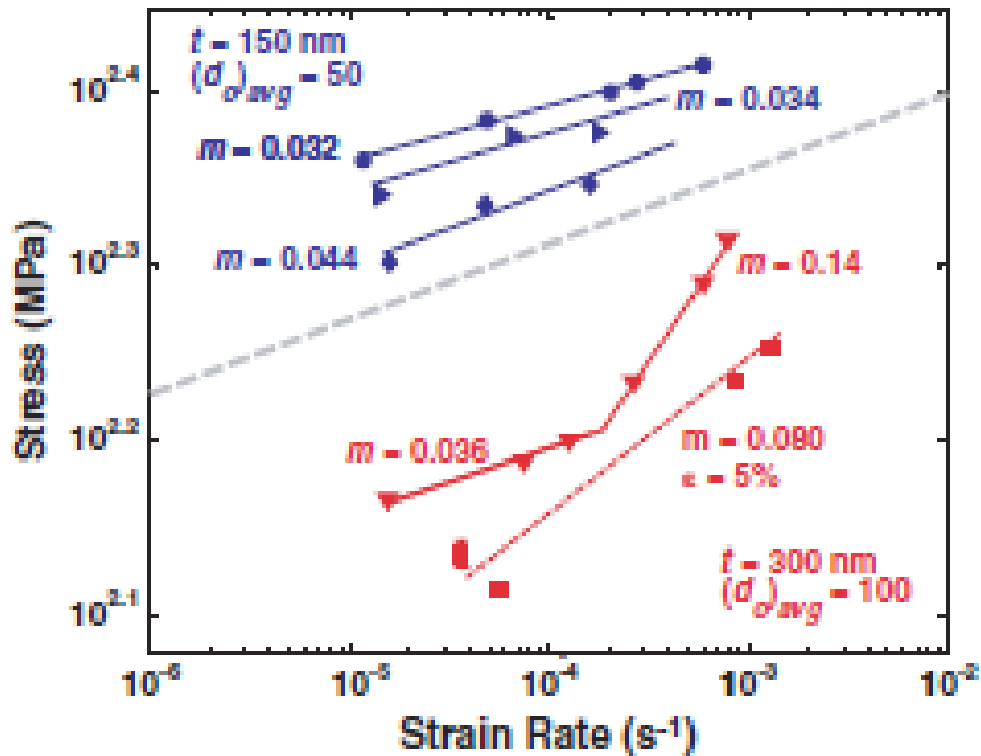
Figure 7: Strain rate sensitivities from two different thicknesses of Al foils [35].

Here it should be noted that the *m* value is not always positively proportional to the increases of strain rates. Materials such as titanium alloys (Ti-6%, Al-4%, V), steels, aluminum alloys, and some ceramics have super-plastically mechanical properties. Super-plastic materials can be stretched extensively, and can reach extremely high strains (~tens) without failure. These materials become more stretchable under high strain rate loading [28], which leads to a negative value of *m*. It should be noted that BCC metals such as Cu has a smaller activation volume for obstacles which leads to a relatively small strain rate sensitivity in comparison with FCC metals such as Ta [35].

2.2.4 Strengthening mechanisms

In order to satisfy the specific requirements for each application, materials must have adequate mechanical strength and flexibility. There are numerous methods to strengthen materials. For instance, inclusion strengthening is known as that the easiest way to obtain strong and ductile materials by mixing two or more elements with high strengths or good ductility. Aluminum based composites are of inclusion hardeened materials. These composites usually include hard and high strength materials such as Ti, W, or Ni added and dispersed in a soft and ductile Al matrix. In this case, the hard and high strength materials support the alloy to sustain high stress, while the ductile Al matrix keeps the flexibility.

Multi-elemental compounds have mechanical properties integrating all of added materials. There is a mathematical method to predict the mechanical properties of these alloys, which is called the law of mixtures [28] or the additive rule, shown as the following:

$$E = E_a \times f_a + E_b \times f_b + E_c \times f_c \ldots \qquad \text{Eqn. (8)}$$

where E represents the elastic modulus (or hardness, yield stress, etc.), f is the volumetric fraction of the material, a, b and c are symbols corresponding to each element. However, the law of mixtures can only provide an uncertain evaluation, which can be easily altered by extrinsic properties, for example the porosity and the microstructure of the materials in terms of inclusion morphologies and grain sizes [36].

The formation of the intermetallic phase is one of the strengthening mechanisms. Most of the intermetallic products have the relatively high strength compared to their

parent reactants [37]. Intermetallics perform as the hard and high strength inclusion. Nevertheless, these phases generated by an exothermic reaction help to eliminate the porosity and increase the bonding strength between different elements.

Other strengthening factors such as dispersions, phase changes (martensite), and grain sizes also play important roles in the strengthening mechanisms of materials. However, these factors are not the major subjects in our study, therefore we are not going to discuss them in this study.

2.2.5 Reactions of reactive materials

There are several mechanisms which induce chemical reactions in reactive mixtures, for example thermite reactions, combustion synthesis, and self-propagating high-temperature synthesis (SHS). As aforementioned in the introduction, these chemical behaviors have practical applications which help to create new materials, enhance functionalities, strengthen mechanical properties, and repair functional materials. This provides many benefits in a variety of aspects. The theoretical reaction module for each reaction mechanism is worthy of a further discussion. However, in this study, we focus on the SHS reaction of the Ni/Al reactive materials, therefore it is not going to discuss other reactions in this dissertation.

2.2.6 Self-propagating high-temperature synthesis (SHS)

Exothermic chemical reactions release an enormous amount of heat that can melt adjacent materials and induce sequential reactions. If the conditions of materials fit

certain requirements, the exothermic reaction can propagate through entire sample spontaneously after the reaction ignited. Ma *et al.* [2] theoretically derived the thermal reaction mechanism of SHS. The SHS reaction is a thermally activated process. Diffusion mechanism is the principle of this self-propagating reaction. Alternatively stacking Al/Ni laminates produced by physical vapor deposition were tested by conventional annealing, or ignited by an electrical explosion. The original and recovered samples were examined by TEM (Figure 8). The annealed multilayer samples had a similar granular structure as the electrically ignited sample. Due to the highly exothermic reaction (Al_3Ni = -36 kJ/mol [38]), the samples could be heated up to a very high temperature >1127K, which can melt the material and enhance the re-crystallization process. It resulted in a larger average grain size in electrically ignited samples.

The thermal activation mechanism can be sketched in Figure 9. The scheme illustrates that the reaction front propagates from left to right with a velocity *V* (Figure 9 (a)). The reaction started from the initial Ni/Al alternatively stacked layers (Figure 9 (b)). After the electrical ignition, the reaction front propagated in two different directions: one perpendicular to the stacking direction, and the other one parallel to the stacking direction as shown in Figure 9 (c). Figure 9 (d) shows a fully reacted sample after the reaction front propagated through the whole sample. This evolution basically was dominated by thermal diffusion. An energy in-equilibrium is required inside the reaction front in order to be self-sustaining. This can be shown in the following:
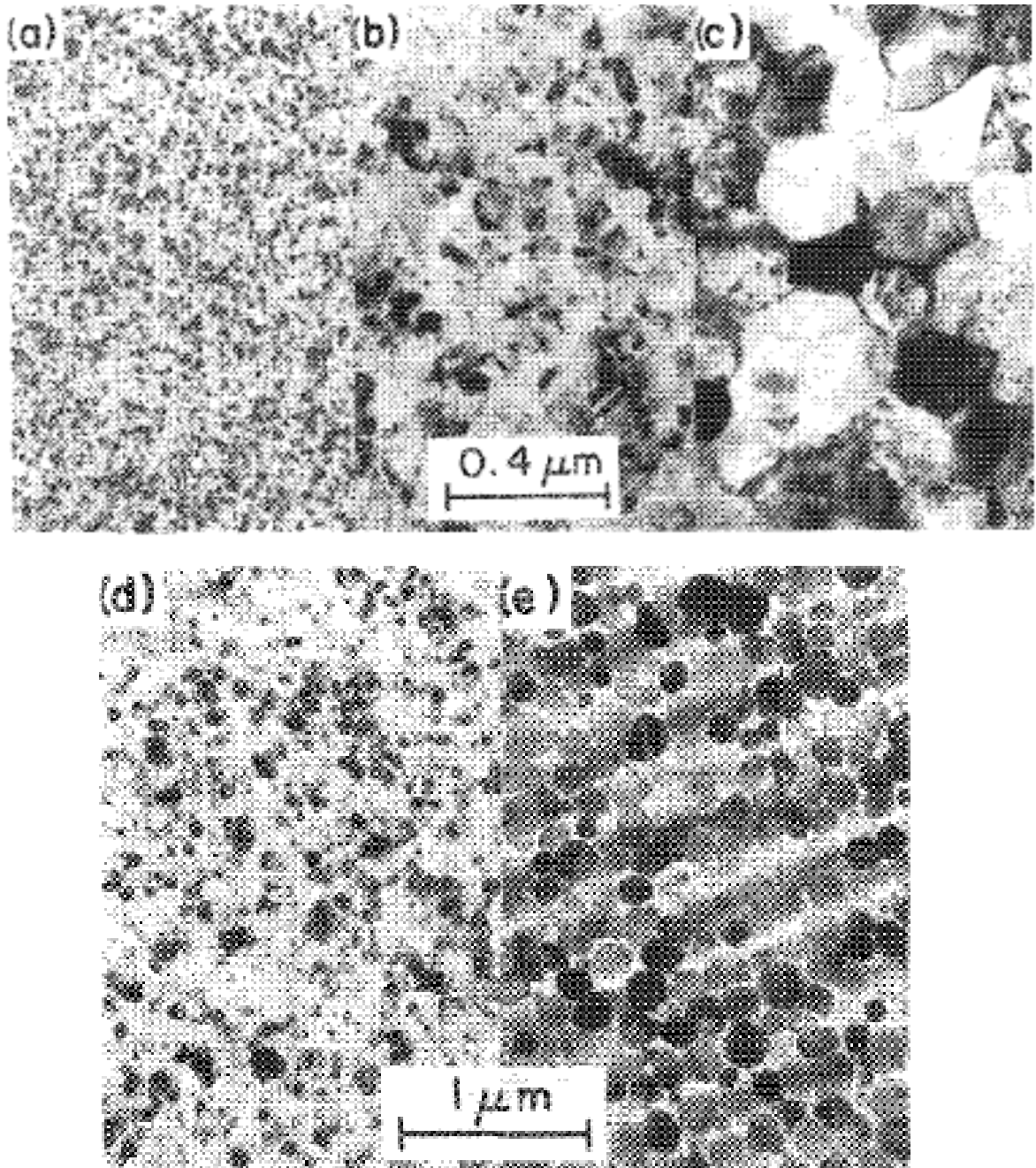
Figure 8: (a-c) TEM micrographs for 3Ni:Al multilayer films: (a) as-deposited, (b) annealed to 750K, (c) electrically ignited; (d,e) Al3:Ni multilayer films: (d) annealed to 1000K, and explosively reacted [2].

$$\frac{dH}{dt} > C\frac{dT}{dt} + \frac{dE_1}{dt}, \qquad\qquad\qquad\qquad \text{Eqn. (9)}$$

where the term on the left is the rate of heat release, which is faster than the heat absorption rate of the requirements for intermetallic formations ($C\frac{dT}{dt}$) and initiation barriers ($\frac{dE_1}{dt}$). Looking at the right hand side of Eqn. 9, H is the heat generation from the exothermic reaction, C is the specific heat of the intermetallic formation, and E_1 is the thermal energy barrier due to the heat dissipation by radiation or conduction.
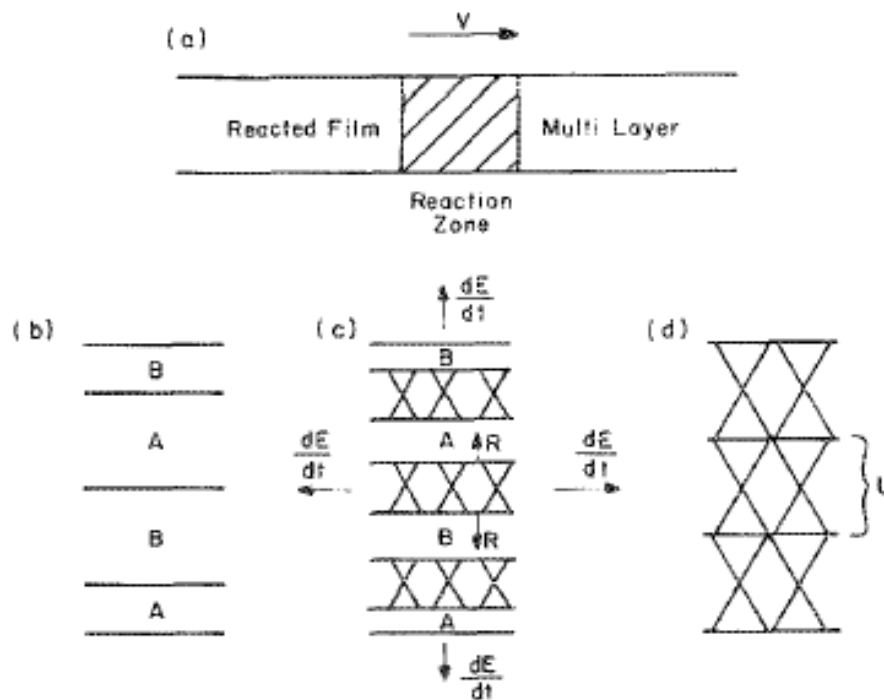
Figure 9: Sketches of SHS in multilayer thin films: (a) self-sustained reaction propagated in the multilayer sample, (b) initial sample with A (Ni) and B (Al) alternatively stacked, (c) reactions proliferated in both directions parallel and perpendicular to the staking direction, (d) fully reacted Ni/Al multilayer sample [2].

The releasing heat *(H)* is shown:

$$\frac{dH}{dt} = (\frac{H_v}{L})R(T),$$
<div align="right">Eqn. (10)</div>

where H_v is the heat of formation per unit volume, and *L* is the bilayer length, which is the summation of the thickness of the element A and B. By substituting Eqn. (10) for Eqn. (9), the following inequality is obtained:

$$L < \frac{H_v R(T)}{f(T,T_0)},$$
<div align="right">Eqn. (11)</div>

where the *f(T, T₀)* is a polynomial function of the reaction temperature *T*, and T_0 is the ambient temperature. Therefore the limited bilayer thickness *L* for specific reaction temperature do exist. In the Ni/Al thin film case, the maximum bilayer thickness for SHS is about 50nm [2]. This result is consistent with the work done by Gavens *et al.* [39]. They proposed that the SHS reaction can possibly be prohibited due to the bilayer thickness and intermixing layer. Since the SHS reaction is a thermal diffusion process, the total time to finish the reaction usually takes several micro or milliseconds [2, 38]. This diffusion controlled reaction is significantly slower than the reaction presented in the next section.

2.2.7 Shock-induced and shock-assisted reactions

The significant factors that dominate shock induced or assisted reactions are the prevailing high pressure, stress, strain-rate, and temperature states during the micro-scale

duration of the shock front propagation [20]. The important associated effects during the shock compression, such as void collapse, particle deformation and flow, particle fracture, intermixing, caused inter-particle fusion, phase transformation [40], and chemical reactions are possibly existing phenomena in the recovered samples.

In solid state, a mathematical description of the state of the material behind the shock wave with respect to the state variables ahead of it can be obtained from the conservation of mass, momentum, and energy, assuming hydrodynamic behavior. This results in the famous Rankin-Hugoniot relationships [41]:

$$U_p - U_o = U_s \left(1 - \frac{V}{V_o} \right),$$ Eqn. (12)

$$P - P_o = \left(\frac{U_s}{V_o} \right)(U_p - U_o),$$ Eqn. (13)

$$E - E_o = \frac{1}{2}(P + P_o)(V_o - V),$$ Eqn. (14)

here the U_o, V_o, P_o, E_o corresponded to the particle velocity, volume, pressure and energy in the initial state respectively, and the V, P, E are the specific volume, pressure, and

internal energy, respectively. The U_p and U_s variables are particle and shock velocity respectively. An additional equation of state is also required in order to determine all the shock wave parameters. This equation empirically relates the shock velocity U_s, and the particle velocity U_p :

$$U_s = C_o + SU_p$$
Eqn. (15)

where C_o is the elastic sound velocity in the materials and S is a characteristic constant of the material. Using these equations, all the shock parameters can be determined, once any two variables are known.

The shock compression and recovery experiments are carried out by a variety of geometries and tools on solid materials. There are several common approaches for generating shock waves such as the impact of a projectile accelerated in a gun driven by compressed gas or gun powder [19, 20], the detonation of explosive with a shock-transmitting driver plate [6, 7, 21], the laser-driven shock compression with direct or indirect laser exposure [42]. Due to the experimental setup, the reactions are commonly found at the peripheral area and the center of the bottom end of the samples in the projectile or flyer shock experiments [6, 7, 21, 43, 44] corresponding to the two-dimensional focusing effect, caused by the mismatch of the shock impedance between the sample and the containment. This effect can be numerically simulated by a two-dimensional Eulerian CSQ code [45]. Figure 10 shows the simulation results that represent the sequential progress of the two-dimensional focusing effect. The incident wave from the copper flyer initially generates pressure waves in the powder compact (Figure 10 (a)). The shock pressure propagates faster in the containment than in the

porous powder compact due to the faster shock wave velocity in denser materials [20, 46]. Batsanov carried out a variety of experiments and found that for porous materials, the shock wave velocity, D, can be theoretically expressed as

$$D = A + BU,$$

<div align="right">Eqn. (16)</div>

$$U^2 = U_o^2 + k(m-1)PV_o,$$

<div align="right">Eqn. (17)</div>

$$m = V_{00}/V_0,$$

<div align="right">Eqn. (18)</div>

where A is the bulk sound velocity, B is a constant, U_o is the mass velocity for the monolithic material, U is the mass velocity, k is equal to 6/7, P is the pressure corresponding to U_o, and V_o and V_{oo} are the volumes of the porous and monolithic materials respectively. It leads to a significant inconsistency between theoretical estimations and experimental measurements. Because k, P and V_o are all positive values, when the V_{oo} approaches V_o, the porous material has the lowest shock velocity. Batsanov [46] proposed that this inconsistency was owed to the inhomogeneous structure in the porous materials, which resulted in numerous shock wave propagation obstacles. This is consistent with the Kiselev's discovery [47], which shows that porosities make the shock wave width become longer. This shock wave velocity mismatch causes a wave propagation profile shown in Figure 10 (b). After the shock wave propagated to the

bottom end of the containment, the radial wave proliferates into the sample and interacts with the shock wave propagating in the sample, which results in a variety of void collapses, grain deformations, and fractions in this shock wave interacting section. Finally, the radial wave dominates the loading process, generating a high pressure region along the center axis of the compact (Figure 10 (c) & (d)).
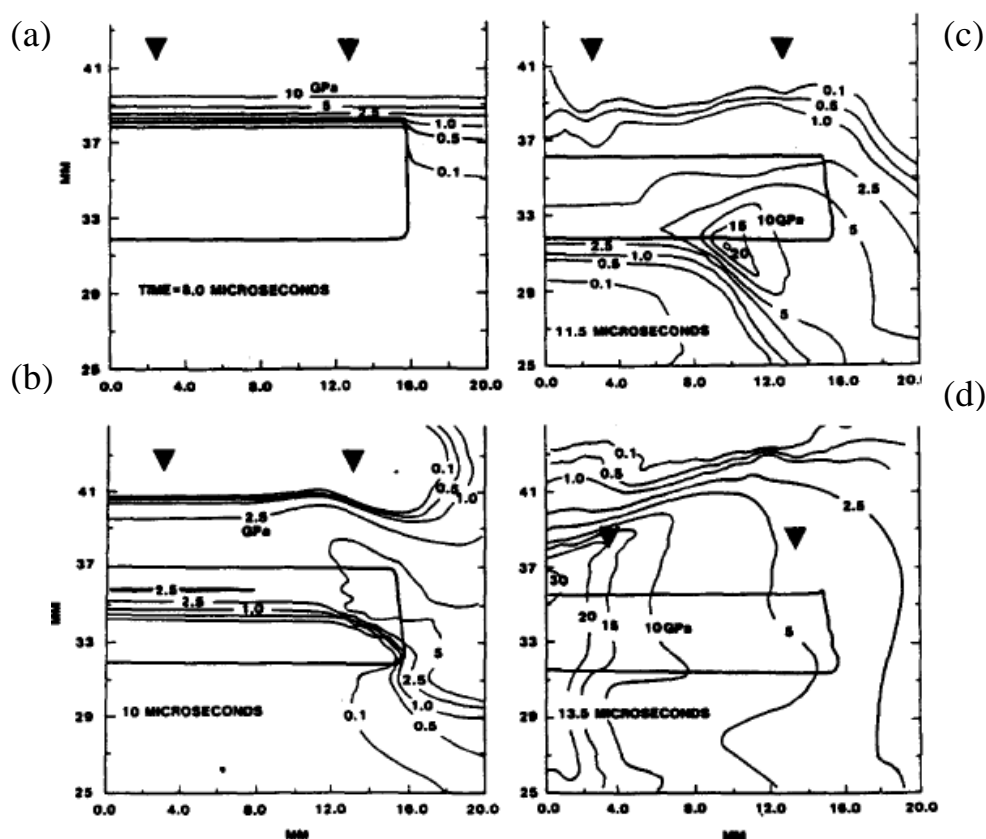
Figure 10: Typical CSQ simulated pressure contours in a rutile powder sample and copper containment at (a) 8, (b) 10, (c) 11.5, and (d) 13.5 microseconds [45].

The chemical reactions of the shock induced and assisted reaction were used to facilitate the bonding strength between different materials and produce new materials. These reactions may have different morphologies depending on each distinctive

experimental setup. The shock initiated reaction from conventional flyer plate experiments are shown in Figure 11. The reaction can be defined as three explicit regions: (a) non-reacted, (b) partially reacted and (c) & (d) fully reacted region [48, 49]. A variety of distributions of reaction regions are contributed by different experimental setups. An explosive-driven shock compression can generate concentric distributions in a cylindrical sample [50] (see Figure 12).
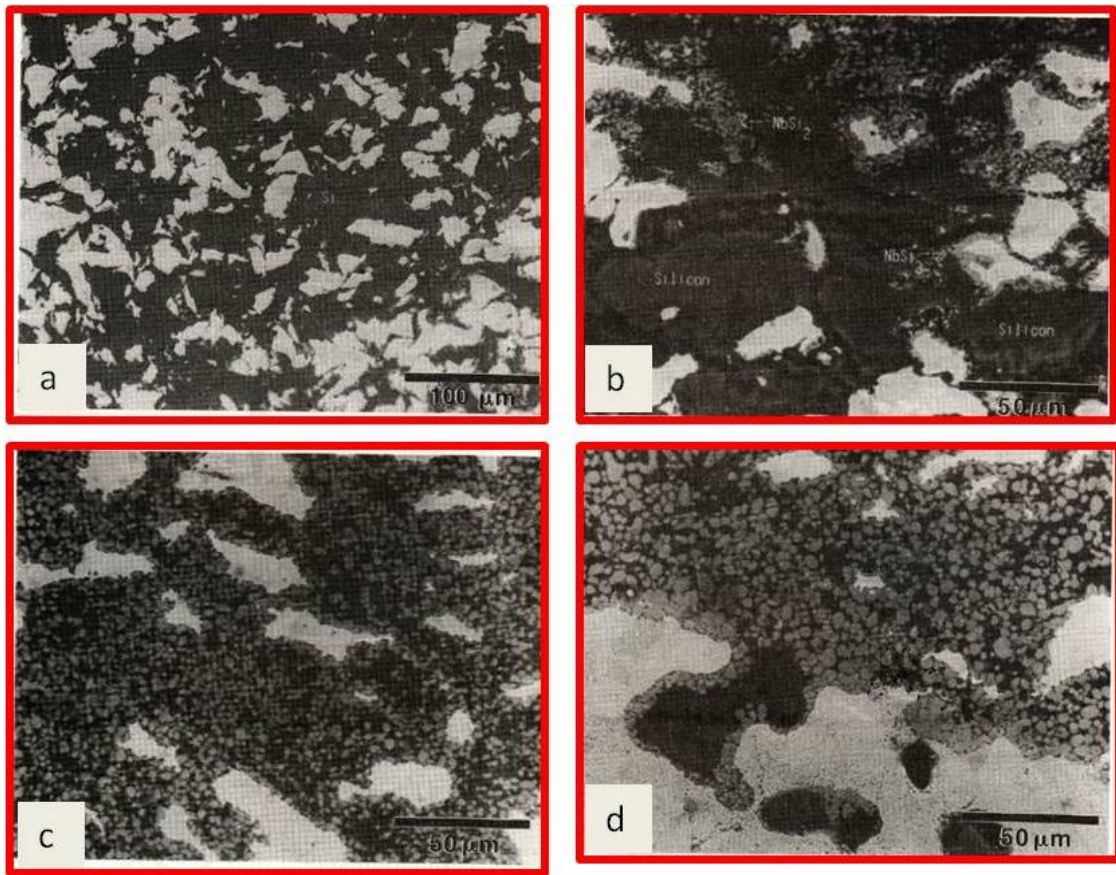
Figure 11: Mo-Si binary system: (a) the non-reacted region has no reaction phenomena such as molten phases or intermetallics, (b) the partially reacted region has some portions with intermetllics in spherical shape, and some non-reacted regions, (c, d) fully reacted regions have intermetallics all over the Si matrix and the Mo-Si interfaces [48, 49].

Other mechanisms of shock initiated reactions are going to have further discussions in the content of this dissertation. It should be noted that these mechanisms are still not well-understood due to the difficulties of obtaining a real-time investigation under the extremely short reaction time (usually several nano-seconds to micro-seconds).
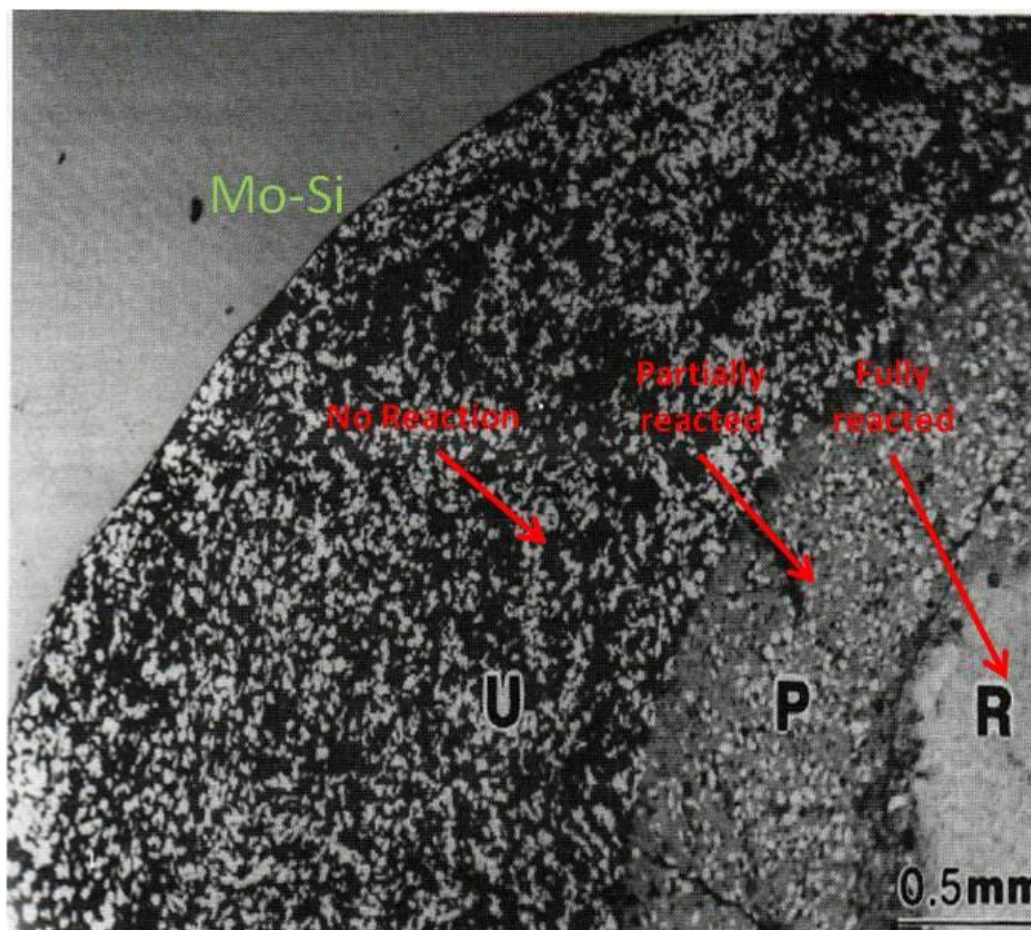
Figure 12: A cylindrical sample shock by an explosive compression setup. U is the non-reacted region, P is the partially reacted region, and R is the fully reacted region. These three regions are distributed concentrically [50].

Chapter 3.

Experimental techniques

There were several quantitative, qualitative, and computational analyses used to investigate original and recovered samples. Quantitative methodologies such as scanning electron microscopy (SEM), transmission electron microscopy (TEM), x-ray diffraction spectrometer (XRD), electron discharge spectrometer (EDS), etc. were used to systematically study compositions of initial and recovered samples. Mechanical methodologies including quasi-static compression and tensile tests, the split Hopkinson bar test, and Vickers hardness tests were applied for characterizing the hardness values of materials. Two simulation approaches, HYADES and RAVEN, were used to interpret the fracture behaviors and predict the meso-scale mechanical responses. The experimental method by means of the test setup, theoretical principle and practical issues is discussed in this chapter.

3.1 Sample preparation:

In this study, the reactive materials were produced as cold-rolled laminates and powder consolidated compacts in order to mimic the commercial materials used in construction, aerospace, and military applications. There are five different nearly fully dense (> 95% TMD) reactive mixtures, Nb+Al, Ni+Al, Mo+Al, W+Al, Ta+Al, compacted by means of double tube explosive shock consolidation. Also the poly- and mono-crystalline vanadium were obtained from commercial products and machined to required dimensions. Nano-scale Ni-Al laminates were produced using the magnetron

sputtering physical vapor deposition (PVD). These sample preparation procedures are introduced in the following sections.

3.1.1 Accumulative roll bonding (cold rolling for micro-laminates)

In 1848, the continuous rolling mill was built in 1848 by R. M. Daelen of Lendersdorf Germany [51]. It was the first generation of the rolling mill industry. There were two different rolling processes which were used commonly in the industry, cold rolling and hot rolling [51]. Hot rolling process was commonly used on shaping materials, and cold rolling process was mainly applied for reducing the thickness. Due to a large shear strain and the severe friction while the material was rolled, the mechanical alloying phenomena were found in many sheets and alloys produced by cold rolling process. In the cold-rolled elemental layers, the amorphous phase and intermixed layers were usually found [52] in the materials. For instance, Ni-Al, Cu-Zr, Mg-Ni, Al-Pt [52] and Zr-Al-Ni-Cu [53], those laminated foils underwent an amorphization reaction induced by cold rolling process. Figure 13 TEM plane-views (a), (b), (c), and (d) show the original states of the Ni and Al foils, and the states of the 30 and 70 times cold-rolled Ni-Al layered samples respectively [52]. These TEM characterizations proved that Ni-Al layered foils were broken into small grain sizes and tended to form amorphous structure after cold-rolling (the lower left inset of Figure 13 (d)). Qureshi *et al.* [54] published that in FCC metal, a network of laminar twins was found after cold-rolling (see Figure 14). These tendencies for amorphization and crystallographic transformation significantly affected mechanical and chemical properties of the material.
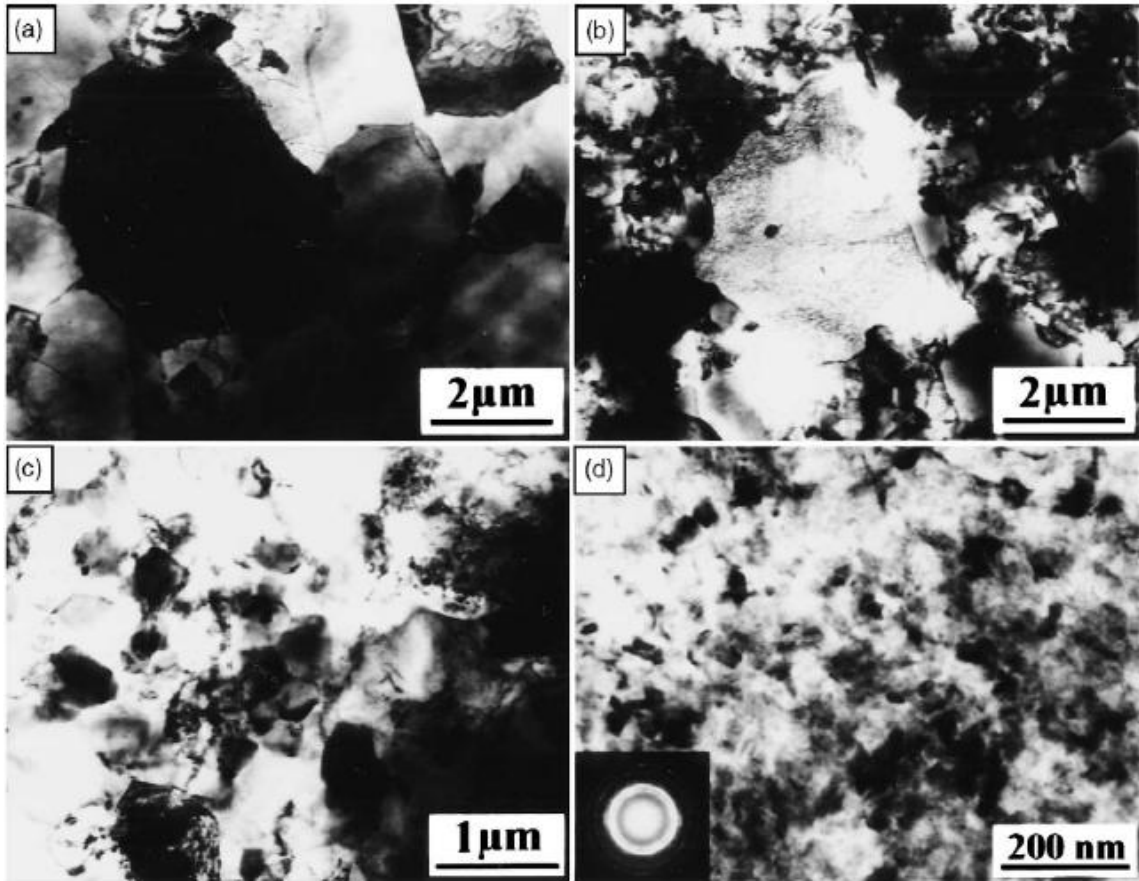
Figure 13: Sieber et al. [52] TEM plane-view images of (a) the initial Al foil, (b) the initial Ni foil, (c) Ni-Al layered sample after 30 rolling cycles, and (d) after 70 rolling cycles.

In this study, the Ni/Al laminates with micro-scale bilyaer thickness, 5 and 30 μm were produced by a successfully accumulative cold-roll bonding [55-62]. It will be discussed in the following sections.
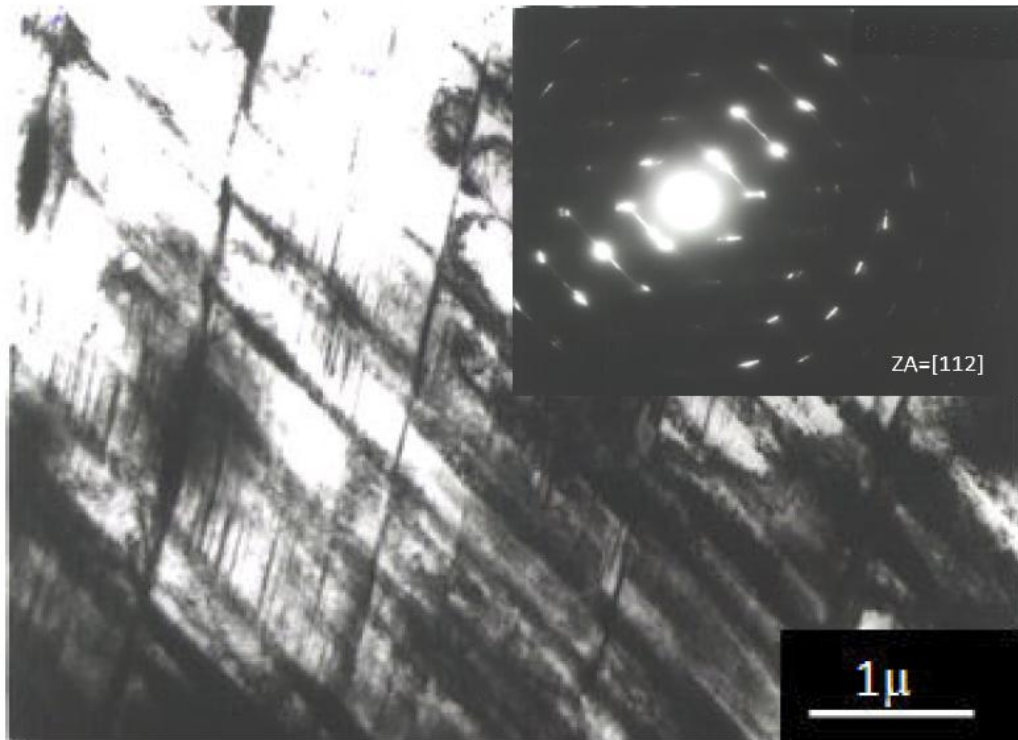
Figure 14: Bright field TEM image and corresponding diffraction pattern of cold rolled sample aged at 550°C from Qureshi et al. [54].

Three different Ni-Al laminates were used: micro-laminates with bilayer thicknesses, 5 and 30 µm; and a nano-laminate with 54 nm bilayer thickness. These two micro-scale laminates were made by a successful cold-rolling process. It should be noted that the most common manufacturing procedure for generating reactive laminate was the physical vapor deposition (PVD) which was capable to produce a bilyaer thickness on the submicron scale (~ tens or hundreds nano-meters) [16, 17]. However, the PVD cannot produce the laminar structure with sufficient mechanical strength and properties for the aerospace, construction, and military applications.

The cold rolling process was used for producing the micro-scale Ni-Al laminar structure [55-61]. Figure 15 is the scheme of the cold rolling process. Pure Al and Ni sheets with different thicknesses were used to produce the cold-rolled multilayer Ni-Al laminates. There were two distinct combinations chosen for making two unique Ni-Al laminates. One was made of a 25 µm thick Al sheet and a 18 µm thick Ni sheet; the other was made of an 178 µm Al sheet and a 127 µm Ni sheet. These two Ni/Al layer-staking sheets were rolled and folded repeatedly to obtain the required bilayer thicknesses of 5 and 30 µm respectively. The details of the sample conditions are listed in Table 1. The schematic plots of the manufacturing procedures were officially published by Qiu *et al.* [55-58] and Weihs *et al.* [60].

Table 1. Details of the Ni-Al laminates

Sample	Initial Ni	Initial Al	Bilayer Thickness	Total Thickness	Total Bilayers
Ni-Al-5 µm	18 µm	25 µm	5 µm	0.85~0.9 mm	~ 175
Ni-Al-30 µm	127 µm	178 µm	30 µm	0.8~0.85 mm	~28
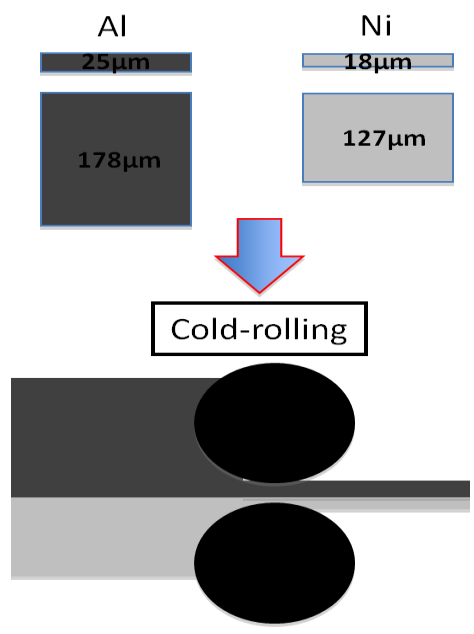
Figure 15: Scheme of the cold-rolling process: two different materials, Al and Ni, with two distinct combinations, 25 µm Al + 18 µm Ni and 178 µm Al + 127 µm Ni, were rolled and fold repeatedly.
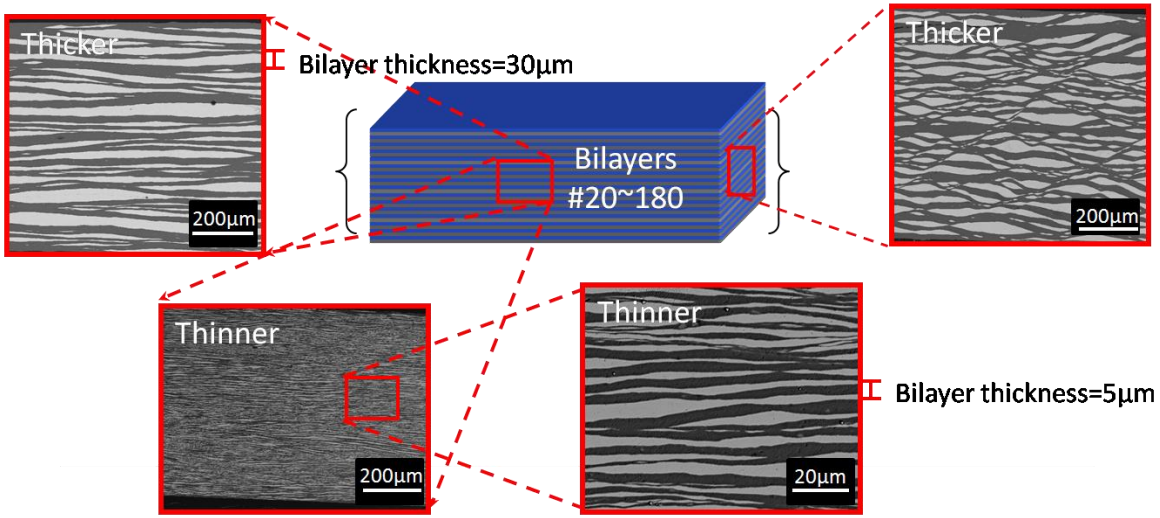
Figure 16: The cross-sections of two different laminates have three distinct morphologies: the non-uniform laminar structure in the thicker bilayer sample (top-left inset), the wave form layers with isolated Ni fragments in Al matrix in the thicker bilayer sample.

Figure 16 depicts varied morphologies of the cross-sections of the Ni-Al laminates in this study. Due to the high strain caused by the cold rolling process, the laminar structures had distinguishable morphologies depending on the rolling direction, the dimension and the mechanical properties of the materials. The thicker bilayer samples have two different morphologies of the cross-sections. The non-uniform laminar structure was along with the cold-rolling direction, and the wavy layer structure was perpendicular to the rolling direction in the laminate with 30 µm bilayer thickness. However, for the sample with thinner bilayer thickness (Figure 16 lower insets), the micro-morphology showed only the localized homogeneous distribution of Ni-Al binary phase. Nevertheless, it should be noted that the as-produced laminates were shattered and ground for the qualitative analysis such as DSC [5] and XRD [56]. There was no reaction and intermixing found in the micro-scale Ni-Al laminates. In fact, the as-produced Ni-Al laminates can also has pre-existing intermetallics or intermixing phase due to different manufacturing methods such as PVD or CVD. The detail of the chemical properties and reactions for as-produced and recovered laminates is discussed in section 2.2.1.

3.1.2 Physical vapor deposition (nano-laminates)

The advanced thin film production for submicron or nano-scale films was usually conducted by physical vapor deposition [63]. Physical vapor depositions such as magnetron sputtering, electron-beam evaporation, or thermal evaporation had the capacity to precisely control the thickness of the film within several micro-meters (10^{-6} m) to few angstroms (10^{-9} m). Due to its high vacuum manufacturing condition which is 10^{-7}

$\sim 10^{-10}$ torr, the film can be deposited with a extremely high purity without oxidations and impurities.

Figure 17 (a) shows the scheme of the electron beam physical vapor deposition chamber [64]. It should be noted that the designs of these types of PVD machines could vary greatly depending on the evaporators, manufacturing companies, and other specific requirements such as vacuums and other processing steps that lead to residual stresses, but the general principle is basically the same. In the high vacuum chamber, there are three major parts, evaporator, substrate holder and feeder holder. The evaporator could be an electron beam or a thermal coil. It supplies sufficient heat or physical bombardment for melting and evaporating the feeding materials. The feeder holder usually is made of ceramic which can sustain the high temperature and prevent unwanted chemical reactions. The feeding materials can be metals, ceramics, or alloys depending on the specific manufacturing needs. The substrate holder carries substrates, which can be silicon, glass, or metals. The mechanical rotor is commonly embedded in the substrate holder, which helps to have uniform films.

The nano-scale laminar structure was produced by magnetron sputtering physical vapor deposition in this study. By using this method, the bilayer thickness can be precisely controlled. Other setups of PVD machines are with different evaporators such as thermal heat sources for evaporative deposition, plasma for sputter deposition shown in Figure 17 (b) and (c) [63].
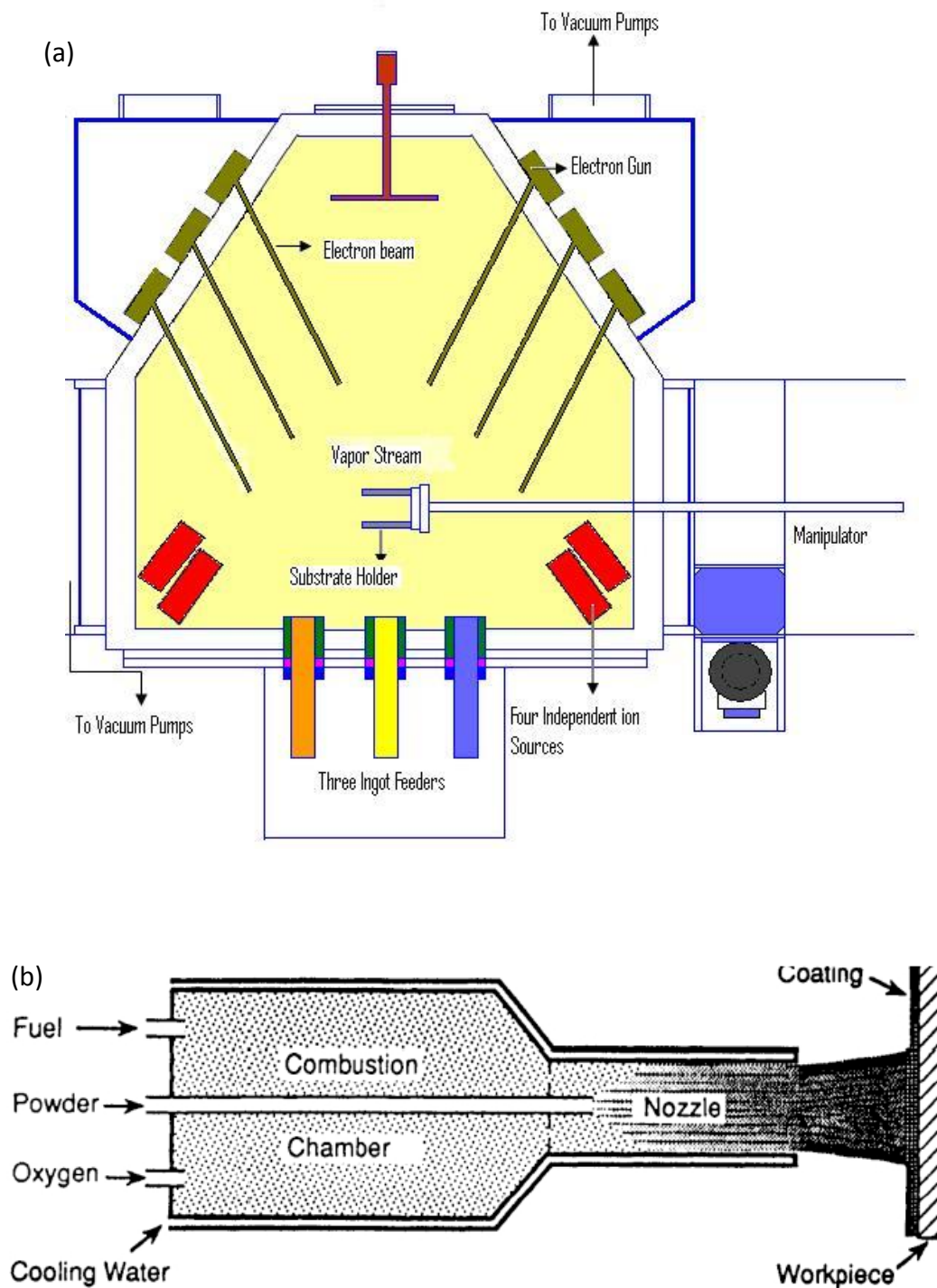
Figure 17: (a) Ebeam sputtering physical vapor deposition [64]. (b) Advanced thermal spray deposition. (c) Sputtering deposition [63]. (figure continued)
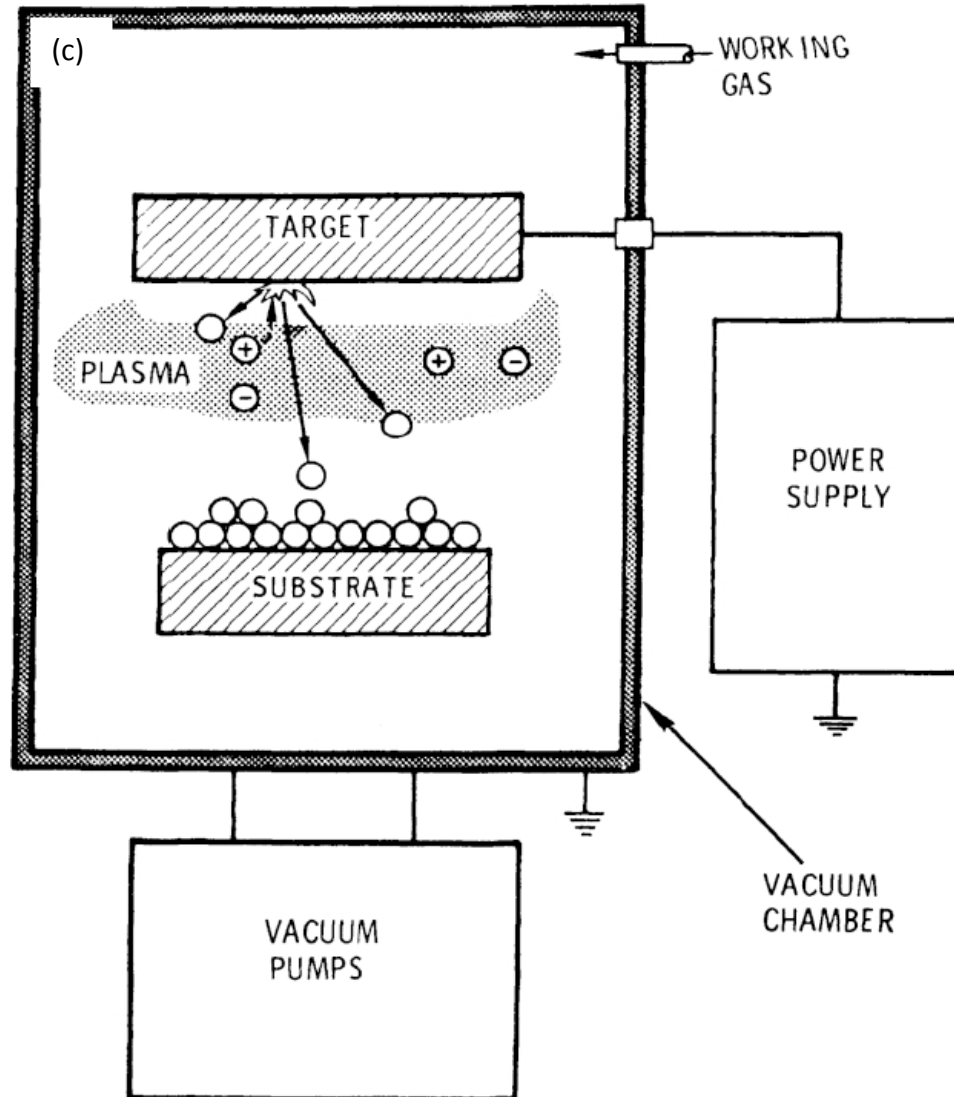
Figure 17: Continued.

3.1.3 Double explosive shock consolidation (powder consolidated cylinders)

Powder consolidated cylinders were prepared by using double tube explosive shock consolidation at Georgia Institute of Technology [65, 66]. Five commercial elemental powders (mesh: 325 = 44 μm, and purity higher than 98%), Al, Ni, Nb, W, Mo, Ta, were employed for producing binary reactive mixtures. Each elemental powder has

specific particle morphology and size (Figure 18). The Ni, Al, and W powders (Figure 18 (a, b, e)) have relatively homogeneous shapes and particle sizes while the Nb, Ta, and Mo (Figure 18 (c, d, f)) have arbitrary shapes and sizes (in a range of less than 1 μm to 50 μm diameter). The particle sizes of Ni, W, and Al are 30~80 μm diameters. It should be noted that the powders with relatively small particle sizes such as Nb, Ta, and Mo are easily clustered due to the significant increase in the surface area causing strong van der Waal forces [67]. This might ultimately affect the macroscopic morphologies of the compacts.

The powders were blended in a equivolumetric ratio of Nb/Al, Ni/Al, Mo/Al, W/Al, and Ta/Al mixtures using a V-blender, then placed into the inner tube of the double tube explosive consolidation system as shown in Figure 19, which was developed by Meyers and Wang [68]. This setup had a cylindrical geometry with two co-axial tubes. An outer cylinder isolated the inner cylinder of the inner tube and the powder mixture was placed in the inner tube that surrounded the Al mandrel, which helped to prevent the Mach stem (Figure 19) [68]. The inner tube containing the powder mixture was enclosed by ANFO, which detonated and obtained the explosive velocity of 2.6km/s. The peak pressure was in the range of 4~7 GPa through the entire explosive consolidation process [65, 66]. After consolidation, the reactive mixtures, Ni+Al, Nb+Al, Mo+Al, W+Al, and Ta+Al, were machined into cylindrical rods.
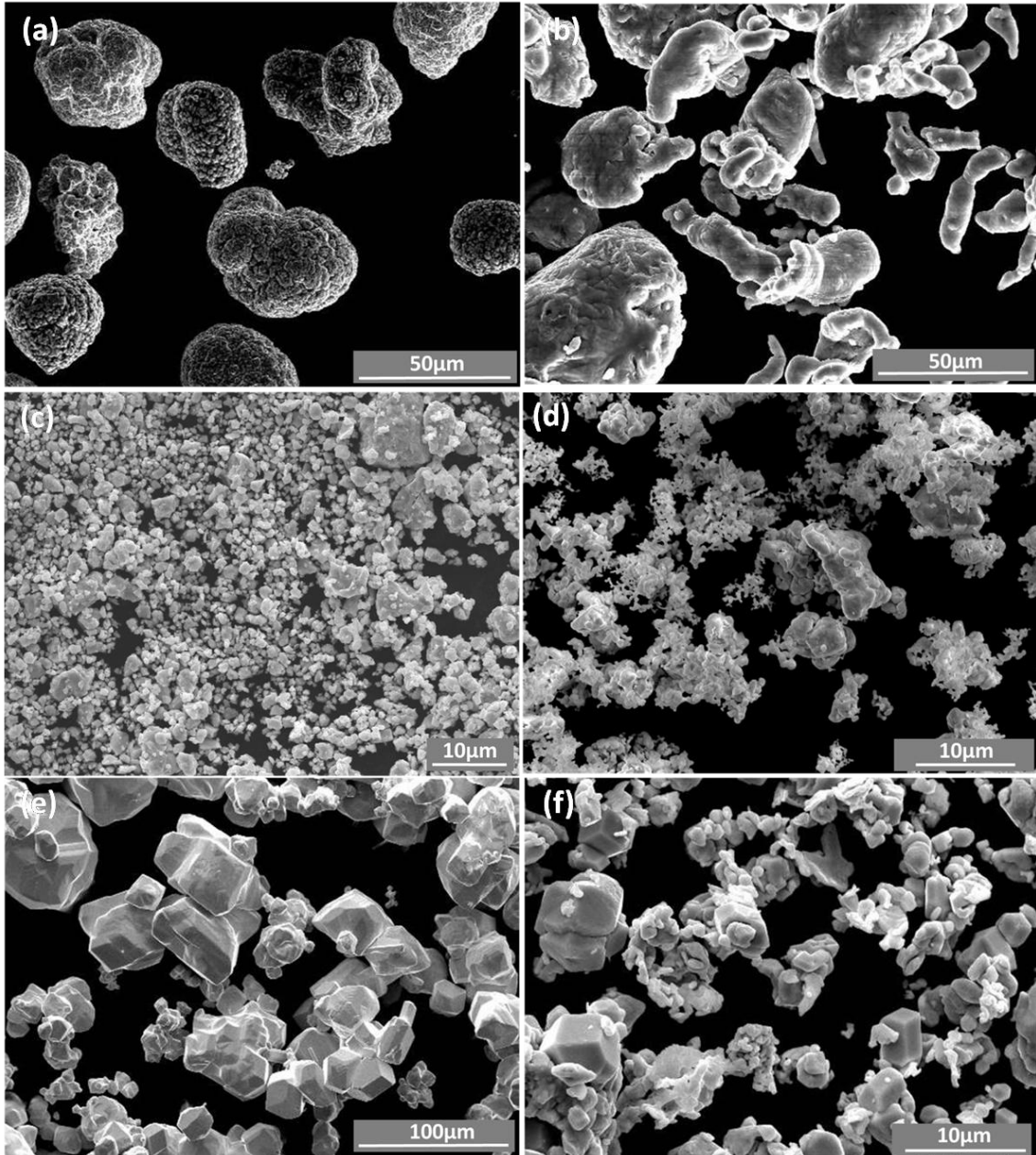
Figure 18: The SEM images of original (a) Ni, (b) Al, (c) Nb, (d) Ta, (e) W, (f) Mo powders.
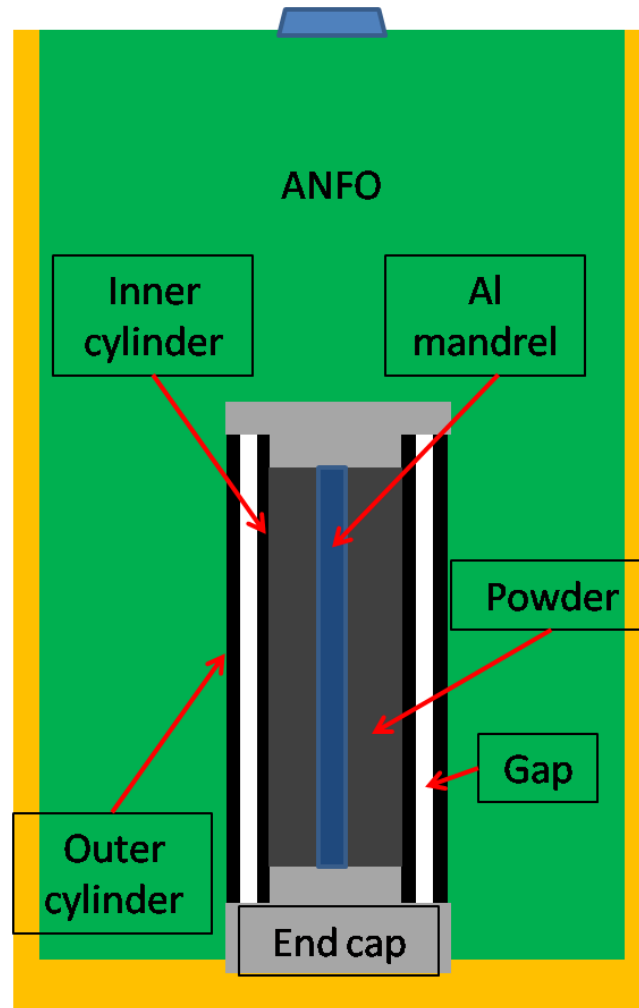
Figure 19: Double tube explosive consolidation setup [68].

By using the double tube explosive consolidation, these compacts could reach very high densities which is about ~99 % TMD. These highly dense compacts had the mechanical properties close to the fully densified bulk materials. However, due to the high peak pressures, these powder mixture compacts might have certain amounts of intermetallics and pre-existing cracks after shock-consolidation. These intermetallics and pre-existing defects may influence the mechanical properties of the shock consolidated

powder mixtures significantly. Table 2 shows the details of the a-produced powder consolidated cylinder [66].

Table 2. Powder mixtures and densities characteristic of double shock consolidated samples [66].

Powder	Packing density (g/cm3)	Final shock consolidated compact (g/cm3)
Ni-Al, ρ=5.8	ρ=3.79, 65%	Top ρ=5.527, 95.3% Bottom ρ=5.768, 99.5%
Ta-Al, ρ=9.65	ρ=5.50, 57%	Top ρ=9.088, 94.2% Bottom ρ=9.275, 96.1%
Nb-Al, ρ=5.62	ρ=4.04, 72%	Top ρ=5.521, 98.2% Bottom ρ=5.535, 98.5%
Mo-Al, ρ=6.45	ρ= 4.07, 63%	Top ρ=6.204, 96.2% Bottom ρ=6.241, 96.8%
W-Al, ρ=11	ρ=7.48, 68%	Top ρ=10.850, 98.6% Bottom ρ=10.957, 99.6%

3.1.4 Vanadium (single and poly crystal)

The polycrystalline vanadium foils used in this work were obtained from Alpha Aesar and had a purity of ~99.8%. Three different foil thicknesses were used: 75, 127 and 250 µm. Polycrystalline specimens from each of the three as received foils were cut, polished and etched to measure the grain size. Monocrystalline specimens with the orientations <1 1 0> and <1 0 0> and thickness 250 lm were used. They were obtained from Accumet Materials and had a reported purity of ≥99.999%. The monocrystalline elemental materials can be produced by a slow RF-couple plasma spray deposition process [69], molecular beam epitaxy (MBE), or slow thermal deposition.

3.2 Quasi-static tensile and compression test

Universal test machine was employed to characterize elastic and plastic behaviors of materials. This basic mechanical test setup provided the essential information of mechanical properties of materials. Elastic and plastic behaviors of materials related to a variety of factors such as manufacturing methods, grains sizes, dislocations, etc. Hence the information from the quasi-static tests played a significant role in the practical point of view.

The universal test machine is show in Figure 20. A cylindrical specimen is tested in the universal test machine through compressing or tensile loadings. The shape of the testing specimen can be various depending on different requirements and materials' conditions. In Figure 20, the upper part of the specimen is fixed on the crosshead of the machine. Two lateral screws control the movement of the upper load cell. Strains are measured by extensometers, strain gages, or from the indirect motion of the load cell. The machine is usually connected to a computer for recording the measurement and controlling the machine.

The normal force applying on the sample can be qualitatively presented as engineering stress σ defined as the resistance per unit area:

$$\sigma = \frac{F}{A_o} \hspace{4cm} \text{Eqn. (19)}$$

where F is the normal force and A_o is the original area of the cross-section surface which is perpendicular to the loading direction. This force results in a corresponding deformation which can be presented as the engineering strain ε:

$$\varepsilon = \frac{\Delta l}{l_o}$$

<div align="right">Eqn. (20)</div>

where Δl is the change of the length, and l_o is the original length. However these stress σ and strain ε cannot represent the real time deformation of materials while compressing or stretching due to a three dimensions deformation, hence the true stress σ_t and strain ε_t are employed in order to obtain more accurate values:

$$\sigma_t = \frac{F}{A} = \sigma \frac{A_o}{A}$$

<div align="right">Eqn. (21)</div>

$$\varepsilon_t = \ln(1+\varepsilon)$$

<div align="right">Eqn. (22)</div>

where the A is the real time cross-sectional area changing with testing time. It should be noted that the elastic deformation in metals and ceramics rarely exceeds 0.005, therefore the differences between engineering and true stress and strain are negligible for most of the cases.
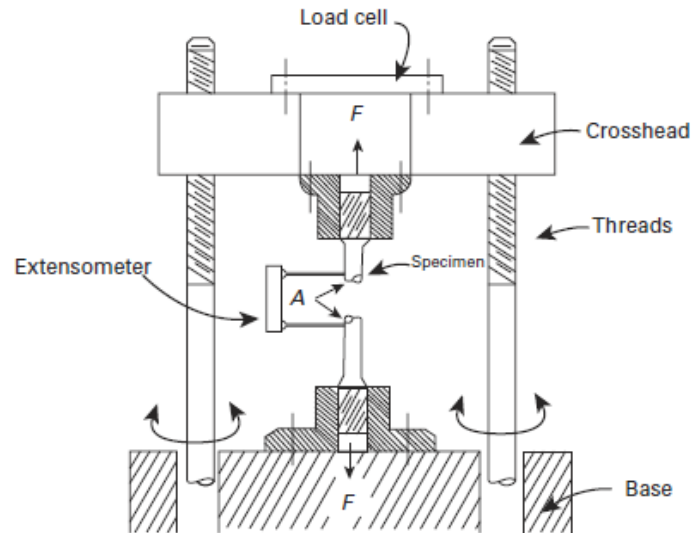
Figure 20: Sketch of screw-driven tensile-strength testing machine [28].

3.3 Split Hopkinson pressure bar

The split Hopkinson pressure bar are employed to investigate dynamic behaviors of materials. An elastic shock-wave propagates through a cylindrical or rectangular sample and induces a corresponding dynamic process. The five major parts assembled to build a split Hopkinson pressure bar system are listed as follows [70]:

1. Two long and symmetrical bars

2. Bearing and aligned fixtures to allow the bars and striking projectile to move freely while retaining precise axial alignment

3. Compressed gas launcher/gun tube or alternate propulsion device for accelerating a

projectile, termed the striker bar, to produce a controlled compressive pulse in the incident bar

4. Strain gages mounted on both bars to measure the stress-wave propagation

5. Associated instrumentation and data acquisition system to control, record, and analyze the stress-wave data in the bars.

Figure 21 presents the schematic plot of the split Hopkinson pressure bar. A striker bar is pushed by a compressed-air driven gas gun. The striker generates elastic shock-waves, which propagate through an incident bar to the sample, and then reach a transmitted bar. Two pairs of sensitive strain gages are attached on the transmitted and incident bar respectively. A momentum trap is placed and aligned after the rear end of the transmitted bar in order to stop the movement. All parts are fixed by a set of aligned fixtures. The

pulse shape of transported shock waves is presented at the lower part of Figure 21. The

shock wave ε_I propagates from the incident bar, then reaches the cylindrical sample.

Here a reflected wave ε_R forms due to the shock impedances corresponded to two

different materials of the incident bar and the sample. This reflected shock wave can be

measured by the strain gages attached on the incident bar and used for investigating the

dynamic responses of the tested samples. After the shock wave ε_T propagates through the

transmitted bar, the rest of the shock energy is trapped by a momentum trap usually made

of Pb or other soft materials.
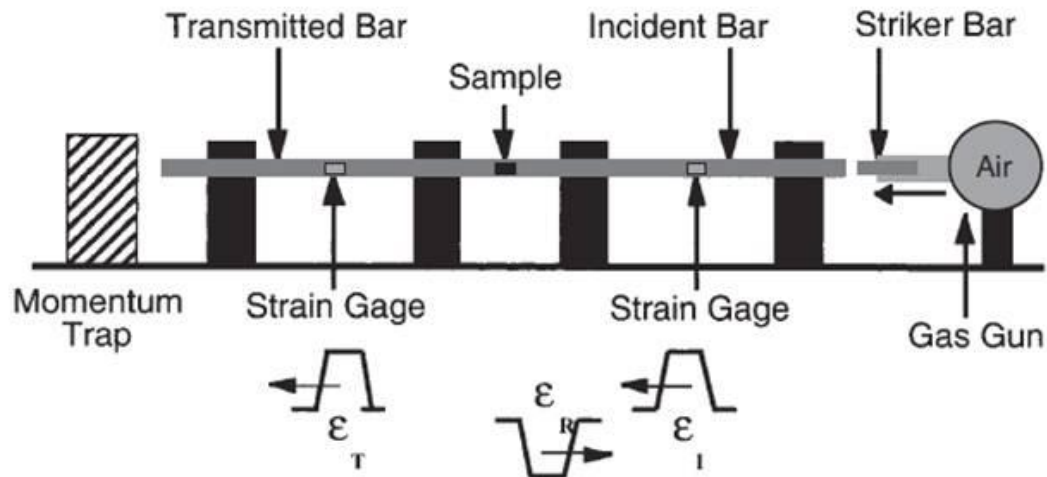
Figure 21: The split Hopkinson pressure bar system [70].

The dynamic strain rate of the split Hopkinson pressure bar can reach several

thousand per second. The strain rate usually is not constant due to the work hardening

mechanism of materials (see Figure 22) [71]. Figure 22 shows the NiTi superelastic alloy

has suffered a non-uniform stress while the shock wave propagate through the sample

due to the strain hardening effect (see the reflected wave of Figure 22). This strain

hardening phenomenon causes the strain rate vs. strain curves to decrease as well(Figure 22 (b)). Therefore it becomes a critical problem for researchers, who use the split Hopkinson pressure bar to study the dynamic behaviors of materials. In order to obtain a constant strain rate during shock compression, a shaped incident shock wave is necessary.
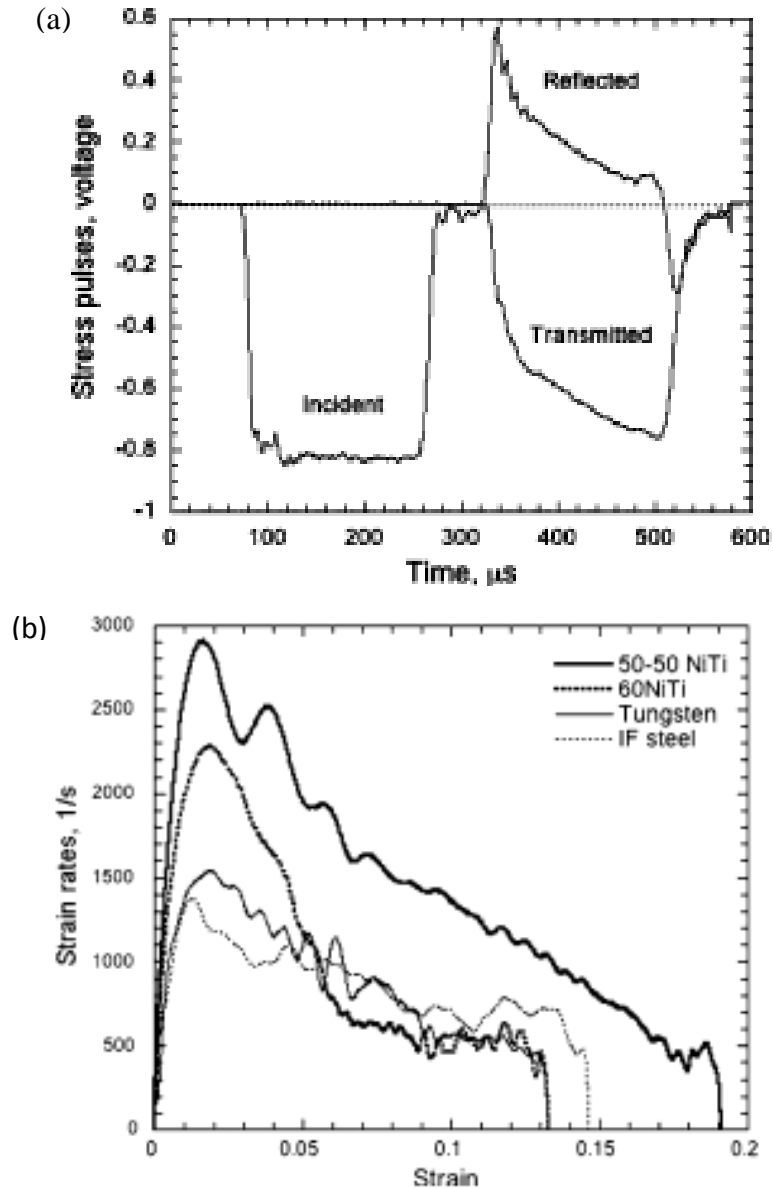
Figure 22: (a) Stress vs. time plot of 50-50 NiTi super-elastic alloy at room temperature. (b) Strain rate vs. strain curves of metals show the strain hardening induced inhomogeneous strain rate [71].

Therefore a variety of pulse-shaping methods are proposed [72-81] in order to achieve a constant strain rate and dynamic stress equilibrium in samples to obtain reliable mechanical properties of the materials. By applying pulse-shaped incident wave, the constant strain rate can be obtained. For example, Figure 23 presents incident and reflected waves after applied pulse shapers placed at the front end of the incident bar (transmitted pulse shaper) [71]. The pulse shaper alters the incident shock wave and increases the rise time. These results in a flat and smooth reflected wave, demonstrating a constant strain rate is obtained.
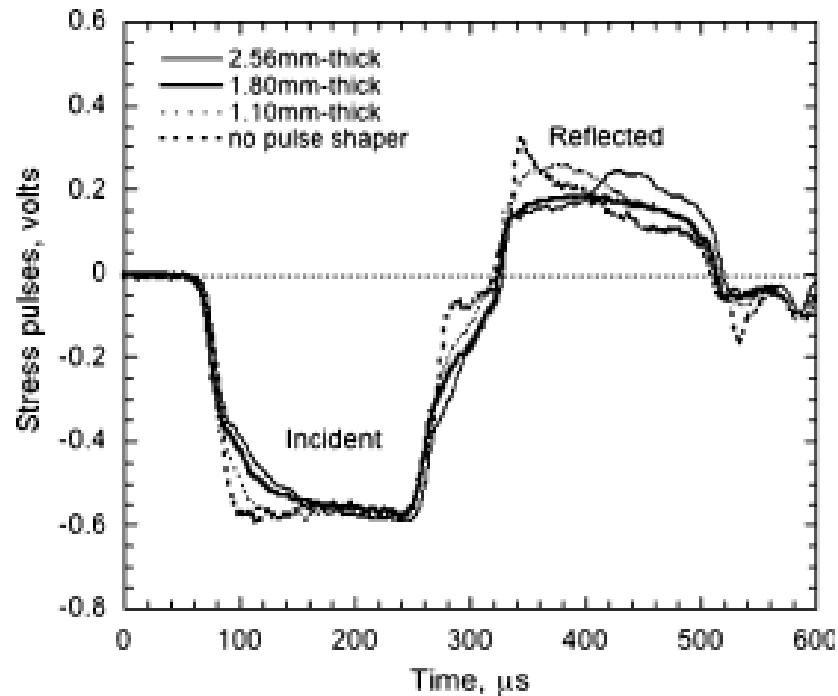
Figure 23: Incident and reflected waves with different thicknesses of pulse shapers. [71]

The measured strains ε_I, ε_T, ε_R corresponded to incident, transmitted, and reflected waves can be written in an equation:

$$\varepsilon_T = \varepsilon_I - \varepsilon_R \qquad\qquad\qquad \text{Eqn. (23)}$$

due to the energy conservation. The dynamic stress σ(t), strain ε(t), and strain rate ε̇(t), are calculated based on one-dimensional stress wave theory [78]:

$$\sigma(t) = E\frac{A_o}{A}\varepsilon_T(t) \qquad\qquad\qquad \text{Eqn. (24)}$$

$$\varepsilon_T(t) = \frac{2C_o}{L_o}\int \varepsilon_R(t)dt \qquad\qquad\qquad \text{Eqn. (25)}$$

$$\dot{\varepsilon}(t) = \frac{2C_o}{L_o}\varepsilon_R(t) \qquad\qquad\qquad \text{Eqn. (26)}$$

where E is the Young's modulus of the pressures bars; A is the cross-sectional area of the bars; A_o and L_o are the initial cross-sectional area and length of the sample, respectively; C_o is the bulk sound speed of bars. These equations provide the basic information which can obtain from the split Hopkinson pressure bar tests.

3.4 Micro-hardness measurement

Vickers hardness test used for measuring the hardness values of materials is employed in this study. There are several types of hardness evaluating measurements, such as the Knoop test and the Rockwell test, commonly used because of their practical aspect. The Vickers hardness test is developed by Smith and Sandland [77] of the United

Kingdom. It has a square-based pyramidal-shaped indenter made from diamond. Figure 24 shows the indenter of the Vickers test which leaves an indented mark on the sample with the diagonal D. It should be noted that in the test, a known load is applied smoothly and has to hold in contact for about 15 seconds. After the load is removed, both diagonals are measured and the average is used to calculate the hardness value (HV):

$$HV = \frac{1854.4P}{d^2}$$

Eqn. (27)

where d is the mean diagonal in µm, P is the applied load in gf.
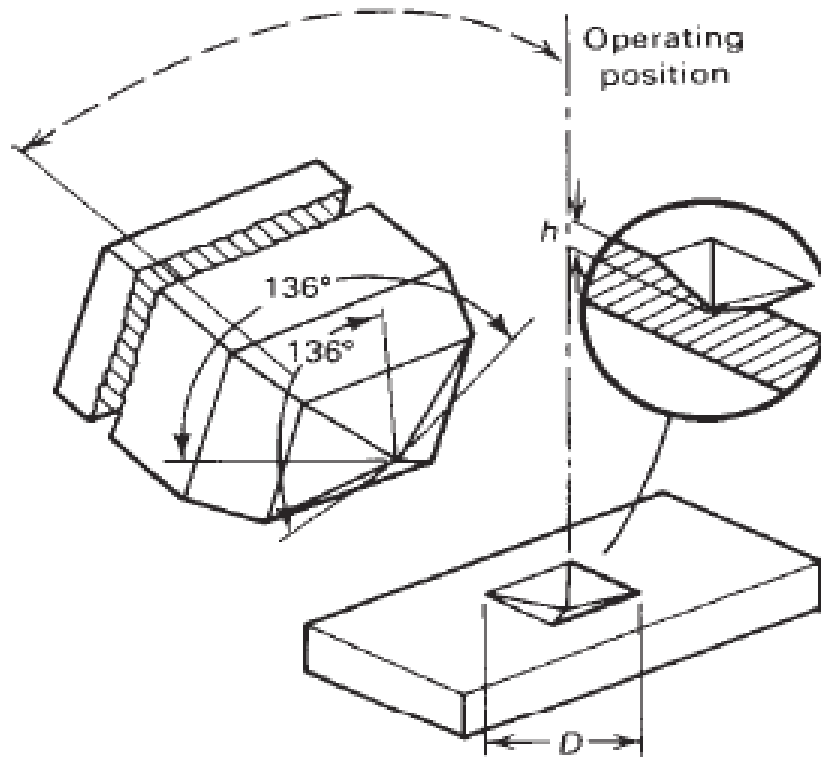
Figure 24: Schematic of the square-based diamond pyramidal indenter used for the Vickers test and an example of the indentation it produces.

3.5 Laser shock technique

Direct laser shock compression

Recently, powerful and high intensity laser has been used to generate localized shock pulse in order to study materials responses under extreme strain rates, temperatures, and pressures [82-85]. This extremely intensive energy source has a broad range of power, from 1mW (common laser pointer) to 700 TW (National Ignition Facility at Lawrence Livermore National Laboratory (LLNL) in Livermore, California). Askarion and Morez [86] first proved that laser energy can create shock pulses in metals due to the laser-pulse-induced vaporization and explosion on the metal surface. Laser shock waves can have a short pulse duration (nano-seconds) in comparison with the conventional ones generated by gas gun or explosive-driven flyer plates, which have the pulse duration in micro- or millisecond scale.

Many techniques are used to produce shock waves by laser. Figure 25 shows four different types of laser shock experiments: (a) a direct laser irradiation, which generates a plasma explosion on the surface of the metal, thus inducing shock waves sequentially; (b) a laser-driven flyer foil, which conveys the kinetic energy from laser-induced plasma explosion and generates shock compression on the materials; (c) a laser-driven compression generated by the ablator and reservoir; (d) a shock generated by Hohraum effect.
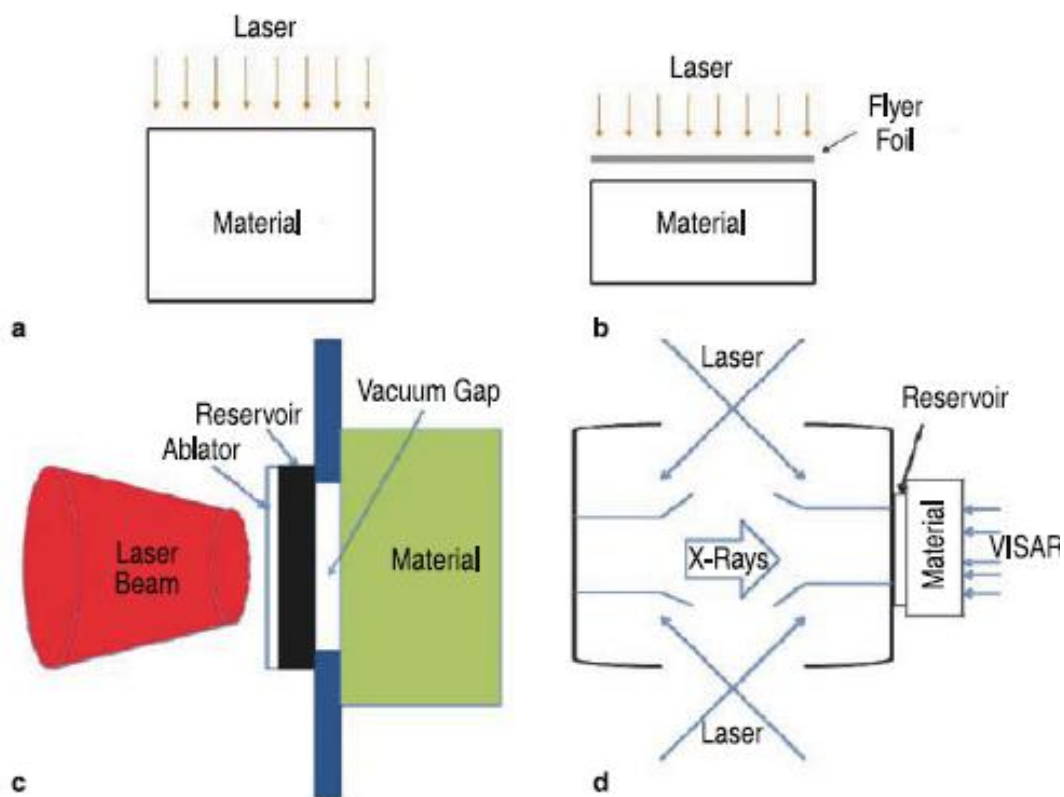
Figure 25: Laser driven methods to produce compression pulses: (a) direct laser incidence on the sample; (b) use of the laser to drive a flyer foil; (c) use of an ablator and reservoir to create a quasi-isentropic compression; (d) use of the Hohlraum effect to create x-rays from lasers [42].

The direct laser shock and laser-driven indirect shock are employed in this study. The laser shock experiments are carried out in the Jupiter laser facility of Lawrence Livermore National Laboratory using the Janus laser, which is a Nd-glass laser with a 532 nm pulse width. The laser energies vary from ~24 to ~440 J. The durations of laser pulses are 3 and 8 ns. The laser beam size is 1.12 mm^2 and has a square footprint. Laminates are cut into 5×5 mm squares and attached to two steel washers having a 10 mm outer diameter and 2.5 mm inner diameter. Figure 26 shows the laser instruments and experimental chamber (target chamber). The associated conditions of the laser

experiments are given in Table 3. The experimental setup is schematically shown in Figure 27.
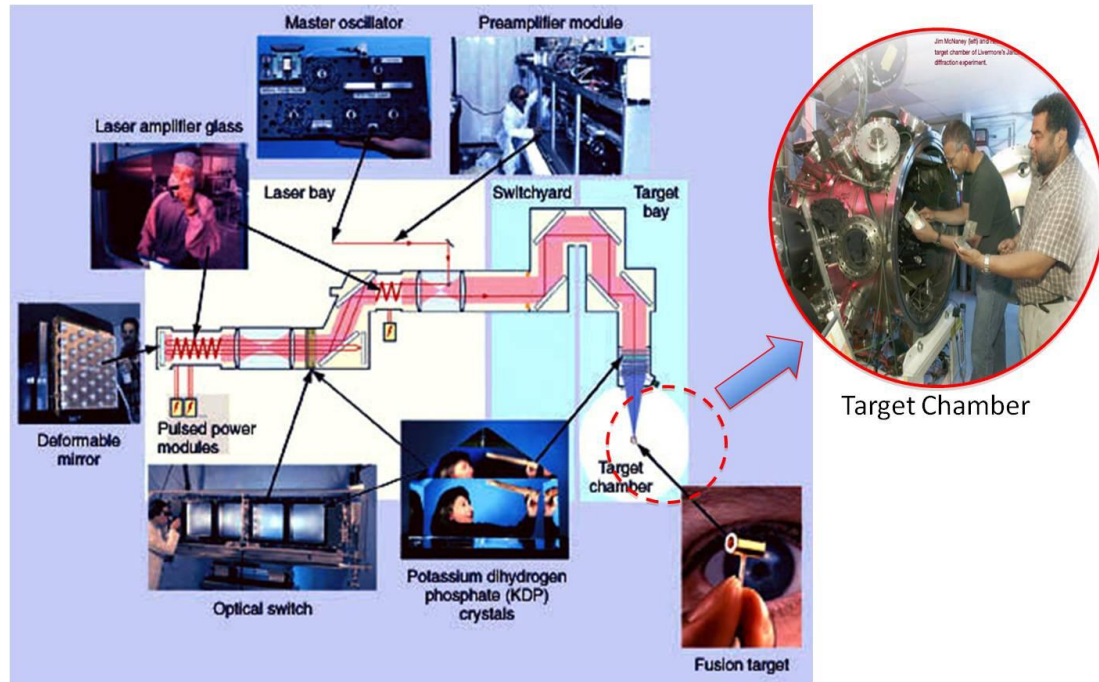
Figure 26: Laser instruments and target chamber in Lawrence Livermore National Laboratory (Courtesy of Lawrence Livermore National Laboratory).

Table 3. Conditions of Experiments

Bilayer Thickness	8ns Laser Energy (J)	Intensity of 8ns laser (W/cm^2)	3ns Laser Energy (J)	Intensity of 3ns laser (W/cm^2)
5 μm	229	~2.56×10^{12}	107	~3.18×10^{12}
			430	~1.28×10^{13}
30 μm	24	~2.68×10^{11}	105	~3.13×10^{12}
	409	~4.56×10^{12}	421	~1.25×10^{13}
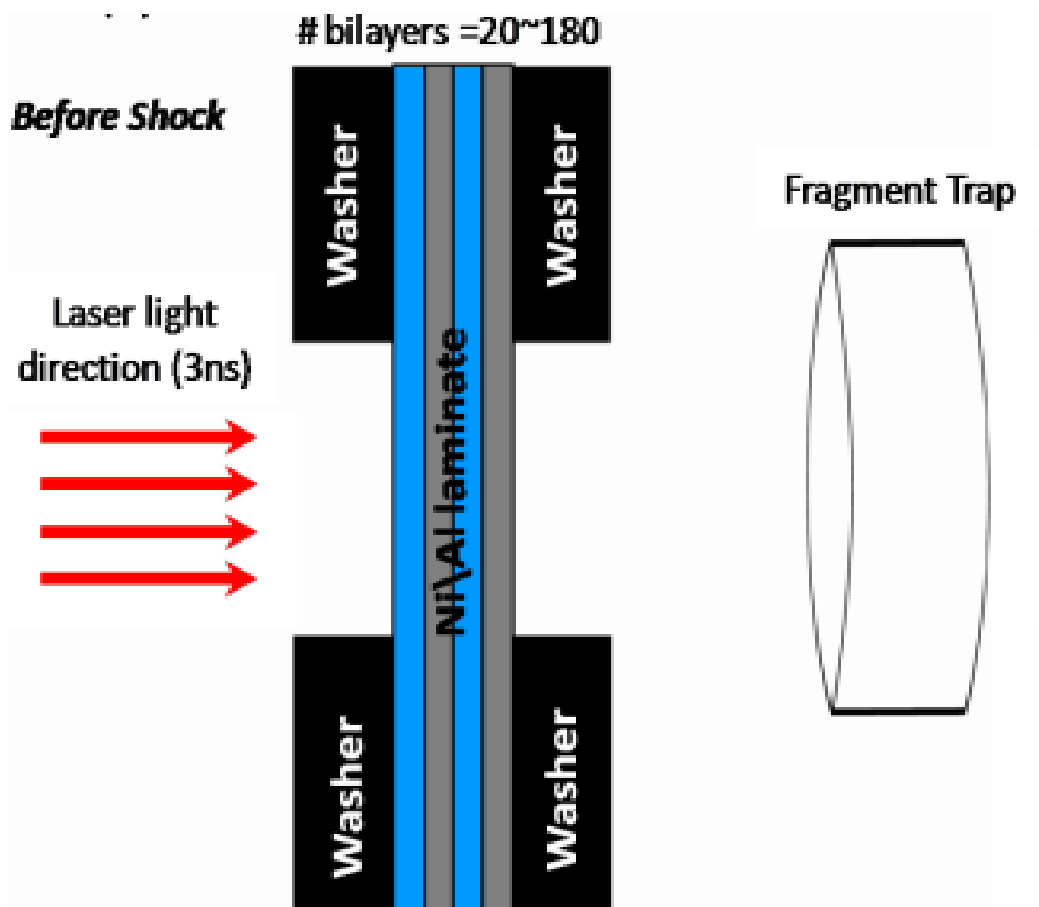
Figure 27: Laser shock experimental setup: (a) sample placed between laser irradiation source and fragment trap, washers used to fix samples.

Direct laser irradiation produces a plasma explosion on the metal surface, and generates shock waves. In order to estimate the initial shock pressure, Lindl's equation [87, 88] is used, which considers the pressure produced by laser shock as a strong function of laser intensity. The laser intensities in this study vary from $\sim 2.68 \times 10^{11}$ to $\sim 1.28 \times 10^{13}$ W/cm^2. This laser intensity I_{15} (in 10^{15} W/cm^2) can be translated into pressure P (in GPa) using:

$$P = 4 \times 10^3 \left(\frac{I_{15}}{\lambda} \right)^{\frac{2}{3}}$$ Eqn. (28)

where λ is the wavelength of the laser pulse in micrometers. For laser energies of 100, 200, and 400 J with pulse durations of 3 and 8 ns, a spot area 1.12 mm^2, and a wavelength of laser equal to 532 nm, the initial pressures vary from 66.3 GPa to 321.3 GPa. The specific initial pressures are given in Table 4. This is a very approximate estimation, since no material parameters is considered. The initial pressures are strongly related to the pulse duration, since the laser intensity is inversely proportional to the pulse duration: $I_{15} = \left(\dfrac{E(J)}{t(s) \times A(cm^2) \times 10^{15}} \right)$, where the E is the laser energy in Joule, t is the pulse duration in seconds, and A is the beam's cross-sectional area in centimeter square. By considering the optical properties of Ni/Al, the reflectivity R (60%) [89] of materials can be incorporated into Lindl's equation as following:

$$P = 4 \times 10^3 \left(\frac{(1-R) \times I_{15}}{\lambda} \right)^{\frac{2}{3}}$$ Eqn. (29)

The modified initial pressures are shown in Table 5. Table 4 and Table **5** show that by increasing the laser duration to 8 ns, the laser intensity dramatically drops to nearly half of the value corresponding to 3 ns pulse duration under the same laser energy. Thus, the 8 ns laser experiments have a significantly decreased laser intensity while the duration of the thermal interaction is increased.

Table 4. Initial Pressures from Lindl's equation

Laser Energy (J)	Pressure (GPa) 3ns	Pressure (GPa) 8ns
100	127.5	66.3
200	202.4	105.2
400	321.3	167.1

Table 5. Initial Pressures from modified Lindl's equation

Laser Energy (J)	Pressure (GPa) 3ns	Pressure (GPa) 8ns
100	68.4	35.6
200	108.6	56.5
400	172.4	89.7

Laser-driven shock-less compression

Conventional laser shock in solid materials was leaded by a rapid formation of the hot and dense plasma on the surface layer caused by the direct irradiation of focused laser beams [90-92]. This methodology generating mechanical waves from laser was affected significantly by many influencing factors, which resulted significant irregularities. For instance, different laser absorption rates of materials [92, 93] corresponding to materials'

reflectivity *R,* which is presented as $R = |(n-1)/(n+1)|^2$ and *n* was the refractive index, result in different absorbed energies on different materials. The inhomogeneous (Gaussian) laser-intensity (*I*) distribution, $I(r) \propto \dfrac{p}{\pi \cdot r_0^2} \exp(-r^2/r_0^2)$, caused by the focal spot of the laser beam [92], where *p* is the total laser power, r_0 and *r* is the radius of the laser beam and the distance corresponding to the center of the laser effected area respectively, and the drastic decreases of the shock pressures in solids [94] are also the critical issues of the direct laser shock. These phenomena have restricted the applications of direct laser-driven shock compression. Direct laser-driven shock compression cannot maintain the ultrahigh strain rates (> 10^6 s^{-1}) in the Ni/Al laminates and introduces extended thermal damages on the irradiated surface which made the post-analysis complicated.

An innovative laser-driven shock-less compression method was recently developed [95, 96]. This new approach generates compression stress by the soft stagnation of the expanding plasma across a vacuum gap from the reservoir made of plastic materials against the sample surface instead of the directly laser irradiation on the exposed surface of the sample. Edwards et al. [95] and Lorenz et al. [96] conducted laser-driven shock-less compression experiments on aluminum samples on the OMEGA laser facility and proved this approach induced quasi-isentropic compression stresses with amplitude 1~2 Mbar (= 100~200 GPa) within 20~40 µm depth. This shock-less compression was much less influenced by the thermal heating than direct lasers. The compression waves steepened and formed a relatively steady shock loading through the

entire samples. These are advantages to the study of the mechanical properties and the phase transformation of the bulk materials in a high stress, high strain rate and lower temperature regime. This laser-driven shock-less compression has heretofore not been applied to study the chemical and mechanical response of reactive Ni/Al laminates. This is one of the primary objectives of our research.

There were three stages of generating the shock-less compression using expanding plasma. First, the incident laser energy flux is converted in the ablator-reservoir to a low density plasma. This transformation depended on the ablator-reservoir's EOS and the laser conditions [95]. In the second stage, after the plasma generation, it expands across the vacuumed gap. Due to the relative low temperature and the fast stretching speed of the plasma, this ion wave can be seen as an approximately adiabatic plane wave. In the third and final stage, the plasma stagnated and piled up against the front surface of the laminates producing a monotonically rising pressure. The amplitude of the pressure wave propagating into the laminates gradually increased and steepened into a shock wave, thereby extending the high stress and high strain rate regime, which benefit the dynamic study of the bulk materials under extreme loading conditions.

The experimental setup is shown in Figure 28, Figure 29. Accumulative roll-bonding [55-61] and magnetron sputter deposition [16, 17] were applied to produce the micro- and nano-laminate respectively. Two laminates, with 5 µm bilayer thickness and total thickness ~0.85 mm, were machined into 5 mm disks with three ~0.3 mm well-aligned screw holes used to sandwich a nano-scale laminate with 54 nm bilayer thickness and 8.5 µm total thickness as shown in Figure 29. The sandwich structure was assembled

and adhered to a 300 µm thick tungsten washer with 10 mm outer diameter and 2 mm inner diameter. A 3 mm diameter and 20 µm thick polycarbonate ablator ($C_{16}H_{16}O_4$), density 1.2 g/cm^3, followed by 180 µm thick polystyrene reservoir ($C_{50}H_{48}Br_2$), density 1.23 g/cm^3, was adhered on the front surface of the tungsten washer in Figure 29. The tungsten washer with a machined radial groove designing for vacuuming the gap between ablator-reservoir and the sandwich laminates was of the fixture of the sample and ablator, which was clamped between the cap and the front end of the tube (Figure 29).
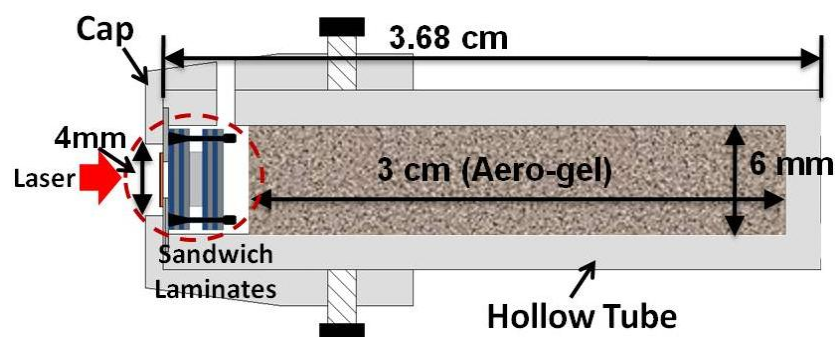
Figure 28: Sample holder for OMEGA laser experiments with assembly containing laminar samples.
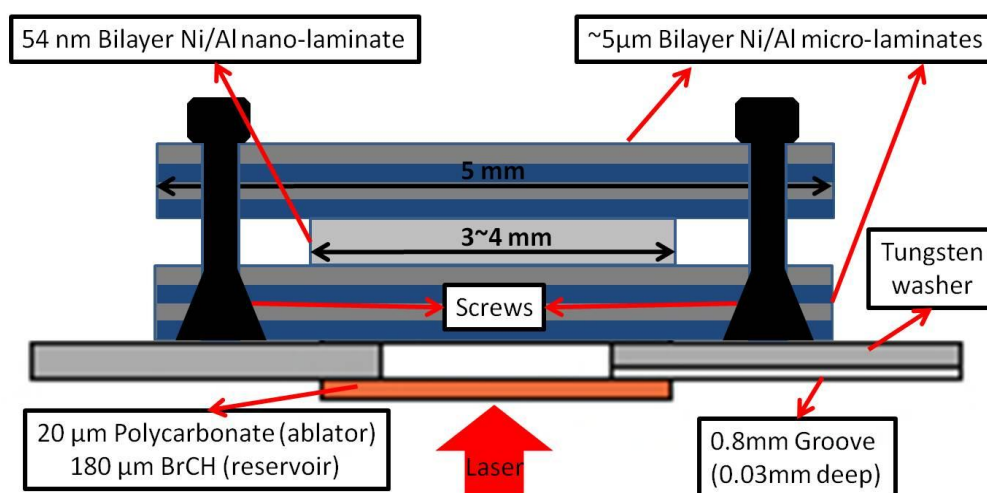
Figure 29: Schematic of the three layers of laminates with polycarbonate ablator and tungsten washer; Two Ni/Al micro-laminates with 5 µm bilayer thickness sandwich an 8.5 µm thick nano-laminate with 54 nm bilayer thickness.

3.6 Scanning electron microscopy

Scanning electron microscope (SEM) allows researchers to investigate a huge variety of materials, such as metals, ceramics and polymers, and can reach the resolution down to several nano-meters. In 1935, Knoll proposed the concept of a scanning electron microscope [97]. Two years later, in 1938, van Ardenne constructed the first scanning transmission electron microscope. Later on, lots of scientific advances were developed and used to improve the capability of SEM. The first commercial model SEM was built by A.D.G. Stewart at Cambridge Scientific Instrument Co., and the components of this first generation SEM were applied and modified in its descendents.

The basic components of modern SEMs are shown in Figure 30. Inside the Microscope column, an electron gun provides electron beams which are used to scan the specimen. An electron beam passes through electron lenses made of magnetic materials and are controlled by the scan coils as shown in Figure 30 (a). A computer system as shown in Figure 30 (a) is used to acquire electron data and convert to SEM images is necessary, and recently, for all the modern SEM, the digitalized imaging system is essential to the commercial model. The electron beams come from the electron gun, which has a LaB_6 filament or a file emission source as shown in Figure 30 (b). The two electron lens are made of magnetic materials using for focusing the electron beam. After focusing, the electron beam passes through an aperture, then goes through the magnification controlled scan coils. The electron beam scans the specimen and generates several different types of electrons such as secondary electrons, backscattered electrons, and Auger electrons. The secondary (SE) and backscattered electrons (BSE) are utilized

to compose the SEM images. Due to their distinct properties, the SEM images produced by secondary electrons are suitable for investigating the topography of the sample. However, the different gray levels on the images composed by backscattered electrons corresponded to elemental difference as well as phase transformation. Figure 31 shows the BSE and SE images of a laser shocked mono-crystalline vanadium. Rather than shows the clear roughness the BSE image presents different phases after laser shock compression.
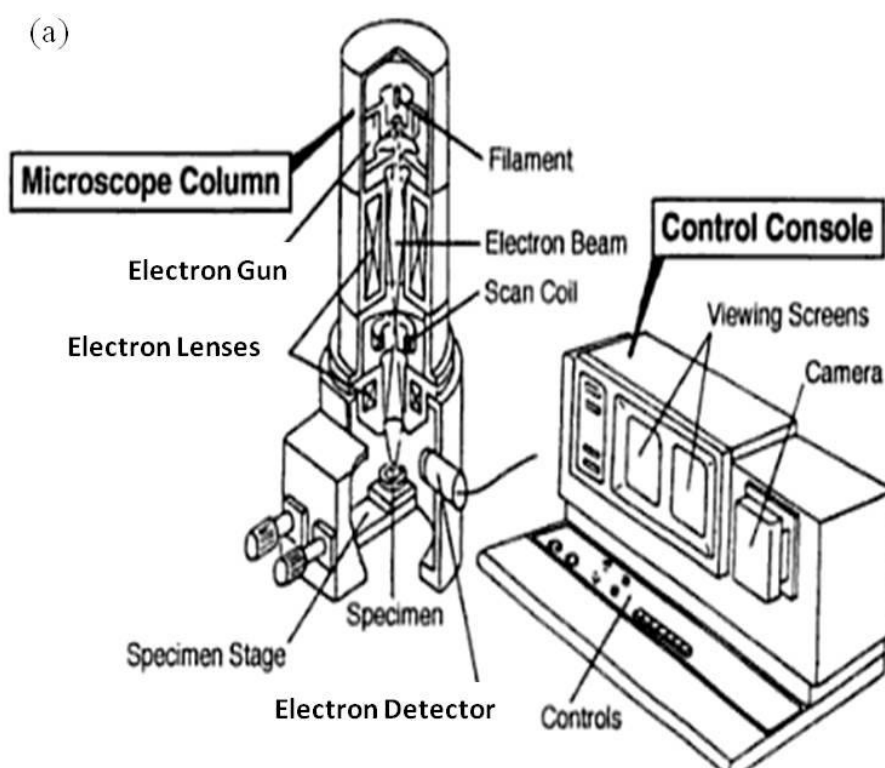
Figure 30: (a) Basic components and the control console of SEM, (b) the detail in the chamber of SEM [97]. (figure continued)
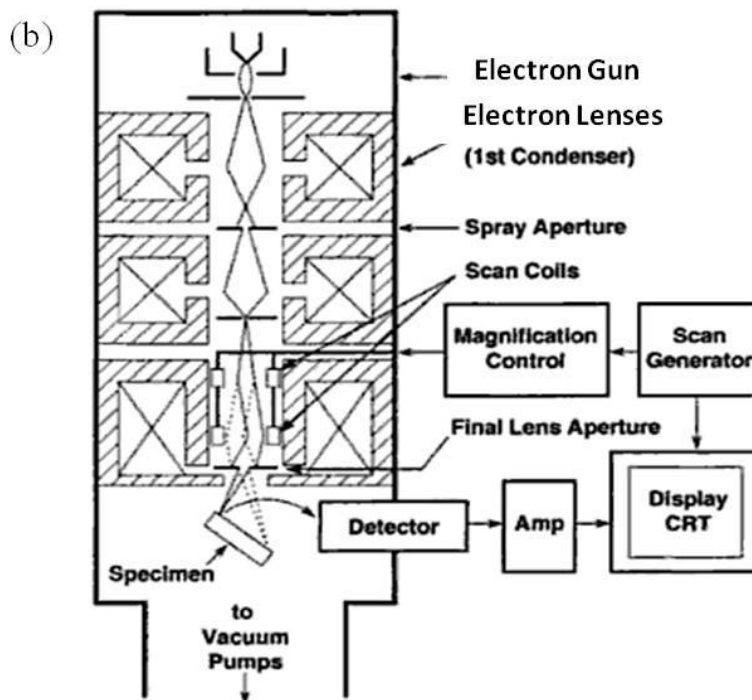
Figure 30: Continued.
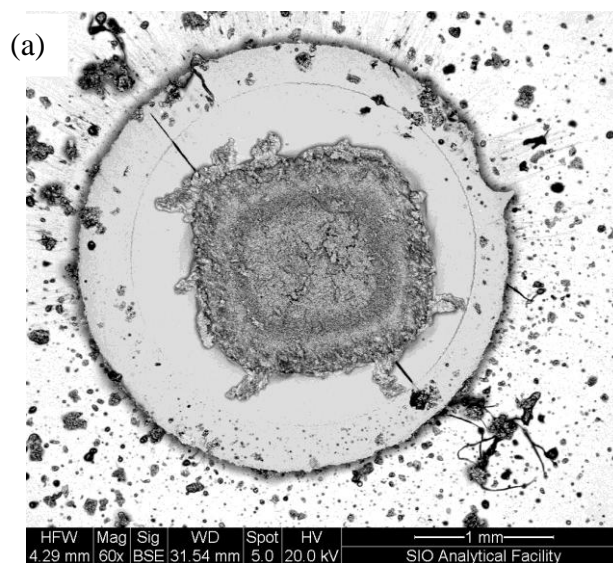
Figure 31: (a) The BSE image of a laser shocked mono-crystalline vanadium. (b) The SE image of (a). (figure continued)

(b)

HFW | Mag | Sig | WD | Spot | HV
4.29 mm | 60x | SE | 31.54 mm | 5.0 | 20.0 kV | ————1 mm———— SIO Analytical Facility
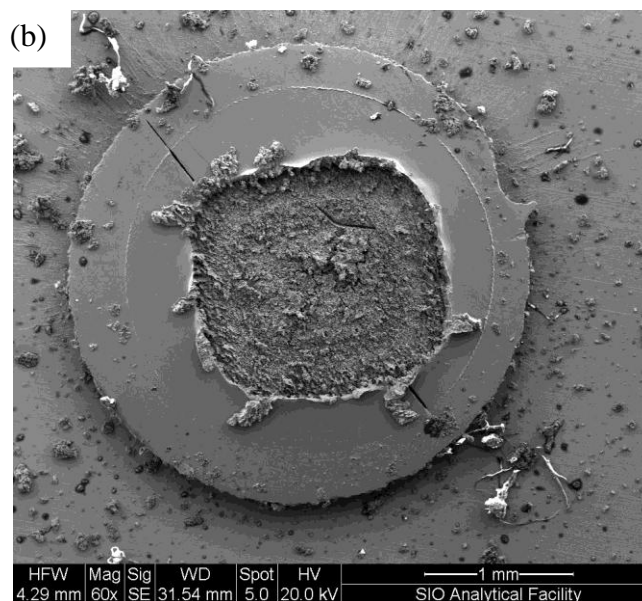
Figure 31: Continued.

3.7 Transmission electron microscopy

Transmission electron microscopes (TEM) utilize transmitted electrons to project a magnified image at the rear side of the specimen. Figure 32 shows the electrons generated by electron beam bombardment. Each electron has its own property and can be used for many different electron microscopes, or to quantify the components of the materials. For instance, the secondary electrons and backscattered electrons are used for SEM, and the transmitted electrons are utilized in TEM.

The basic components inside the TEM chamber are the same as what is inside the SEM, however the arrangement of these parts and the requirement of the sample preparation are different. Figure 33 shows the scheme of the new in-situ TEM in LLNL [98, 99]. The specimen is placed in between two electronic lenses, and the image is

shown at the rear side of the object. The principle of TEM and SEM are similar to the optical microscope. Due to the extremely short wavelength of electrons, the resolution of the electron microscope can have a significant increase.
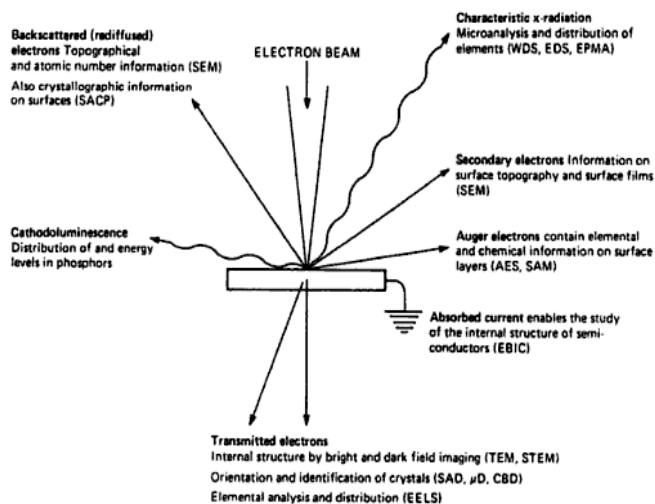
Figure 32: Specific electrons generated by electron beam bombardment, and their corresponding applications [98].
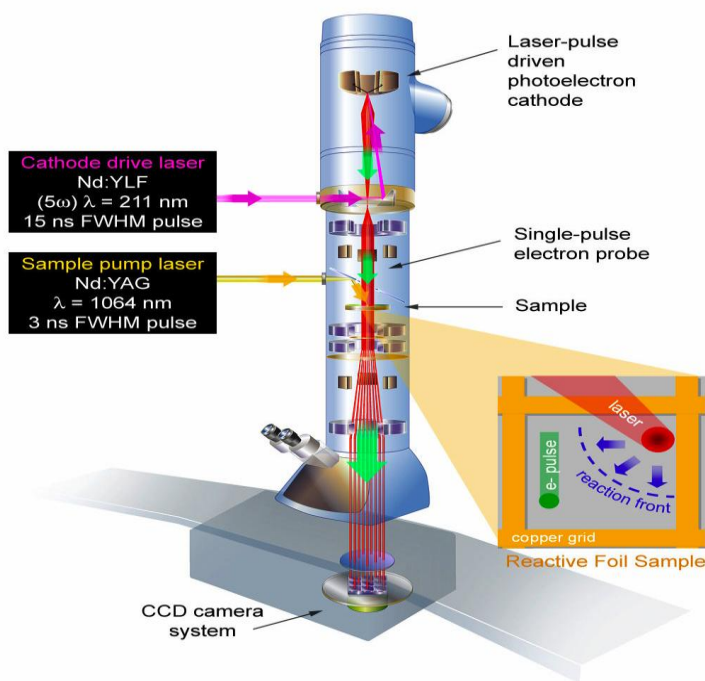
Figure 33: In-situ TEM for investigating laser initiated reactions [99].

TEM also is used to investigate the orientations of crystals, and the elemental compositions of materials by analyzing the selected area's diffraction pattern. Due to the light diffraction theory, for instance, x-ray, the well-arranged diffraction pattern can be seen if the incident angle fits the requirement of Bragg's law (see Figure 34) [100]:

$$2d \sin \theta = n\lambda \qquad\qquad\qquad \text{Eqn. (30)}$$

where d, θ, λ, and n are the crystallographic plane spacing, the incident angle, the wave length of the incident light, and an integer which can fit the Bragg's law. The diffraction patterns have three different morphologies: periodic array of dots, concentric rings, halo rings (or circles). These different diffraction patterns represent distinctive crystal structures. Figure 35 shows the diffraction patterns from three different micro-structures: (a) a well-arranged periodic pattern representing a perfect crystalline structure of the periodically atomic structure; (b) concentric rings mixed with bright diffraction dots revealing a mixture of ploy-crystalline and amorphous structures; (c) halo rings representing a pure amorphous structure. It should be noted that the unknown crystal orientation can be identified by measuring the reciprocal spacing of the diffraction patterns if there is no residual strain in the crystal [101-103].
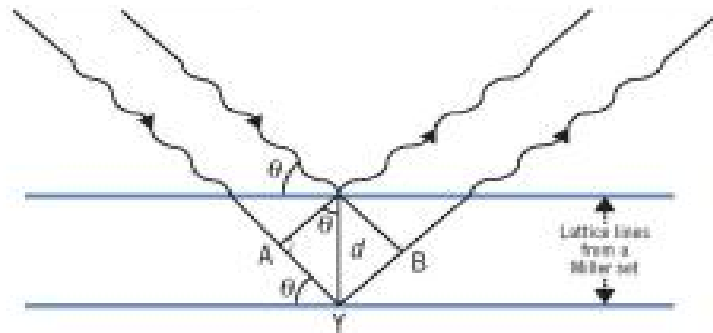
Figure 34: Schematic plot of Bragg's law [100].
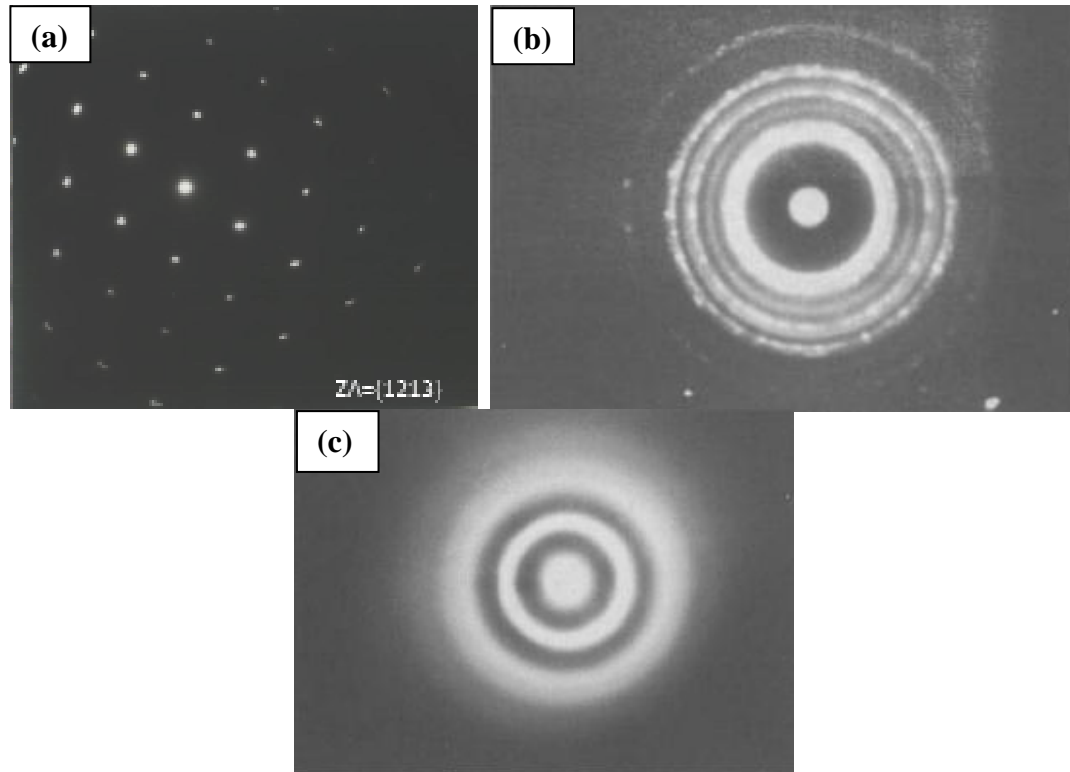
Figure 35: Diffraction patterns of (a) an as-rolled sample [101], (b) a mixture of crystalline and amorphous structures [103], (c) a shock-induced amorphous structure [102].

3.8 Energy dispersive x-ray spectroscopy (EDS)

Energy dispersive x-ray spectroscopy (EDS) is a sensitive, nondestructive analysis for studying the chemical composition of unknown materials. It can provide both quantitative and qualitative information of the composed materials. Recently, most of the modern SEMs integrate EDS system, which accomplished the fast and in-situ analysis. SEM with EDS system become a popular and powerful micro-analysis instrument [98].

The principle of EDS, developed by Fitzgerald *et al*. in 1968 [104], bases on the intrinsic semiconductivity of the micorcalorimeter which provides a high energy resolution for analyzing a variety of different x-ray energies. Figure 36 illustrates the

cross-section of the ED spectrometer. Specific x-rays are ignited by the electron beam of SEM, and then passed through the outer vacuum window where the ED spectrometer is placed behind the window and shielded by a heat isolating chamber. An intrinsic semiconductor, the microcalorimeter, is aligned and positioned behind Al-coated parylene windows which are used for filtering the IR irradiation in the SEM chamber. In the microcalorimeter, electron-hole pairs are created while the intrinsic semiconductor absorbs the incident x-ray, and then these charge pulses are converted to voltage steps by a charge-to-voltage preamplifier [98, 105]. These voltage steps are then utilized for analyzing the chemical components of the specimen as that shown in Figure 37 [105].
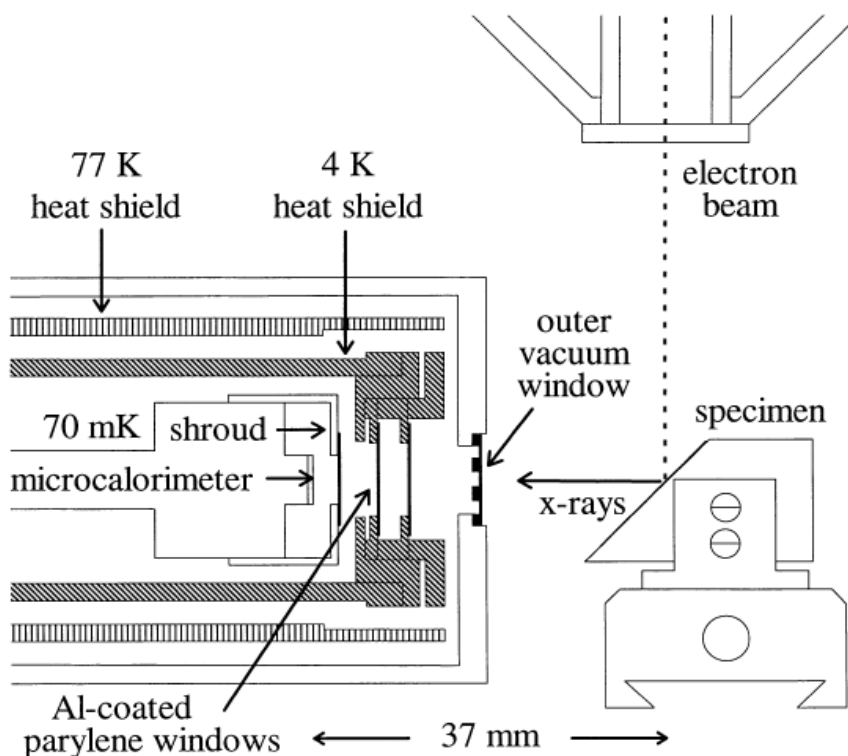
Figure 36: Schematic plot of the x-ray window's cross-section [105].
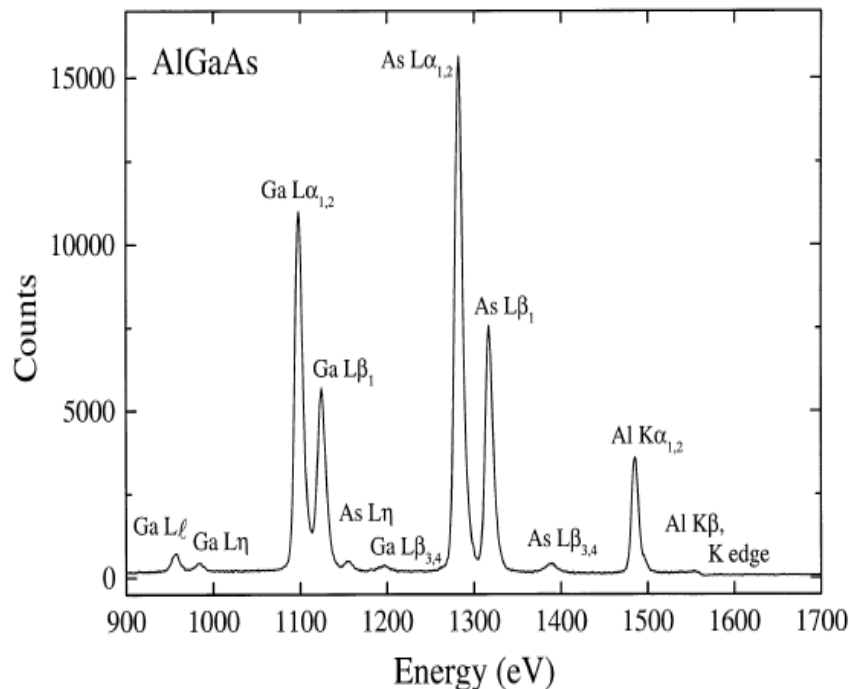
Figure 37: Voltage spectrum of AlGaAs alloy [105].

3.9 X-ray diffractometer

X-ray diffractometer is a powerful methodology for qualitative analysis. Due to the constructional diffraction phenomena of the Bragg's law (Figure 34), for a specific crystalline structure, it has an identical diffraction pattern corresponding to each crystallographic phase and plane. There are fourteen different Bravais lattices shown in Figure 38. These basic lattices construct most of the crystalline structures in nature. Different elemental crystals have their own crystal structures and lattice parameters. Some materials may have the same crystal structure, for instance, Ni and Al have the face center cubit (FCC) structure, but their lattice parameters are different due to their distinct atomic sizes. These special features are utilized in the x-ray diffractometer for doing qualitative analysis in terms of identifying the chemical compositions.
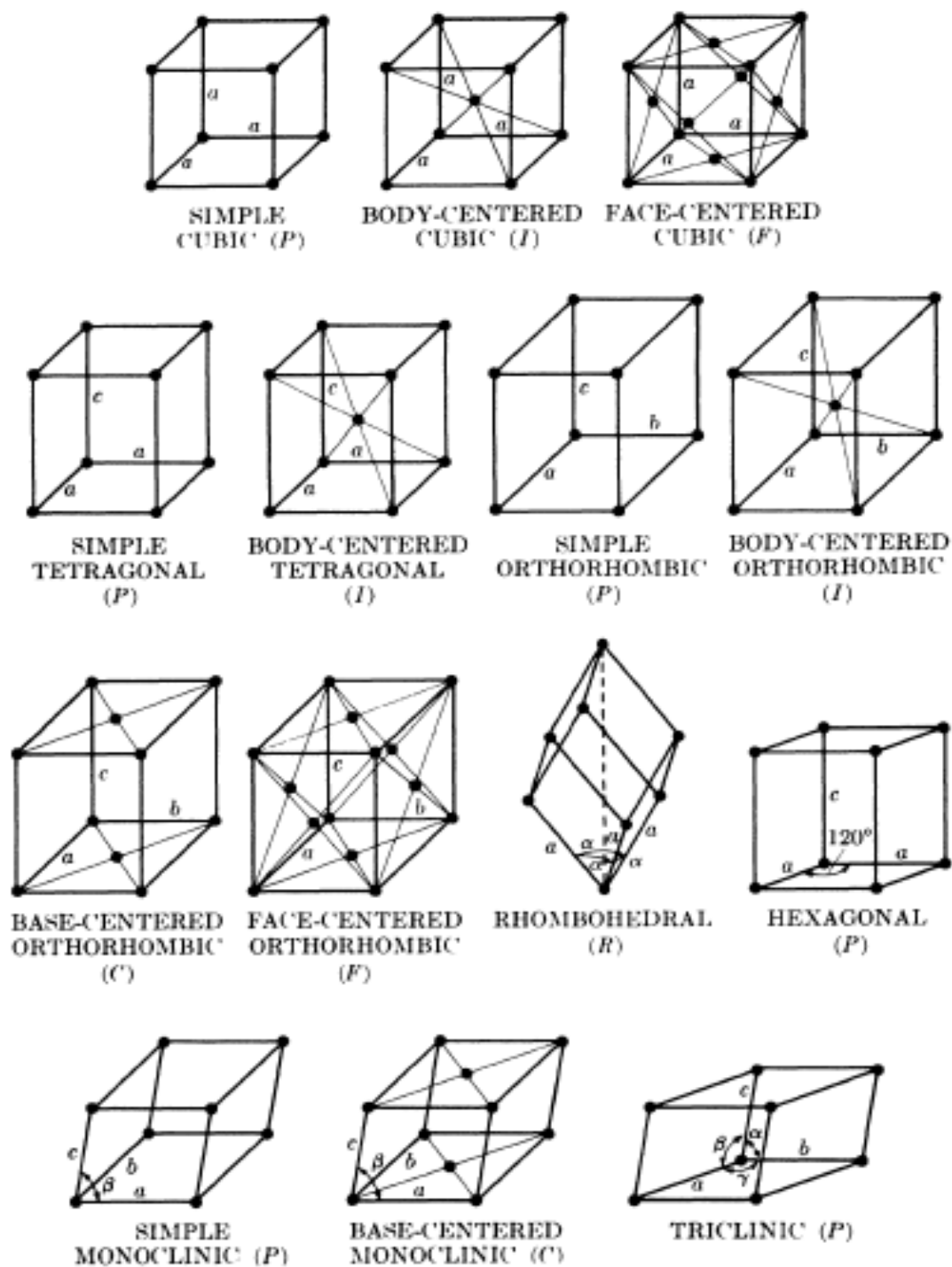
Figure 38: Fourteen Bravais lattices [28].

The x-ray diffraction spectrum shown in Figure 39 presented specific profiles from laser shocked Ni/Al laminates. The Joint Committee on Powder Diffraction International Centre for Diffraction Data (JCPDS-ICDD) data is employed to analyze the diffraction profiles. Based on the initial components of the materials, the possible intermetallics can be recognized by referring the JCPDS data.
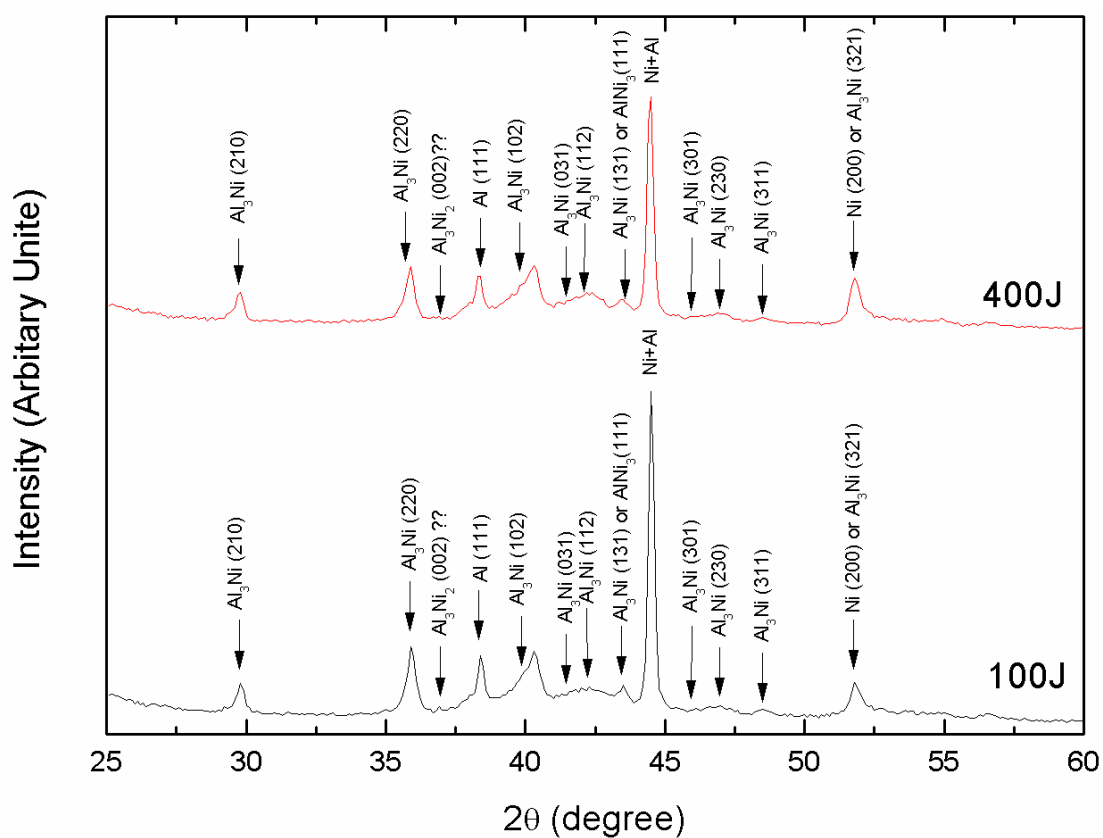
Figure 39: X-ray diffraction profiles from 100 and 400 J laser shocked Ni/Al laminates.

3.10 Simulation tools (HYADES & Raven)

Computational simulations are widely employed to solve many engineering problems. Many industries such as aerospace, automobile, and military utilize computational techniques frequently in order to reduce the cost of massive experiments. In addition, simulation tools are also carried out for investigating small-scale subjects such as semiconductors and micro-scale materials, and studying the phenomena under extreme conditions such as the laser-induced shock loading [85, 106].

In this study, two different simulation tools, HYADES and Raven, are employed to investigate the mechanical behaviors of the materials under dynamic and extreme loadings. HYADES is a basic radiation hydrodynamics simulation code. It contains the fundamental hydrodynamics and energy transport models for simulating the behavior of laboratory experiments especially for the laser experiment [107-116]. Many experimental situations can be adequately simulated using this code. The primary advantages of selecting this version are the simplicity of use as well as the efficient use of computer resources. In addition, Raven, a two-dimensional Eulerian hydro-code, developed by Benson [106] for solving dynamics problems in solid mechanics and materials science with an emphasis on the micromechanics is employed. Several features unique to this program are useful for materials science. Individual microstructural features may be isolated for statistical averaging by using the objects facility.

The detail of the simulation process and boundary conditions are discussed in the results. All of the Raven simulation results are obtained from the collaboration with Dr. Vitali and Prof. Benson.

3.11 VISAR

Velocities of Fragment and spall surface were observed using VISAR technique [85]. The Hamamatsu streak camera with 50 ns sweep were used to recorded the time-dependent pressure history. It had a 800 µm spatial scale of the line at the target plane in VISAR system.

The principle of using VISAR to measure the surface and fragment velocities is to utilize the fringe shifts caused by reflected light due to the Doppler effect [117-120]. The correlation between the fringe phase shifts φ, and the velocities of the reflecting surface u can be presented using the following equation:

$$u = \frac{\lambda \varphi}{4\pi\tau(1+\delta)},$$ Eqn. (31)

where λ is the wavelength which is 532 nm, δ is equal to 0.0318 and τ is the optical delay produced by a glass etalon in the interferometer which can be calculated by a function of the etalon thickness d and the refraction index n:

$$\tau = \frac{2d(n-1/n)}{c},$$ Eqn. (32)

where c is the sound velocity.

The discontinuous changes of the fringe phase are resulted by the movement of the rear surface probed by the laser light of VISAR. Thus, two independent interferometers using to different etalon thickness, $d_1 = 50.074$ and $d_2 = 28.77$ mm, were

employed to resolve this fringe jump ambiguity. In this study, the velocity sensitivities were estimated which were about 0.995 and 1.732 km s^{-1} for d_1 and d_2 respectively.

3.12 Differential thermal analysis (DTA)

A thermometric analysis system, DTA, is commonly used as a probe for investigating the reaction behavior of compacts composed of multiple elements [121-123]. Figure 40 shows the scheme of the DTA cell which is composed of four major parts: 1. Al_2O_3 crucibles as the sample holders; 2. vacuum furnace; 3. thermocouples measuring the differences of the temperature between the reference material and sample; 4. recording system (computer). Differential thermal analysis is applied for characterizing shock-compressed reactive powder mixtures [121]. From the DTA data, one can evaluate the reactions, temperatures, intermetallic phases of the shock compressed reactive mixtures.
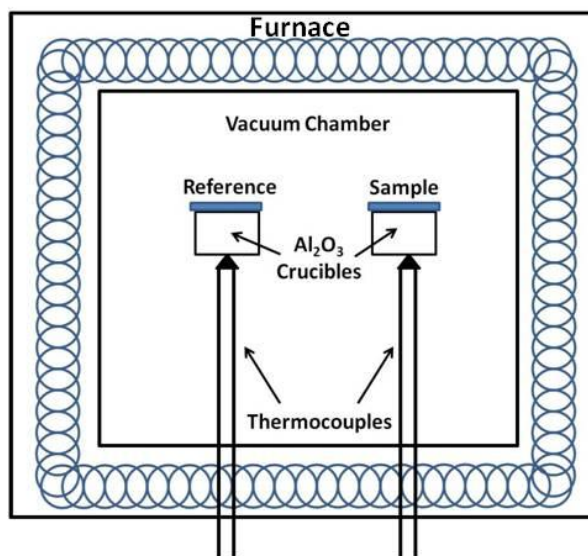
Figure 40: Scheme of DTA cell.

Chapter 3, in part, is published or being currently prepared for submissions as the following papers: Reaction in Ni–Al laminates by Llaser-Shock Compression and Apalling, 2011, C. T. Wei, B. R. Maddox, A. K. Stover, T. P. Weihs, V. F. Nesterenko, M. A. Meyers, Acta Materialia; Laser Shock-Induced Spalling and Fragmentation in Vanadium, 2010, H. Jarmakani, B. Maddox, C. T. Wei, D. Kalantar, M. A. Meyers, Acta Materialia; Response of Ni/Al Laminates to Laser-Driven Compression, C. T. Wei, V. F. Nesterenko, T. P. Weihs, B. Remington, H. -S. Park, M. A. Meyers, Acta Materialia, to be submitted; Quasi-static and Dynamic Response of Explosively Consolidated Metal-Aluminum Powder Mixtures, C. T. Wei, E. Vitali, D. J. Benson, F. Jiang, K. S. Vecchio, N. N. Thadhani, M. A. Meyers, Acta Materialia, to be submitted. The dissertation author was the primary or co- author of these papers.

Chapter 4.

 Results and discussion

Three objectives are presented in this study. First, in order to realize the basic mechanics under an extreme condition (a high strain rate regime), the monolithic material, vanadium, is subjected to laser irradiation with mono- and poly-crystalline structures (section 4.1). The second objective is to study the dynamic and quasi-static behaviors of the consolidated aluminum-metal powder mixtures (section 4.2) produced by a double tube explosive shock consolidation process with five different reactive mixtures. The third objective is to investigate the mechanical behaviors and self-sustaining high temperature reactions of the micro- and nano-scale Ni/Al alternatively stacking laminates, produced by the cold-rolling and physical vapor deposition process, under extreme loading conditions (section 4.3).

4.1 Laser shocked mono- and poly-crystalline vanadium

Vanadium is a candidate material for the first wall and blanket components of fusion power systems because of its low irradiation-induced activity, high stability and good compatibility with lithium [124-126]. The dynamic spalling and fragmentation of metals induced by laser irradiation is a concern of great significance to the successful operation of the National Ignition Facility (NIF). Protection from spalling and fragmentation is necessary to preserve the functionality of the laser optics systems and diagnostic tools of the main target chamber. In addition to the practical concerns of conducting successful laser-shock experiments, studying the singular element, vanadium,

with poly and mono-crystalline under extreme conditions can also provide valuable knowledge towards understating the mechanics of the materials at a high strain rate regime.

4.1.1 Shock wave behavior

The laser shock experiments were conducted at the Jupiter Laser Facility, Lawrence Livermore National Laboratory. Figure 41 is an illustration of the cross-sectional view of the experimental set-up. Figure 41 (a) shows the original set-up of the experiment, and Figure 41 (b) and (c) are depictions qualitatively showing the damage that occurred to the vanadium targets with different thicknesses. Figure 41 (b) shows complete blow-off of the thinnest vanadium samples; Figure 41 (c) shows blow-off surrounded by a spall surface in the intermediate thickness samples; Figure 41 (d) shows only spall that occurs in the thickest samples. A Nd glass laser with a 532 nm pulse width was used to generate high pressure laser shocks in the vanadium samples. Both 3 and 8 ns square pulse lengths were used to study the effect of pulse duration on material behavior. A 1 mm kineform phase plate (KPP) was used to generate a flat intensity profile that was ~1 mm square in size. The vanadium samples were cut into small 3.5×5 mm rectangles and glued between two steel washers having a 10 mm outer diameter and 2.5 mm inner diameter. Glass slides were placed parallel to the targets, approximately 12 cm behind, to collect vanadium fragments and to analyze the resultant damage [85].

Poly- and mono-crystalline vanadium were obtained from Alpha Aesar, and Accumet Materials respectively (see section 2.1.4). Three different thicknesses, 75, 127,

250 µm, of poly-crystalline vanadium were subjected to laser shock experiments and compared with the results obtained from the mono-crystalline vanadium with thickness 250 µm. It is essential to understand the behavior of shock waves propagating in materials. Theoretical calculations and computational estimation HYADES were used to interpret the propagating shock waves which were presented in Figure 42 and Figure 43. Three different laser energies, 100, 200, 400 J, were employed to irradiate the vanadium samples. The laser intensity is positively proportional to the shock energies, but inversely proportional to the pulse duration as shown in section 3.4. The calculated pressures and decay profiles estimated by one-dimensional computational code, HYADES, are shown in Figure 42. The pressure pulse decay profiles were calculated at the three different energy levels around which the experiments were conducted: 100, 200 and 400 J. The results were calibrated for the reflectivity of vanadium, taken as 61% [127]. The pressures decayed rather rapidly as the pulse duration increased. The triangular nature of the pulse shape was retained throughout propagation in the 250 lm thick specimens. The initial pressures, which were equal to 107, 161 and 234 GPa for the three energy levels (100, 200 and 400 J), were reduced to approximately one-quarter of their original values at the free surface. The original HYADES code is shown in Appendix (a) at the end of the text, which presents that the monolithic vanadium is divided into 200 meshes and the laser source irradiates on the mesh #1 without introducing any material strength models.
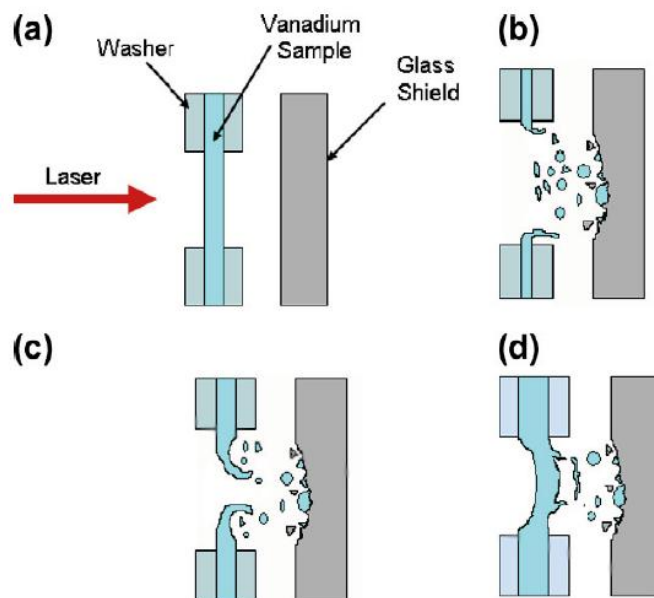
Figure 41: Schematic of the cross-sectional view of the laser shock experiments: (a) initial setup, (b) laser-shocked 75 µm vanadium, (c) laser-shocked 127 µm vanadium, (d) laser-shocked 250 µm poly- and mono-crystalline vanadium [85].
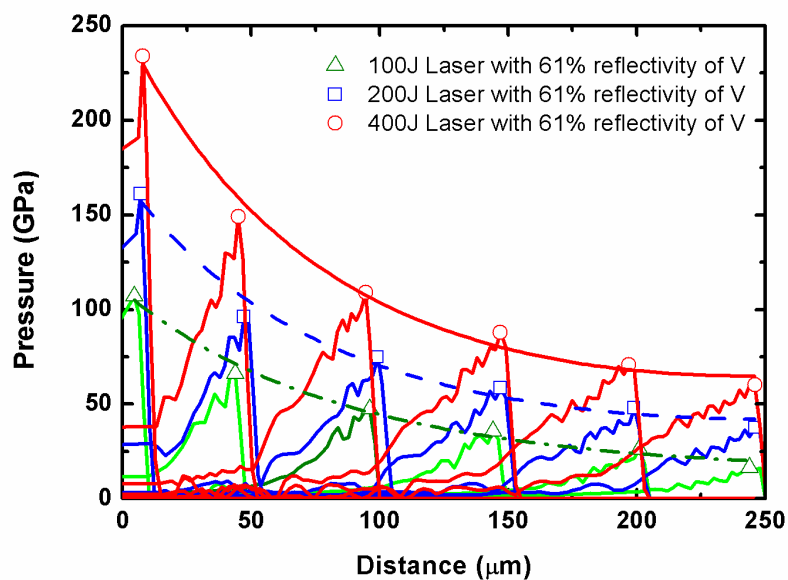
Figure 42: HYADES code simulation of laser pulse propagation in vanadium with 61% reflectivity [127]: ○ represents 400 J laser propagated in V: initial pressure 234GPa; free surface pressure 60.1 GPa; duration of propagation ~32 ns. □ represents 200 J laser propagated in V: initial pressure 161 GPa; free surface pressure 37.5 GPa; duration of propagation 36 ns. Δ represents 100 J laser propagated in V: initial pressure 107 GPa, free surface pressure 16.4 GPa; duration of propagation 41.1 ns.

The pressure profiles were also theoretically computed based on calibrated laser shock experiments on tantalum carried out at 200 J (D. Eder, unpublished work). Jarmakani *et al.* used the experimental results from tantalum and the conservation of energy equation to simulate the shock wave decay in the vanadium. Eqn. 33 shows the conservation of energy equation:

$$\Delta E = \frac{1}{2} U_P^2 \qquad \text{Eqn. (33)}$$

where ΔE is the energy change and U_p is the particle velocity. The internal energy inside the shock-compressed material is a function of the laser energy and, to a first approximation, we assumed that this function is material independent. The difference in reflectivity between vanadium (61%) and tantalum (78%) was neglected. The experimental pressure values as a function of distance into the material obtained from the tantalum experiments (D. Eder, unpublished work) are listed in Table 6. The predicted pressure pulse decay profiles in vanadium for an input energy of 100, 200, 400 J is presented in Figure 43.
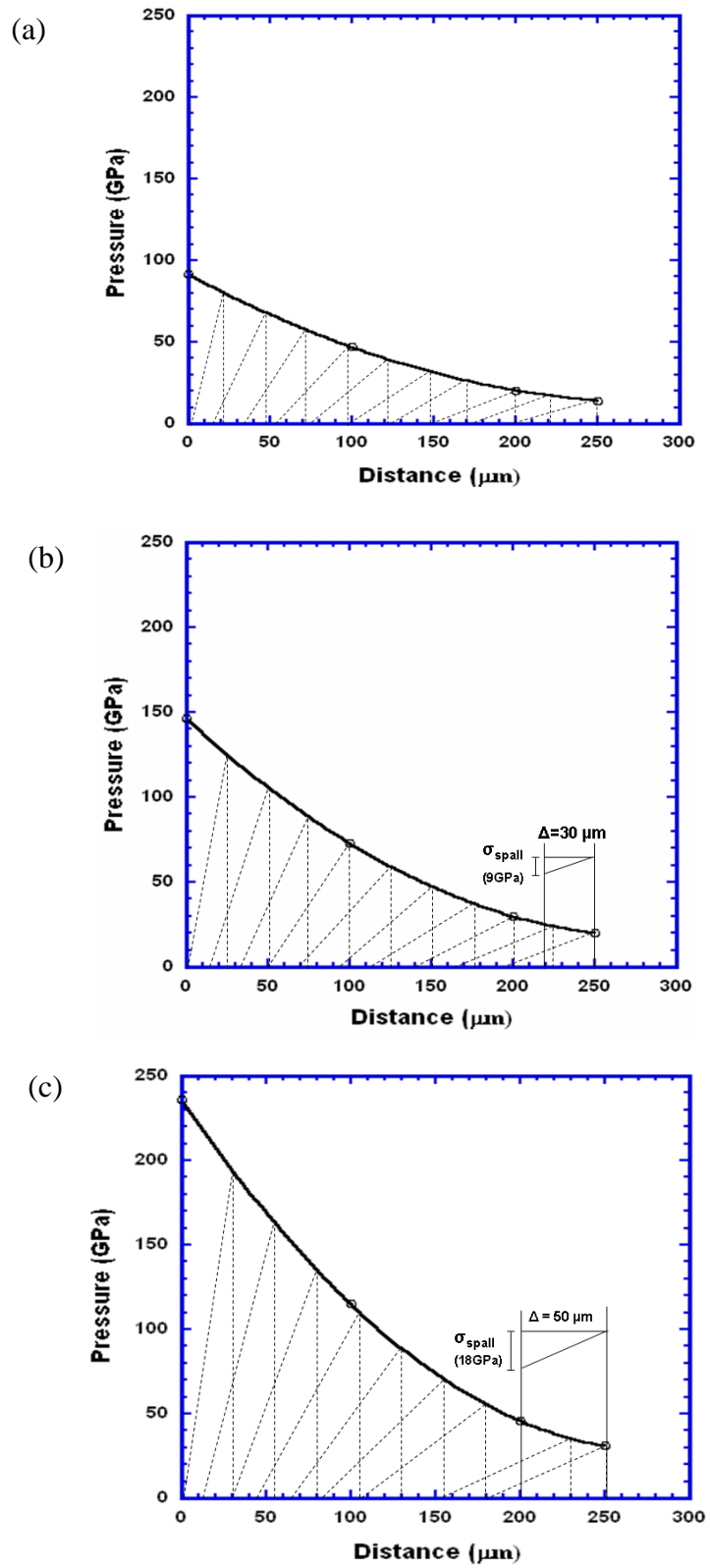
Figure 43: Predicted pulse decay: (a) 100 J; (b) 200 J; (c) 400 J [85].

Table 6. Pressure and U_p values as a function of distance obtained from laser shock experiments on tantalum from Eder *et al*. (unpublished).

Distance (µm)	Pressure (GPa)	U_p (km/sec)
100	150	1.664
200	60	0.819
250	40	0.584

Spall strength is obtained from the spall thickness and the corresponding reflected wave [128]. Figure 44 shows the schematic plot where the shock wave propagates to the free surface and causes a spallation. The correlation between the maximum stress *P* at the back surface, the spall thickness Δ and the spall strength σ_T is shown in Eqn. 34:

$$\sigma_T = \frac{2\Delta}{L} P$$

Eqn. (34).

From the shock wave simulation (by HYADES) and experimental conversion (from tantalum), the spall strength can be obtained by directly measuring the spall thickness and the corresponding pressure values of the reflected waves. The measured spall thicknesses of 200 and 400 J laser shock were about 30 and 50 µm respectively. No spallation was found when the laser irradiation energy less than 100J. Figure 45 shows the reflected waves obtained from HYADES. The spall strength is about 10 and 13 GPa for a laser irradiation of 200 and 400 J respectively, which is consistent with the experimental conversion shown in Figure 43.
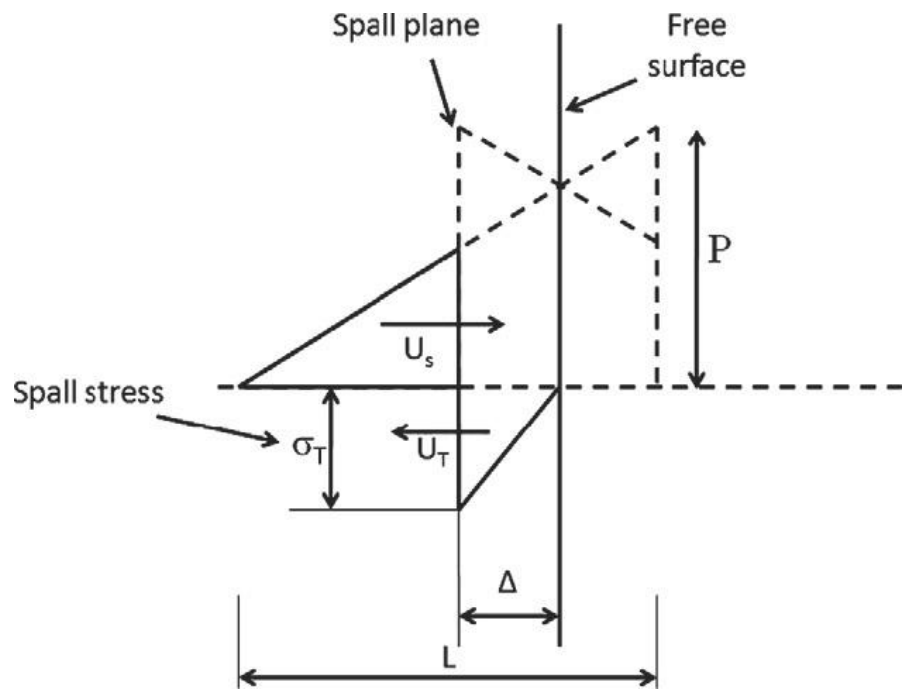
Figure 44: Calculation of spall strength from reflected pulse at the free surface
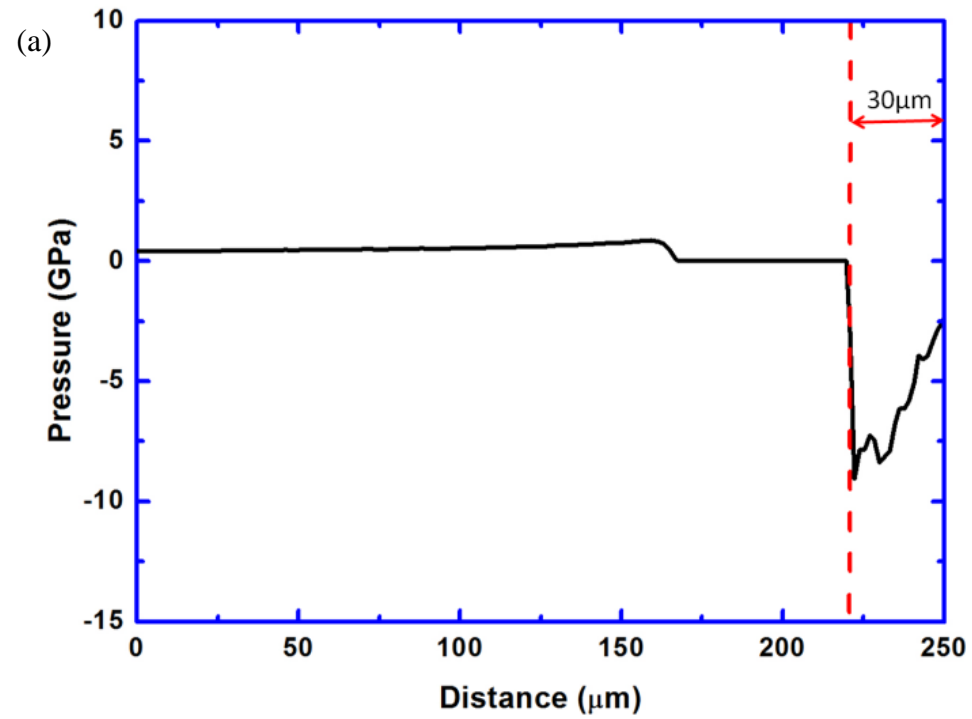
Figure 45: Reflected waves from HYADES: (a) 200 J laser irradiation, (b) 400 J laser

irradiation. (figure continued)
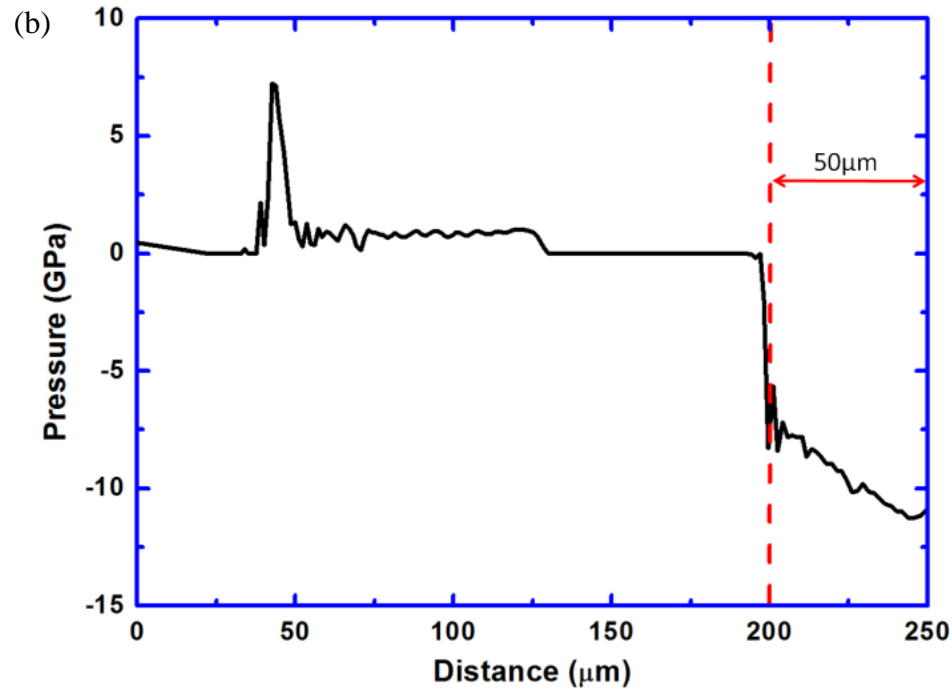
Figure 45: Continued.

4.1.2 Spallation and fragmentation analysis

Spallation and fragmentation are two important types of fractures that need to be thoroughly investigated in order to maintain the laser facility. Their fracture mechanisms also provide valuable information towards a better understanding of the mechanics of materials [129]. Vanadium, a BCC metal, is used in this study (see Section 2.1.4) with mono- and poly-crystalline micro-structures. The laser instrument and experimental conditions are presented in Section 3.4 and Table 3. Recovered samples and fragments were characterized using a scanning electron microscope (SEM) and an optical microscope respectively.

Poly-crystalline vanadium foils with 250 μm thickness are subjected to laser irradiations with energies varied from ~100 to ~400 J and the 3 ns pulse duration. Figure 46 shows that while the laser energy is less than 11.4 J, there is no spallation at the rear surface of the vanadium foil. By using the laser shock pressure equation described in Section 3.4, the pressure threshold of the laser-shock-induced spallation is higher than 22.3 GPa. It should be noted that this initial pressure is not the spall strength. In comparison to the estimated spall strength in the previous section, the spall strength for 250 μm vanadium is in the same order (10~20 GPa) as the initial pressure of 11.4 J laser. This suggests that the laser-induced shock wave attenuates drastically in the vanadium foil. Once the initial pressure exceeds the threshold for spallaiton (<50 J), spall fracture occurs at the rear side of the foil. The spall has a square fracture area due to the original square footprint of the incident laser beam [42]. Its size increases as the incident laser energy increases. However, the washers confined the fracture area, which can be seen in the 300 and 407 J laser experiments in Figure 46, where the fracture areas are nearly identical regardless of the differences in incident laser energies.

Morphologies of the spall surface of these 250 μm thick poly-crystalline samples are quite similar. Elongated grains and ductile fractures are distributed evenly all over the spall surface as shown in Figure 46. The 75 and 127 μm thick samples have almost identical fracture morphologies which are completely blow-off holes. We found that thinner samples can be completely fractured and created blow-off holes at the laser irradiated center due to the lower mechanical strength [85].
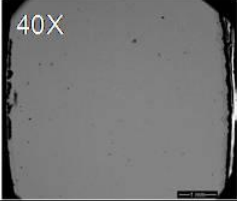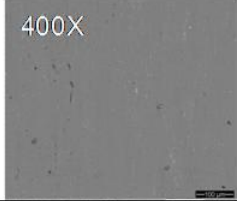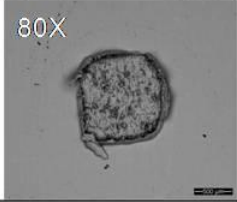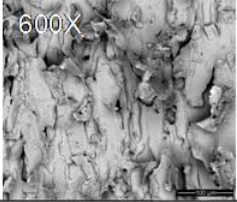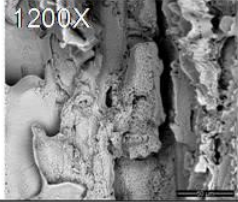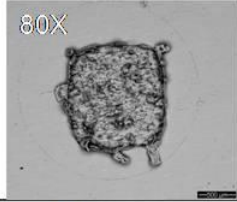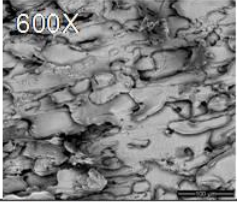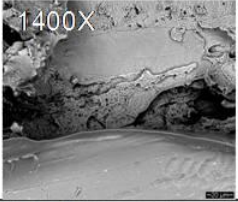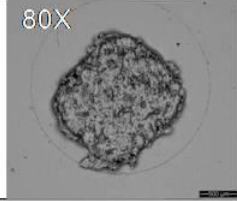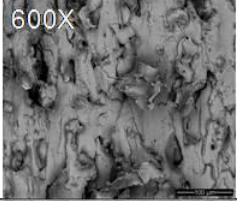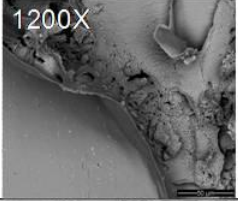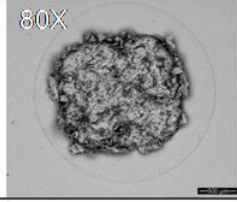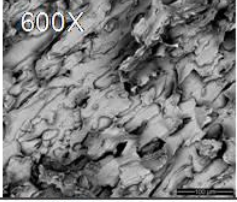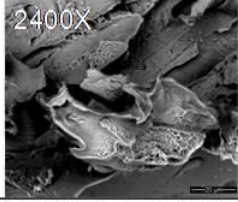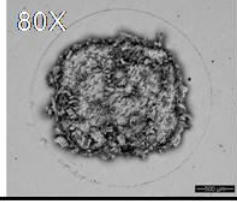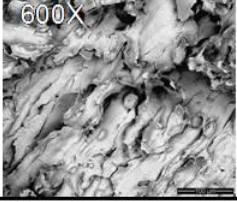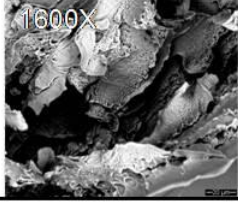
Figure 46: Polycrystalline vanadium, 250 µm thick, irradiated by laser with energies, 11.4, <50, 133, 253, 300, and 407 J.

Mono-crystalline vanadium foils with 250 μm thickness were subjected to laser shock experiments. This perfectly organized crystal structure yields different fracture morphologies and fragmentations. Figure 47 shows the completed spallation is not found in the 80J laser shock experiment. Compared to the results of poly-crystalline samples, the threshold pressure for spallation of the mono-crystalline vanadium is much higher. Using the equations shown in Section 3.4, the threshold pressure of <100> oriented single crystal is ~81.8 GPa which is higher than the threshold pressure of poly-crystalline vanadium, which is <59 GPa. This difference is possibly due to the pre-existing grain boundaries, dislocations, voids, and other defects in the poly-crystalline vanadium foils. Since the spall is caused by the progress of initiations, accumulations, and spallations sequentially, those pre-existing defects become the preferable locations for spall initiations and accumulations, which significantly decrease the threshold pressure of the spall.

The poly-crystalline vanadium has the brittle facture surfaces with a considerable amount of ductile fractures. However, the mono-crystalline structure has distinct fracture morphologies that contain ductile fracture surfaces with few brittle cracks. The perpendicularly intersected cracks (brittle cracks) shown in Figure 47 (36 Joule laser) present that {110} slip planes in <100> direction, which cannot be found in poly-crystalline recovered samples. Nevertheless, unlike the elongated crystals shown on the spall surface of the poly-crystalline vanadium, the surface morphologies of mono-crystalline spallation show that only dimples and ductile fractures are presented on the spall surface. These phenomena prove that pre-existing defects, such as grain boundaries,

play an important role in the spallation process. A noticeable correlation between the increase in the size of the spall area and the rise of the incident laser energy is seen in the poly-crystalline recovered samples as well as the mono-crystalline recovered samples.

Figure 47: Mono-crystalline vanadium, which has the 250 μm thick, and the crystal orientation <100>, irradiated by laser with energies, 36, 80, 198, 407, 424 J.

Different orientations of single crystal may influence the spall morphologies. Single crystal vanadium with <110> orientation was subject to ~400 J, 3 ns, laser shock (see Figure 47). The spall surfaces of 392 J and 416 J laser experiments as shown in Figure 48 present square rings concentric to the center of the spallation. This suggests that orientation differences can cause noticeable changes in spallation of mono-crystalline metals, and result in identical spall morphologies. The concentric rings might be the slipping planes of the <110> vanadium. The corresponding blow-off area of the 396 J laser energy shown in Figure 48 might happen due to the completely broken square ring.
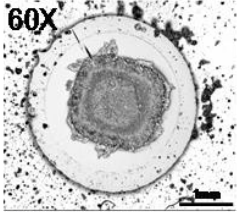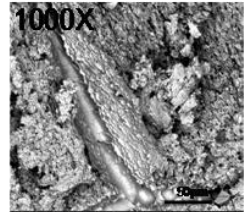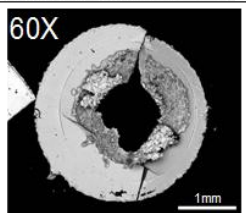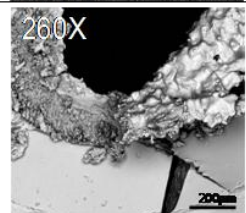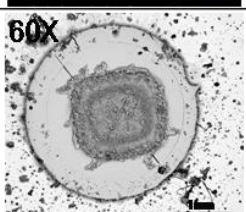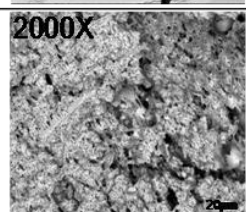
Vanadium Single Crystal (250µm) Conditions & SEM Images		
Orientation	Laser Joule(3ns)	SEM Images
<110>	392J	
<110>	396J	
<110>	416J	

Figure 48: Mono-crystalline vanadium, which has the 250 µm thick, and the crystal orientation <110>, irradiated by 392, 396 and 416 J laser.

Fragmentations are the critical problems for the LLNL laser instrument. This dynamic fracture happens in a very short time duration (several micro-seconds), and flies off the spall surface with a very high velocity (~hundreds meter s^{-1}). Grady *et al.* [130-137] have done a systematic study for predicting and determining failure and fragmentation properties of different metals. Based on these investigations, theoretical models for spallation and fragmentation are established.

In this study, fragmentations of the poly- and mono-crystalline vanadium are investigated using the glass shields placed at the rear side of the sample (see Figure 41). The fragments with great momentums cause damages on the glass shields, and the sizes of the damages are proportional to the volumes of fragments. Figure 49 shows the 75 μm samples irradiated by (a) 290 J and (b) 167 J laser. Apparently, the extent of damage from the ejected fragments was greater in the 290 J experiment. In order to quantify the damage on the glass shields induced by the vanadium fragments, a circular grid was superimposed on the glass shield images, and the imaging software, ImageJ, was used to determine the number of fragments per unit area as a function of distance away from the central damage zone [85]. Clearly, the plot in Figure 49 (c) shows that the extent of damage (fragments per unit area) to the 290 J glass shield was more significant compared with the 167 J glass shield. The experimental data is well fitted using a power function. It should be noted that the reduction in damage away from the central crater was also found in the 175 and 250 μm thick samples' fragmentations.

SEM analysis of the glass shields shows that vanadium might melt due to the shock compression. Jarmakani *et al.* applied a theoretical melting and shock temperature

rise modeling. It was found that vanadium melted under the shock compression should re-solidify immediately upon pressure release. Due to this swift re-solidification, the splash marks and vanadium debris show on the glass shields. Energy dispersive X-ray spectroscopy (EDS) was conducted on the glass shields and the energy spectrum was analyzed to confirm the elements present.
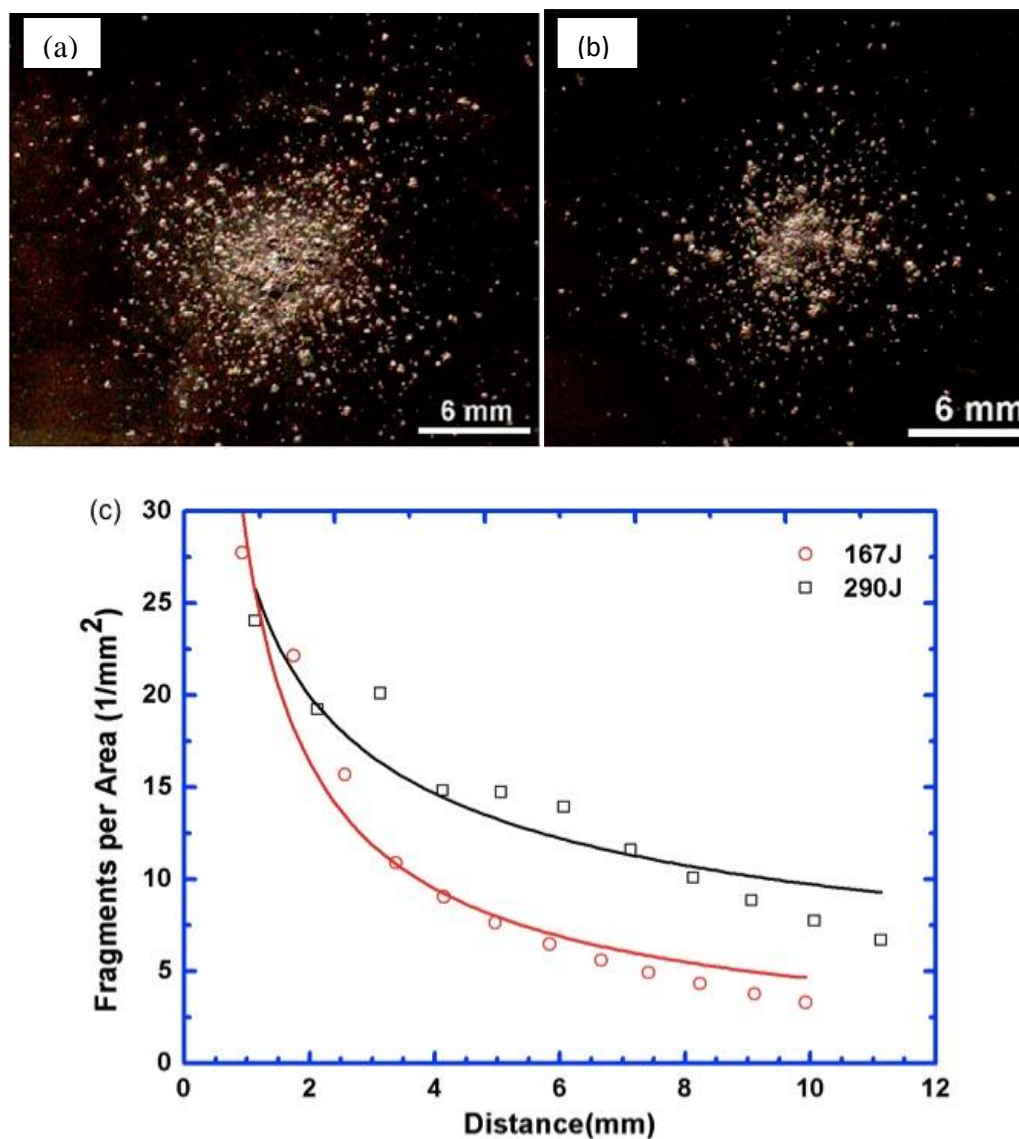
Figure 49: Glass shields damaged by poly-crystalline vanadium, 75 μm: (a) 290 J, (b) 167 J; (c) fragments per area as a function of distance from the central damage.

Fragmentations of mono-crystalline vanadium also have similar damage patterns as the ones shown in Figure 49. However, due to the difference of the crystal structure, the glass shields of the mono-crystalline vanadium somehow present different damage patterns, which are shown in Figure 50. For the mono-crystalline vanadium, the spall initiation pressure is much higher than the poly-crystalline sample inasmuch as the description in the prior section. This suggests that the spall strength of the mono-crystalline vanadium is higher, which results in less fragments presented in Figure 50. For instance, the fragmentation from <100> mono-crystalline vanadium irradiated by 198J laser has less than 10 fragments (Figure 50 (a)), however the poly-crystalline vanadium has more than a hundred fragments under similar laser conditions (Jarmakani *et al*. [85]). Glass shields from mono-crystalline vanadium irradiated by ~400 J laser were also collected (Figure 50 (b, c)). These damage patterns were processed using the image processing software, ImageJ, and the same approach used for calculating the fragment numbers of the poly-crystalline vanadium in the previous section. These results are shown in Figure 50 (d) and fitted by power function curves.

The theoretical prediction of an average fragment size S while the flow stress dominates the spallation is given by the Grady-Kipp theory. The theory based on energetic conservations, where the sum of the kinetic energy of an expanding body *T* and the elastic energy *U* is more than or equal to the ductile fracture energy $W=Y\varepsilon_c$:

$$T+U \geq W \qquad \text{Eqn. (35).}$$

This leads to an equation that determines the average fragment size *S*:

$$S = \left(\frac{8Y\varepsilon_c}{\rho\dot{\varepsilon}^2} \right)^{1/2},$$

Eqn. (36)

where Y is the dynamic yield stress, ρ is the density, ε_c is the critical strain to failure and $\dot{\varepsilon}$ is the imposed strain rate. Jarmakani $et\ al.$ proposed that the strain rate of this study could be obtained approximately using the estimation of the expansion of the spalled region and the maximum strain of vanadium, which was 20% of the original thickness (by Yoshinaga $et\ al.$ [138]). The expansion velocity can be approximated as the free surface velocity U_{fs}, which is equal to two times of the particle velocity at the free surface $(U_{fs} \approx 2U_p)$. Knowing the pressure at a given distance from the front surface, U_p can be obtained from the Rankine – Hugoniot (R – H) equations. Thus, strain rates can be obtained from $2U_{fs}/P$. Scientists have studied the dynamic properties of vanadium under explosive loading, gas gun loading [139] and the split Hopkinson pressure bar technique [141]. The dynamic yield stress was ~480 MPa (Chabildas $et\ al.$ [140]), which was in good agreement with the work done by Batsanov $et\ al.$ [139]. The yield strength of vanadium does not seem to be very sensitive to strain rate, hence, we took the dynamic yield strength Y equal to 480 MPa in our analyses. With all parameters determined, the fragment size S is plotted as a function of strain rate in Figure 51. We also directly measured the vanadium fragment sizes based on the fragments collected on the glass shields. The total number was estimated with the aid of ImageJ. For simplicity, the assumption was made in all cases that the total spall area was $\pi d^2/4$, where d = 2.5 mm (the inner diameter of the washer), and the thickness of the fragments was equal to the spall thickness. By dividing the spalled area by the total number of fragments on the glass

shield for all experimental cases, we were able to obtain the area of each individual fragment. Assuming the fragments were geometrically square and taking the square root of this area, we obtained the experimental fragment size S_{exp}. The experimentally determined fragment sizes were also plotted as a function of strain rate in Figure 51. It is clearly evident that the experimentally determined fragment sizes were smaller than those obtained using the G－K model by a factor of 2－3. One can get a better fit by increasing *Y*, but this is an uncertainty. More recent theories by Glenn and Chudnovsky [142] and Molinari and coworkers [143, 144] predict values that were a factor of six lower than the original G－K model and, therefore, it can be said that the current experimental results are in between these predictions. Considering the uncertainties in experimental measurements and simplifying the assumptions in the G－K model, the agreement is considered satisfactory. Theory predicted and the experiments showed a decrease in fragment size with strain rate. The S_{exp} values were actually in better agreement with some fragment sizes measured at lower strain rate.
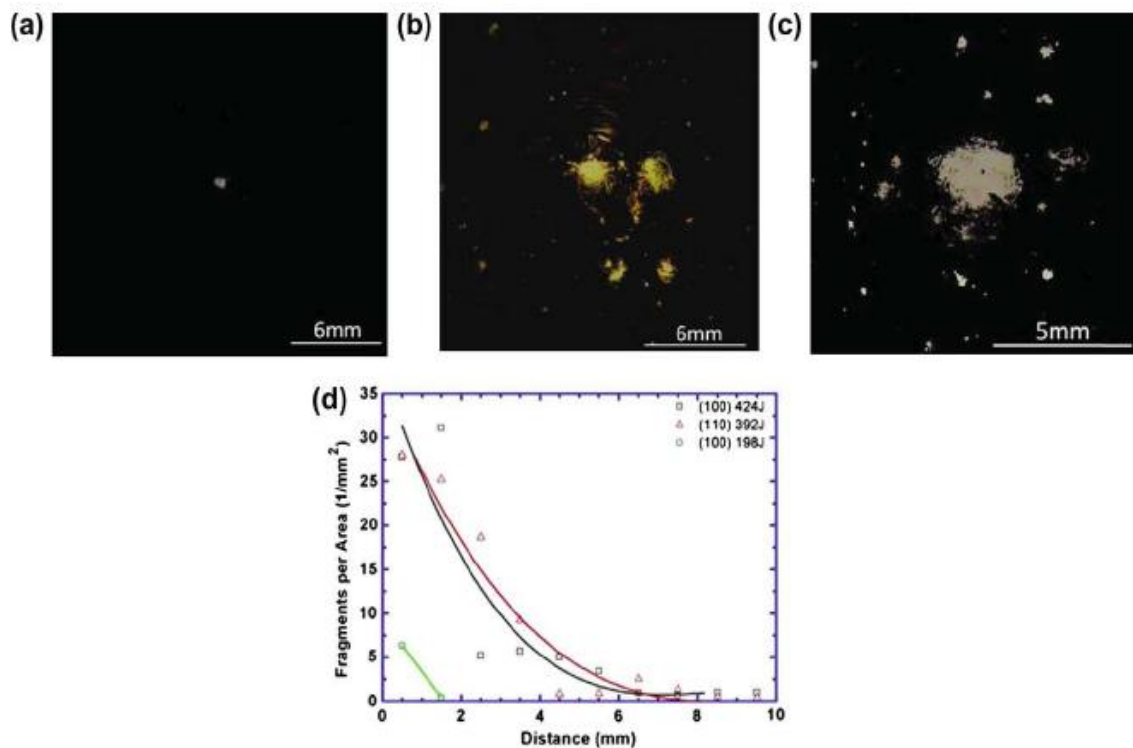
Figure 50: Damage in mono-crystalline 250 μm vanadium targets: (a-c) glass shields damaged by mono-crystalline vanadium fragments: from <100>, <100>, and <110> vanadium irradiated by laser energies of 198 J, 424 J, 392 J respectively.
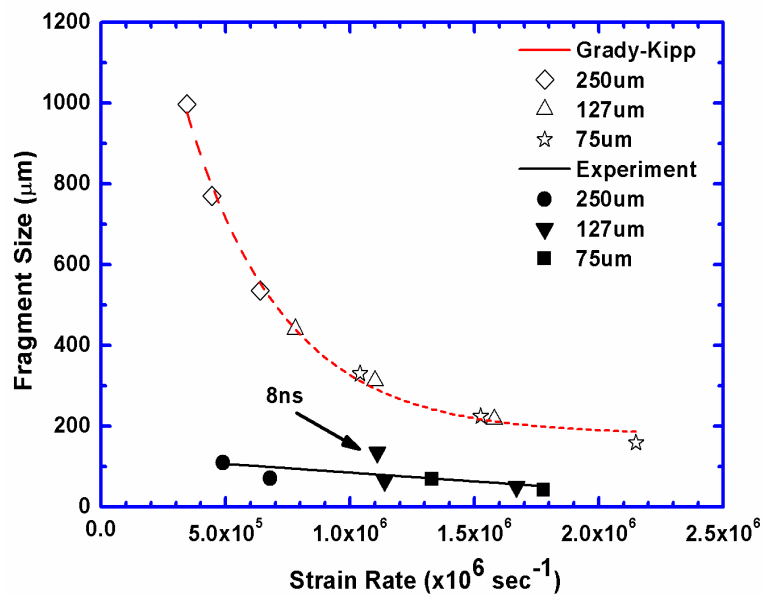
Figure 51: Fragment size vs. strain rate included Grady-Kipp theoretical estimations and the experimental results.

4.1.3 VISAR real-time analysis

The shadowgraphy of the in-flight fragments was carried out for mono-crystalline vanadium. The shadowgraphs show a well formed plume which can be used to calculate the velocities of fragments. Figure 52 shows the shadowgraphs, whereas Figure 53 shows the corresponded velocity distributions. The comparison of Figure 52 (a) and (b) suggests smaller fragments for the <110> crystal, in agreement with greater propensity for cleavage for <100>. These results are also consistent with the markings on the glass target shown in Figure 50. Due to the incompatible numbers of the fragments between the shadowgraphs and glass targets, one conclusion that can be reached is the sizable fraction of the fragments fail to produce visible craters on glass. Approximately 200 fragments were counted for the <110> crystal, whereas the number seen in Figure 50 is considerably lower. At the lower energies, as expected, the number of fragments and their velocity are lower (Figure 53(a, b)).

From VISAR pullback signal in Figure 54, the spall surface velocity and the corresponding pressure profile provide reliable estimates of the spall strength. It was calculated from the pullback signals in the instrumented experiments carried out on the monocrystalline vanadium having 250 um thickness. The procedure was delineated by Grady and Kipp [77]. The following expression was used for the spall strength (Eqn. 8.7 from [77]):

$$\sigma_T = \frac{1}{2}\left(Z_s - Z_w\right)u_{\max} - \frac{1}{2}\left(Z_s + Z_w\right)u_{\min} \qquad \text{Eqn. (37)}$$

where u_{max} and u_{min} are the velocities marked A and B in Figure 54 (a). The impedances

of window and specimen are Z_w and Z_s, respectively. Since VISAR was applied to the surface of the specimen with $Z_w=0$. Thus:

$$\sigma_T = \frac{1}{2}\rho_0 C_0 \left(u_{max} - u_{min}\right)$$
Eqn. (38)

where $\rho_0 = 6.11 \times 10^3 \text{kg/m}^3$ and $C_0 = 4,560$ m/s for vanadium. The calculated spall strengths for the 423, 206 and 106 J experiments are 8.8, 4.8 and 5.6 GPa respectively. These results are somehow consistent with the HYADES simulation results showing that the spall strength 10 and 13 GPa corresponded to 200 and 400 J laser energy respectively in Section 4.1.1. The lower strength measured from VISAR may reflect that the mono-crystalline materials might have impurities or pre-existing flaws inside the crystal structure.

Grady [132] presented explicit expressions for estimating the spall strength of condensed media. He derived an equation for calculating the theoretical spall strength, which gives an upper bound value. It was derived from an analytical representation of the cold compression-tension curve based on a Morse potential [132]:

$$\sigma_{th} = \sqrt{\frac{U_{coh}B_o}{8V_o}}$$
Eqn. (39)

where, U_{coh} is the specific cohesive energy (10.04 MJ/Kg for vanadium, calculated from [132]), B_o is the bulk modulus (160 GPa for vanadium), and V_o, is the specific volume at zero pressure. Eqn. (39) gives a theoretical spall strength of ~ 35 GPa.

Using an energy balance analysis, Grady [132] also provides expressions for both the ductile and brittle spall strength of condensed media, which give estimated values that are more consistent with experimental results. From the empirical results (see micrographies Figure 47, Figure 48), it is rational to conclude that vanadium spalls by ductile behavior. In other words, the spall process involves spherical cavitations (i.e. the nucleation, growth and coalescence of voids) and occurs strictly through plastic flow. Hence, we adopt the expression for the ductile spallation [132]:

$$\sigma_T = (2\rho\, c_o^{\,2} Y \varepsilon_c)^{1/2} \qquad\qquad\qquad \text{Eqn. (40)}$$

where, ρ is density, c_o is the sound velocity at zero pressure, Y is the dynamic yield strength (480 MPa), and ε_c is the critical strain (0.2). This gives a spall strength of 5.5 GPa for vanadium.

Figure 55 shows the theoretical ductile spall strength of vanadium and various other fcc and bcc metals and how they compare with the experimental results tabulated in the published paper [85] from different sources. Most of the theoretical ductile spall strengths of the various materials reported seem to be in the same range with that of the experimental values. It should be mentioned that these experiments are conducted using gas guns.

The experimental values obtained herein for vanadium, however, are considerably higher than the experimental and Grady-Kipp ductile spall strengths by a factor of 2-3. Consistent with the current results, the spall strength measured by Gilath [128] for

aluminum, also using lasers, are on the order of 2.5-5 GPa; this value is considerably higher than the reported value by Grady [132]. In Figure 55 three lines are drawn, corresponding to gas-gun, laser experiments and theoretical calculation by Grady equation. There is a clear time dependence, which can be accounted for by the strain rate dependence of the yield stress, Y:

$$Y = Y_0 \left(\frac{\dot{\varepsilon}}{\dot{\varepsilon}_0} \right)^m \qquad \text{Eqn. (41)}$$

where $\dot{\varepsilon}$ is the strain rate and m is the strain rate sensitivity. The other two parameters are normalizing factors. If one considers that the strain rates imparted in gas-gun and laser compression are on the order of 10^4 -10^6 s^{-1}, and that in laser compression on the order of 10^7 s^{-1}, one would arrive at a reasonable agreement. It should be noted that this approach ignores the complexities of the nucleation-growth-coalescence effects involved in spalling.

Possible reasons for such a discrepancy maybe be due to the fact that the pulse decay profiles we based our calculations on are modeled and not actually based on VISAR data, which could introduce some error. Also, the rapid loading rates achieved in the laser experiments may have caused much higher tensile stresses to develop, producing spall strengths higher than more conventional impact situations (plate impact, explosives) and placing them closer to the theoretical spall strengths [132].

These results are in agreement with the ones by Gilath [128], who measured a spall strength of 6061-T6 Al at a strain rate of (1-4) $\times$ 10^7 s^{-1} produced by laser shock in

conditions similar to the ones in current investigation. In contrast, gas-gun spall strength measurements reported by Grady [132] at strain rates of 10^4-10^6 s^{-1} had a spall strength of 10-20 GPa.
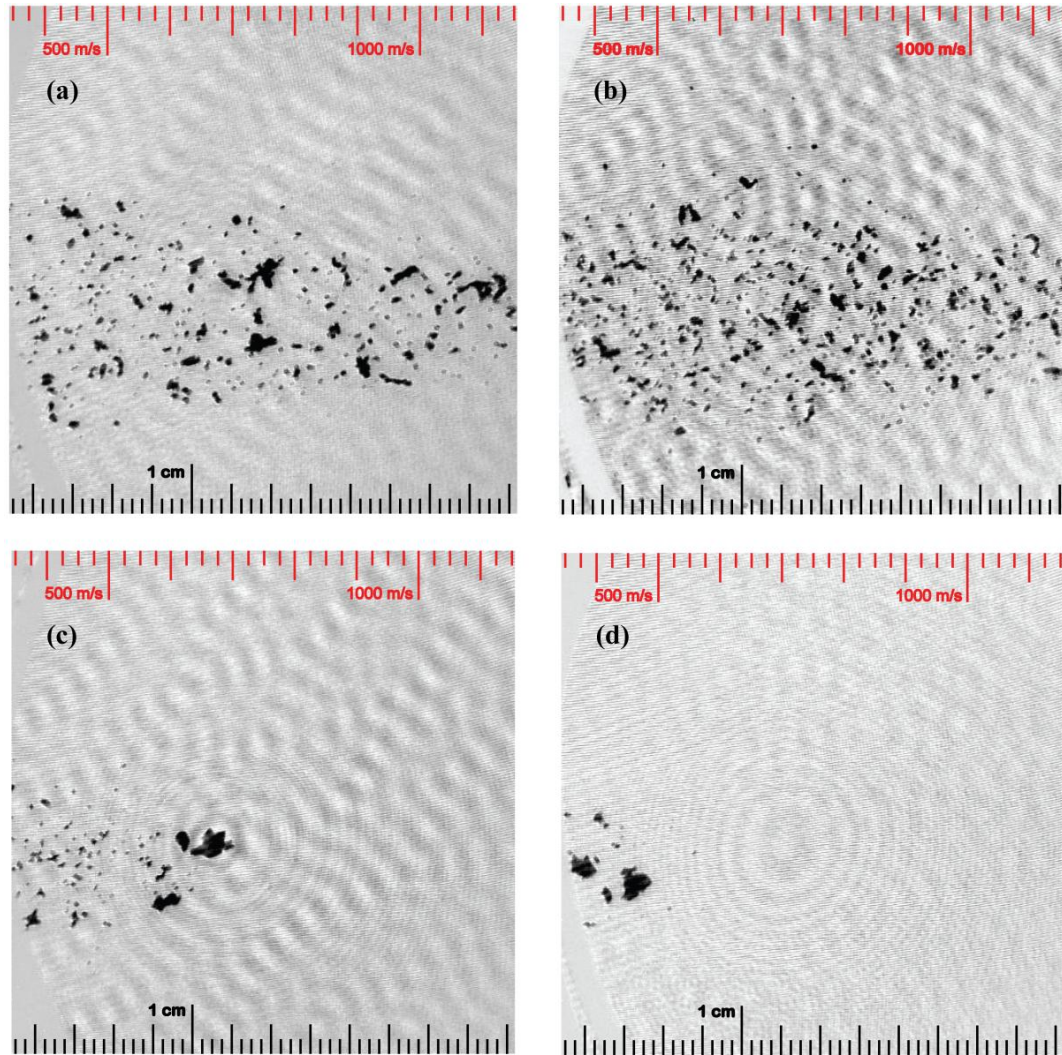
Figure 52: Gated shadowgraphy of in-flight particles ejected from : (a) <100> at 415 J, (b) <110> at 423 J, (c) <110> at 206 J, and (d) <110> at 106 J.
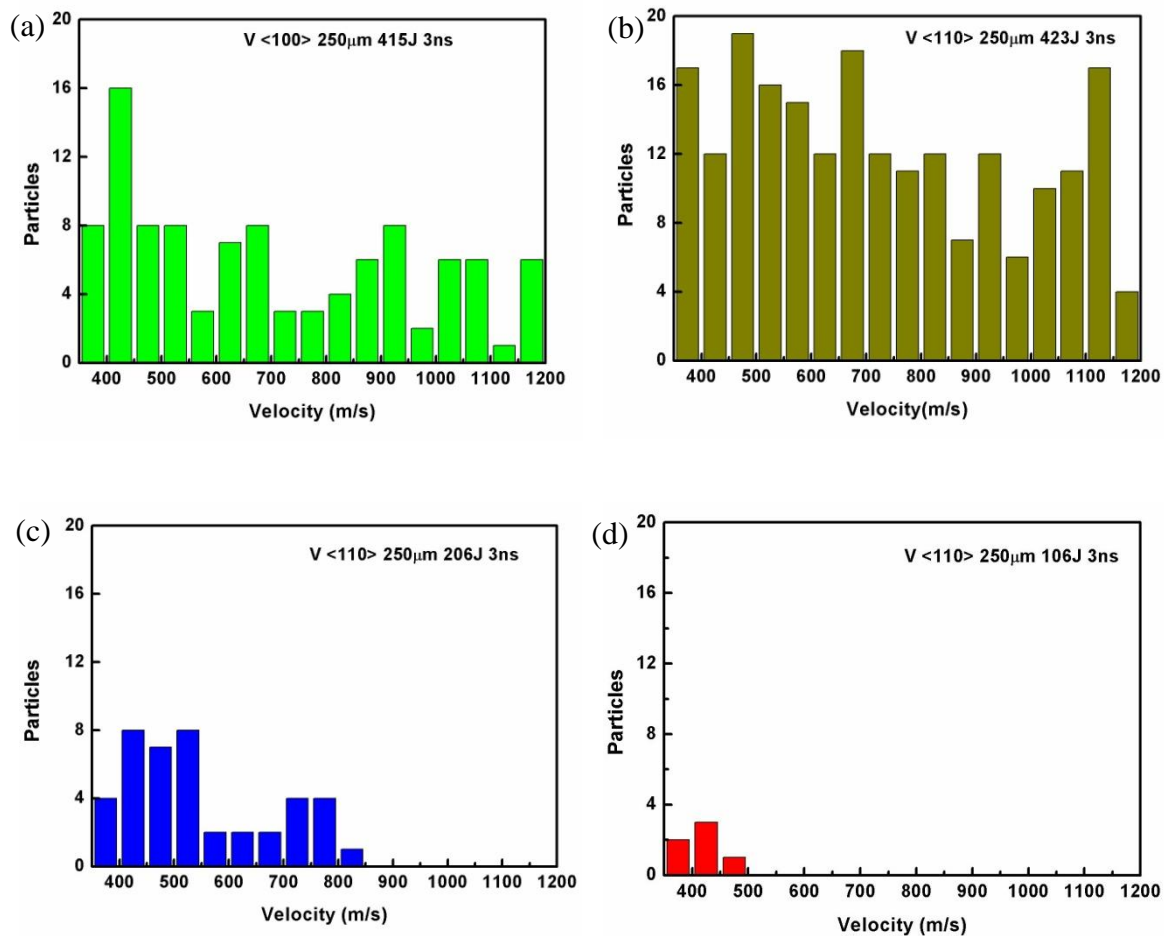
Figure 53: Fragment velocity distribution from gated shadowgraphs in Fig. 24; (a) <100> at 415 J, (b) <110> at 423 J, (c) <110> at 206 J, and (d) <110> at 106 J.
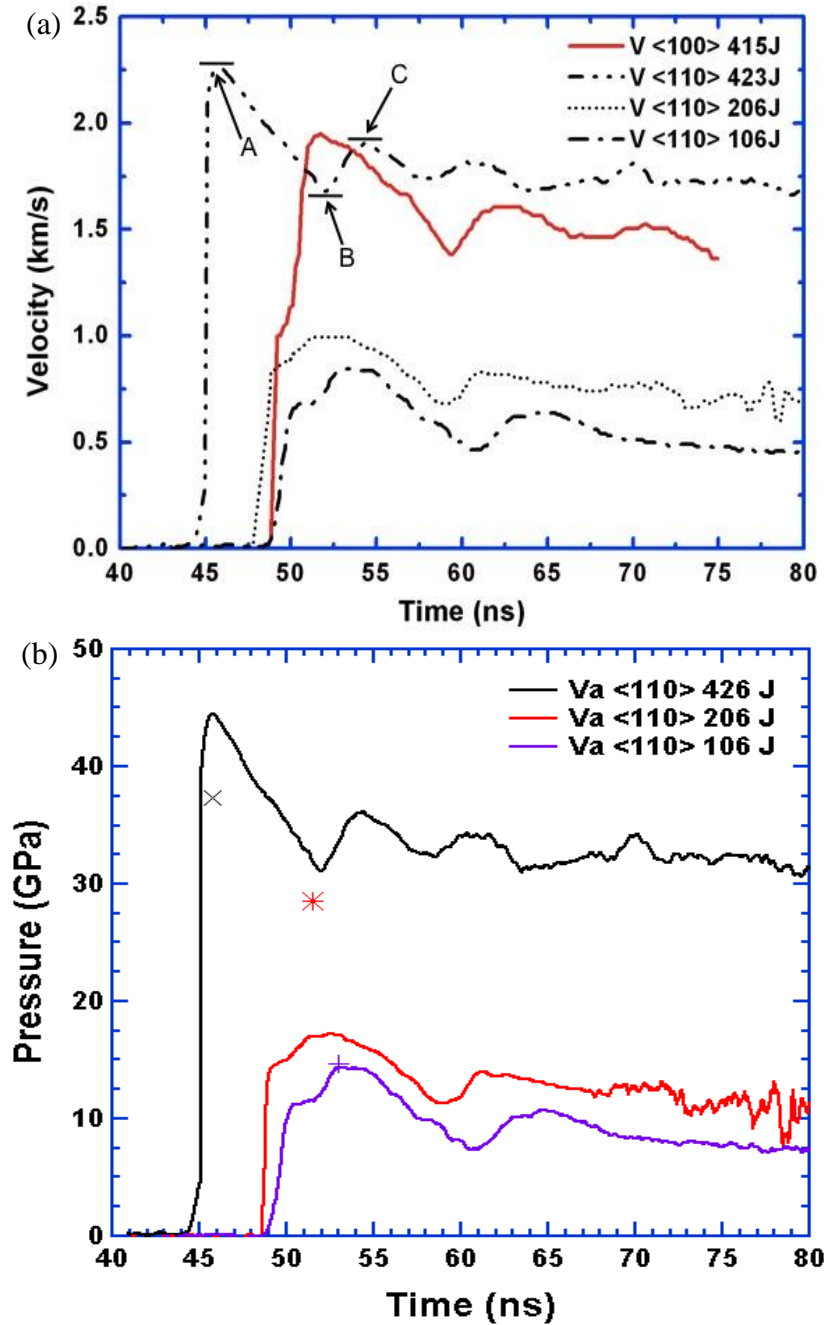
Figure 54: (a) Free surface velocity and (b) pressure as a function of time for Va <110> single crystal samples at 423 J, 206 J, and 106 J. The values at A, B, and C correspond to the peak velocity, pullback velocity, and spall peaks, calculated using the free surface velocity measured from VISAR and VRH shock data. Single points are peak pressure values calculated using the HYADES code.
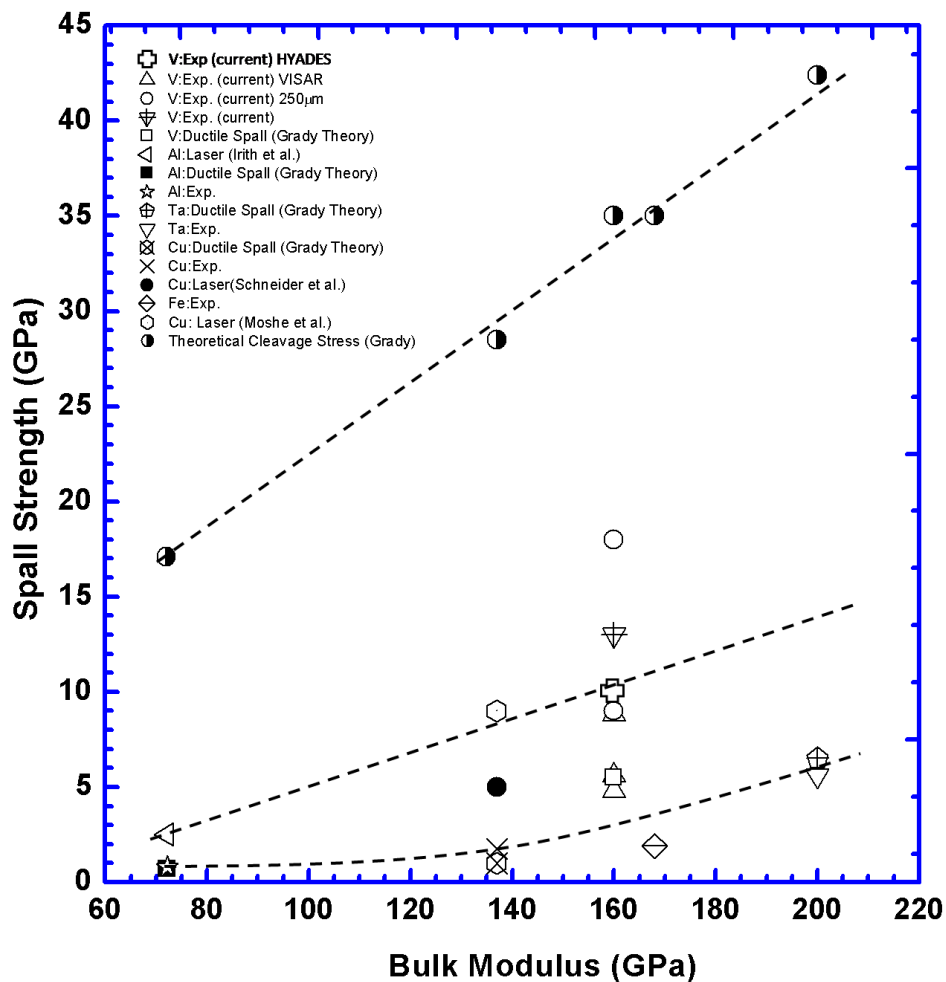
Figure 55: Spall Strength vs. Bulk Modulus for various FCC and BCC metals; comparison of theoretical cleavage strength (Grady [132], upper curve) and experiments. Note separate curves for gas gun and laser experiments suggesting a strong strain-rate or time dependence.

4.1.4 Conclusions

From the theoretical study of the shock wave behaviors in poly and mono-crystalline vanadium, the fragmentation, and the fracture phenomena of the recovered samples, we can obtain the following conclusions.

1. Evidence of molten and re-solidified fragments was observed on the glass shields, in agreement with a solid–liquid transition induced by shock compression.

2. The damage and fragment distribution were significantly affected by laser energy. The highest intensity laser resulted in a high density of very small droplets distributed on the glass plate, while the lowest intensity laser resulted in a few damaged spots on the glass plates.

3. Thicker foils (250 µm) showed incipient spall planes and bulk deformation by shock loading, and samples of intermediate thickness (127 µm) showed tearing away around the laser spot, while the thinnest foils (75 µm) showed almost complete blow-off due to the laser beam interaction. At the same energy level damage accumulation on the glass shields decreased as the target thickness increased. This suggests that thicker samples have a higher shock fracture resistance compared to the thinner sample.

4. In the mono-crystalline samples there were clear differences: a higher spall strength and the appearance of cleavage cracks associated with brittle fracture. This is in accordance with enhancement of the ductile–brittle transition increasing the grain size. The debris and damage area on the glass plate of mono-crystalline vanadium are dramatically decreased compared to the poly-crystalline sample. It implies the mono-crystalline structure has a relatively higher shock fracture resistance.

5. Spalling and fragmentation were found to proceed by ductile void nucleation, growth and coalescence. The grain boundaries were favored paths for decohesion.

6. The fragmentation was quantitatively estimated as a function of laser pulse energy and duration and compared with the G–K analysis. The measured spall strengths were higher, by a factor of 2–3, than the expected results and calculations using G–K analysis. The discrepancy can be attributed to the strain rate sensitivity of the yield stress, which is considered satisfactory in view of the experimental uncertainties and theoretical assumptions. Other factors, such as the spall thickness, could also play a role.

7. Shadowgraph pictures reveal the velocity distribution corresponding to the different incident laser energy. The high incident laser energy produced more fragments with higher velocities which was consistent with the measurements of fragments on the glass plate.

8. The spall strength measured from VISAR pull-back signal was in the range of 5 to 9 GPa which was lower than the estimated spall strength from HYADES and theoretical calculations. These results are higher than the empirical results obtained using gas guns and the difference can be attributed to the strain rate sensitivity of the flow stress.

4.2 Dynamic and quasi-static responses of explosive shock consolidated Al base powder mixtures

Shock consolidation process was commonly used for producing solid and nearly fully dense compacts included ceramic powder mixtures [145-153]. In this study, the double tube explosive shock consolidation system was employed, which was thoroughly introduced in Section 2.1.3. The objective of this study was to investigate the mechanical response and failure mechanisms in powder mixtures densified by shock compaction

prior to reaction. The densification pressure was kept intentionally low, avoiding any significant shock-induced melting and reaction [20]. The results and discussion are shown as the following.

4.2.1 Compact micro-structure

Figure 56 shows the cross-sectional microstructure of each individual reactive mixture. For all mixtures, the darker phase is (BSE) aluminum, by virtue of its lower atomic weight. These compacts have over 96% TMD after explosive consolidation, which is close to the fully dense materials (Table 7). The Ni+Al (Figure 56 (a)) compact has spheroid Ni particles (Figure 56 (a) brighter particles) surrounded by Al matrix (Figure 56 (a) gray matrix). The W+Al has similar morphologies as Ni+Al (Figure 56 (a, b)); the W particles (Figure 56 (c) brighter particles) are more irregular and have multi-angular shapes, as shown in Figure 18 (e). In addition, the Al phase became a continuous matrix after the explosive shock consolidation in Ni+Al and W+Al compacts. For other compacts, Mo+Al, Nb+Al, Ta+Al (Figure 56 (c, d, e)), the microstructures are dissimilar to Ni+Al and W+Al compacts. The Mo, Nb or Ta particles deformed and connected, and became the continuous phases. The explanation for this difference in compaction morphology is in the morphology of the initial powders. The Mo, Nb, and Ta powders agglomerated and flowed more freely. These pre-existing agglomerations of Ni, Nb, and W particles caused by van der Waals forces on the surface of the particle [67] can induce the significant influences on the microstructures of the shock consolidated powder compacts. These Ta, Mo and Nb continuous phases (Figure 56 (c, d, e) brighter areas)

enveloped the Al powders during the explosive compaction event. In some cases the compacts might have limited intermetallic phases due to localized reaction during explosive shock consolidation.
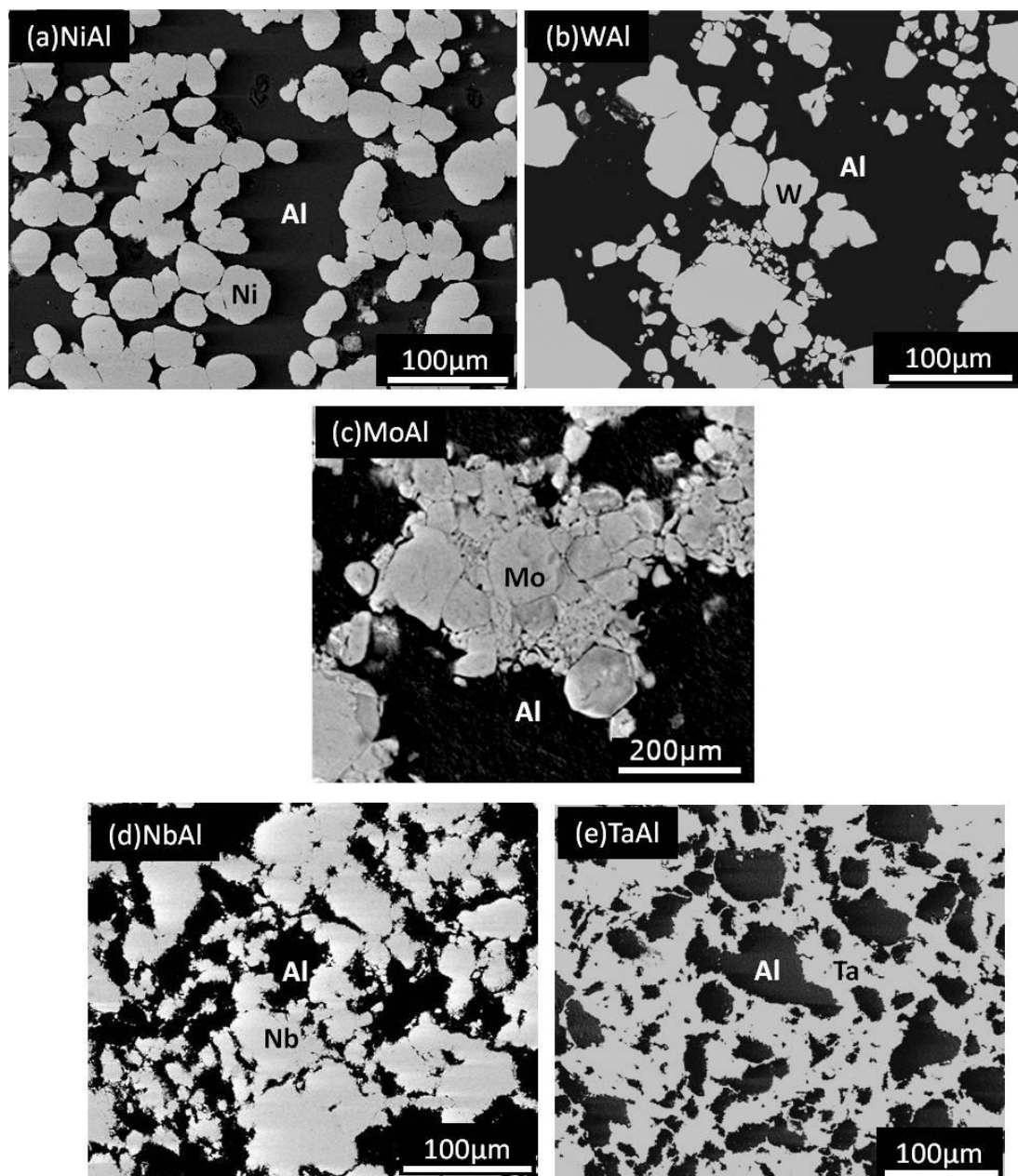
Figure 56: Cross-sectional sample morphologies: (a) Ni+Al, (b) Nb+Al, (c) W+Al, (d) Ta+Al, (e) Mo+Al. (Notice that the brighter areas represent heavier metals Ni, Nb, W, Ta, Mo in Figs. (a), (b), (c), (d), (e), respectively.

Table 7. of the as-produced explosive shock consolidated compacts *Du et al. [65].

Compacts	Ni+Al	Nb+Al	W+Al	Mo+Al	Ta+Al
Molar ratio	1.483:1	0.908:1	1.026:1	1.044:1	0.903:1
	(Ni:Al)	(Nb:Al)	(W:Al)	(Mo:Al)	(Ta:Al)
TMD%	97.4%*	99.1%*	99.1%	96.5%*	98.3%*
ρ (kg/m^3) (Sample)	5649*	5528*	10903*	6222*	9181*
ρ_0 (kg/m^3) (Theoretical)	5800*	5620*	11000*	6450*	9650*

The consolidating pressures can reach 4~7 GPa, which produced by the double-tube explosive shock consolidation system [68]. The shock compressibility possibly determined the microstructure of the as-produced reactive mixtures. By considering the Rankine-Hugoniot relations, one can estimate the volume changes corresponding to specific shock pressures for each elemental phase. Here two Rankine-Hugoniot equations demonstrate that P (pressure) is a function of U_p (particle velocity) in Eqn. (42),and V/V_o (volume change) is a function of U_p in Eqn. (43). The two equations are used to evaluate the volume changes under the shock loading, 3, 4, 5, 6, 7 GPa, as shown in Figure 57:

$$P = \rho_0(C_0 U_p + S U_p{}^2) \qquad\qquad \text{Eqn. (42)}$$

$$\frac{V}{V_0} = 1 - \frac{U_p}{C_0 + S U_p} \qquad\qquad \text{Eqn. (43).}$$

By using V/V_0-U_p relationship Eqn. (43) and substituting U_p in Eqn. (42), one can obtain

the P-V/V_0 relation:

$$P = \rho_0 C_0^2 \left(\frac{V/V_0}{\left(1 - S\left(V/V_0\right)\right)^2} \right) \qquad\qquad \text{Eqn. (44)}$$

here ρ_o, C_o, and S represented respectively the density, elastic wave velocity, and shock empirical parameter of each elemental metal, which are shown in Table 8 [154]. The results of the shock pressure, P, versus normalized volume changes, V/V_0, are presented in Figure 57. It shows that tungsten is the preferable material for forming the continuous phase in the Al base binary mixtures due to its lower shock compressibility, however it is contrary to the experimental observation in Figure 56 (b). This suggests that the morphologies and sizes of the original powders and the van der Waals force significantly influence the microstructure of the explosive-shock-consolidated compacts instead of the intrinsic properties in terms of the compressibility of these elemental metals.
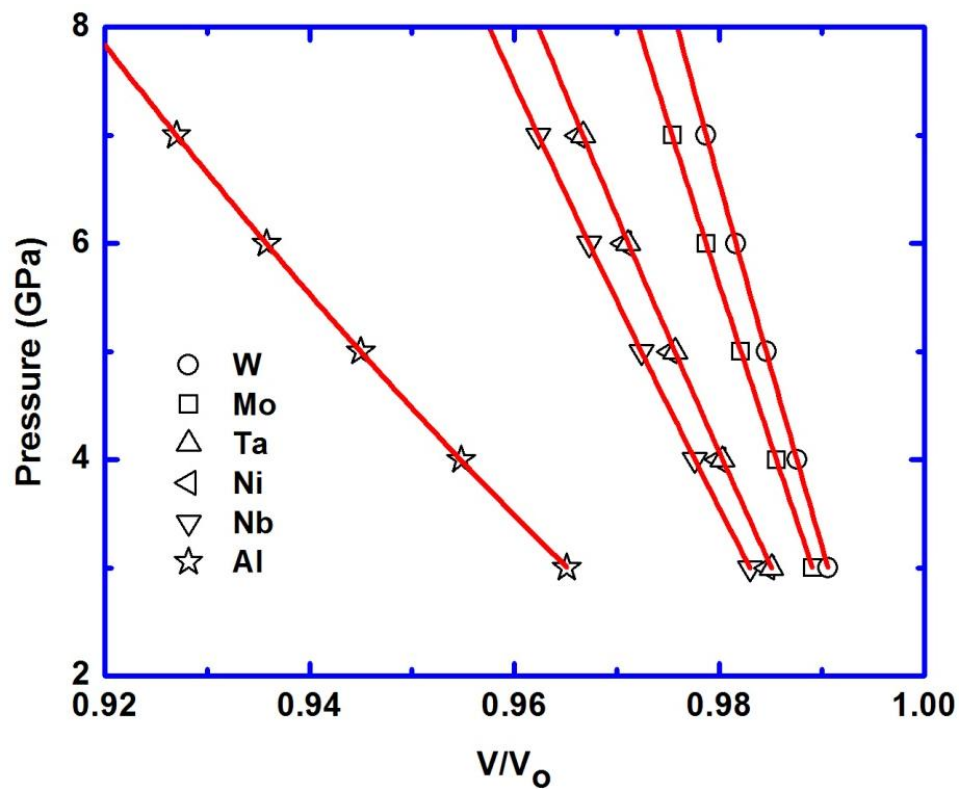
Figure 57: Pressure versus normalized volumetric changes for W, Mo, Ta, Ni, Nb and Al.

Table 8. Parameters for Rankine-Hugoniot equations [154]

Material/Parameter	ρ_o (10^3 kg/m^3)	C_0 (10^3 m/s)	S
Mo	10.21	5.12	1.23
Nb	8.59	4.44	1.21
Ni	8.87	4.6	1.44
Ta	16.65	3.41	1.2
W	19.22	4.03	1.24
Al	2.75	5.33	1.34

4.2.2 Estimated mechanical properties

It is challenging to propose a rational interpretation of the elastic and plastic behavior for the explosive shock consolidated powder mixtures due to the imperfections such as cracks and voids, and the varied morphologies of the initial powders in the compacts in comparison with monolithic alloys.

Ledbetter and Datta [155] addressed that the Young's modulus were not superposable values, if the volume fraction of the inclusion was too high (30% SiC in Al matrix). Madhavi *et al*. [156] also proposed an estimation much more close to the experimental measurement by comparing the experimental and theoretical ultrasonic wave velocity in composites, but there was a considerable uncertainty. However, it is still worth the effort to evaluate the elastic properties of the perfect binary alloys with the same volumetric ratio as shown in Figure 56, which help us understand the influences of the continuous elemental phases on the elastic and plastic behaviors, as well as the effects caused by the imperfections from explosive shock consolidation of the as-produced compacts.

The volumetric ratio of each explosive shock consolidated sample was measured using the image processing software, ImageJ, as presented in Table 9. By employing the Hashin's constitutive equations [157], which is based on the empirical results and designed for qualifying the elastic behaviors of materials, the following constitutive approximations are used to obtain the bulk *(B)* and shear *(G)* modulus of the compacts:

$$\frac{B}{B_m} = 1 + \frac{3\left(1 - v_m\right)\left(\frac{B_p}{B_m} - 1\right)C_p}{2\left(1 - 2v_m\right) + \left(1 + v_m\right)\{\frac{B_p}{B_m} - \left(\frac{B_p}{B_m} - 1\right)C_p\}}, \qquad \text{Eqn. (45)}$$

$$\frac{G}{G_m} = 1 + \frac{15\left(1 - v_m\right)\left(\frac{G_p}{G_m} - 1\right)C_p}{7 - 5v_m + 2\left(4 - 5v_m\right)\{\frac{G_p}{G_m} - \left(\frac{G_p}{G_m} - 1\right)C_p\}}, \qquad \text{Eqn. (46)}$$

where G is the shear modulus and B is the bulk modulus, which can be applied to estimate a material's Young's modulus (E) using the well-known equation for isotropic media:

$$E = \frac{9BG}{3B + G} \qquad \text{Eqn. (47).}$$

The B_m, B_p, G_m, G_p, C_p, v_m are the bulk modulus of the matrix, bulk modulus of the inclusion, shear modulus of the matrix, shear modulus of the inclusion, heat capacity and volumetric friction of the matrix respectively. This equation gave an exact prediction of the elastic behavior for the perfect binary alloys [157]. Hashin's estimations compared with experimental measurements of the explosive shock-consolidated samples were shown in the Table 9. The results suggest that these compacts have the elastic modulus close to the perfect binary alloys. The elastic modulus of Ni+Al compact is much lower and inconsistent with the estimated result which is possibly due to its relatively large portion of Al phase, lower bulk density, and the pre-existing critical defects.

Table 9. Volumetric fractions shown in Fig. (4) measuring by ImageJ, Hashin's estimated elastic moduli and measured elastic moduli of the powder consolidated compacts.

Compact	Al phase (Volumetric %)	2nd phase (Volumetric %)	Hashin's estimated E (GPa)	Measured elastic modulus (GPa)
Ni+Al	51	49	109.4	37.6
W+Al	61	39	87.6	70.4
Mo+Al	48	52	87.5	91
Nb+Al	33	67	72.3	67.1
Ta+Al	40	60	78.6	78.3

The microindentation Vickers hardness (VHN) of each phase in the explosive shock consolidated compacts are shown in Table 10. This enables an approximate estimate of the yield stress (σ_y) of the material through the Tabor equation: $\sigma_y = VHN/3$ [158]. By using a simple rule of mixture for metal base composites [159, 160], estimates of the yield stress, σ_c, can be obtained. Eqn. 48 shows the rule of mixture for binary metal base composites:

$$\sigma_c = \sigma_m x_m + \sigma_s x_s \qquad\qquad \text{Eqn. (48)}$$

where σ_m and σ_s are the yield stress of the matrix and second phase respectively which are estimated from the hardness, x_m and x_s are the corresponding volume fractions shown in the Table 9. The estimated and measured yield stress corresponding to the hardness of the second phase are plotted in Figure 58. Interestingly, from the experimental measurements, the compact with hardest second phase, tungsten, has the lowest yield stress, which is ~ 240 MPa, and the one with relatively softer second phase, Ta, has the highest yield stress,

which is ~ 450 MPa. These experimental results were inverse to the estimates by the rule of mixture which presented that the second phase strengthened the compacts while the hardness increased. This inconsistency suggested that the yield stress of the explosive shock consolidated compacts is not determined by the mechanical properties of the components.

The microstructural characterization in Figure 56 provides the possible strengthening mechanism. It shows that the high yield strength compact, such as MoAl, NbAl, TaAl (Figure 56 (c, d, e)), has the continuous second phase of Mo, Nb and Ta. Nonetheless, the low yield strength compact, such as NiAl and WAl, has the continuous Al phase. This suggests that the different continuous phases in the compacts determine the yield strength of consolidated mixtures.

Table 10. Micro-hardness tests of reactive mixture.

Compacts	Al+Ni	Al+Ta	Al+W	Al+Mo	Al+Nb
Hardness (Al) GPa	0.53±0.06	0.49±0.04	0.55±0.07	0.5±0.06	0.67±0.16
Inclusion	Ni	Ta	W	Mo	Nb
Hardness GPa	2.7±0.32	2.24±0.89	4.17±0.24	2.21±0.8	2.92±0.27
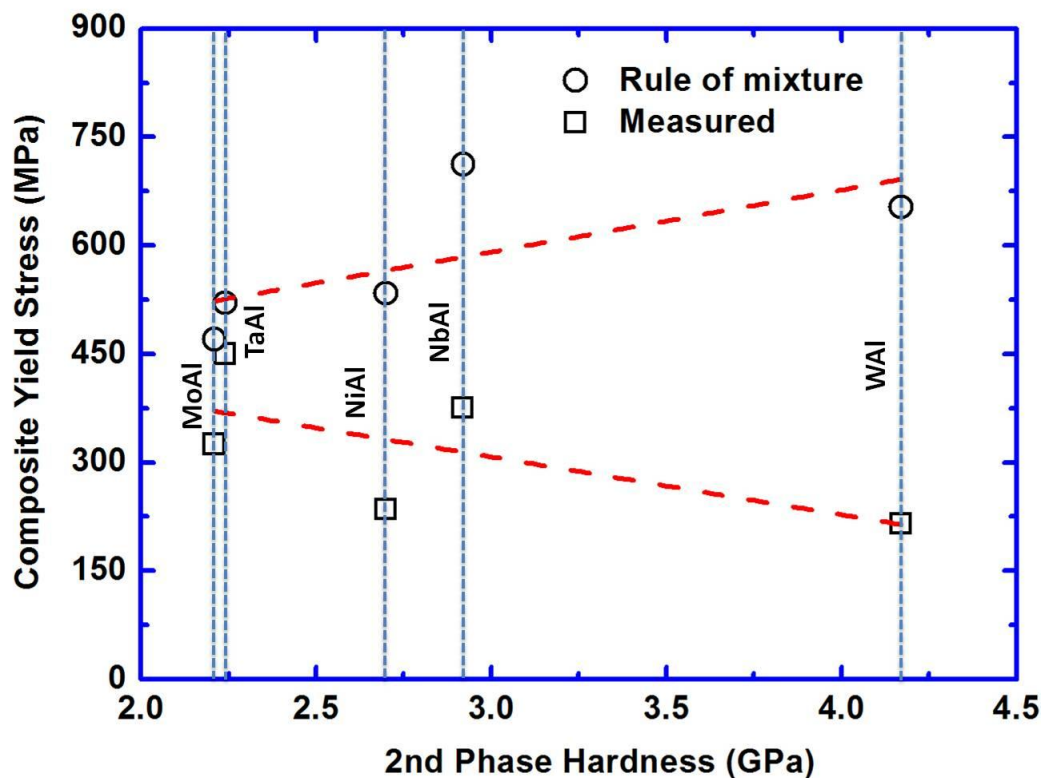
Figure 58: Yield stress of the consolidated powder mixtures estimated from the hardness measurement and the rule of mixture corresponding to the hardness of the second phases.

4.2.3 Qualitative analysis

The intermetallic phases are known to be a significant factor for determining the mechanical properties of the composites due to their high strength and low density. In this study, the explosive shock consolidation process provided low energies, but limited intermetallics is a possibility due to the solid diffusion mechanism [161-164] or shock-induced reaction mechanism. A qualitative evaluation was conducted using the x-ray diffractometer (XRD) and differential thermal analysis (DTA). The XRD analysis as shown in Figure 59 exhibits the contained elements in each compact. Except for the Nb+Al compact, these as-produced powder compacts had no intermetallic phases after

the explosive shock consolidation. The intermetallic phase found in the Nb+Al compact was the Al_3Nb [165], which was the intermetallic that can be formed by SHS from powder mixtures [166]. However the intermetallic phase in Nb+Al compact did not show any solid evidence of strengthening the mechanical properties and the XRD peaks showed that this intermetallic phase was in a minor amount.

Differential thermal analysis (DTA) is an important probe for identifying the configurations and the reaction temperatures of the powder mixtures [121-123]. DTA was conducted on the original (as-produced), quasi-static and dynamic compressed samples of the Ni+Al and Nb+Al explosive shock consolidated mixtures with a temperature ramping rate, 10 ^{o}C/min, as shown in Figure 60. The results of the Ni+Al samples show that a primary heat exotherm at about 650 ^{o}C representing the formation of the intermetallic $NiAl_3$ [121]. There is a convex at about 620 ^{o}C, previous to primarily exothermic point, which might indicate that there is a intermixing phase in the as-produced Ni+Al compact caused by explosive shock consolidation. This reactive intermixing phase generates $NiAl_3$ intermetallic before the primary exothermic reaction. After quasi-static and dynamic compression, more defects are produced and the Ni/Al interfaces are drastically decreased which significantly delays and smoothes the first exothermic peak as shown in Figure 60 (a).

The Nb+Al original and recovered samples only show strong endothermic reaction corresponding to the Al melting which means there is no intermixing/reaction produced by the compression tests and the explosive shock consolidation.

As the aforementioned qualitative analysis shows, it can be concluded that intermetallics and intermixing phase pre-existed in the as-produced compacts. However these heterogeneous phases did not significantly influence the mechanical properties of the explosive shock consolidated compacts as shown in Figure 61Figure 62 where the mixture without pre-existing intermetallics such as Ta+Al had the highest yield stress, and the one with intermixing phase such as Ni+Al had the lowest yield stress.
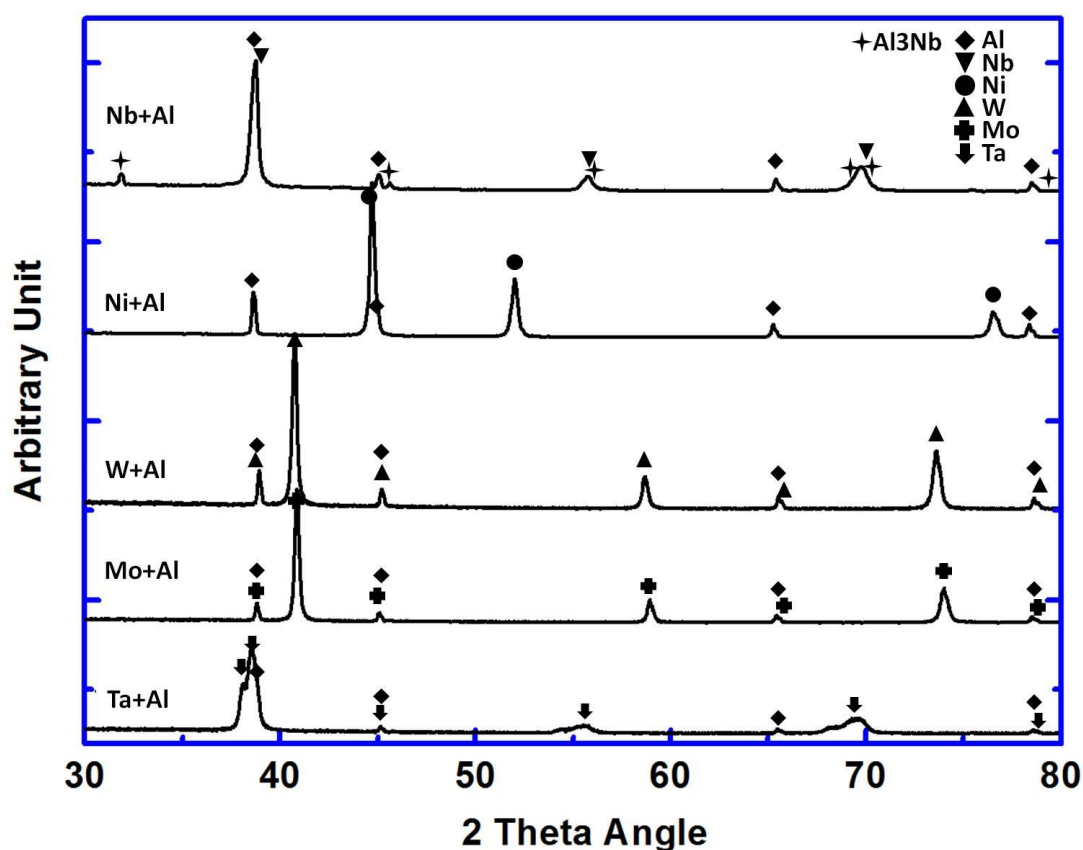
Figure 59: The XRD patterns of as-produced powder consolidated cylinder (Ni+Al, Nb+Al).
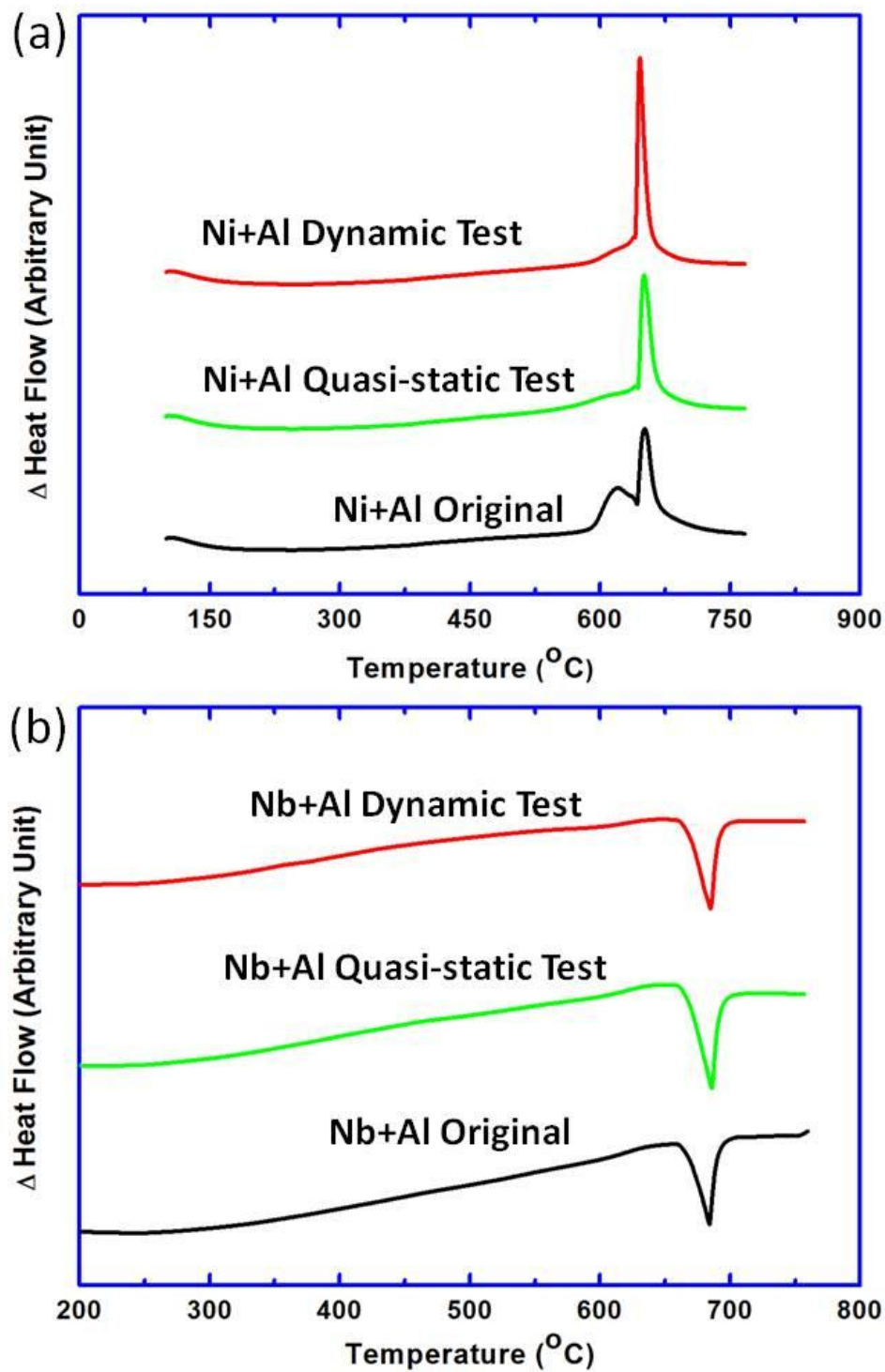
Figure 60: Differential thermal analysis (DTA): (a)DTA results of original, quasi-statically, and dynamically tested Ni+Al reactive mixtures; (b) the results from Nb+Al reactive mixtures with the same test conditions as (a).

4.2.4 Quasi-static and dynamic tests

Quasi-static compression test

The quasi-static compression test results, shown in Figure 61, reveals the stress-strain behaviors of the double tube explosive shock consolidated mixtures. No extensometer was used and the results are corrected from load-displacement plots by subtracting machine effects. The elastic modulus for each reactive mixture are listed in Table 9. The experimental Young's modulus of Al+Ta, 78.3 GPa, and Al+Mo, 91 GPa, are consistent with the theoretical estimations for Al+Ta, 79.96 GPa, and Al+Mo, 99.2 GPa, reactive mixtures. However, for other reactive mixtures, Al+Ni, Al+W and Al+Nb, the experimental results deviated from the theoretical estimations by a significant amount. It demonstrated that the uncertainty (such as the porosity, agglomeration, peak pressure [159] of the consolidation, and the de-bonding syndrome in the explosive consolidation compacts) of estimations of the elastic modulus were significantly influenced the mechanical properties of materials. Nonetheless the relatively lower Young's modulus of Al+Ni, Al+W, Al+Nb, suggest that Al is the dominant material for the elastic behaviors of these compacts. This is also consistent to Ledbetter and Datta's observation on the SiC+Al composite [155]. The consistent results of Al+Ta and Al+Mo corresponding to the cross-sectional morphologies seen in Figure 56 (c) and (d), prove that different continuous phases of the compacts can alter the elastic behavior of the explosive shock consolidated powder mixtures.
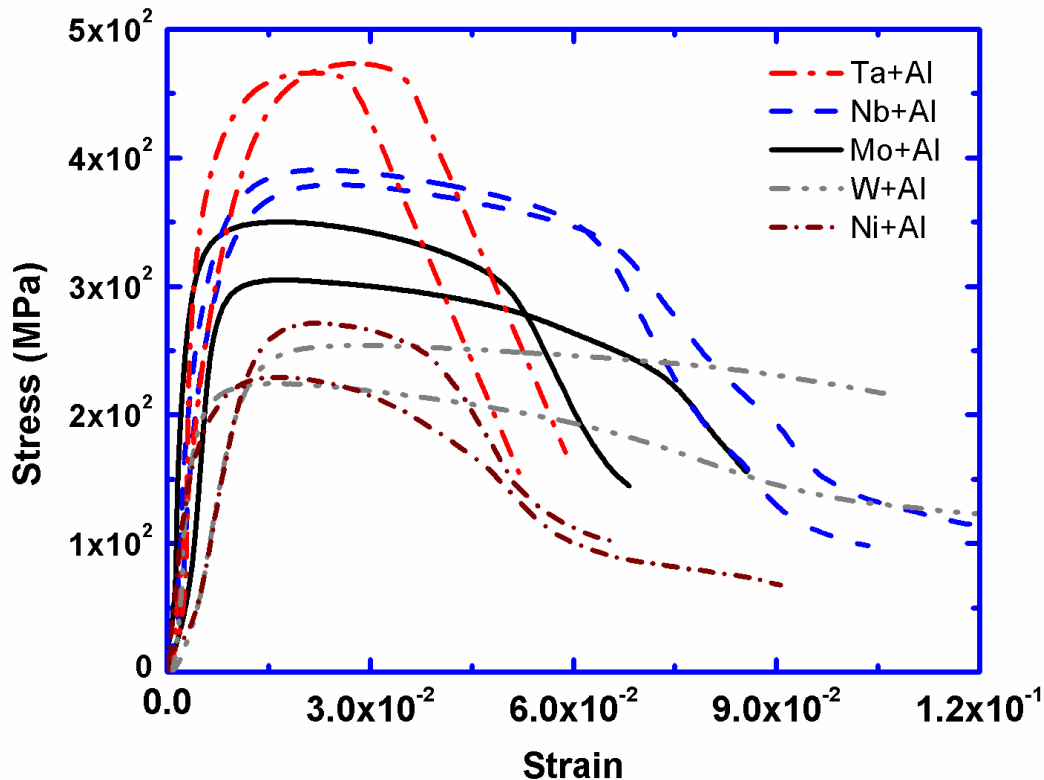
Figure 61: Quasi-static compressions of consolidated mixtures (Strain rate $\approx 10^{-3}$).

Dynamic test (the split Hopkinson pressure bar test)

The dynamic test results using split-Hopkinson pressure bar (SHPB) are shown in the Figure 62 (a). A pulse-shaper (Al slab) with high-work-hardening rate was applied in order to generate a long rising time and ensure a nearly square strain rate wave [71], which helped to obtain the yield stress equilibrium and maintain a constant strain rate. The constant strain rate of approximate 2.5×10^3 s^{-1} was achieved by using this technique as shown in Figure 67.

These quasi-static and dynamic SHPB test results are plotted as a function of strain rate in the Figure 62 (b). The nonlinear tendency shown in the dynamic regime

(from 10^3 to 2.5 x10^3 s^{-1}) by the compacts with Ta, Mo and Nb, with higher strain rate sensitivities, are a clear consequence of the continuous phase determining the strain rate sensitivity as well as the yield stress. BCC metals (Mo, Nb, Ta) have a higher strain rate sensitivity at higher strain rates because the flow stress is determined by short range obstacles (P-N stresses) rather than long range stresses in FCC metals (dislocation forests). The activation volumes for obstacles in BCC crystals are ~ 1 b^3 (b is the Burgers vector), whereas they are much higher (10-100 b^3) in FCC crystals. These nonlinear mechanical properties in the mixtures containing Nb, Ta, and Mo can be quantitatively characterized using the strain rate sensitivity parameter m:

$$m = \frac{\partial \ln \sigma_y}{\partial \ln \dot{\varepsilon}}$$

Eqn. (49)

where the σ_y is the yield stress, and the $\dot{\varepsilon}$ is the strain rate. It should be noted that materials with small grains have a higher strain rate sensitivity value due to the grain boundary (GB) deformation mechanisms such as grain boundary migration, grain boundary sliding, and grain boundary dislocation nucleation [33-35]. In this study, the mixtures with cores inclusion grains, such as Ni and W, have the lowest yield stress especially in the quasi-static compression regime. The relatively smaller particle, Mo, Ta, and Nb, result in higher yield stresses at the low strain rate regime and high strain rate sensitivity in the dynamic tests (strain rate over 10^3 s^{-1}), as shown in Figure 62 (b). The strain rate sensitivity of Ta+Al changes from 4.4×10^{-2} to 2×10^{-1} in the high strain rate regime (about 10^3 s^{-1}); however for the compacts with continuous Al phase there is no

obvious change of the *m* value. Hence, the character of the continuous phase is manifested in the response of the compact.
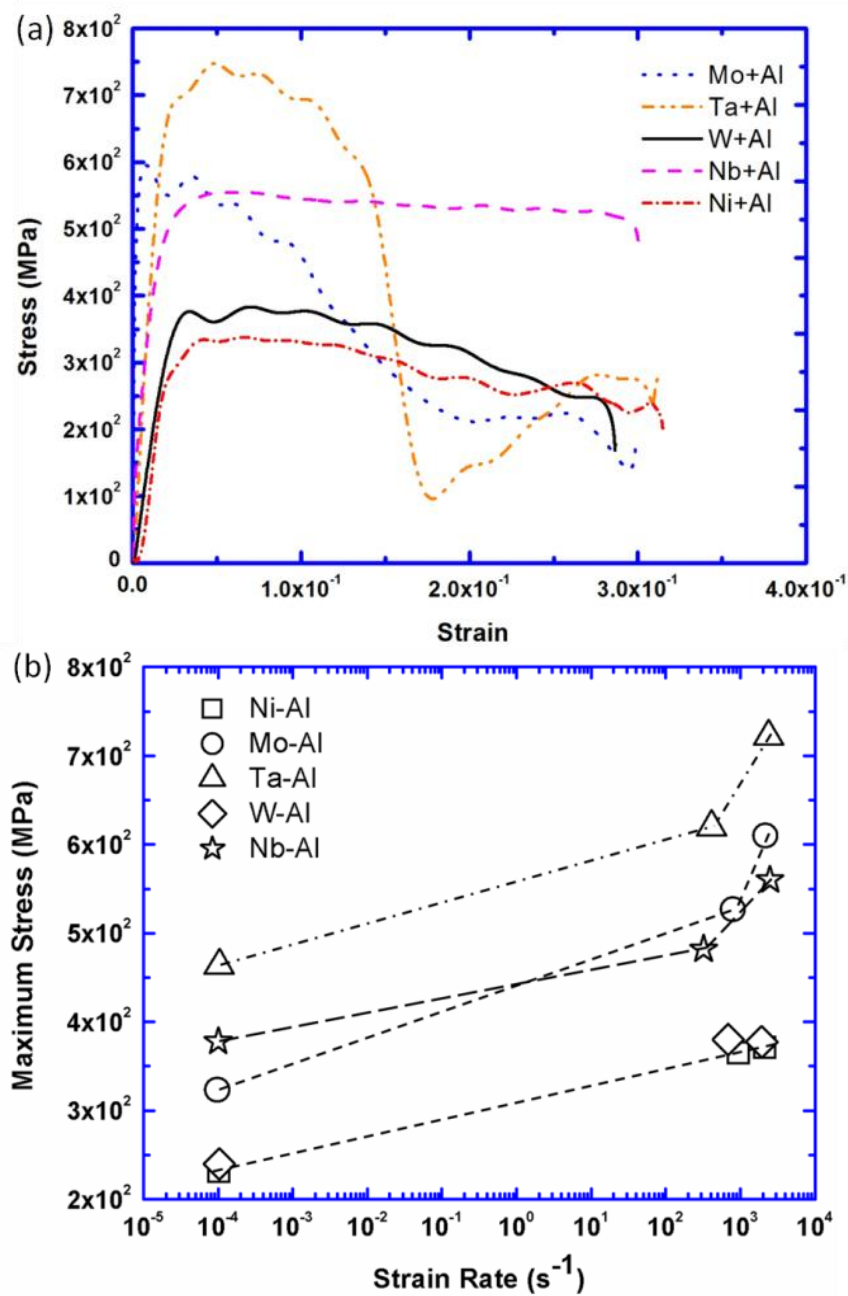
Figure 62: (a) The split Hopkinson bar tests. (b) Flow stress vs. strain rates.

4.2.5 Characterization of fracture morphology

The sequential images in **Error! Reference source not found.**, obtained from the high speed camera, Phantom V 710, show the evolutions of the fractures in the cylindrical specimens subjected to dynamic compression. It presents the real-time evidence of the different fracture morphologies. There are two distinct fracture types: one is the axial splitting fracture parallel to the loading direction on the compacts (**Error! Reference source not found.** (a, b)); the other is the shear fracture with cracks propagating diagonally at about a 45° angle to the compression direction through entire samples as shown in **Error! Reference source not found.** (c, d, e). The axial splitting mode corresponds to the specimens with continuous Al phase: Ni+Al, and W+Al. The shear mode corresponds to the other specimens: Mo+Al, Nb+Al, and Ta+Al. The corresponding cross sectional SEM images corresponding to the two failure failures are shown in Figure 64 (a, b, c). The Ni+Al cross section (Figure 64 (a)) shows axial splitting failure. However, for the compacts Nb+Al and Ta+Al, the propagation direction of the cracks is altered and results in primarily shear failures, as shown in Figure 64 (b, c). Figure 64 (d, e) reveals the high magnification images of Ni+Al, and Nb+Al compacts. The images clearly shows that the detail of two different facture morphologies. The axial splitting fracture in Figure 64 (d) reveals that the debonded Ni particle surrounded by cracks. This surrounding cracks seem to proliferate and connect which possibly leads to the axial splitting fractures. On the other hand, the shear fracture in Nb+Al of Figure 64 (e) has no debonded phenomenon. This suggests the dominant factor which results in different fracture mechanisms is correlated to the continuous phases in the compacts.
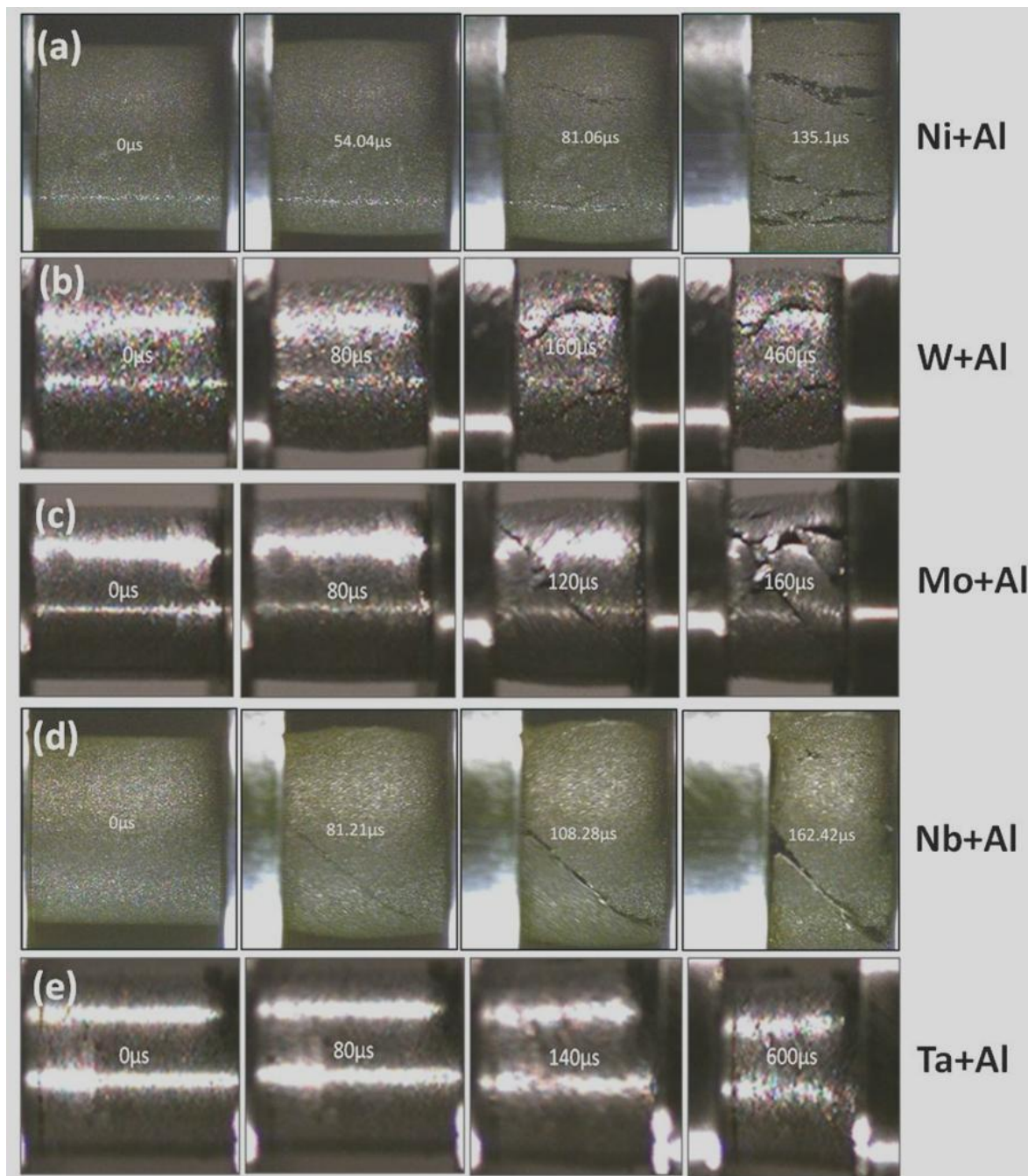
Figure 63: Snapshots from high speed cinematography of dynamic compression showing (a) Ni+Al, (b) W+Al axial splitting and (c) Mo+Al, (d) Nb+Al, (e) Ta+Al, shear failure.
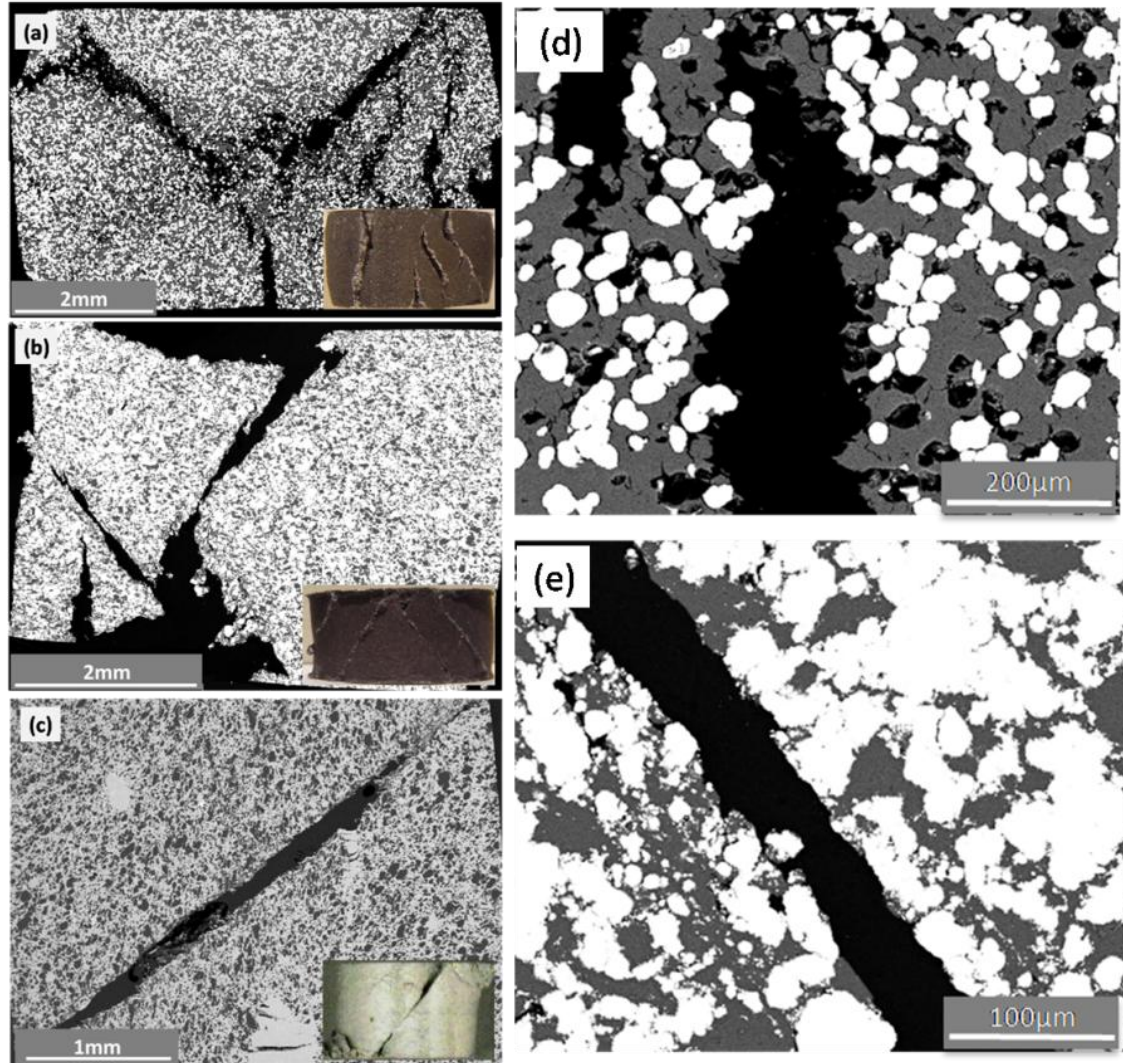
Figure 64: SEM(BSE) images: (a)Ni+Al, (b)Nb+Al, and (c)Ta+Al samples after dynamic test corresponded to the three different fracture structures, axial splitting, axial splitting mixed shear, and shear fracture, respectively. (d) The SEM-BSE images showing cracks propagating along the Ni powders but traverse Nb particles (e).

The two failure mechanisms corresponding to their distinctive microstructures are shown schematically in Figure 65. Figure 65 (a) illustrates how the axial splitting failure forms in the compact with the continuous Al phase. The discontinuously distributed second phase particles dispersed in the continuous Al phase can be considered as rigid during plastic deformation in uniaxial compressive loading because their hardness

significantly exceeds that of Al. The crack is initiated at the interface between these 'rigid' Ni or W particles and the Al matrix. During compression loading, the rigid particles move and cluster in the Al matrix. As the compact continues to be compressed (vertically), these clustered particles are crowded out and move laterally (horizontally) creating gaps. The low bonding strength between particle and matrix enable the creation of cracks with longitudinal axis parallel to the loading direction as shown in Figure 65 (a) (right inset). Eventually, these micro-cracks accumulate and become macro-cracks, propagating through the entire sample as axial splitting. This is shown in the corresponding experimental result of Figure 65 (c), for Ni-Al.

Figure 65 (b) illustrates the shear failure mechanism. In this case, the continuous phase has a yield strength higher than the discontinuous phase (Al). Table 10 shows that the microhardness of Mo, Nb, and Ta is 3~4 times that of aluminum. Thus, as the compact is deformed in compression, the 'hard' matrix and the 'soft' discontinuous phase combine to enhance shear failure. (Figure 65 (b) right inset). The discontinuous phase no longer restricts the shear of the continuous phase, but actually assists it because it has a lower strength. This results in the diagonal shear crack propagation and enhances the mechanical strength of these compacts. Cai et al. [167, 168] and Herbold et al. [169, 170] found that in the consolidated powder composites, the metallic powder granules with fine particle sizes can tailor the dynamic fracture and enhance the mechanical properties due to the meso-scale force chain formation. This is consistent with our experimental results.
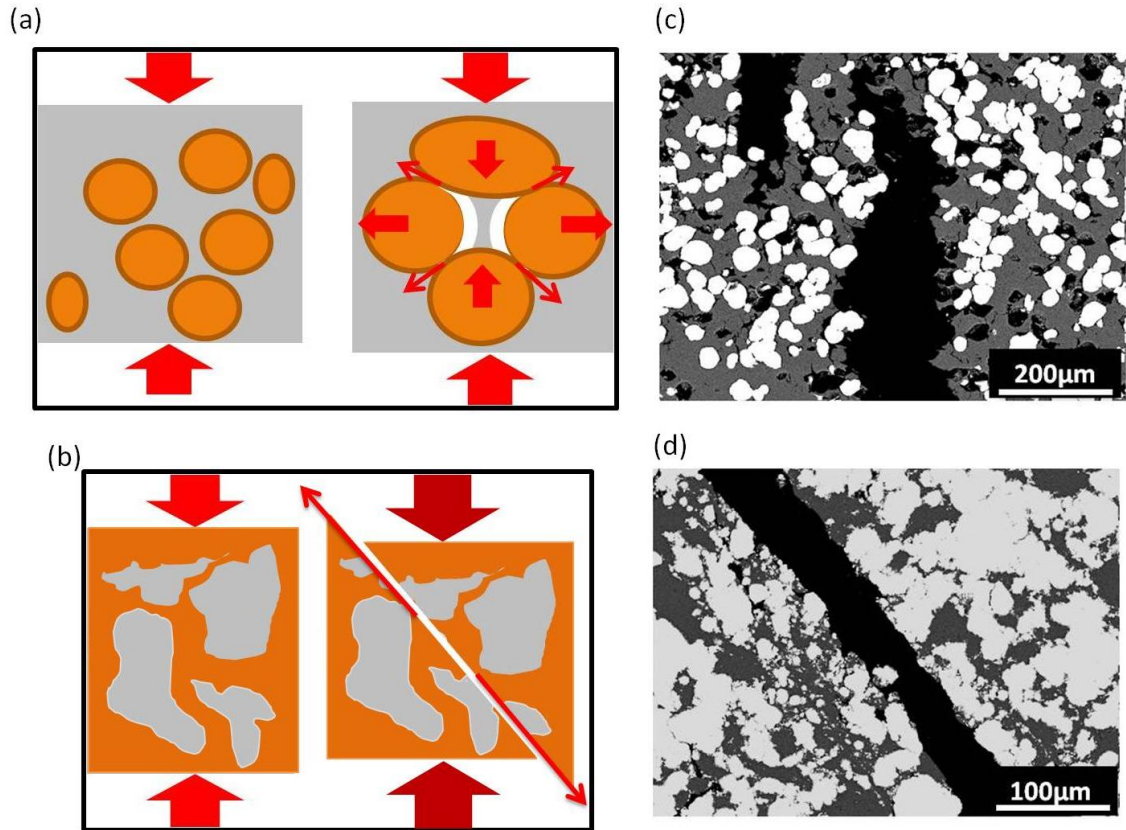
Figure 65: Fracture mechanisms: (a) Axial splitting, (b) Shear failure, (c)recovered Ni+Al axial splitting, (d) recovered Nb+Al shear failure.

4.2.6 Computational Examination (RAVEN simulation)

The following numerical calculation is utilized in order to build a reliable computational model for investigating and predicting the mechanical and failure properties of the explosive consolidated compacts. Two dimensional simulation code "RAVEN" was used to acquire computational information during dynamic compressing [171]. This yield stress was modeled by using the Johnson-Cook equation:

$$\sigma_y = \left[A + B(\bar{\varepsilon}^p)^n\right]\left[1 + C\ln\dot{\varepsilon}^*\right]\left[1 - T^{*m}\right],$$

Eqn. (50)

where A, B, n, C and m for nickel, aluminum and tantalum are presented in Table 11 [154, 171-176], and

$$\dot{\varepsilon}^* = \frac{\dot{\varepsilon}}{\dot{\varepsilon}_o} \quad \text{for } \dot{\varepsilon}_o = 1\text{s}^{-1} \quad \text{and } T^* = \frac{\Delta T}{T_{Melt-Room}},$$

Eqn. (51)

where the $\dot{\varepsilon}$ is the strain rate, ΔT is the temperature changes, and $T_{Melt-Room}$ is the difference between the room temperature and the melting temperature of the materials.

The failure strain of Johnson-Cook failure model is specified by the equivalent equation,

$$\varepsilon_f = \left[D_1 + D_2 \exp\left(D_3\sigma^*\right)\right]\left[1 + D_4 \ln\dot{\varepsilon}^*\right]\left[1 + D_5 T^*\right]$$

Eqn. (52)

where the D1 through D5 are the damage factors which are shown in Table 11, and σ* is the modified stress term defined by the Gruneisen equation of state,

$$P = \frac{\rho_0 C_0^2 \mu\left[1 + (1 - \frac{\Gamma_0}{2})\mu - \frac{a_0\mu^2}{2}\right]}{\left[1 - (S_1 - 1)\mu - \frac{S_2\mu^2}{(\mu+1)} - \frac{S_3\mu^3}{(\mu+1)^2}\right]^2} + (\Gamma_0 + a_0\mu)E, \quad \text{for } \mu \geq 0$$

Eqn. (53)

$$P = \rho_0 C_0^2 \mu + (\Gamma_0 + a_0\mu)E, \quad \text{for } \mu < 0$$

Eqn. (54)

$$\mu = \frac{\rho}{\rho_0} - 1$$

Eqn. (55)

where C_0, S_1, S_2, S_3, Gamma-zero and a_0 are the materials properties of Grueisen EOS, and the ρ and ρ_0 are the initial and current density, and E is the energy per reference

volume. The parameters of Grueisen EOS and the initial densities are presented in Table 12. These parameters were referenced from the computational investigation on Ni+Al laminar composites by Vitali et. al [171]. The simulation tool used here is employed for investigating its capability to study the mechanical and fracture behaviors of compacts with several different boundary conditions.

The simulation models of RAVEN at zero micro-second are shown in Figure 66, where the Al-Ni and Ta-Al micrography are imported from the SEM images as shown in Figure 56. The color bar shows the material difference. For Al-Ni micrography, Ni particles are in three different colors, dark blue, light blue and bright green and Al is the yellow matrix. For Ta-Al micrography, the Al is the light blue islands in the dark blue Ta matrix. We applied the compression profiles same as the experimental uses in the split Hopkinson bar tests, as shown in Figure 67. There were three different interfacial bonding strength, zero, 120 and 560 MPa, used in these simulations. The simulation results and corresponding stress-strain curves of Ni+Al compacts are shown in Figure 68 and Figure 69 respectively. The Ni parameters of J-C damage model were employed for both of Ni and Ta particles in order to rule out the elemental difference and simplify the simulation setup. This also narrowed the influencing factors and help to understand if the different microstructures can induce distinct fracture types or not.
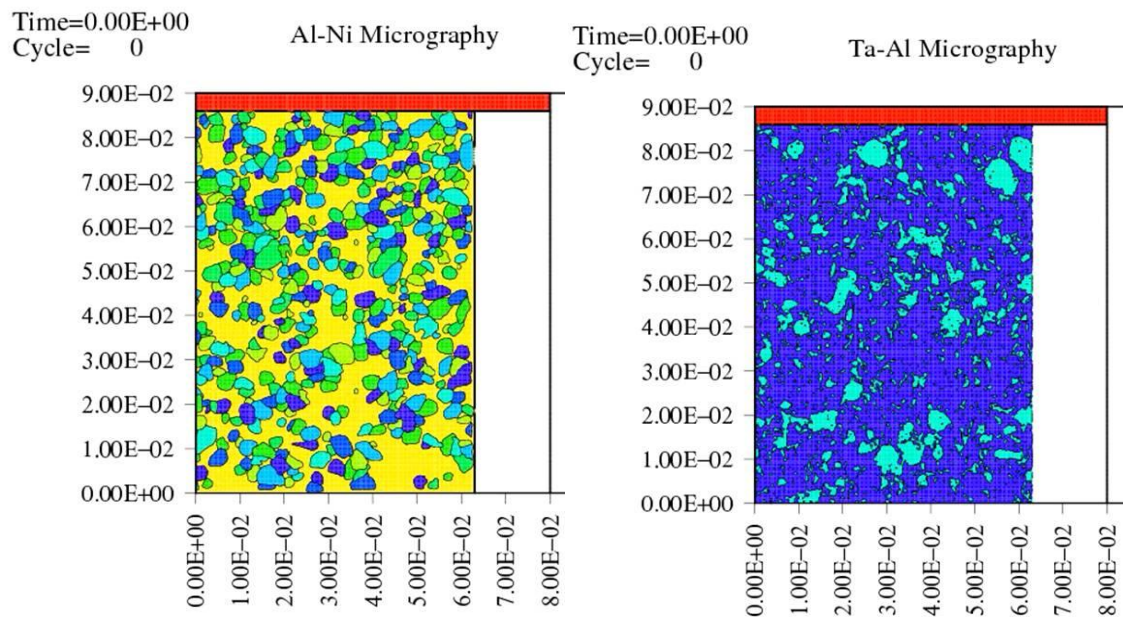
Figure 66: The initial model for RAVEN simulation: on the left side Al-Ni with Ni particles in dark blue, light blue and bright green, and the Al matrix in bright yellow; on the right side Ta-Al with Ta matrix in dark blue and Al islands in light blue.
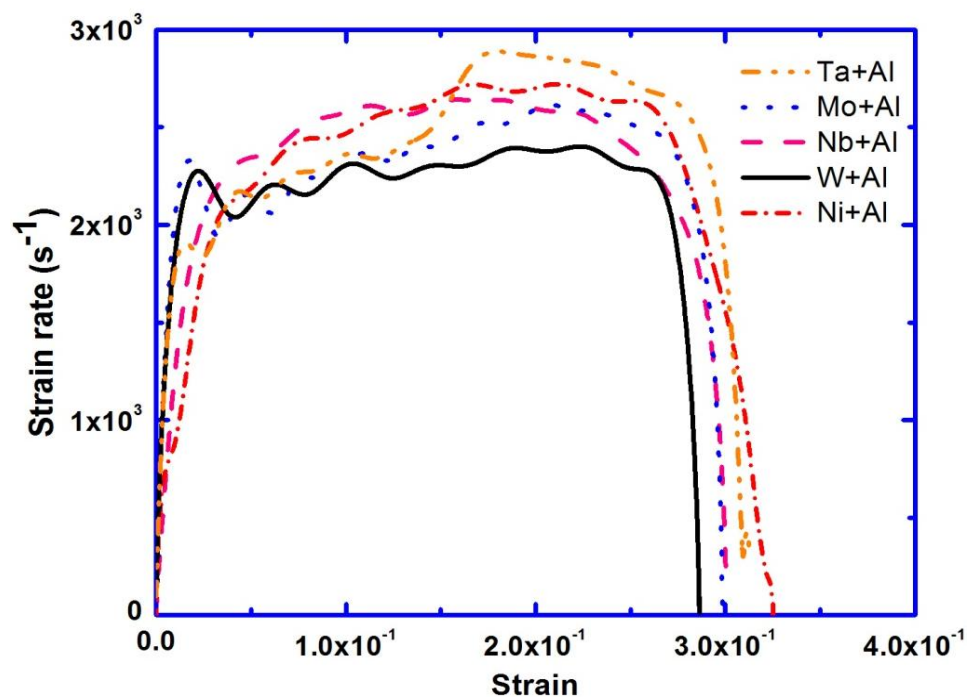
Figure 67: Strain vs. Strain rates of split Hopkinson pressure bar tests.

Table 11. Parameters for Johnson-Cook yield and damage models

Parameters	Al	Ni	Ta
A (Mbar)	[a] 1.76×10^{-3}	[a] 9×10^{-3}	[a] 7.4×10^{-3}
B (Mbar)	4.26×10^{-3} [176]	[c] 2.4×10^{-3}	[d] 2.84×10^{-3}
n	[b] 0.1	[c] 0.34	[d] 0.41
C	[b] 0.01	[b] 0.006	[e] 0.015
m	[b] 1	[b] 1.44	[e] 0.251
$T_{melt\text{-}room}$ (K)	[b] 650	[b] 1433	[e] 2957
D_1	[f] 0.13	[f] 0	
D_2	[f] 0.13	[f] 4.04	Assuming those are the
D_3	[f] -1.5	[f] -1.84	same as the J-C failure
D_4	[f] 0.011	[f] 0	parameters of Ni.
D_5	[f] 0	[f] 0	

a. converted from micro-hardness measurements in Table 10.

b. obtained from [154].

c. calculated from Viguras' master's thesis [173]

d. calculated from Chen's PhD dissertation [174]

e. obtained from Kim et al. [172]

f. obtained from Johnson et al. [175]

Ni+Al simulation:

Figure 68 (a) shows that the simulation results of Ni+Al compact without interfacial bonding strength. The cracks initiated on the interface between Ni particles and Al matrix as the small white areas shown on Figure 68 (a) 18 micro-second. At simulation time 24 mico-second, these cracks developed and connected each other which resulted in long and narrow breaks with the longitudinal direction parallel to the loading direction. These small breaks kept growing and turned into axial splitting failures as shown on Figure 68 (a) 34 micro-second. On the contrary, the Ni+Al simulation with bonding strength, 120 and 560 MPa, reveals no interface separation on the initial stage as shown on Figure 68 (b) 24 micro-second. The fractures initiated in the Al matrix due to the highly localized strain, which resulted in local stresses over the Al failure stress. Figure 68 (b) 30 micro-second shows that fractures developed in the Al phase while compressing, and the propagating direction of the factures was altered due to the hard inclusion, Ni. At the final stage, Fig. 13 (b) 37 micro-second, the shear fracture formed and the compact completely failed. The simulation results demonstrated a great consistency in the axial splitting fracture. The interface separation in the simulation result (Figure 69 (a)) is nearly identical with the empirical observation on Figure 69 (b). The stress-strain behavior of the Ni+Al simulations is plotted in Figure 70. Interfacial bonding plays an important role which resulted different dynamic yield stress: ~ 640 MPa for 120 and 560 MPa bonding strength; ~ 400 MPa for zero bonding strength. The stress-strain behavior of zero bonding Ni+Al compact demonstrated a dynamic yield stress, ~ 400 MPa, consistent with the experimental result, which was ~350 MPa. This suggested that

Ni+Al compact was densified by the explosive consolidation without any increase of the interfacial bonding strength.

Table 12. Parameters of Grueneisen EOS [176]

Grueneisen EOS	Al	Ni	Ta
C_o (cm μs^{-1})	0.5328	0.465	0.341
ρ_0 (g cm^{-3})	2.768	8.902	16.65
S_1	1.338	1.445	1.2
S_2	0	0	0
S_3	0	0	0
Γ_0	2	1.93	1.67
a_0	0.48	0.5	0.42
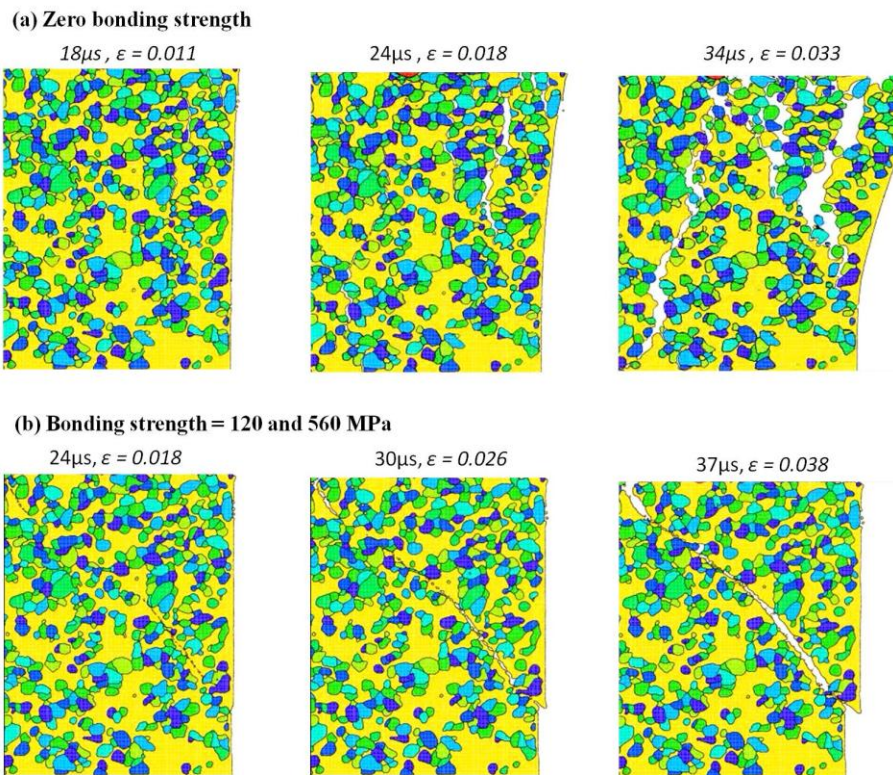
Figure 68: Simulation Ni+Al: (a) zero bonding strength; (b) 1/2 Al bonding strength & full bonding strength (120 and 560 MPa respectively)

(a)

(b)

200 µm
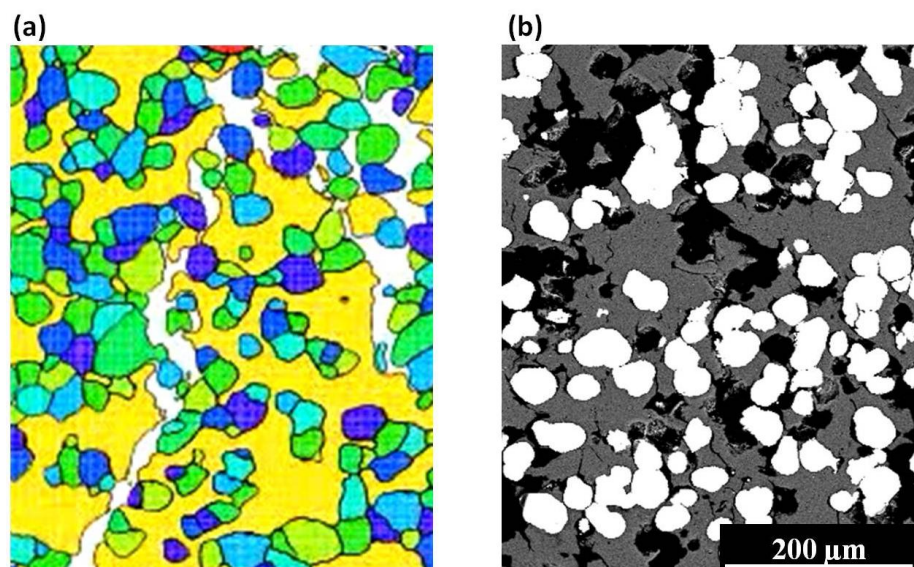
Figure 69: Compressive deformation of Ni-Al compact. Rigid Ni particles act as barriers to shear and boundary separation leads to microcracks aligned with compression direction: (a) RAVEN simulation; (b) SEM micrograph.
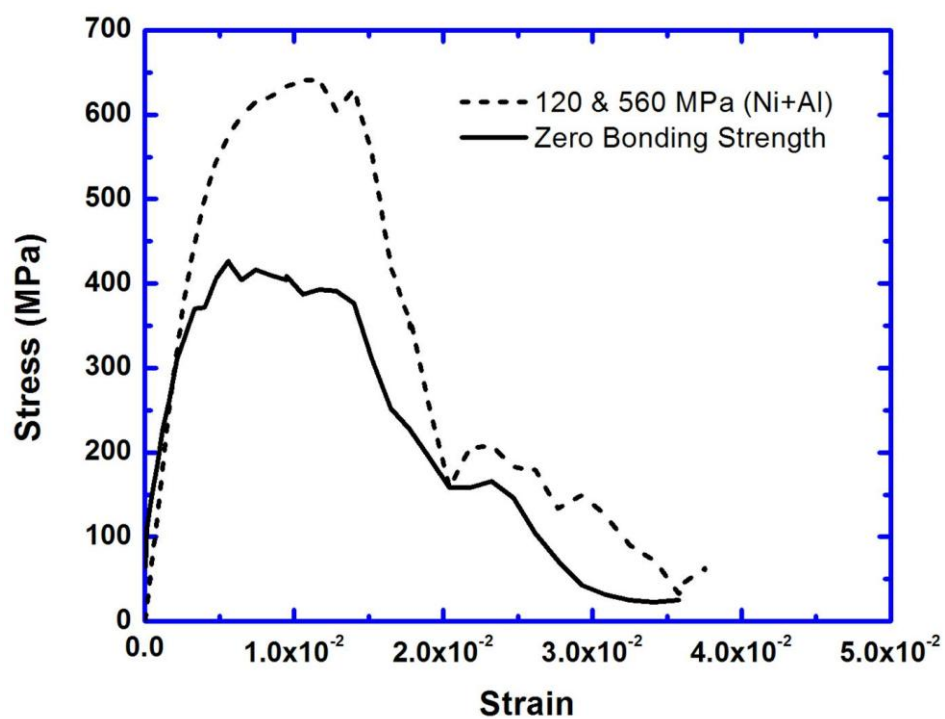
Figure 70: Stress-strain behavior of the NiAl simulation.

Ta+Al simulation:

Figure 71 shows the simulation results of Ta+Al compacts with zero, 120 and 560 MPa interfacial bonding strength. Interestingly, the failure types for different bonding strength are identical, which present shear failures for all three different bonding conditions. This implies that in the Ta+Al compacts, the failure structure is not determined by the interfacial bonding strength. Shear failure initiated from the localized shear deformation of the Al islands surrounded by the Ta matrix as shown in Figure 71 at 47 μs simulation time. The localized shear deformation in Al is mainly due to the irregularities of the bulk compressions of the Ta+Al compact which has the continuous Ta phase with bulk modulus 200 GPa and the surrounded Al phase with bulk modulus 76 GPa compensating most of the deformation. These irregular deformation caused shear fractures and developed into the diagonal shear cracks as shown in Figure 71 at 58μs.

From the stress-strain curves of the Ta+Al simulations (Figure 72), interestingly, the bonding strength has no effect on the stress-strain response, which shows a flow stress of ~ 600 MPa comparable with the experimentally observed value at the same strain rate of 2.5×10^3 s^{-1}, which is shown in Figure 62 (a). This structure-determined failure mechanism was successfully proved by the computational tool, RAVEN, which was also consistent with our speculation in Figure 65. This simulation is also consistent with the work that Thadahani and Meyers did [6, 20, 68]. They proved that the geometries of powder particles had significant influences over the dynamic behavior of the powder compacts.
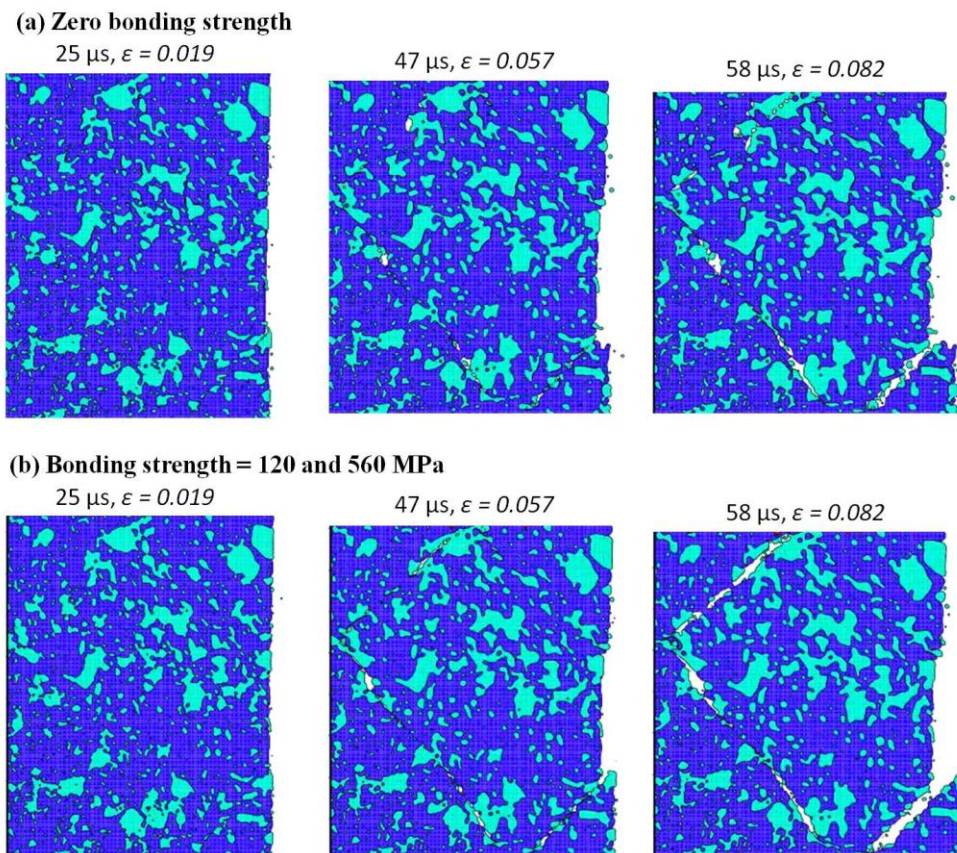
Figure 71: Simulation Ta+Al: (a) zero bonding strength; (b) 1/2 Al bonding strength & full bonding strength (120 and 560 MPa respectively).
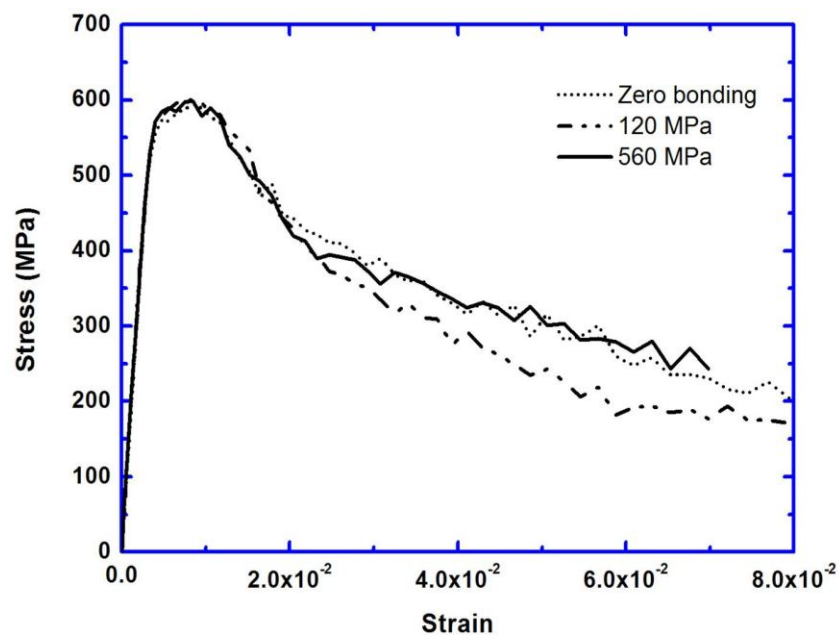
Figure 72: Stress-strain behavior of the Ta+Al simulation.

It should be pointed out that the compressive strains withstood by the simulated strains are much lower than the experimental values. The stress drops significantly for $\varepsilon=0.05$. The experimental maximum strains are on the odor of $\sim10^{-1}$. This difference is, at least partially, due to the size of the specimen which is about 10 times larger than the simulation setup. The region modeled by RAVEN has dimensions of 850×600 µm, whereas the actual specimens have a dimensions of 6×6 mm. Thus, much longer cracks and shear bands can develop prior to failure.

The computational results successfully provided a practical approach to predict and evaluate the mechanical properties affected by the different micro-structures on the explosive consolidated compacts. This gives us the confidence to apply computational method before massive production in order to reduce the expense and increase the time efficiency. It should be noted that other mechanisms, such as second-phase strengthening [158] which added the impenetrable inclusion in the soft matrix, can also significantly influenced the mechanical strength regardless of the changes of interfacial bonding strength.

4.2.7 Conclusions

The following are the principal conclusions drawn from the research:

1. Explosive consolidation in the double-tube cylindrical configuration successfully yielded compacts with good mechanical strength.

2. The consolidation of Ni, W, and Mo with Al yielded a continuous Al phase in which the other particles were embedded. For Ta and Nb with Al, the former formed the continuum phase. This is the consequence of the small particle size of Ta and Nb.

3. The mixtures with Al as a continuous phase exhibit a lower strength than the ones with Ta or Nb as a continuous phase. The strength is primarily determined by the mechanical properties of the continuous phase.

4. The mechanisms of failure are identified: shear localization in the continuous phase and tensile separation. A primary failure mode is due to the weak boundary of the interface in the Ni-Al compact which leads to axial splitting.

5. The Ni-Al mixture is modeled by an Euler FEM code and the interfacial strength is shown to have a strong effect on the damage evolution and the strength of the compounds. However, the FEM simulation of Ta-Al mixture presents no influence corresponding to the interfacial bonding strength.

4.3 Reactive laminates under laser-driven shock compression

Many commercial materials have a laminar microstructure, ranging from the sub-micro-scale in the integrated circuit (IC) devices to the macro-scale of the nickel-copper laminate used in the common quarter. The search for composite structures with specific mechanical properties requires scientists to analyze the behavior of different combinations of materials tested under different loading conditions.

4.3.1 Mechanical response by quasi-static loading (Uniaxial tensile tests)

The longitudinal and transverse tensile test results, revealed in Figure 73 (a, b), show the anisotropic mechanical properties of the cold-rolled laminates. In the transverse tensile direction, the stress-strain curves show that the laminates have almost no plastic deformation. The laminar structure strains elastically and fractures after a certain amount of deformation. The elastic modulus of the laminates varies from ~15 GPa to ~80 GPa due to the inhomogeneities of the laminar bonding strength caused by the cold rolling process.

The longitudinal tensile tests show that the thick bilayer laminates have higher failure strengths than the thin bilayer laminates, suggesting that the thick bilayer samples may have fewer defects, or pre-existing cracks, caused by the cold-rolling process. Table 13 shows the average fracture stress of both 5 and 30 µm bilayer Ni/Al laminates in the longitudinal and transverse direction. The transverse direction has a lower fracture stress due to the weaker interface bonding of this accumulative cold-rolling process.
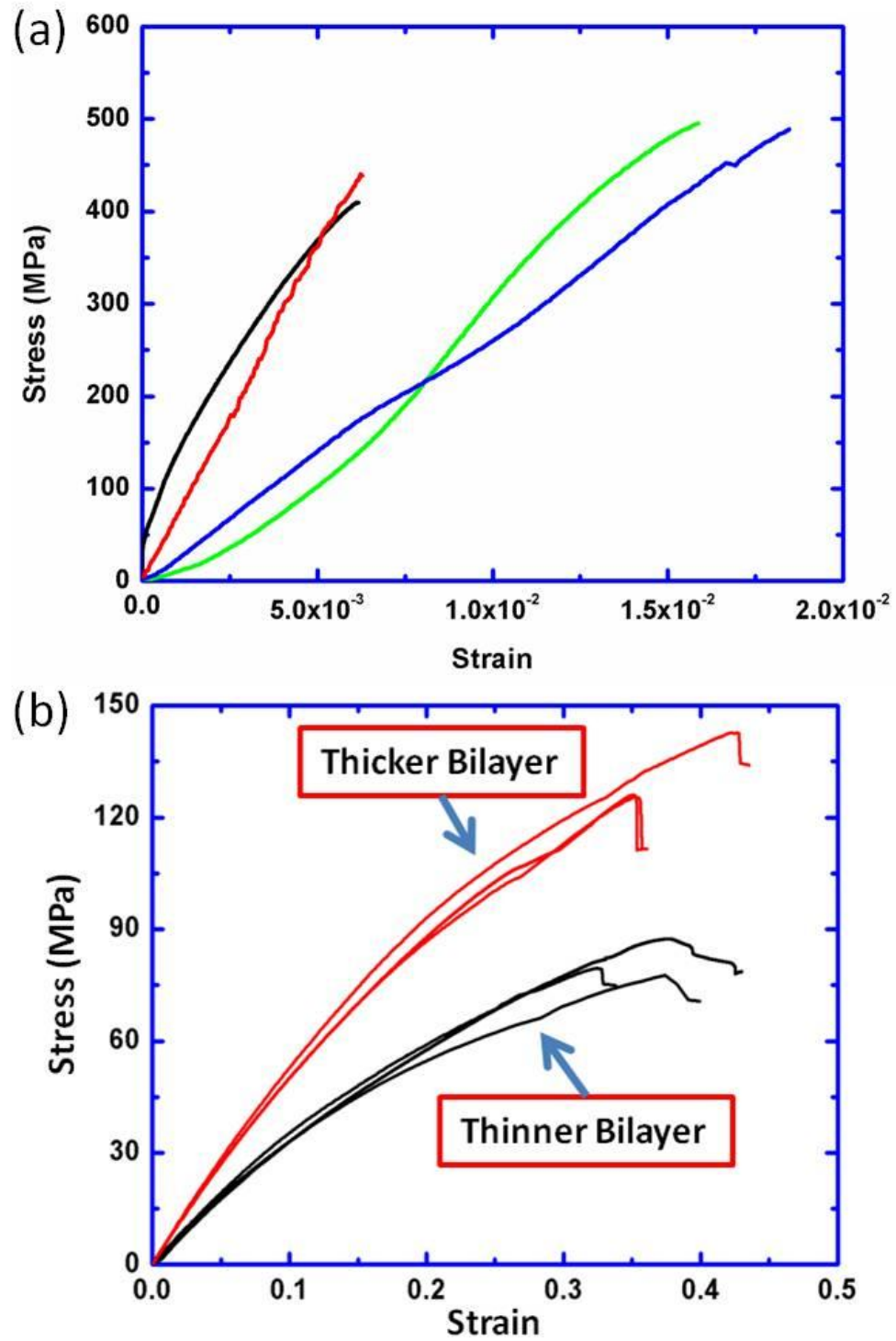
Figure 73: The results of tensile tests: (a) transverse direction tests, (b) longitudinal direction tests.

Table 13. Average fracture stress of 5 and 30 µm bilayer Ni/Al lamiantes.

Sample conditions \Fracture stress	5 µm bilayer thickness	30 µm bilayer thickness
Longitudinal	~402 MPa	~391 MPa
Transverse	~83 MPa	~132 MPa

4.3.2 Weibull Statistical Analysis

Weibull analysis is commonly used to characterize the stochastic response of engineering materials. The plastic deformations of ductile materials are usually sufficient to compensate the effects of flaws on strength. However, for brittle materials, the pre-existing defects are responsible for catastrophic failure. Owing to the variations in orientation, size, and distribution of defects, the failure strengths of brittle materials may vary significantly from specimen to specimen [28, 128]. The typical Weibull analysis utilizes the relation between the failure probability, F, and the failure strength, σ, to evaluate the suitability of the material for engineering applications. This Weibull equation is shown below:

$$F = 1 - P = 1 - \exp\left[-\left(\frac{\sigma - \sigma_u}{\sigma_o}\right)^m\right],$$ Eqn. (56)

where P is the survival probability, σ_u is the smallest failure strength, σ_0 is the characteristic strength, and the m is the Weibull modulus. A large Weibull modulus indicates that the the sample-to-sample variation of failure strength is small, allowing smaller safety factors in engineering design. The Weibull distribution can be re-written as

$$\ln \ln[1 - F] = -m\left(\ln \sigma - \ln \sigma_o\right), \qquad\qquad \text{Eqn. (57)}$$

where the σ_u is chosen to be zero. Plots of ln ln [1/(1-F)] versus $\ln(\sigma/\sigma_o)$ and $\ln(\sigma)$ for the laminates are shown in Figure 74 (a, b). The Weibull modulus is 3.4 for the longitudinal direction ($\square$) and 8.8 ($\bigcirc$ and Δ) for transverse direction. For comparison, the Weibull modulus of conventionally processed alumina, controlled particle size alumina, and steel are 4.7, 9.7, and infinity, respectively [28]. The longitudinal direction apparently has greater sample-to-sample variation compared to the transverse direction. This suggests that the rolling process can induce anisotropic fracture in the direction perpendicular to the longitudinal tensile orientation, producing a large variation in the longitudinal failure strengths.

The average failure strength for a material in a plot of ln ln [1/(1-F)] versus $\ln(\sigma)$ occurs at the point where ln ln [1/(1-F)] =0 (Figure 74 (b)). From the fits of the longitudinal ($\square$) and transverse ($\bigcirc$) data, the acquired average failure strengths are 449.9 and 114.5 MPa, respectively. The lower average failure strength of the material in the transverse direction significantly restricts the utility of the laminates. For comparison, the conventional processed alumina has an average failure strength of 286 MPa, and the controlled particle size alumina has an average failure strength of 578.1 MPa [28].
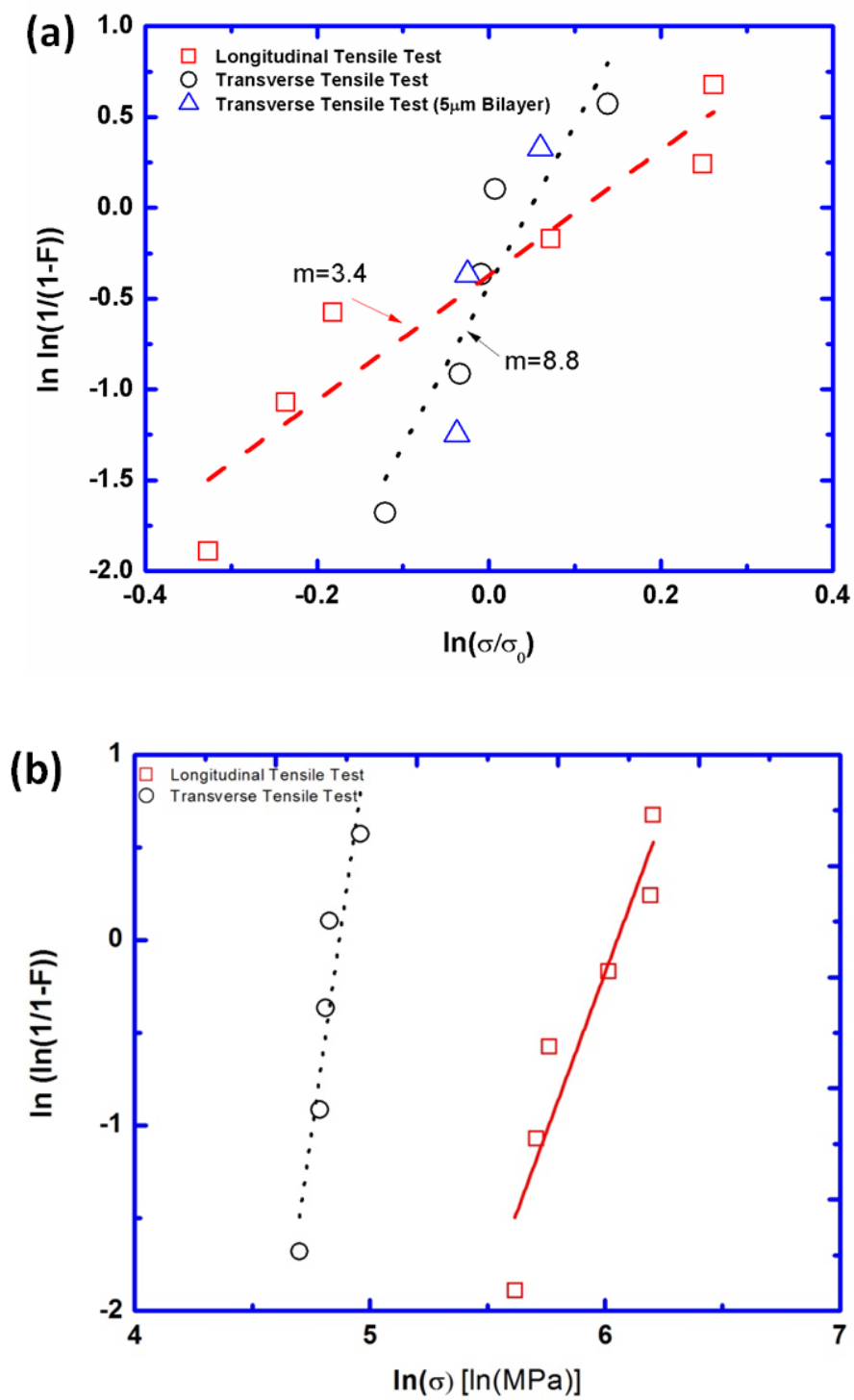
Figure 74: The Weibull distributions

4.3.3 Rankine-Hugoniot and HYADES calculations (laser-shock wave behavior)

Two different methods were used to estimate the laser-induced shock-wave propagation in the laminates and to calculate the initial pressures. The first method was to directly use Lindl's equation [87], which considers the pressure produced by laser shock as a strong function of laser intensity. The laser intensities in this study vary from ~2.68×10^{11} to ~1.28×10^{13} W/cm^2. The details of the initial pressures and the corresponding laser energies in this study are systematically discussed in section 3.4 and Table 3-Table **5**.

The second method was the computational prediction using the hydrodynamic code HYADES for characterization of laser shock propagation in materials. This radiation hydrodynamic code provides a reasonable one-dimensional model for the simulation of laser-induced shock-wave propagation. In order to simplify the simulation process, the strength parameters (strength and elastic modulus) were not introduced into this simulation. The detail of the HYADES code is shown in Appendix (b). Figure 75 (a) shows shock propagation induced by the 400 J, 3 ns laser pulse through Ni-Al laminate, as compared to monolithic Al. The computation reveals that the pressure rises when the shock wave reaches the first Ni layer after passing through the Al layer. In a pure Al slab, a monotonic decay is observed (Figure 75 (a), dash curves). The initial pressures in the first Ni layer obtained from the simulation results for 100 and 400 J laser energies with 3 ns pulse duration are ~120 and ~300 GPa. The difference in shock impedances results in multiple reflections at the interfaces (Figure 75 (b)) [154]. The shock wave enters the laminate through the Al layer (surface) and propagates through the Al layer to the

adjacent Ni layer. From the Rankine-Hugoniot pressure-particle velocity curves of Ni and

Al (in Figure 75 (b)), one can find the first transmitted shock fom point 1 of the Al layer

(incident shock in Al), corresponding to pressure P_1, to point 2 of the adjacent Ni layer,

corresponding to pressure P_2. Along with the propagation of the shock wave in Ni/Al

bilayers [89], the interfacial pressures can be estimated using the same pressure-particle

velocity plots (Figure 75 (b)), following the sequence *1→2→3→4→5*. This reverberation

sequence shows that as the shock front exits an Al layer and enters a Ni layer, the

pressure increases (Figure 75 (b) from 1 to 2). The reverse occurs when the shock front

enters an Al layer from a Ni layer (Figure 75 (b) from 2 to 3). This provides the rationale

for the HYADES results. It should be mentioned that this procedure can be used only for

relatively short shock waves; more complex situations need to be considered for long

shock waves propagating in laminates [177]. Their impedance mismatch may cause the

interfacial region of the nickel and the aluminum sheets to become more reactive.
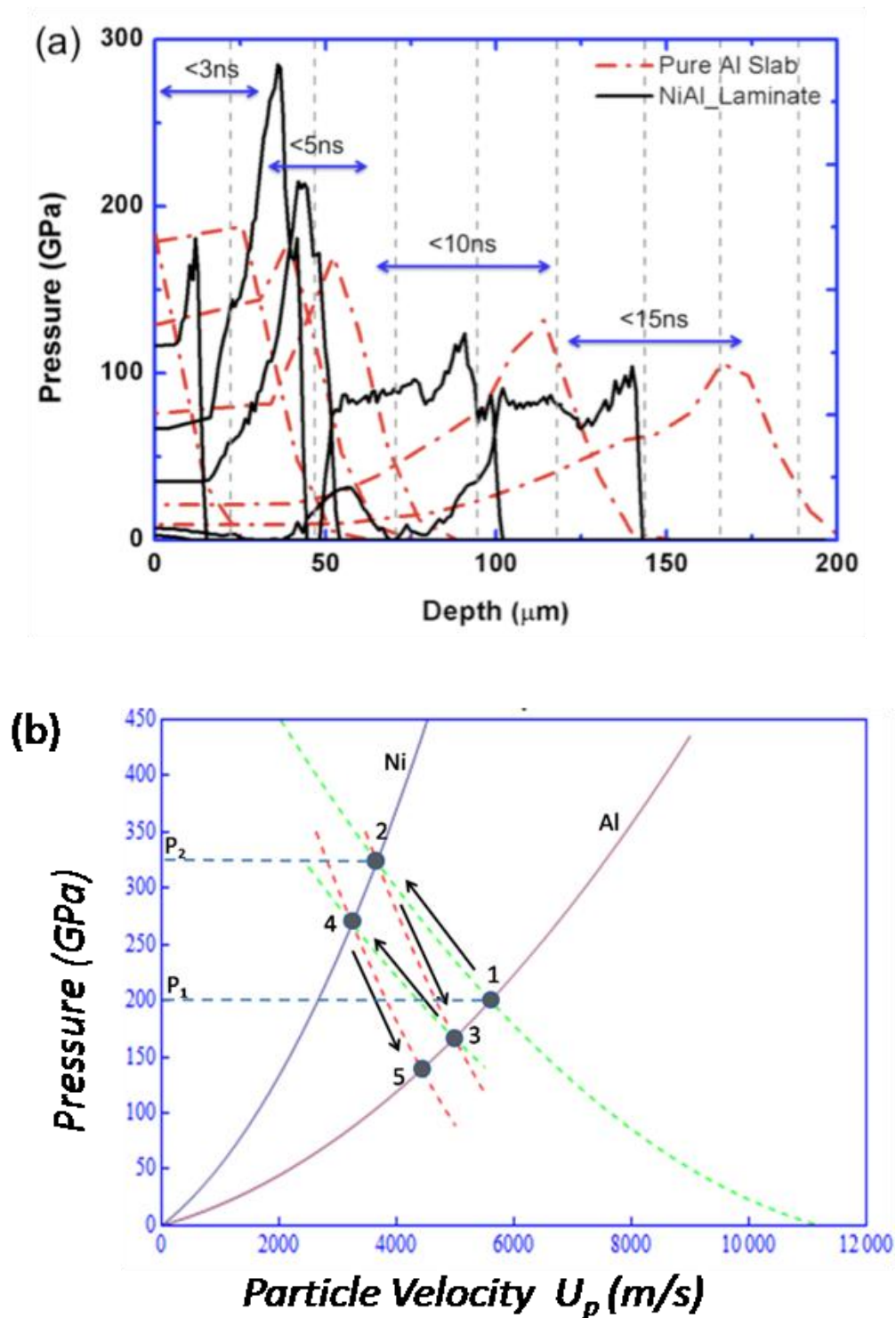
Figure 75: Calculation of pressure pulse amplitude in Ni-Al: (a) Laser shock wave (400 J; 3 ns) propagation in pure Al slab and laminate (HYADES Simulation); (b) Rankine-Hugoniot Pressure vs. particle velocity plot for Ni and Al showing wave reflections.

These calculation procedures provided the following consistent results:

Condition	Lindl	Mod. Lindl	HYADES for Ni & Al respectively
3 ns, 100 J:	127.5 GPa ;	68.4 GPa;	~120 & 72 GPa
3 ns, 400 J:	321 GPa;	172.4 GPa;	~300 & 180 GPa

It should be noted that the pressure in Al predicted by HYADES is lower because of its lower shock impedance. The initial pressures from the computational methods indicate that on the irradiated surface, the laser shock pressures exceed the pressure (3.5 ~ 5.4 GPa) of the intermetallic reaction barrier for the Ni+Al powder mixture reported by Eakins *et al*. [124]. This suggests that the laminates should have a certain amount of intermetallics in the recovered samples. However, the experimental results did not show intermetallics for a few of the laser irradiated samples. The detailed results and possible explanations will be presented later.

4.3.4 Failures by laser shock loading (fragmentation and spalling analysis)

Spalling was investigated and the observed fragment sizes were correlated to calculated values based on the Grady–Kipp theory [130-132, 134-137]. This theory is based on the energetic balance between, on one side, the kinetic energy of an expanding body *T*, and the elastic energy *U*, and on the other side, the fracture energy *W*:

$$T + U \quad > W \qquad\qquad\qquad \text{Eqn. (58).}$$

This leads to predicted fragment size*s* for brittle materials,

$$s = 2(\frac{\sqrt{3}K_c}{\rho c_0 \, \dot{\varepsilon}})^{\frac{2}{3}} \qquad\qquad\qquad \text{Eqn. (59),}$$

and ductile materials,

$$s = (\frac{8\sigma_y \varepsilon_c}{\rho \, \dot{\varepsilon}^2})^{\frac{1}{2}} \qquad\qquad\qquad \text{Eqn. (60),}$$

where K_c is the fracture toughness, ρ is the density, c_0 is the bulk velocity, $\dot{\varepsilon}$ is the strain rate, σ_y is the yield strength, and ε_c is the critical strain. It should be noted that the fragmentation may change from brittle to ductile in the high strain rate regime, $\sim 10^7 \text{ s}^{-1}$. Due to the strain rate and temperature dependence, Kipp et al. later modified the equations for spall [131]. For fracture toughness dominated spallation, they proposed

$$s = (\frac{\sqrt{24}K_c}{\rho c_0 \, \dot{\varepsilon}})^{\frac{2}{3}} \qquad\qquad\qquad \text{Eqn. (61),}$$

and for flow stress dominated spallation,

$$s = (\frac{1.2\sigma_y}{\rho \, \dot{\varepsilon}^2})^{\frac{1}{2}} \qquad\qquad\qquad \text{Eqn. (62),}$$

where c_0 is the elastic sound speed. The differences between Eqn. 57 and 59, and between Eqn. (58) and (60), are minor. The yield strength, σ_y, is given by

$$\sigma_y = \sigma_{y0}\left(\frac{\dot{\varepsilon}}{\dot{\varepsilon}_o}\right)^m$$

<div align="right">Eqn. (63),</div>

where the σ_{y0} is the reference yield strength, which is about 449.9 MPa from Section 4.3.2; the reference strain, $\dot{\varepsilon}_o$, is 1 s^{-1}, m is the strain rate sensitivity which is chosen as 0.1 (for steel) [134], and K_c is the fracture toughness which can be seen as a constant to a first approximation.

The two equations, ductility and fracture toughness dominated fragmentation, were applied. It is possible to estimate the strain rate experienced by the spalled region as it bulges out of the back. This estimate can be obtained from the free surface velocity (U_{fs}) divided by the original size of the spall area (d) [85]. Figure (a) shows the schematic of the crater formation and spalling in the back surface with the free surface velocity (U_{fs}) and spall diameter d.
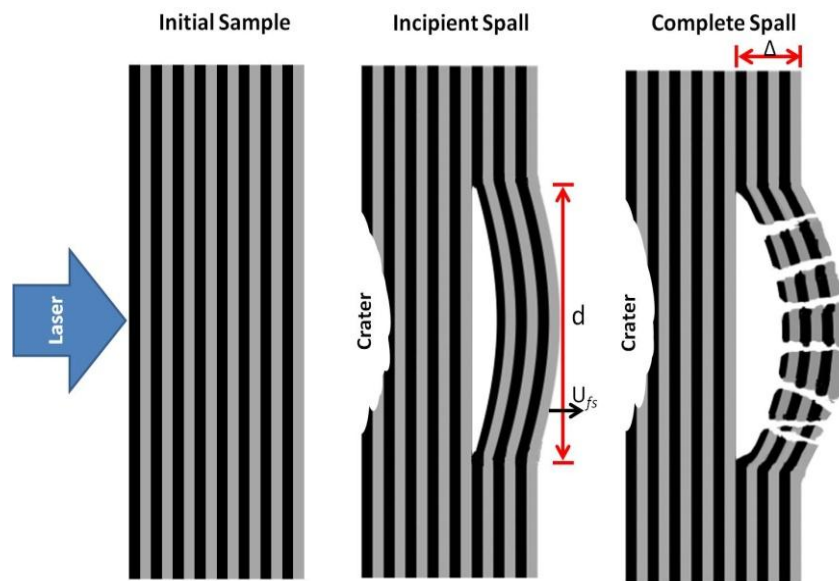
Figure 76: Spallation sequence: Initial sample → Incipient Spall → Complete Spall

The HYADES code was used to estimate the pressures as the shock wave arrives at the free surface for the 100 and 400 J shots. Fig. (b) shows the shock wave propagation for 400J laser energy shot at 13.4 ns after the laser irradiation. The stress fluctuates due to the interactions of the wave with the Ni and Al lamellae. The shock wave pressure decreased to about 14 GPa at the depth of ~950 µm. For the the 100 J laser in laminar structure was also estimated by the same way and is about 3.5 GPa.
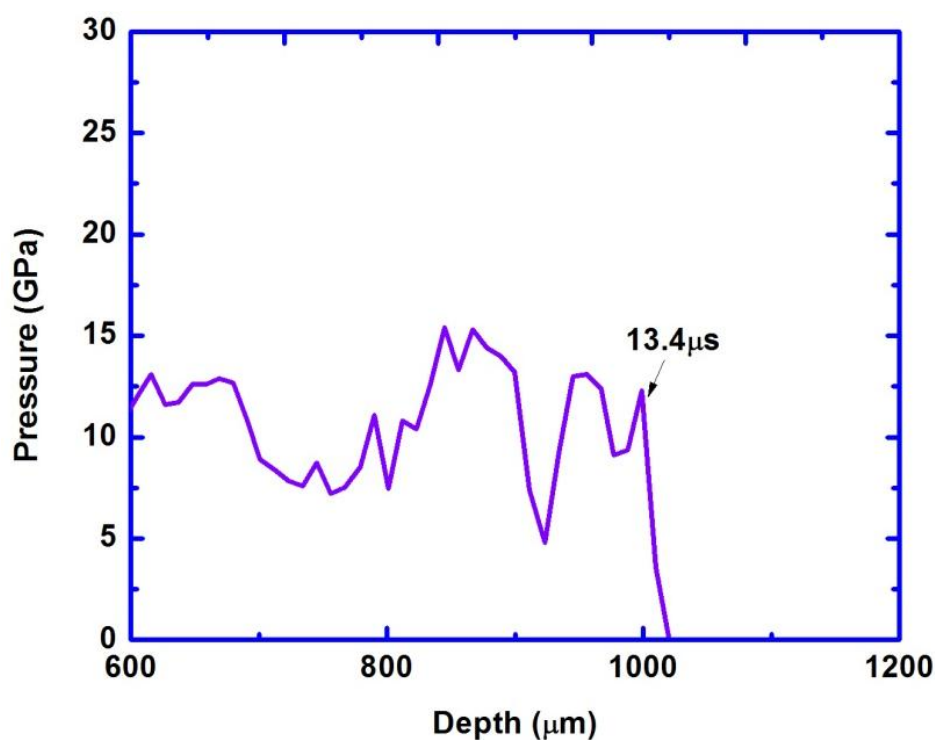
Figure 77: HYADES simulation: 400 J, 3ns, laser shock wave propagates to the rear surface of the laminate with bilayer thickness 30 µm.

From the HYADES predicted pressure one can estimate the shock and particle velocities using the Hugoniot relationships and equation of state. A rule of mixtures was

used to estimate a single value for the laminate, giving : c_o (4950 m/s), s (1.4) , and ρ_o (5.83×10^3 kg/m^3).

$$p = \frac{\rho_o}{s}(U_s^2 - C_oU_s)$$ Eqn. (64)

$$U_s = C_o + sU_p$$ Eqn. (65)

The free surface velocity is equal to 2 U_p. The spall diameter (d) was measured by two different approaches: using the image processing software, ImageJ from direct inspection of SEM images; and average diameter converted from the area measurement of the spall surface. The results of the free surface velocity and spall size are listed in Table 1.The calculated strain rates are given in Table 1. They are on the order of $1\text{-}5x10^5$ s^{-1}.

The yield strength, Y, was obtained from Eqn. (61) is about 1.6 GPa. From the Eqn. (59) and (60), we can calculate fragment sizes for the ductile and brittle fracture mechanisms. The normal fragment size which is about 2.7×10^{-3} m for ductile fracture mechanism and 9.3×10^{-4} m for brittle fracture mechanism by assuming K_c equal to 40 MPa*m$^{1/2}$ [134]. The detailed results are shown in Table 1 as well. We also measured the size of the fragments collected in the recovery capsule as shown in Figure 78 using image processing software ImageJ. The average diameters of the fragments measuring from Figure 87 are shown in the Table 15. Compared to the estimated results, the measured fragments size was consistent with the estimated fragment size caused by the brittle failure as shown in Table 14.
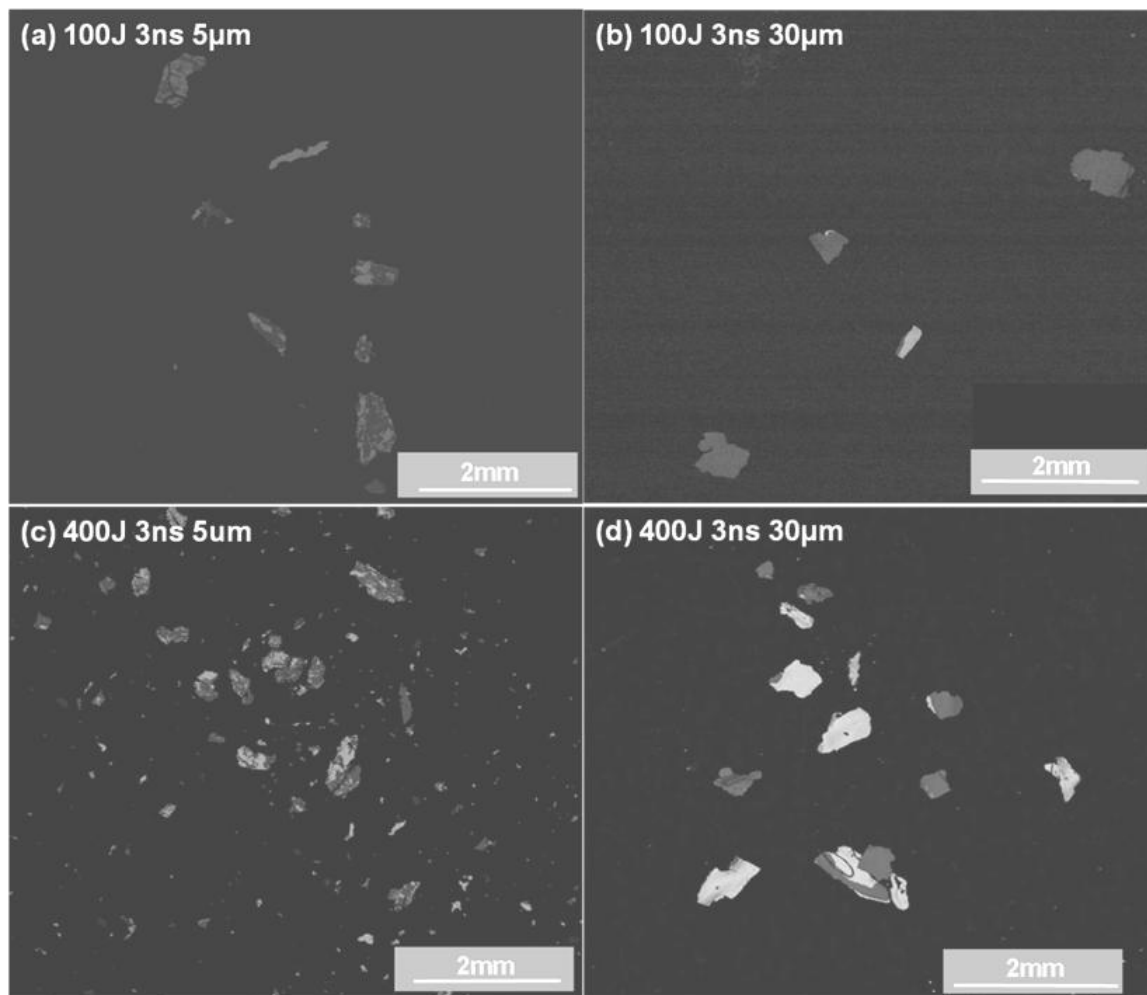
Figure 78: Fragmentations debris: (a) from the thin bilayer sample shocked by ~100 J, 3 ns laser; (b) from the thick bilayer sample shocked by by the same laser condition as (a); (c) from the thin bilayer sample shocked by 400 J, 3 ns laser; (d) from the thicker bilayer sample shocked by the same laser condition as (c).

Table 14. Experimentally measured parameters and predictions from modified Grady-Kipp equations (Kipp et al. [134], Eqns. (59) and (60)).

Laser Energy	100 J	400 J
$U_{fs} = 2 U_p$	234.8 m/s	864.6 m/s
Spall size for 5 µm bilayer sample	1.51±0.5 (mm)	1.59±0.35 (mm)
Spall size for 30 µm bilayer sample	1.85±0.79 (mm)	1.94±0.78 (mm)
Strain Rate (for 5 µm)	1.6×10^5 /s	5.4×10^5 /s
Strain Rate (for 30 µm)	1.2×10^5 /s	4.5×10^5 /s
G-K ductile fragment size(for 5 µm)	3.68 mm	1.09mm
G-K brittle fragment size(for 5 µm)	1.22mm	0.54mm
G-K ductile fragment size(for 30 µm)	4.91mm	1.31mm
G-K brittle fragment size(for 30 µm)	1.47mm	0.61mm

Table 15. Measured average fragment size from Figure 87.

Experimental Condition	100J_3ns, Thicker Bilayer Sample	400J_3ns, Thicker Bilayer Sample	100J_3ns, Thinner Bilayer Sample	400J_3ns, Thinner Bilayer Sample
s	0.464 mm	0.434 mm	0.134 mm	0.131 mm

Kipp et al. [134] proposed that the critical strain rate for brittle-ductile transition can be obtained by setting Eqn. (57) equal to Eqn. (58) (or alternatively, setting Eqns. (59) and (60) equal). The result is:

$$\dot{\varepsilon}_t = \left(kc^2 \rho^{1/2} \sigma_y^{2/3} \varepsilon^{2/3}\right) K_c^{-2}$$ Eqn. (66),

where K_c and σ_y are the reference fracture toughness and yield strength and k is a parameter (equal to 0.94 for Eqns. 57 and 58). We already knew the yield stress from Section 4.3.2 which was about 449.9 MPa. By ploting K_c vs strain rate curve (Figure 79), one can understand that in this experiment, the rational brittle-ductile transistion point is about 10^7 s^{-1} due to the drastically degraded fracture toughness of the laminates causing by the cold-rolling induced carcks and voids [82, 94]. Since the strain rate from our estimation was lower than 10^6 s^{-1}, the fracture toughness dominated spallation model was used to estimate the fracture toughness of the laminar samples. There are two significant differences: (a) Grady-Kipp predicts an increase in fragment size with increase in bilayer thickness, contrary to our results; (b) the Grady-Kipp fragment sizes are higher than the measured values by a factor of 5-10. There seems to be a scaling factor with bilayer thickness that is not incorporated into the simple Grady-Kipp model. It is possible that the thinner bilayer has more initiation sites for fracture. There are more refined treatments that predict smaller fragments, such as the ones by Glenn and Chudnovsky [142] and Zhou et al. [144]. They predict sizes that are smaller than the G-K by a factor of six.
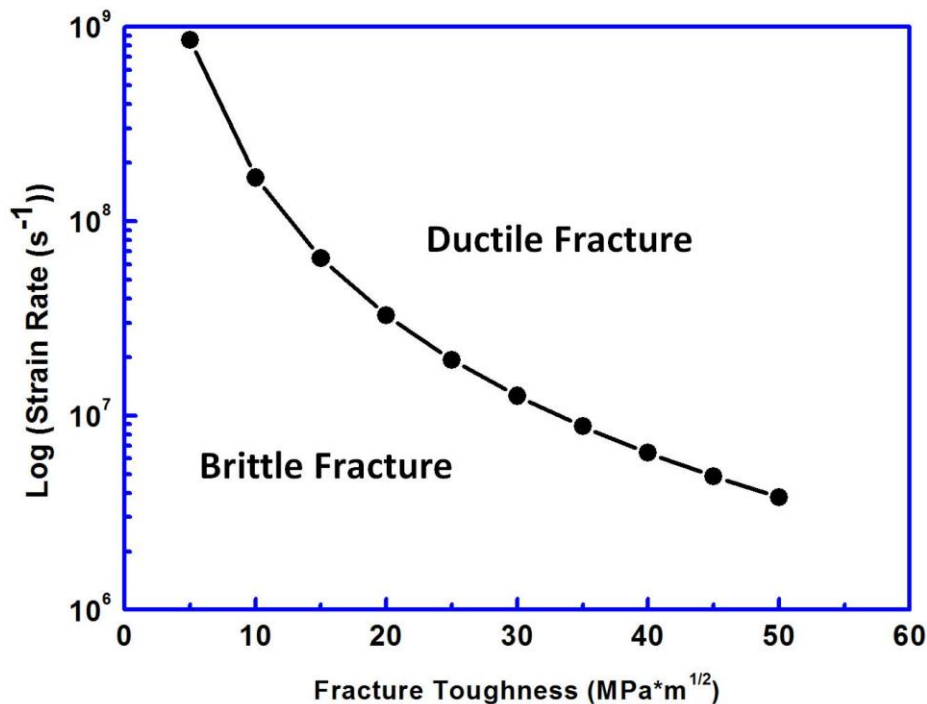
Figure 79: Critical strain rate versus fracture toughness.

4.3.5 Computational investigation: Effects of the interface bonding strength

The correlation between interface bonding strength of the laminates and the fracture morphologies was estimated computationally using a two-dimensional Eulerian finite-element research code Raven [178-184]. The empirical results in terms of the cross sections of the as- produced Ni-Al laminate with 30 µm bilayer thickness and the 200 J laser shocked laminates as shown in Figure 80 were employed for investigating the effects of the interface bonding strength. The pressure input was obtained from HYADES results. The micrograph, Figure 80 (a), was imported into Raven and the colors on the imported image separate the two different materials, Ni in blue and Al in green, as shown in Figure 81. There were two different interface bonding strength used in our simulation: one was that the bonding strength equaled zero; the other one the bonding strength was

equivalent to 120 MPa incorporating a prescribed failure strength which meant that materials failed only when the normal stress exceeded the prescribed failure strength. The Johnson-Cook yield and failure constitutive equations were used to model this laser shock experiment conducting on the Ni-Al laminate as presented in Section 4.2.6. Figure 82 (a) shows that the simulation results with zero interface bonding strength is completely delaminated with spalls and fragments at 25 µs after 200 J laser shock loading, however the one with 120 MPa interface bonding strength has no delamination and the spall morphology is close to the experimental result in Figure 80 (b). The other corresponding empirical observations are presented in Figure 88 which shows consistent failure types with the computational results. As the aforementioned, the computational and empirical results prove that interface bonding strength plays a significant role which dominates the failure morphologies of the laminates. This computational work is operated by Dr. Efrem Vitali in Prof. Benson's group and the results are published in the co-authored paper [171].
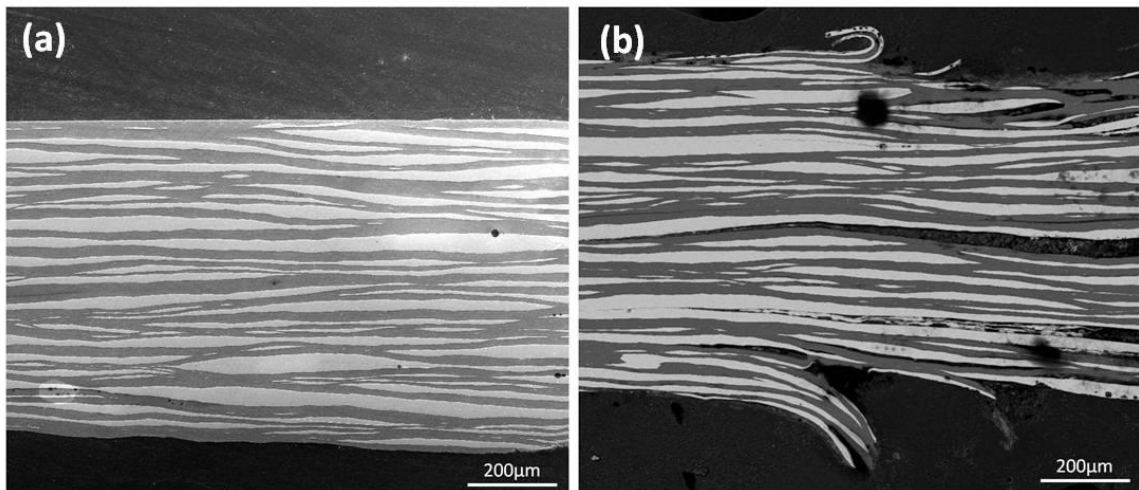
Figure 80: (a) as-produced Ni-Al laminate with 30 µm bilayer thickness; (b) 200 J laser shocked Ni-Al laminate.
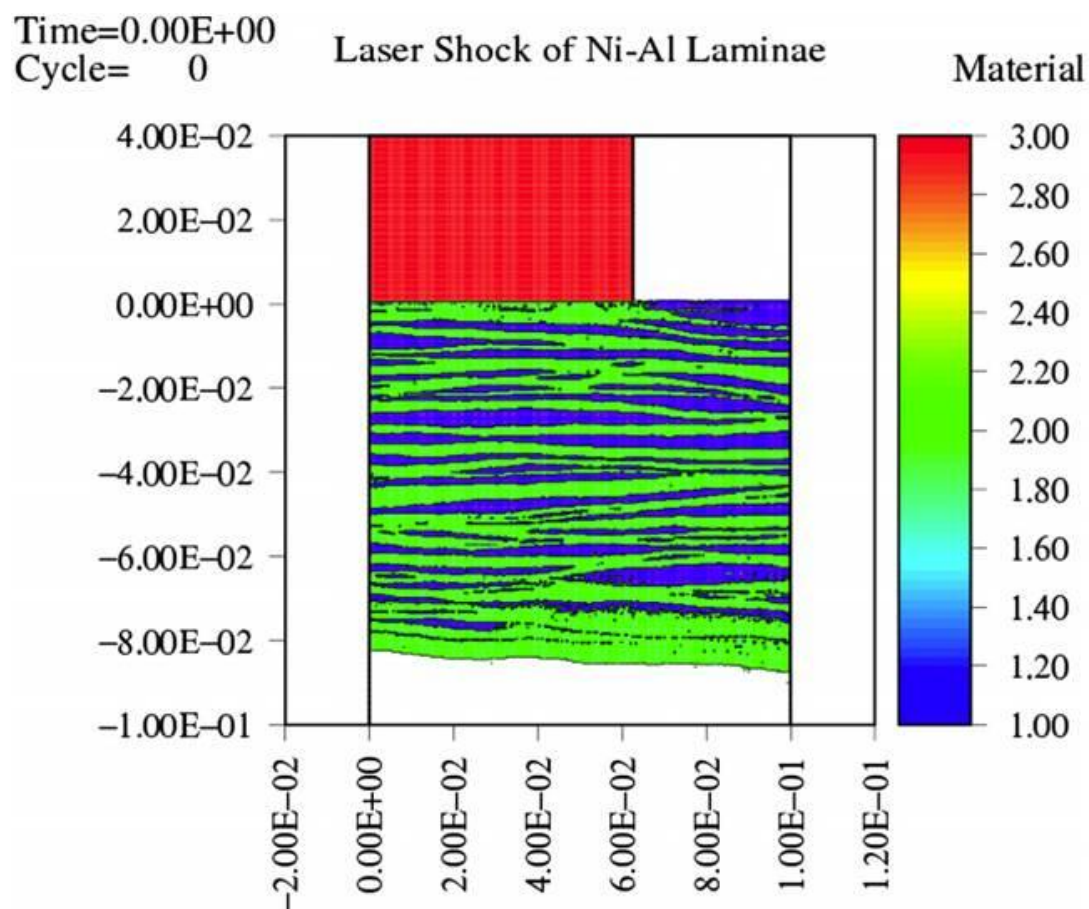
Figure 81: Original input of Ni-Al laminate with 30 µm bilayer thickness.

(a) No-bonding strength
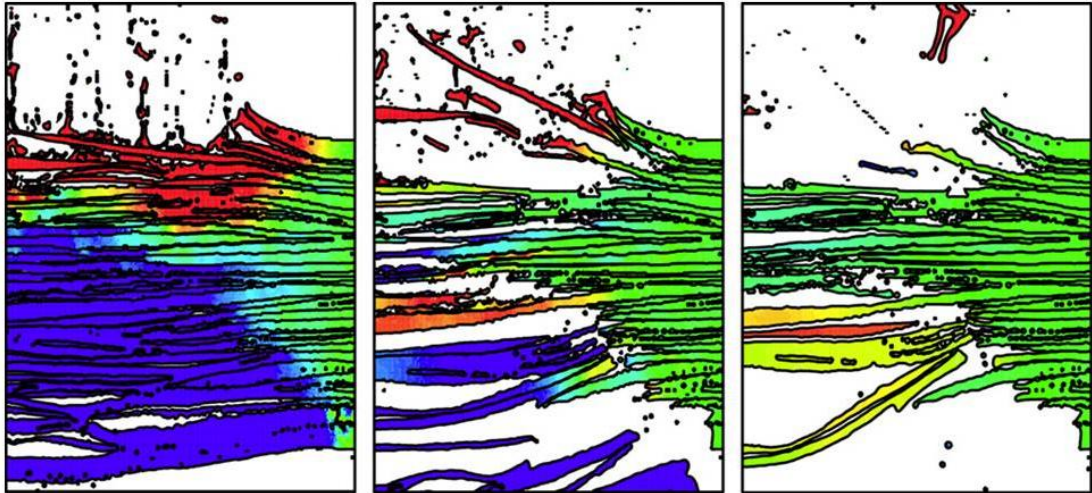
(b) 120 MPa bonding strength
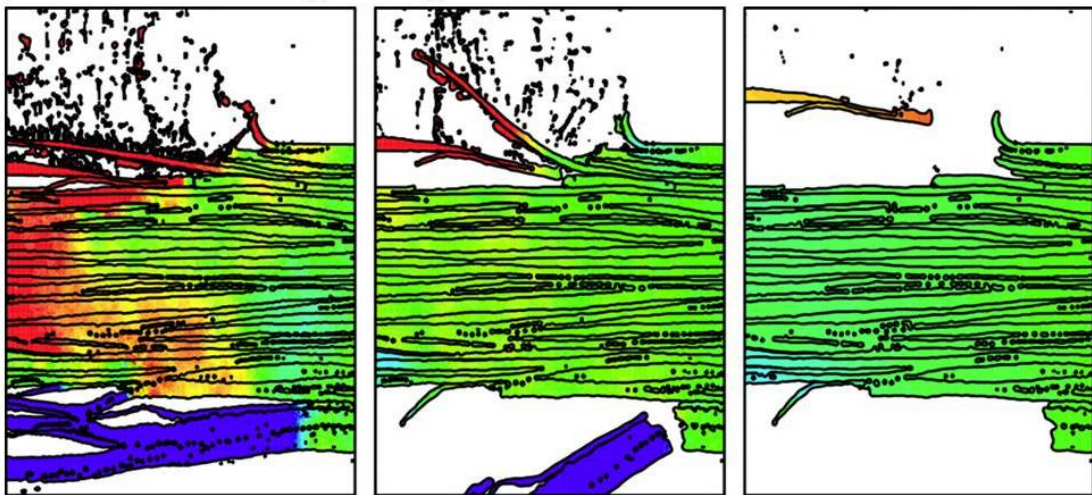
Figure 82: Raven simulation: (a) zero interface bonding 1, 5, 25 micro-seconds; (b) 120 MPa bonding strength 1, 5, 25 micro-seconds

4.3.6 Recovered sample analysis

Surface morphologies

100 and 400 J, 3 ns laser experiments: The irradiated surfaces show cratering whereas the back surfaces show evidence of spalling. The irradiated and spall surfaces of the 30 μm laminate are shown in Figure 83; the corresponding micrographs for the 5 μm laminate are shown in Figure 84. The spall regions of 30 and 5 μm bilayer samples show no evidence of reaction, melting, or diffusion (Figure 83 (b, d), and Figure 84 (b, d)). Since the shock wave expanded radially in the materials, the spall regions are considerably larger than the laser beam size (1.12 mm^2); these are represented by dashed squares (Figure 83, Figure 85). The bilayers were broken into metal strips and formed convex areas on the spall surfaces due to the expansion, fracture, and plastic flow resulting from the reflected tensile pulse. The fragments of these strips were ejected and captured as debris (Figure 78). It should be emphasized that no intermetallic reaction was found on the spall surface, which supports the observation of the fragmentation (Figure 87 (b, d)) in Section 4.3.4.

Recoiled strips of fractured laminar bilayers were found on the irradiated surfaces of thicker bilayer laminates. The irradiated surfaces of the thinner bilayer samples have distinct macroscopic structures as compared to the thicker samples. The sample with the 30 μm bilayer had fractured foils and rings marking by the vaporization (Figure 83 (a, c)). The fractured foils were peeled up and bent upward due to their motion during spalling.
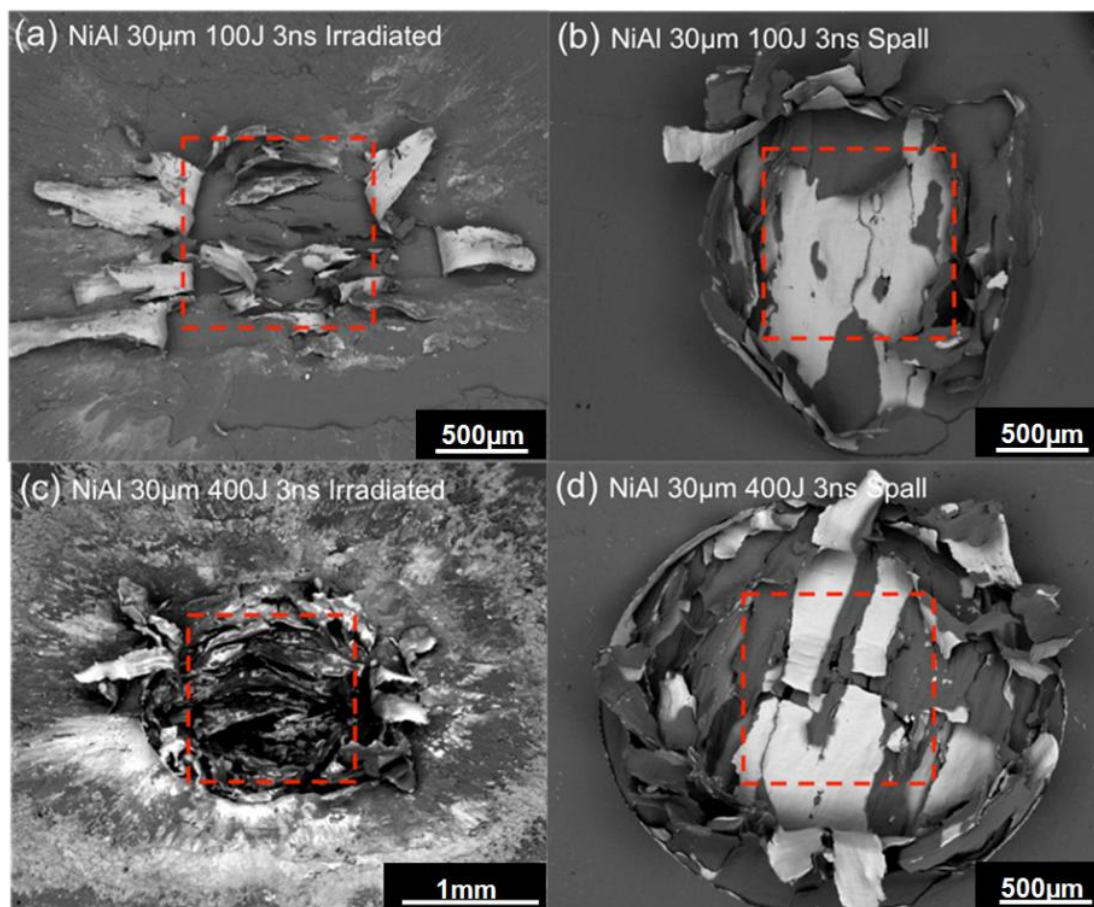
Figure 83: SEM-BSE observations of samples with thicker bilayer (30 µm) exposed to (a, b) 100 J 3 ns and (c, d) 400 J 3 ns laser irradiation; (a, c) Irradiated surface presenting melt, deposition from metal vaporization, and foil recoiling. (b, d) Spall surface side reveals broken and peeled strips, without evidence of reaction.

The irradiated surfaces of thinner bilayer (5 µm) samples show significant melting on the laser-exposed regions (Figure 84, insets in (a, c)). There are no peeled foils or fractured sheets on the surface, since the thinner bilayer sample does not have a continuous layer structure. The layer structures are broken up into segments due to the high strain ductile rolling. The microscopic morphologies on the irradiated surfaces of thinner bilayer samples show dendrites (Figure 84 (a, c)), which are identified as intermetallic compounds by EDX. Dendritic structures are widely distributed around the

molten pool of the crater. The reaction products on irradiated surfaces show that the laser energy induces an increase in temperature greater than the melting temperature of Al. The extent of intermetallic formation was greater in the 5 µm bilayer samples, which have more closely spaced Al-Ni interfaces. This evidence proves that bilayer thickness is a significant factor for laser shock-induced intermetallic reaction. It is also coincident with the studies of Ma *et al*. [2] and Gavens *et al*. [39], which proved that bilayer thickness of the sample is one of the dominant factors for reaction.
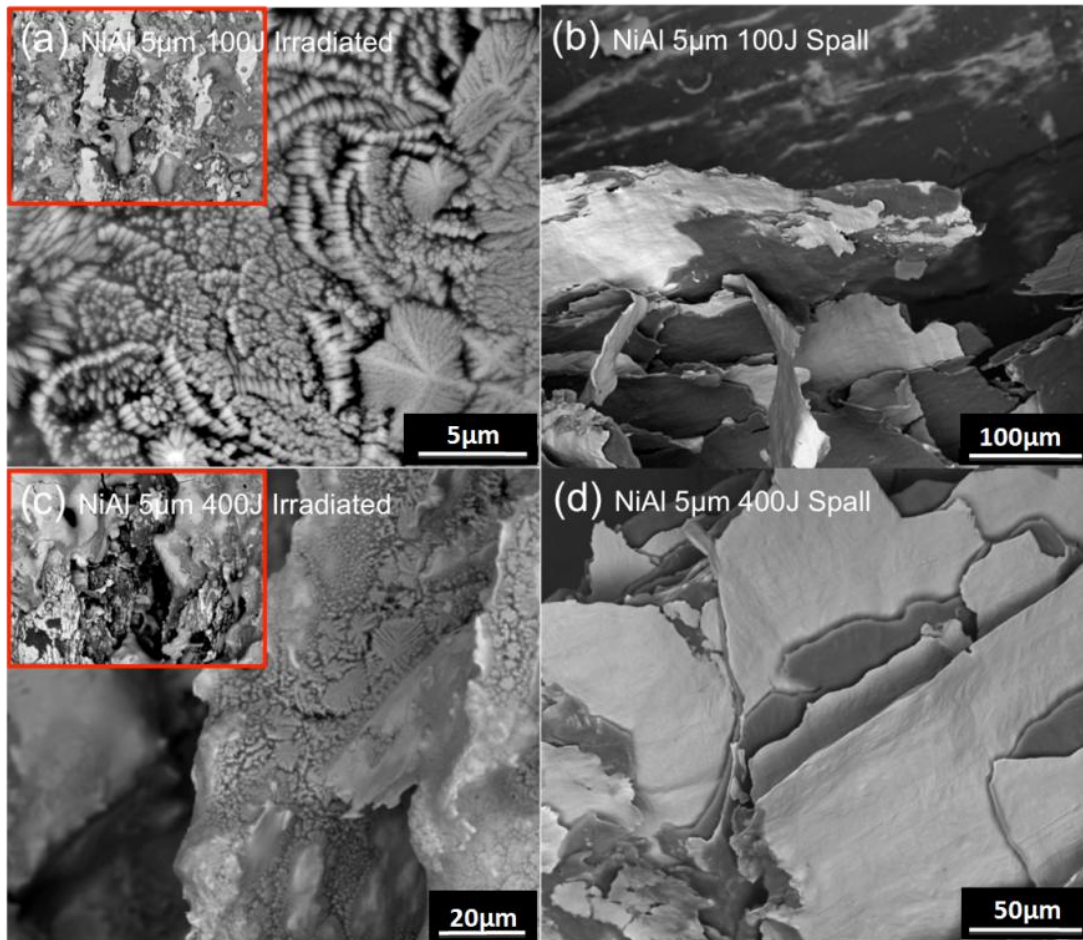
Figure 84: SEM-BSE observations of samples with 5 µm bilayer irradiated at (a, b) 100 J 3 ns and (c, d) 400 J 3 ns laser; (a, c) Dendrites, melt pools, and granules were found on the irradiated surface. (b, d) Fractures observed on spall surfaces.

24, 229 and 409 J, 8 ns laser experiments: By increasing the pulse duration at the same energy level, the intensity of laser was reduced; e.g. 400 J, 3 ns laser had nearly three times higher intensity than 400 J, 8 ns laser (Table 3). Figure 85 (a, c) show dendrites distributed on the irradiated surface of the 30 μm bilayer sample, which did not occur in the 3 ns laser pulse experiments. Dendrites are discovered, even in the 30 µm laminate with the lowest laser energy (24 J) exposure. This implies that longer pulse duration can help reactants to overcome the energy barrier of reaction and indicates that the threshold for intermetallic reaction depends on shock duration. The dendrites were also found on the thinner bilayer sample after 229 J (8 ns) laser exposure (Figure 85 (e)). As in the 3 ns experiments, these dendrites were distributed around the molten pools of the crater.

The microscopic characteristics of the spall area after 8 ns laser experiments were similar to the 3 ns laser experiments. On the spall surfaces, peeled foils and bent layers were seen, but no reaction was observed (Figure 85 (f)). The 8 ns laser experiments demonstrated that laser duration plays an important role on the reaction of the irradiated surfaces; nevertheless, neither the 100 nor 400 J laser energies were sufficient enough to propagate the reaction through the entire sample.
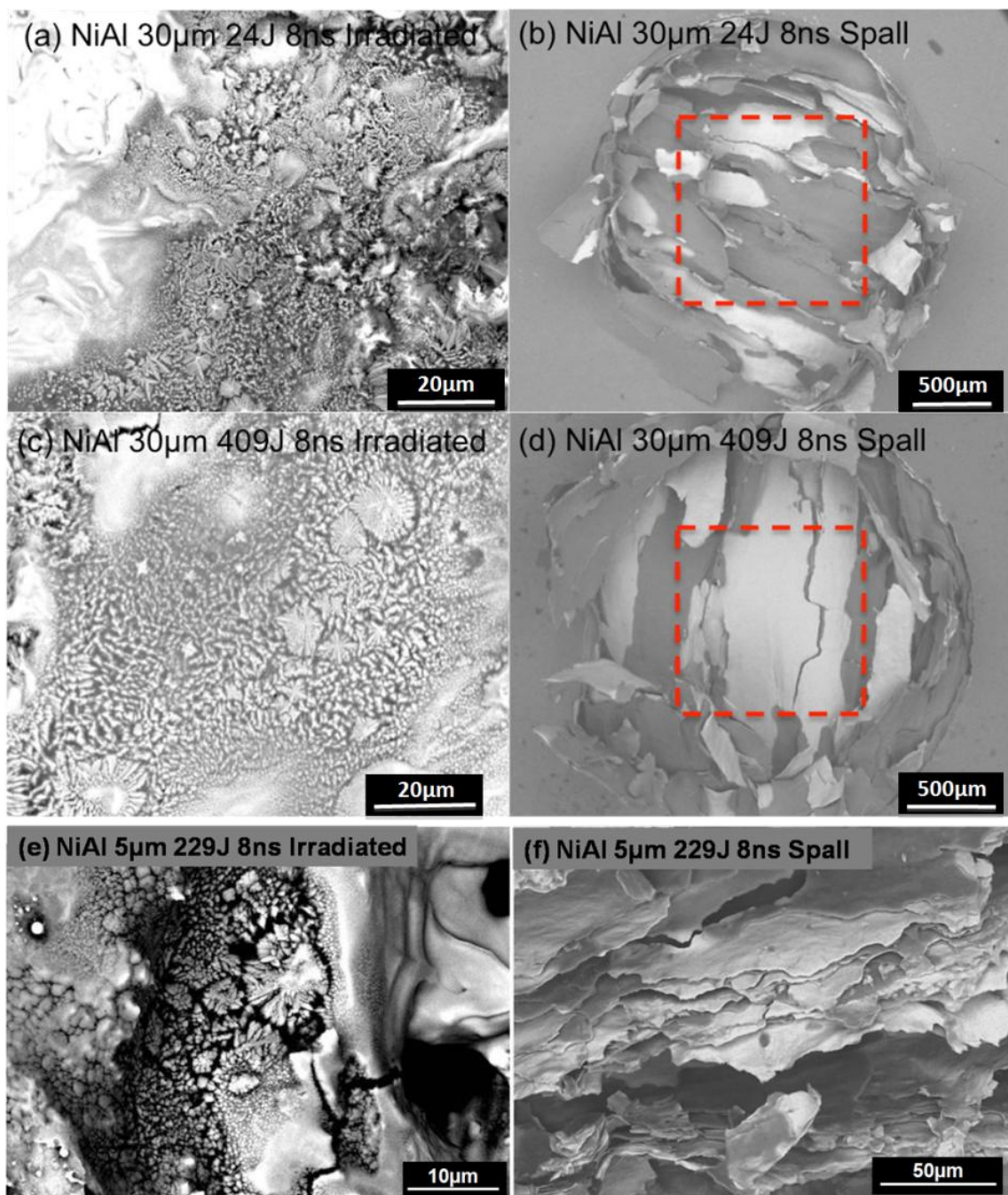
Figure 85: 30 μm bilayer laminates (8 ns pulse duration): (a) 24 J irradiated surface; (b) 24 J spall surface; (c) 409 J irradiated; (d) 409 J spall; (e) Ni/Al laminates with 5μm bilayer subjected to 229 J; (f) No reaction on spall surface.

The intermetallics formed at the longer laser pulse duration experiments suggested that laser shock-assisted thermal reactions occurred intensively at the longer laser irradiation time [19, 20]. In fact, for most of the laser shock experiments conducted on reactive materials, both laser shock-induced and laser shock-assisted thermal reactions coexisted and cannot be separated [20]. In order to discriminate between these two reaction mechanisms, the recovered samples were sectioned, and characterized by SEM in the following section.

Cross-sectional observations

Figure 86 (a) shows that intensive reaction took place in the thinner bilayer sample irradiated by 400 J, 3ns laser. The reaction propagated into the sample to a depth of about 50 µm (~10 bilayers). This contrasts with Figure 86 (b), the cross-sectional image at the edge of crater, suggesting that the reaction did not propagate out of the crater area. It should be noted that the reaction was barely found on the cross-sections of samples with thicker bilayer after 3 ns laser pulse irradiation, which suggests that these laser irradiations were not sufficient to generate reaction in these samples. Increasing the pulse duration (8ns) facilitated intermetallic reaction in the thicker bilayer sample (Figure 86 (c)); however, in the thinner bilayer (Figure 86 (b)), the intermetallic was barely detectable at the edge of the crater (Figure 86 (d)). These incompatible intermetallic phase formations in adjacent areas provide important hints as to the reaction mechanisms.

A solid-state diffusion calculation was applied to clarify the mechanisms of reaction. We assume that the reaction was controlled by diffusion and that the temperature was higher than the melting point of Ni (1728 K) and Al (933 K) at ambient

pressure due to the severe molten pools on the laser-exposed surface shown in Figure 86 (a, b). The total cooling time required to form the dendrites can be obtained by using solid diffusion equation. It is postulated that the diffusion takes place primarily at 2000 K, which is higher than the NiAl eutectic point, 1911 K [185]. The self-diffusion coefficients of Ni and Al ($D^*_{Ni} = 1.5 \times 10^{-8}$ cm^2/s and $D^*_{Al} = 4.1 \times 10^{-8}$ cm^2/s at 2000 K) were obtained from Li *et al*. [126]. The interdiffusion coefficient, $\tilde{D}$, can be estimated by incorporating the self-diffusion coefficients into Darken's equation:

$$\tilde{D} = N_{Al}D^*_{Ni} + N_{Ni}D^*_{Al}$$ Eqn. (67)

where the N_{Al} and N_{Ni} represent the concentrations of Al and Ni, which are assumed to be equal to 0.5. The estimated interdiffusion coefficient is 2.8×10^{-8} cm^2/s. If there is no reaction barrier (diffusion-controlled reaction), and the diffusion length, l (see equation (4)), is taken as the length of the dendrite, 2~3 µm (measured from Figure 86 (a, c)), then the total cooling time, *t*, can be obtained from:

$$l = 2\sqrt{\tilde{D}t}$$ Eqn. (68)

which is about 0.25~0.8 s. It should be noted that the temperature of the diffusion process may be lower than 1728 K considering that the dendrites were still found at ~45 µm in depth from the irradiated surface, where the bilayer maintained a well-defined structure and no melting of Ni was found. The total cooling time can be much longer than 0.8 s, inasmuch as the temperature might be much lower than 1728 K.

At the edge of the crater, Figure 86 (b) and (d), severe melting was also found, confirming that the temperature was indeed higher than the melting points of Ni and Al.

If one assumes that the cooling time is about 0.8 s and the temperature is lower but close to the NiAl eutectic temperature (1900 K), then by a similar calculation (with the self-diffusion coefficients of Ni and Al equal to 2.06×10^{-9} cm^2/s and 1.5×10^{-8} cm^2/s [186] at 1900 K), the dendritic length is about ~2 µm. As aforementioned, the total cooling time might be longer than 0.8 s, therefore dendrites can be larger than 2 µm. However, no dendrite is seen in Figure 86 (b) and (d). This result suggests that the diffusion-controlled reaction is not the dominant mechanism of intermetallic reactions in the high energy / short pulse laser irradiation experiments. This implies that the cooling rate is far faster than the required diffusion time and it is more probable to interpret the intermetallic growth by incorporating the shock-induced reaction mechanism due to its rapid reaction (10^7~10^9 faster than diffusion [49]). Nonetheless, it is interesting that Figure 86 (d), from the 30 µm bilayer shocked at 400 J, 8 ns, shows a small amount of intermetallics, which have a dendrite length about 1 µm, and no expelled intermetallic phase as shown in Meyers *et al*.'s [49] and Vecchio *et al*.'s work [48]. The size of the dendrites seems more consistent with the prediction from the solid diffusion equations. This character provides significant evidence of the effect of the shock-assisted reaction on thicker bilayer sample irradiated by 8 ns pulse duration laser (400 J). It can be concluded that shock-induced reaction plays an important role in both 3 and 8 ns laser shock experiments; however, shock-assisted reaction gains significance as the laser pulse duration increases to 8 ns.

Intermetallic compounds formed along the interface of Ni-Al layers and grew into granular shapes. The mechanism of intermetallic compound formation in shock compression was proposed by Vecchio et al., and Meyers et al. [48, 49]. The schematic

sequence of Figure 86 (e) and the corresponding observation extracted from Figure 86 (a), which is shown in Figure 86 (f), provide a clear proof of each stage. The solid Al and Ni layers (Figure 86 (e) step 1) represent the original state of the laminate. When laser shock compression is applied to the surface of laminates, the Al layer melts and initial intermetallic nucleation takes place at the interface of Ni/Al layers, Figure 86 (e) step 2 and Figure 86 (f) circle "a", respectively. After the reaction proceeds for a certain time, the intermetallic compounds agglomerate into spherules at the interface and turn elongated as they grow into elongated granules (Figure 86 (e) step 3, Figure 86 (f) circle "b"), leading eventually to the formation of dendritic structures. As the granules reach a critical size, the neighboring spheres start to grow as well as to constrain the first spheres. These exerted forces expel the first grown granules. This forces the intermetallic compounds to disperse into the Al layer (Figure 86 (e) step 4, Figure 86 (f) circle "b"). These dispersed granules and dendrites may accumulate and cluster to become full dendrites (Figure 86 (f) circle "c"). Notice that Figure 86 (c) shows the same sequence of reaction in the thicker bilayer sample as well, if the laser pulse duration is increased to 8 ns.
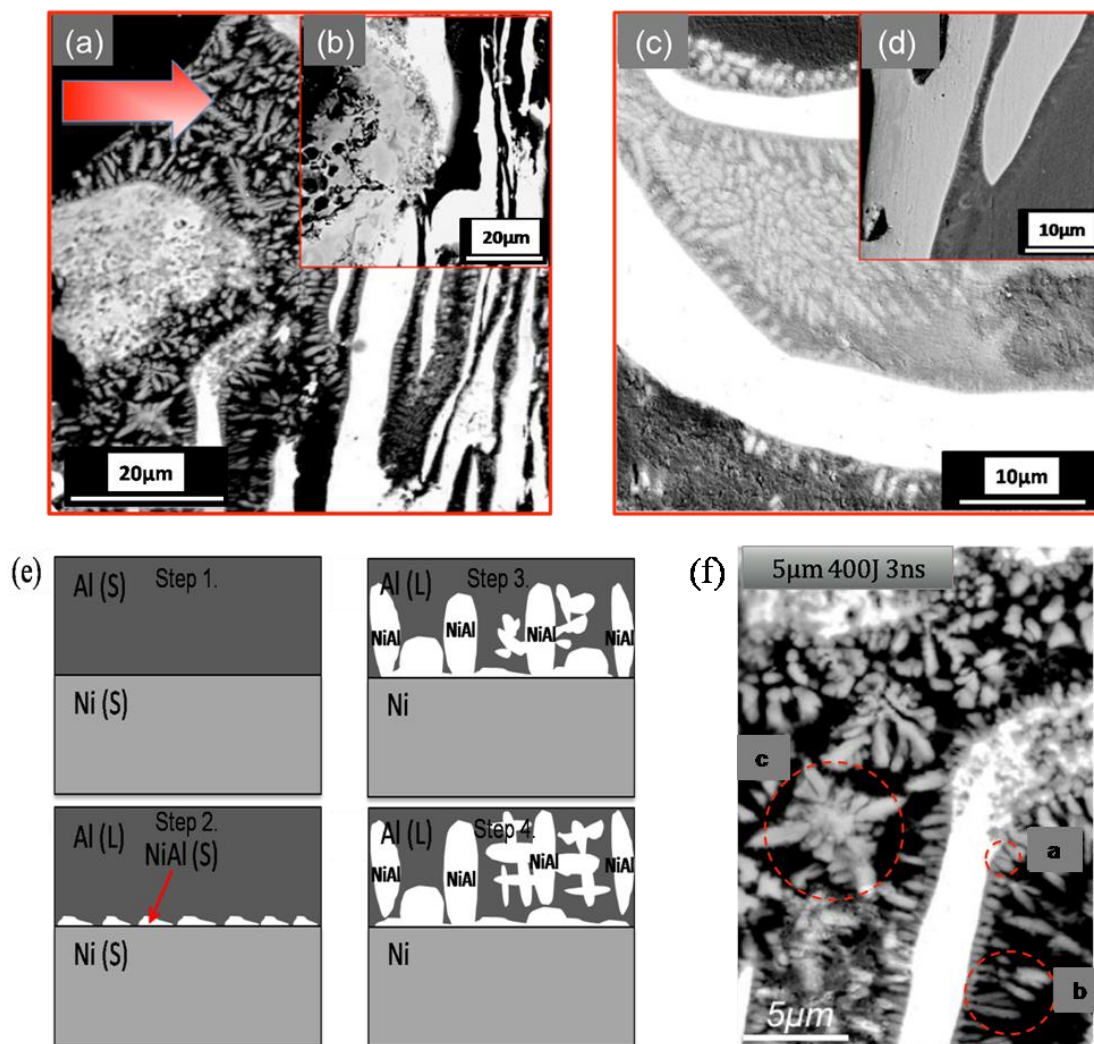
Figure 86: Cross-sectional observations (SEM-BSE): (a) 5 µm bilayer laminate (400 J, 3 ns laser): Dendrites were generated and found at 50 µm depth under the irradiated surface. (b) 5 µm bilayer laminates (400 J, 3 ns) at the edge of crater: It shows almost no intermetallic compound but still has the molten surface. (c) 30 µm bilayer laminate (400 J, 8 ns): Intermetallic granules showed on the first and second bilayer (~35 µm depth). (d) 30 µm bilayer laminate (400 J, 8 ns) at the edge of crater: The dendrites dramatically disappeared on the edge of the crater. (e) Schematic sequence of reaction and intermetallic compound formation. (f) the corresponding image for (e): Circle "a" shows the granules formed by interfacial reaction; they grow becoming elongated and are expelled from interface as shown in circle "b". The expelled granules accumulate and grow to be fully dendritic structures as shown by circle "c".

It should be noted that in the literature, the predicted shock-induced melting pressures of Ni and Al are ~275 GPa and ~125 GPa respectively [187, 188] and the corresponding melting temperatures are ~6400 K and ~4750 K. These pressures are close to the estimated pressure on the laser irradiated surface (see Section 3.4) and thus create opportunity of melting under shock pressure. This temperature increase is incorporated into the thermal energy released by the reaction. Therefore, the reaction has a great opportunity to self-propagate into the adjacent layers and through the entire sample. However, the self-propagating reaction is not found in this study.

The EDX dot-mapping images (insets of Figure 87 (c)) show that Ni (green color) and Al (red color) layers are mixed in many areas of the thinner bilayer laminates after 400 J, 3 ns, laser irradiation. The SEM back scattering electron image (Figure 87 (c)) also provides apparent evidence that the Ni (bright part) disperses uniformly in the Al (gray part) matrix. Interestingly, the samples do not show this intermixing phenomenon at the Ni/Al interface, except for the thinner bilayer recovered sample irradiated by 400 J, 3 ns laser (Figure 87 (a), (b), (d), and insets). This mixing may have been occurred either before or following the laser irradiation, due to the mechanical alloying mechanism from the cold-rolling process [53], or from the severe deformation of Ni and Al layers in spalling region. Our estimates of pressures are higher than the reaction threshold for intermetallics, 3.5 ~ 4.5 GPa [124], at relatively longer shock durations (from milliseconds to several seconds) applied by other methods. The absence of reactions in recovered samples is probably due to the very short pulse duration in the laser shock (3 and 8 ns) and the relatively smaller plastic deformation in cold-rolled solid laminates as

compared to the porous mixtures of powders in [189]. There is no experimental data for the threshold of intermetallic reactions at these pulse durations (3~8 ns).
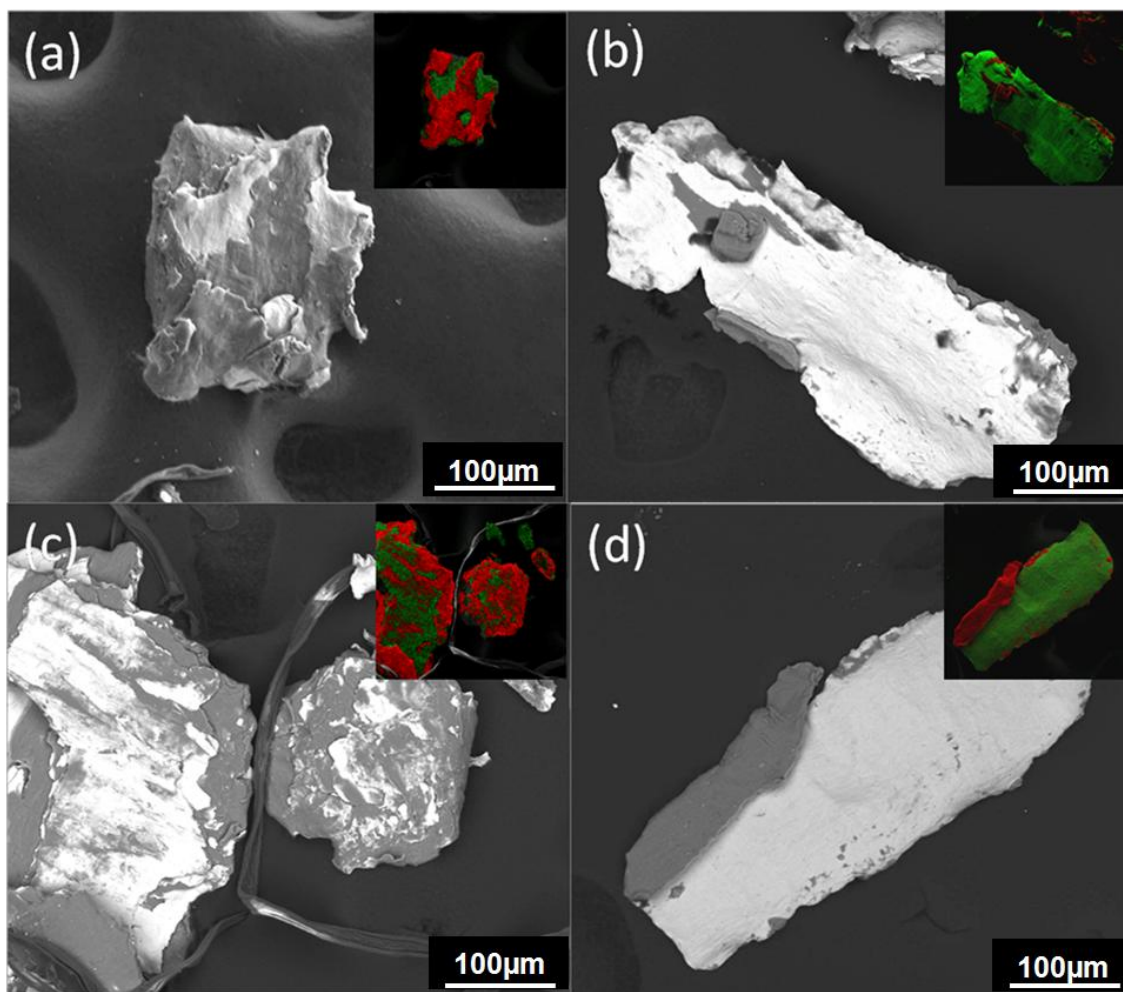
Figure 87: Fragments from spall surface: (a) 5 µm and (b) 30 µm bilayer thickness (100 J 3 ns laser exposure); (c) 5 µm and (d) 30 µm bilayer thickness (400 J 3 ns laser exposure).

4.3.7 Gilath model of spallation analysis

The laser-induced shock wave passed through the sample and reflected off the rear surface, producing a tensile stress that exceeded the tensile strength of the material

that results in spall at the free surface [85, 131, 132, 190]. The spallation is governed by many critical influences such as the laser intensity, the total thickness of the laminate, and its mechanical strength [128]. Figure 88 shows the cross-sectional surface of the 30 and 5 μm thick bilayer Ni/Al laminates irradiated by intense laser with energies about 100 and 400 J. The laser intensity, I, in this study is proportional to the laser energy, E, and inversely proportional to the pulse duration, t,

$$I = \frac{E}{(a \times t)} \ (\text{W/cm}^2)$$
Eqn. (69)

where the *a* was the laser beam area, and the pulse duration, t, was 3 ns for all shots. The laser intensities used in this study were $\sim 3.1 \times 10^{12}$ and $\sim 1.3 \times 10^{13}$ W/cm^2 corresponding to total energies of ~ 100 J and ~ 400 J.

The strain rate is difficult to obtain in real time for laser shock experiments. In Section 4.3.4, we estimated the strain rate from the size of the spallation and fragments. The results were consistent with the emiprical observations and the estimated strain rate was about 10^6 s^{-1}. However Gilath *et al*. [128] also proposed an approach for estimating it by measuring the spall thickness, Δ, from Figure 88 and substituting it into following equation:

$$\Delta = \left(\frac{U_s - C}{U_s + C} \right) d + \frac{t U_s C}{U_s + C}$$
Eqn. (70)

where d is the total thickness of the laminate, t is the pulse duration, U_s is the shock wave velocity, and C is the elastic sound velocity. The total thickness, and pulse duration are known values, which are ~ 0.9 mm and 3 ns respectively. The elastic sound velocity, C, is calculated to have a value of about 4950 m/s by the additive rule, assuming that the

material is a homogeneous mixture composed of equal volumes of Ni and Al. The shock wave velocity U_s was obtained. Using the obtained shock wave velocity and substituting it into Eqn. (70):

$$U_p = \frac{U_s - C}{s}$$
Eqn. (71)

where U_p is the particle velocity, and s is an empirical factor which was chosen to be 1.4 [28]. From the obtained particle velocities, the strain rate $\dot{\varepsilon}$ can be estimated by using Eqn. (72):

$$\dot{\varepsilon} = \frac{2U_p}{Ct}$$
Eqn. (72)

The spall thicknesses were measured and analyzed using a scanning electronic microscope. Based on the Glath's model, the strain rate was obtained and varied from 1.24×10^8 to 4.11×10^8 s^{-1} (see Table 16). It is two order higher than the estimates obtained from Grady's model. If we applied the strain rate from Glath's model, we found that the fractures and the fragments should be resulted by a ductile failure mechanism which is inconsistent with the empirical observations. This inconsistency somehow proves the uncertainty and difficulty of studying laser -condense matter interactions.

Table 16. Strain rates estimated from Spall depths

Sample	105 J, 30 µm	107 J, 5 µm	421 J, 30 µm	430 J, 5 µm
Spall depth Δ (µm)	111.1±6.5	100.9±10.3	250.1±11.5	277.6±9.8
Strain rate (s^{-1})	1.5×10^8	1.24×10^8	3.46×10^8	4.11×10^8
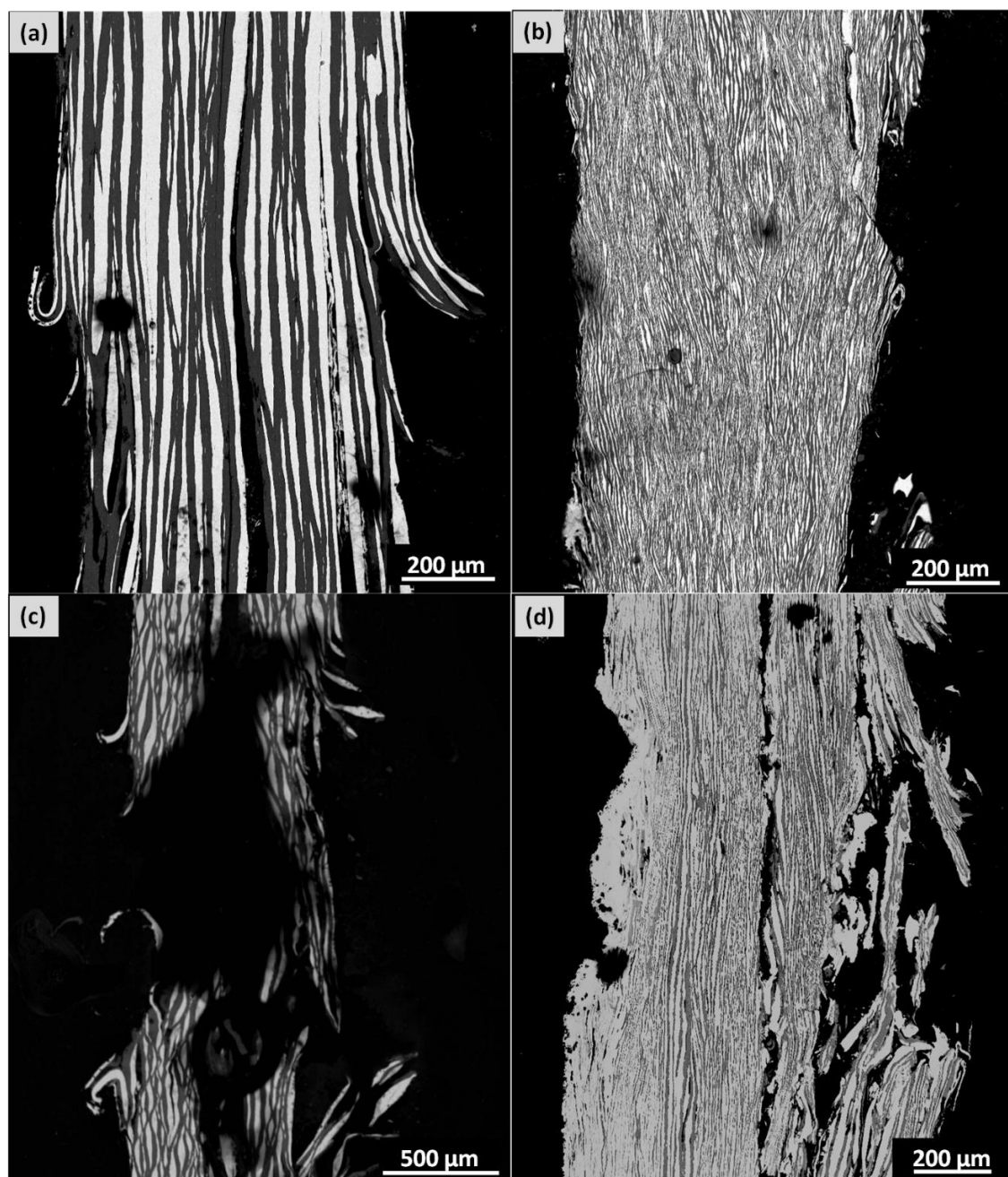
Figure 88: Cross-sectional morphologies: (a) bilayer thickness, 30 µm, shocked by 105 J, 3 ns laser; (b) bilayer thickness, 5 µm, shocked by 107 J, 3 ns laser; (c) thick bilayer shocked by 421 J, 3 ns laser; (d) thin bilayer shocked by 430 J, 3 ns laser.

4.3.8 XRD analysis

X-ray diffraction (XRD) and energy dispersive spectrometer (EDS) analyses were used to investigate the components of the reaction products after laser irradiation. XRD was conducted on cross-sectioned samples before and after laser irradiation. The results showed that before the laser irradiation (Figure 89 (a), (b)), there was no evidence of intermetallic compounds generated during the cold-rolling process; only Al and Ni peaks were found. After laser irradiation, XRD results show that for 3 ns laser pulse duration only the thinner (5 µm) bilayer sample had strong intermetallic compound peaks after 400 J laser irradiation (Figure 89 (a) dashed circle). The intermetallic compound was identified as NiAl. This agrees with recent in-situ studies of self-propagating reactions in Ni/Al multilayer foils [44, 45, 69]. In these in-situ studies, NiAl was the first intermetallic to form, regardless of whether the initial average composition was Al or Ni-rich. Gavens *et al.* [3] also postulated the bilayer thickness effect for the intermetallic reaction. As the duration of the laser pulse was increased to 8 ns with total energies of 24 and 409 J, the XRD results (Figure 89 (b)) reveal more extensive reaction, now for both thinner and thicker bilayer samples. This agrees with the previous microscopic cross-section observations (Figure 86). In addition to the NiAl peaks, the possible Al-rich peaks of $NiAl_3$ were also found. Due to the high residual strain, fast reaction, and short heating time from laser irradiation, the Al-rich intermetallic, $NiAl_3$, has only three peaks in the XRD spectrum. No intermetallic compound was found by XRD for 24 J, 8 ns laser exposure on 30 µm bilayer sample (Figure 89 (b)). Thus, longer duration and higher laser energy benefitted the laser shock reaction. This is consistent with SEM observation on

the irradiated surface (Figure 85 (a)). It suggests that longer duration of laser pulse is not always adequate for reaction if the laser energy is too low.

The EDX technique was also used in the analysis of the fragments and intermetallic dendrites. The EDX data showed that the ratio of components in the dendrites vary from Ni:Al=20:70 to Ni:Al=19:81. Compared with the XRD analyses, which identify the intermetallic compounds as NiAl and NiAl$_3$, the EDX results show that those compounds are Al-rich phases. Due to the diagnostic spot size ~1 μm, and the electron scattering effect, the results of the EDX analysis of intermetallic compounds were always disturbed by the surrounding environment.
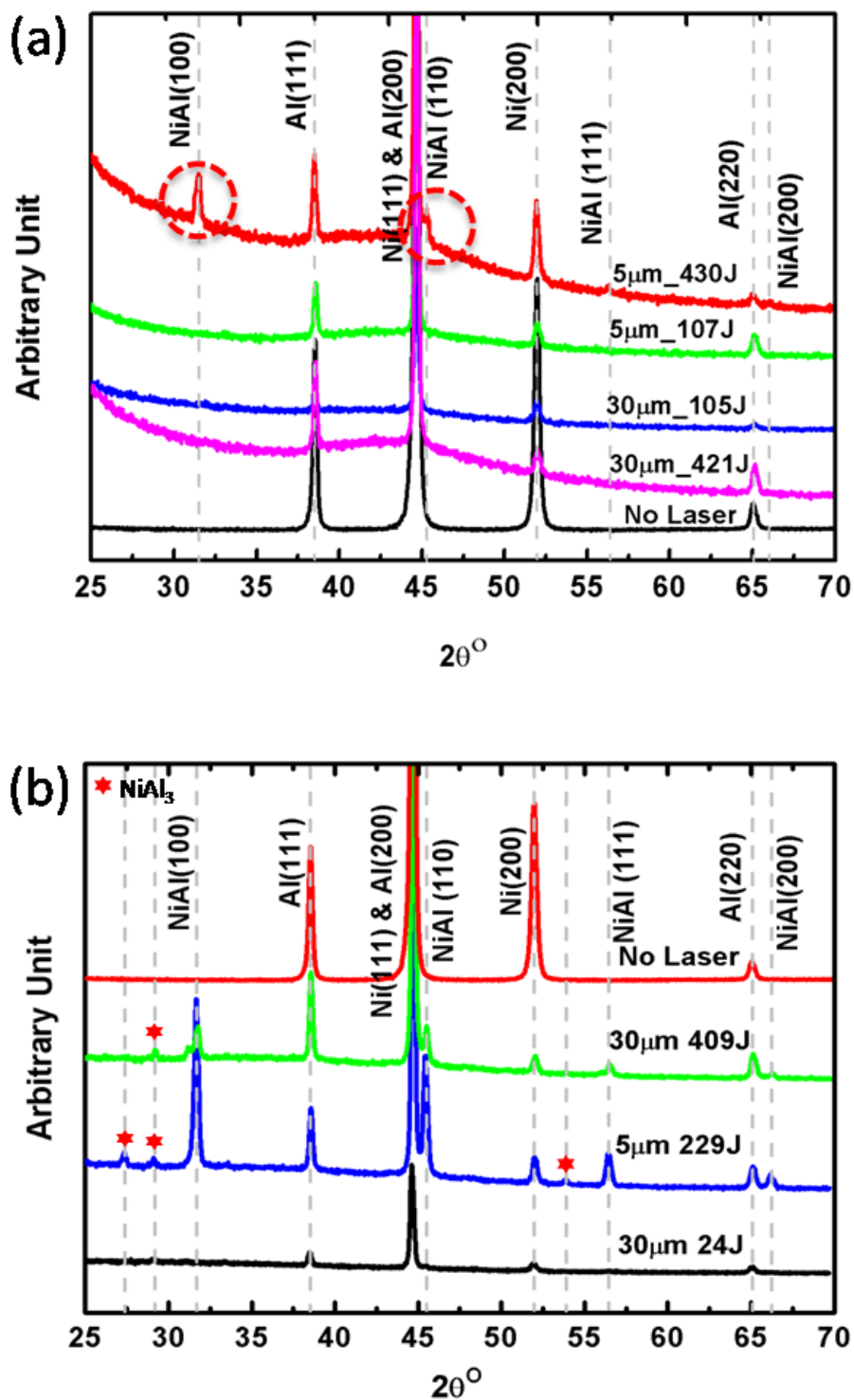
Figure 89: X-Ray diffraction of cross sectional surfaces of (a) 3 ns and (b) 8 ns laser irradiation. (a) Reaction for 430 J irradiation (5 µm bilayer), represented by circles. (b) Reaction from 229 to 409 J and both 5 µm and 30 µm bilayer thickness. NiAl$_3$ intermetallic compound was marked by stars.

4.3.9 Laser-driven shock-less compression on Ni-Al reactive laminates

Ni/Al laminates with bilayer thicknesses in the micrometer (~5 µm) and nanometer (~50 nm) range were subjected to exothermic reactions induced by laser-driven compression. The initial shock-less compression steepened into shock in the microscaled laminate generating a pressure pulse duration several tens of nanoseconds, which induced strain rates varying from 10^7 to 10^8 s^{-1}. The laser energies applied, 650, 875 and 1305 J, generated peak compression stresses of 30, 75, and 118 GPa, respectively at the plasma stagnated Al surface. Large differences in flow stresses and bulk compression moduli of Ni and Al introduced localized shear strains in the Ni/Al interfaces.

The nano-scale Ni/Al laminates were fully reacted, producing NiAl with grain sizes less than 500 nm. The NiAl intermetallic phases, B2 (β) phase (fcc) and martensitic phase (bcc), coexist in the NiAl nano-grains as well as vacancies due to the fast quenching process.

It was confirmed that the intermetallic reaction in the Ni/Al micro-laminate cannot self-sustain under the laser-driven compressive loading. The intermetallics NiAl (equiaxed grains) and NiAl$_3$ (dendrites) were identified on the plasma stagnated surface of Ni/Al micro-laminates. The distribution of intermetallic phases varied according to the incident laser energies.

4.3.10 Experimental method

Laser-driven shock wave have been used to investigate the dynamic behaviors of the materials [85, 90-96, 192-200]: aluminum [95, 96], copper [192, 193], tantalum [194, 195], vanadium [85], nickel aluminide [196, 197], iron [198, 199], nickel [200], and nickel-aluminum laminates [85]. The laser beam with a high energy intensity, $> 10^{13}$ W/cm^2, generates strong ionization and thermal deposition on the irradiated surface creating melting pools and craters [82, 94]. The laser-driven shock wave in solid materials is generated by the rapid formation and expansion of a hot and dense plasma on the surface layer caused by the direct irradiation of the focused laser beams [90-92, 95, 96]. This method of generating shock waves by laser is affected significantly by three factors: different laser absorption rates of materials [92], inhomogeneous (Gaussian) laser-intensity distribution caused by the focal spot of the laser beam [92] and the drastic decrease of the shock pressure in solids [83, 94]. Direct laser-driven shock compression cannot maintain the ultrahigh strain rate ($> 10^6$ s^{-1}) and stress in the Ni/Al laminates and introduces extended thermal damages on the irradiated surface which made the post-analysis complicated. An innovative laser-driven shock-less compression method was developed [95, 96]. It enables an essentially smoother compression pulse propagating through the entire sample, which is similar to the 'z-pinch' technique developed by Asay et al. at Sandia National Laboratory [201].

Ni/Al reactive laminates were subjected to the laser-driven shock-less compression using the OMEGA glass laser in the Laboratory for Laser Energetics at the

University of Rochester. In order to investigate the behaviors of the Ni/Al reactive laminates under a steady high pressure shock compression, the 351 nm wave-length laser [191] with energies of 1305, 875 and 650 J was used to produce expanding dense plasma which generated the laser-driven shock-less compression in the laminates. The laser pulse duration was 3.7 ns and the intensity varied from ~3.8×10^{12} to ~7.6×10^{12} W cm^{-2}. The experimental setup was thoroughly introduced in Section 3.4. The shock-less compression produced by the soft stagnation of the laser-induced high density plasma was conducted on the sandwiched Ni/Al laminates having a nano-scale Ni/Al laminar foil (bilayer thickness = 54 nm) in between two micro-scale laminates (bilayer thickness = 5 µm).

The as-produced and recovered samples were characterized and analyzed using a scanning electron microscope (Philips XL30 ESEM), scanning/transmission electron microscope (EFI Titan 80-300 kV S/TEM) and energy-dispersive X-ray spectroscopy (EDX). The dynamic response of the laminates and the shock-wave propagation in this bulk material were estimated by the one-dimensional hydro-code, HYADES.

4.3.11 Morphology of as-produced laminates

Cross-sections of the Ni/Al micro- and nano-laminate are presented in Figure 90. The irregularly lamellar micro-layers of Ni (brighter area in Figure 90 (a)) and Al (darker area in Figure 90 (a)) elemental sheets with approximate 5 µm bilayer are made by an accumulative roll-bonding (cold-rolling) process which is thoroughly addressed in [82, 94]. The molar ratio of the micro-laminate is Ni:Al = 1:1. The nano-scale Ni/Al laminate

was fabricated by a magnetron sputtering process. It had a well-defined Ni (brighter area in Figure 90 (b)) and Al (darker area in Figure 90 (b)) periodic multi-layer structure characterized by the 54 nm average bilayer thickness as shown in Figure 90 (b). The total thickness of the Ni/Al nano-laminate was about 8.5 µm. Alternatively deposited Ni and Al layers had a thickness ratio of 2/3 and the corresponding stoichiometric ratiomolar ratio is about 1/1 of Ni/Al.

The Ni/Al micro-laminate was sectioned perpendicularly to the rolling direction and then thinned by an ion milling process. Figure 91 (a, b, c, d) demonstrates the bright field (a, c) and corresponding dark field (b, d) TEM micrographs of the initial Ni/Al micro-laminates generated by the accumulative roll-bonding process. Figure 91 (a, c) show that the structure of the aluminum lamellae consists of approximately equiaxed grains which are less than 25 nm. There is a large amount of defects shown in the Al nano-grains caused by severe plastic deformation. The associated selected area diffraction shown in the inset of Figure 91 (a) reveals that sharp diffraction rings and dots reflecting the Al polycrystalline structure and the halo diffraction rings indicating possible nano-crystalline structure caused by the accumulative roll-bonding process [58, 59].

The TEM micrographs of Ni layer from the micro-laminate are shown in Figure 91 (c, d). They reveal elongated grains with a large density of dislocations and other defects. In contrast with Al, there was no complete recrystallization. The width of the Ni grain, measured from the dark filed TEM image, Figure 91 (d), varied from less than 100 nm to over than 0.5 µm. The selected area diffraction pattern has oval bright dots which

indicated that the Ni crystal has a significant amount of defects caused by the accumulative roll-bonding process.
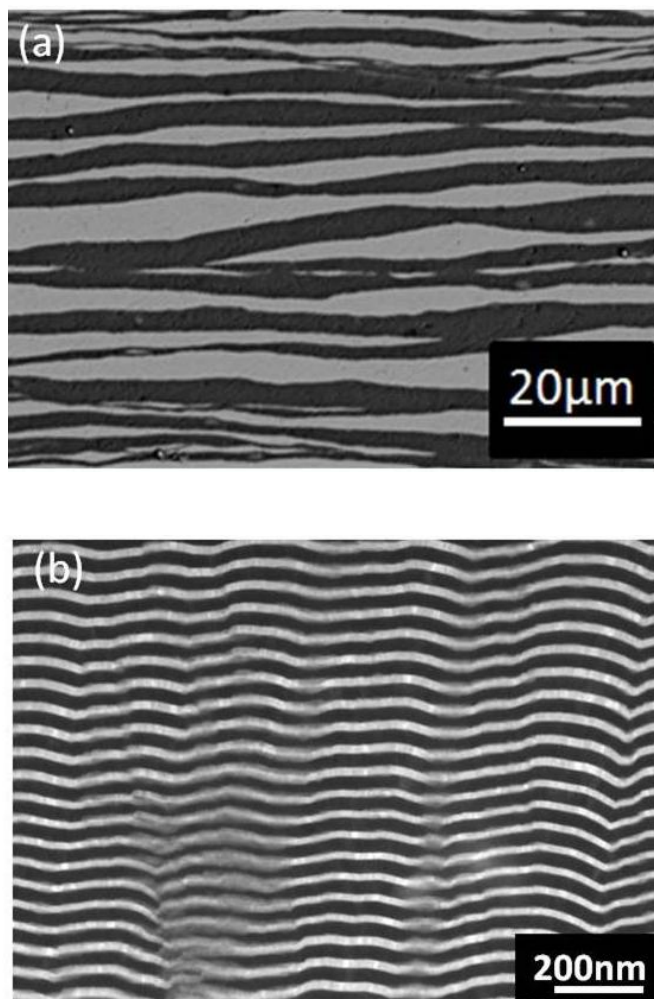
Figure 90: Cross-sections of (a) cold-rolled Ni/Al micro-laminate (SEM) and (b) nano-laminate fabricated by the magnetron sputter deposition (STEM).
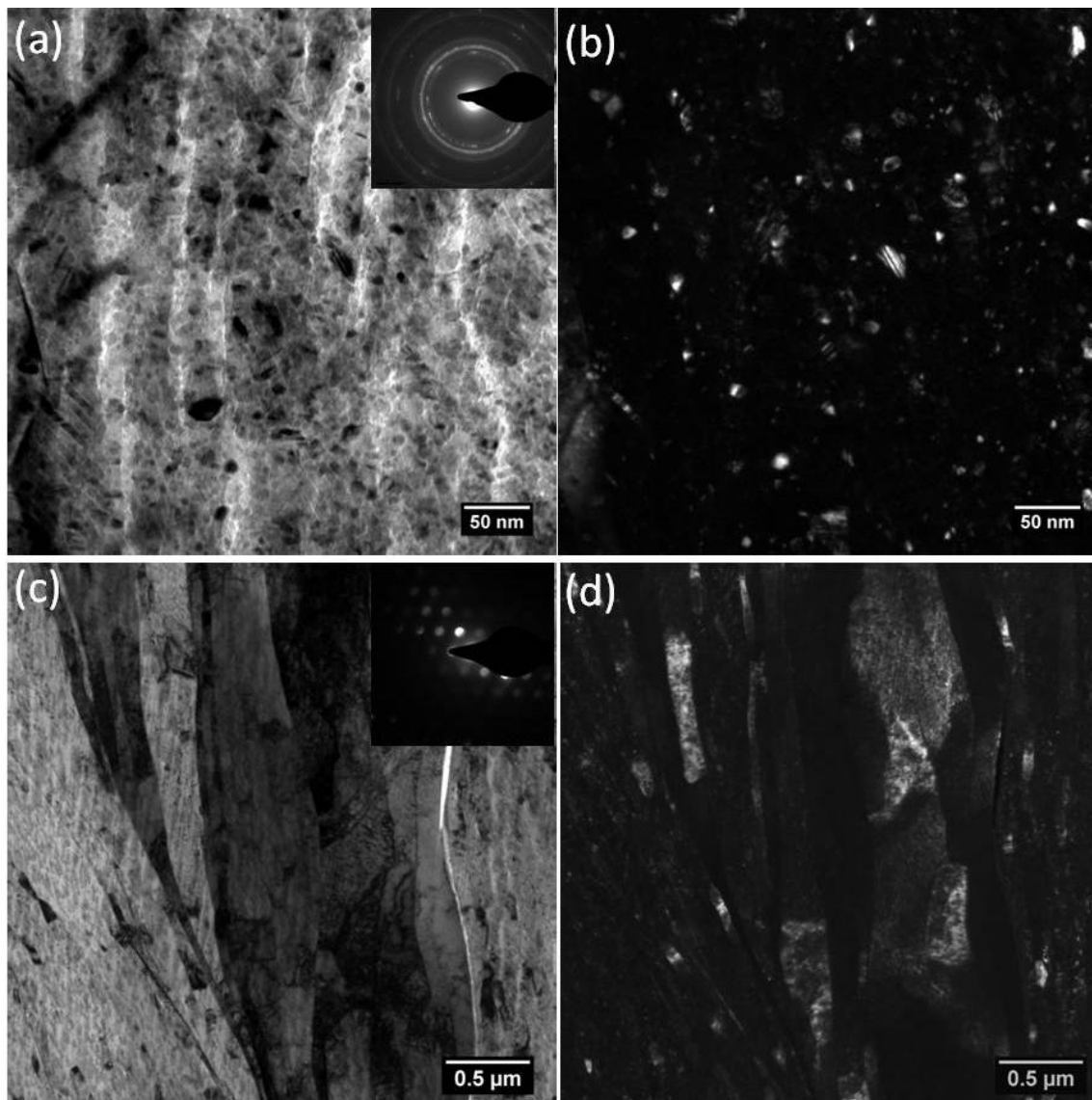
Figure 91: TEM micrographs of Ni/Al micro-laminate prior to shock: (a) Bright field with diffraction pattern, and (b) dark field images of the cold-rolled Al phase; note the nanoscale equiaxed grain structure. (c,d) same for the Ni phase; note elongated grains resulting from cold rolling.

Focused ion beam (FIB) milling was utilized to prepare the TEM sample of the magnetron sputter deposited Ni/Al nano-laminate with the micro-structure shown in Figure 92 (a, b). A platinum layer was deposited prior to FIB milling as shown on the top-right of Figure 92 (a). The Al layer is composed of columnar single crystal domains with a width of ~20 nm; the Ni layer had single crystal columns with a width greater than 10 nm. The magnified high-resolution image of the region shown by the square on Figure 92 (a) is presented in Figure 92 (b). It reveals a clear Al $\left[1\bar{1}0\right]$ mono-crystalline structure and Moiré fringes corresponding to the interaction due to differences in crystal orientations between the adjacent Al grains. The high resolution TEM micrograph on Figure 92 (b) shows that the deposited Ni/Al laminate was fully dense with very low dislocation density.
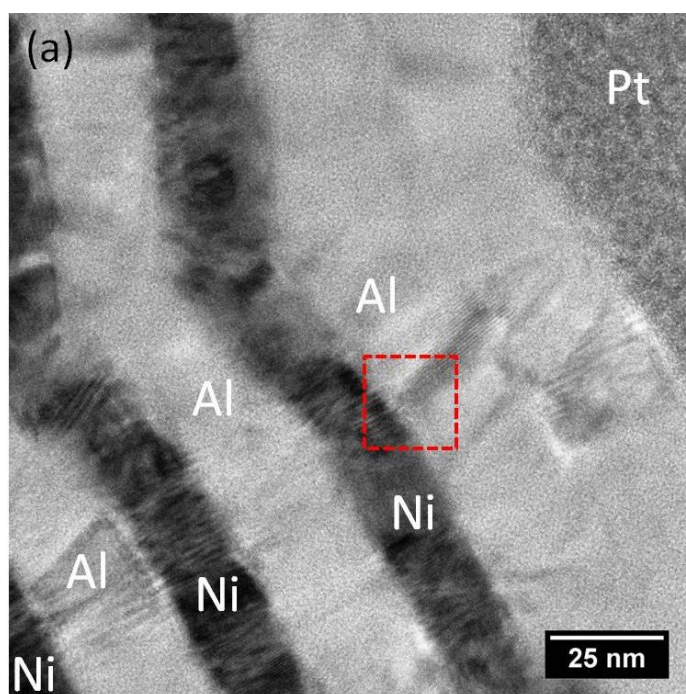
Figure 92: TEM micrograph of nano-laminate prior to shock: (a) Each single crystal domain is small and formed as a column; (b) Moiré fringes appear on the Al and Ni phases due to the overlap of two misoriented single crystal planes. (figure continued)
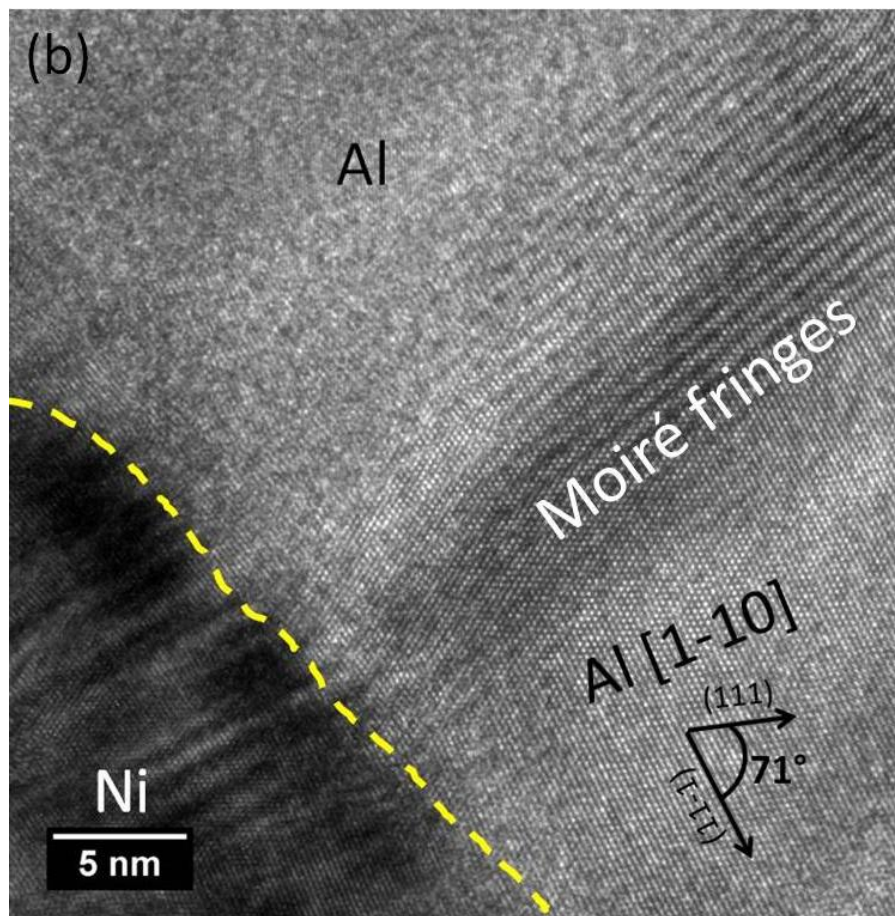
Figure 92: Continued.

4.3.12 HYADES simulation

As the aforementioned in Section 3.4, the use of laser-driven shock-less compression significantly decreases undesirable effects by means of reducing the thermal deposition on the irradiated surface and the drastic attenuation of the shock pressure in the solid. These are two critical problems of the direct laser shock experiments [82, 94]. The schematic of Figure 93 (a) presents the evolution of the laser-sandwich-laminate interaction. The initial experimental setup is presented on the left side of Figure 93 (a). The laser beam irradiated the ablator-reservoir slab generating an energetic plasma which

expanded and stagnated on the front surface of the sandwich laminates as shown in the middle of Figure 93 (a). This results in the shock-less compression with the influenced depth 20~40 µm. This compression wave steepens and develops into a shock wave propagating through the laminates and creating a crater, spall, and fragments on the recovered Ni/Al sandwich laminates, shown in the right side of Figure 93 (a). Intermetallic reactions might occur in the Ni/Al micro- and nano-laminates during/after the shock compression.

The hydrodynamic computational code, HYADES, was used to estimate mechanical responses of laminates to the shock-less compression. Remington et al. [202] conducted similar experiments and found out that the compression pressure induced by plasma stagnation can be represented by the following equation:

$$P \propto \frac{\omega^{0.5} I^{0.76}}{t^{0.13}} \qquad \text{Eqn. (73)}$$

here ω, I and t are the laser frequency, intensity and pulse duration. Edwards et al. [95] had measured the velocity of the rear surface of Al samples and back integrated using Al equation of state (EOS) to obtain the time dependent pressure profile at the front surface. The input compression profiles at the front surface of the sandwich laminates were subtracted and scaled from Edwards et al.'s work [95] using Eqn. (65) regarding the similar experimental setup. The results are shown in Figure 93 (b).
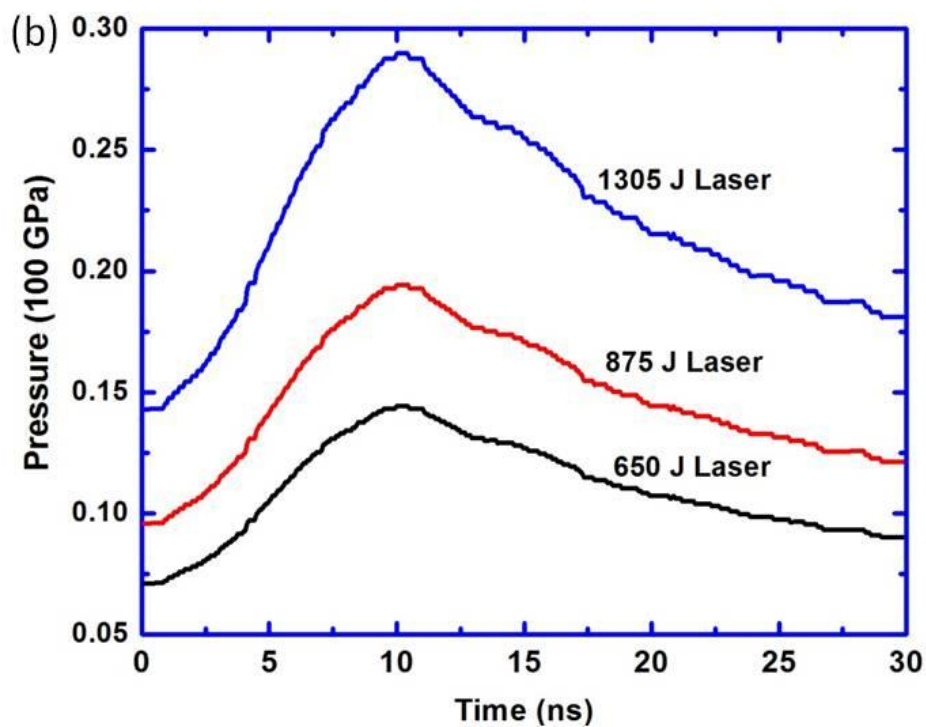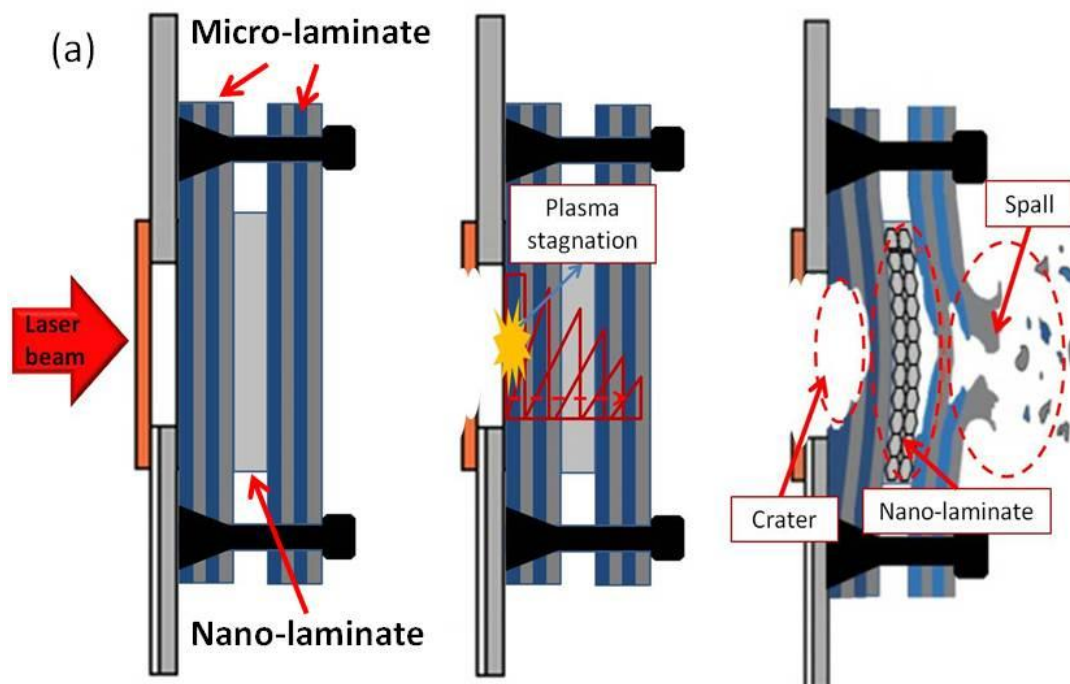
Figure 93: (a) Schematic illustrating, from the left to the right: original sandwich sample; plasma stagnation induced by laser beam and a formation of the shock-less compression; shock wave reflecting at back surface as tensile pulse creating spalling and fragmentation. (b) Input pressure profiles scaled from [95].

These estimated input pressure profiles acting at the front surface were applied as HYADES pressure sources. The Steinberg shear model and Steinberg-Guinan high strain rate elastic-plastic model [203] were incorporated into the computation in order to estimate the mechanical responses of the Ni/Al laminates. The detail of the HYADES code is presented in Appendix (c). Figure 94 (a) shows that the fully-developed shock waves propagate into the irradiated micro-laminates after traveling through the shock-less compression region. Elastic wave precursors appear in the earlier stages of the shock waves (Figure 94(a)) due to the extremely high strain on the plasma stagnated surface [204]. The pressure waves generated by laser-driven shock-less compression at three different laser energies have relatively weak attenuations of peak pressures in the Ni/Al laminates. For instance, the peak pressure of the 650 J laser-driven shock-less compression waves shows less than 20% attenuation for a thickness of ~ 0.85 mm while propagating in the Ni/Al laminate, which is smaller than the direct laser shock experiment, which shows an attenuation of > 90% over the same thickness as shown in Table 17. This semi-steady shock wave propagated through the first Ni/Al micro-laminate and was conveyed to the nano-scale laminate. The shock wave pressure is retained effectively on the nano-laminate for about 70 ns and the peak pressure can reach 28 GPa for 650 J laser experiment, with a 20% variation between the front and the rear surface of the nano-laminate as shown in Figure 94 (b). The peak pressures on the front micro-laminate, P_M, and the nano-laminate, P_N, for each specific laser condition are listed in Table 17 with the variations, ΔV_M, of the peak pressures in the micor-lamiante.
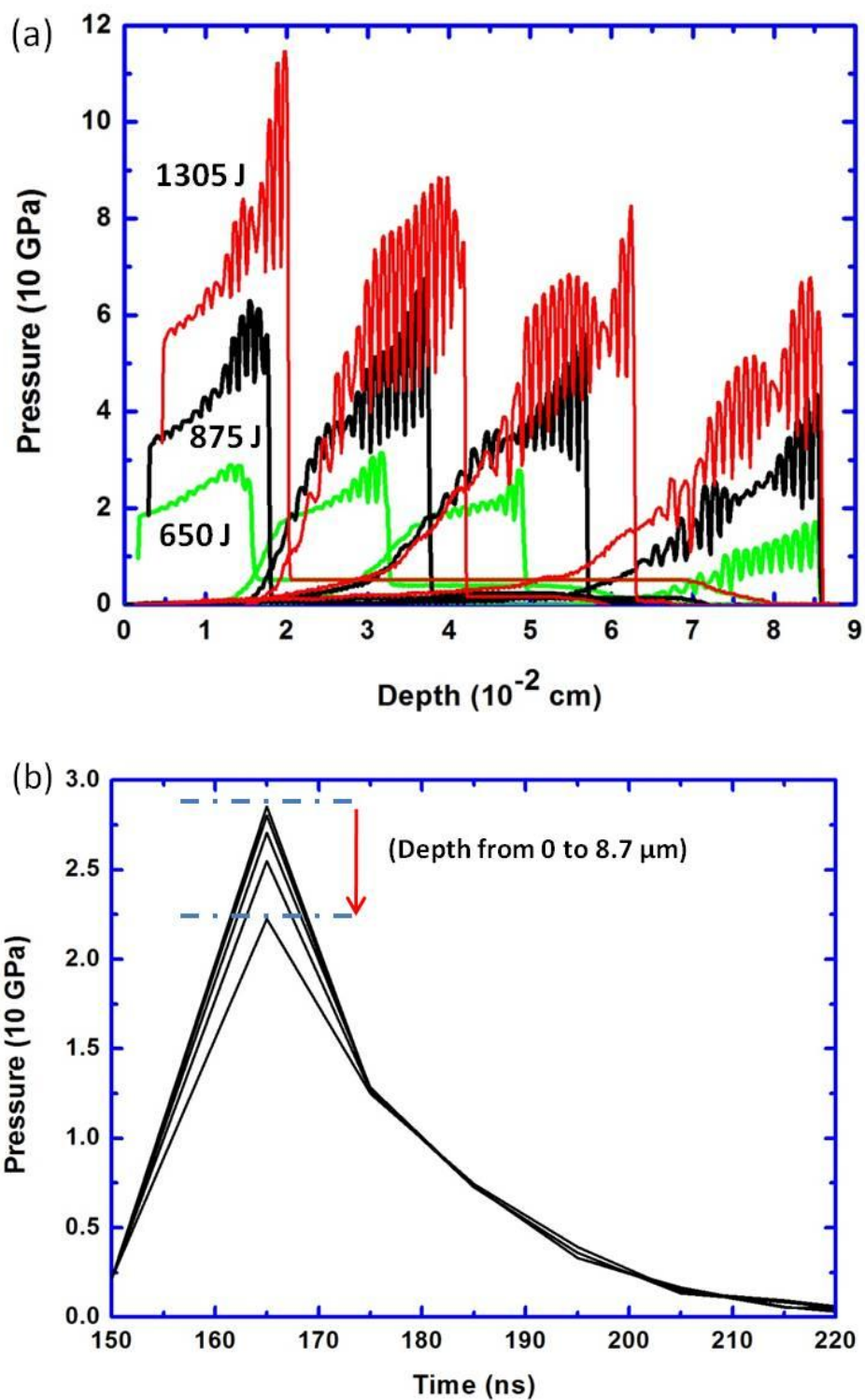
Figure 94: (a) propagation of compression pulse at increasing depths into the micro-laminate. (b) compression pressures vs. time in the nano-laminate.

Table 17. E_L = total laser energy, I_L = laser intensity, t = laser pulse duration, P_M = peak pressure in the front micro-laminate, ΔV_M = variation of the peak pressures in the micro-laminate, Δ_G = gap width between the reservoir and the front surface of the Ni/Al micro-laminate. (* subtracted from [94])

E_L (J)	I_L (W cm^{-2})	t (ns)	P_M (GPa)	V_M	P_N (GPa)	Δ_G (µm)
650	3.8×10^{12}	3.7	30	16%	29	300
875	5.1×10^{12}	3.7	75	27%	59	300
1305	7.6×10^{12}	3.7	118	29%	99	300
430 *	1.28×10^{13}*	3*	~180*	>90%*	---	0

The estimated highest strain rate can reach ~10^6 - 10^7 s^{-1} in the middle of the front micro-laminate, which consistent with [95, 96], and ~10^8 s^{-1} in the nano-laminate from the HYADES simulation results. The increased strain rate is due to the compression pulse 'shocking up' as it travels through the material. The variation in the highest strains of Al and Ni layer was negligible in the laminates of the 650 J laser experiment; however the total strain in Al layers was twice 2 times the one for Ni layers in the 1305 J laser experiment, which is due to the higher strain hardening exponent of Ni in the Steinberg-Guinan model [203]. This resulted in a higher yield stress of nickel while compressing the sample and significantly decreased the total strain of the nickel layer. It can be corresponded to the bulk compression moduli as well, which are 180 GPa for Ni and 76 GPa for Al, in the Ni/Al laminates. The empirical evidence is shown on the cross sections of the recovered samples presented in Figure 96 (d), which presents that the recovered sample has relatively thinner Al layers in comparison with the original laminate of Figure 90 (a). Details of the highest strain in the middle Al and Ni layers in the front micro-laminate are shown in Table 18.

Table 18. Highest strain of the Al and Ni layer in the middle of the front micro-laminate (obtained from HYADES simulation)

Laser Condition	Highest Strain (Al)	Highest Strain (Ni)
1305 J	0.713	0.409
875 J	0.520	0.263
650 J	0.311	0.29

4.3.13 Craters and spalls on the recovered laminates

The recovered sample was disassembled and examined using SEM, TEM, EDX, STEM. The results show that laser-driven initially shock-less compression incorporating the sandwich structure of Ni/Al laminates reveals significant phenomena which are first discovered in the fully dense Ni/Al micro- and nano-laminate.

Thhie kinetic energy of the laser generated plasma produced a compression pressure wave, which developed into a shock wave propagating in the laminates. Craters and spalls were easily found on the plasma stagnated front surface and the rear surface respectively, as shown on Figure 95 (a) and (b), of the sandwich laminates in 650 J laser experiment. Similar fractures were also found identically in 875 J laser experiment. These types of fractures can be found in the directly laser shock compression experiments as well [82, 94, 171]. The 1305 J laser also created a crater on the front surface. The sandwich structure was shattered into small segments due to the strong reflected tensile stress which pulled apart the laminates especially in the high laser energy experiment. In this study, the fracture mechanisms and morphologies are not addressed, however these were carefully characterized by Wei el al. and Vitali et al. [82, 94, 171].
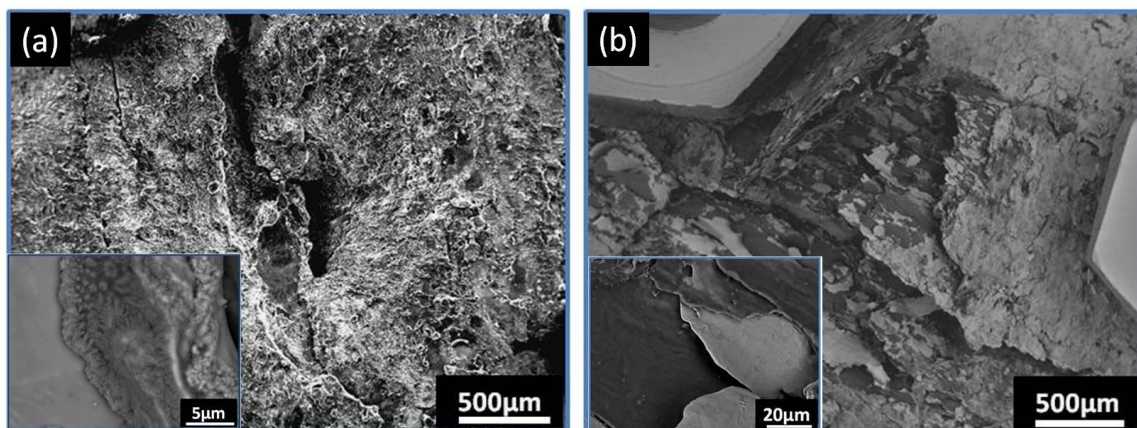
Figure 95: Surface morphologies of recovered micro-laminate samples for 650 J (a) Crater on the front (plasma exposed) surface for 650 J with intermetallic dendrites on the crater in insert; (b) spallation on the rear surface of second micro-laminate for 650 J with separation of laminae and ductile failure edges in inset.

4.3.14 Intermetallic reactions of recovered laminates

Intermetallic phases in the form of granules and dendrites were found on the front surface of the micro-laminate exposed to stagnated plasma in all the experiments as shown in the inset of Figure 95 (a). At the spall surface, there was no intermetallic phase or any intermixing regimes, as shown in Figure 95 (b) and its inset. At the crater center stagnated by the plasma of 1305 J laser experiment, NiAl intermettalic granule particles were found in the recovered sample. These results suggest that the laser energies play an important role in the intermetallic reactions.

The SEM observations conducted on the cross-section of the front micro-laminates were shown in Figure 96, for the 1305 J laser experiment. Figure 96 (a) presents different intermetallic phases with distinct morphologies and compositions. In the center of the crater, Figure 96 (b), the Ni/Al laminate fully reacted and formed equiaxed NiAl intermetallic grains with grain sizes varying from 2 to 7 µm. The NiAl

intermetallic phase was identified by EDX and had a 53:47 = Ni:Al atomic ratio consistent with the Ni-Al phase diagram [185]. In the region adjacent to the crater center, Figure 96 (c), the NiAl$_3$ intermetallic dendrites grew perpendicularly to the aluminum layer identified by EDX analysis; this is similar to our prior findings [2, 5, 82, 94]. It can be speculated that this type of reaction initiates from the interfacial interaction caused by localized shear due to the differences of bulk compression moduli of Ni and Al. The NiAl$_3$ intermetallic phase was the first stable phase to appear when Ni/Al cold-rolled micro-laminates are heated slowly [4, 55-57], and the formation reaction can initiate at a relatively low temperature ~300-500 $^{\circ}$C [4]. At the regime farther away from the center of Figure 96 (d), no intermetallic phase was found; however at the interface of Ni and Al layer, the vortexes, intermixing and localized shear were observed. We identify these features as the initial stage of mechanical alloying in the micro-laminate due to the significant difference in the bulk compression moduli of Ni and Al.

The cross section of the front micro-laminate obtained from the 650 J laser experiment had only a small amount of the NiAl$_3$ intermetallic dendrites, same morphologies as Figure 96 (c), from the top bilayer down to the depth of <10 µm. These dendrites were sectioned and analyzed using the EDX mapping analysis embedded in STEM system. Figure 97 shows the EDX mapping results, which indicate that the NiAl$_3$ phase (from A to B) has a relatively uniform composition ratio of Ni:Al in weight % that is about 40 : 50, regardless of the 10 weight % of impurities, corresponding to the atomic ratio 1 : 3 of Ni:Al. The EDX mapping result in the Al matrix (from B to C) shows that Ni diffuses into the Al matrix; however, the gradual increase of Al and decrease in Ni

weight % suggest that the uniform composition of the intermetallic is not formed in this regime. Deeper into the specimen there are intermixing, vortexes and extrusions of the molten Ni, shown in Figure 96 (d); this image was taken from the area away from the indented center of the plasma stagnated micro-laminate (1305 J laser experiment). It should be noted that in this unreacted area, the aluminum phase was drastically reduced as shown in Figure 96 (d), which is consistent with the HYADES results in Table 18. The recovered sample from 875 J laser experiment had a small amount of NiAl intermetallic grains, and the NiAl$_3$ dendrites propagated inward to a depth of 100 µm in the center of the plasma stagnated areas. In the areas underneath the bilayers with NiAl$_3$ dendrites, the vortexes, extrusions of molten Ni and shear were also found as well as the laminar structure with reduced Al layers.

Figure 98 shows the schematics of the phase distributions observed on the plasma stagnated micro-laminates for the three different laser energies. It should be noted that fractures such as cracks and voids are not illustrated in the plots. The 650 J laser experiment had only NiAl$_3$ dendrites shown in a limited area of the front micro-laminate. A small amount of NiAl grains on the front surface and a considerable quantity of NiAl$_3$ dendrites were observed on the cross-section of the plasma stagnated micro-laminate of the 875 J laser experiment. The result of the 1305 J laser experiment revealed a fully reacted NiAl grains in the center area; the lateral regions were completely filled by NiAl$_3$ intermetallic dendrites as shown in Fig. 7 (1305 J laser).
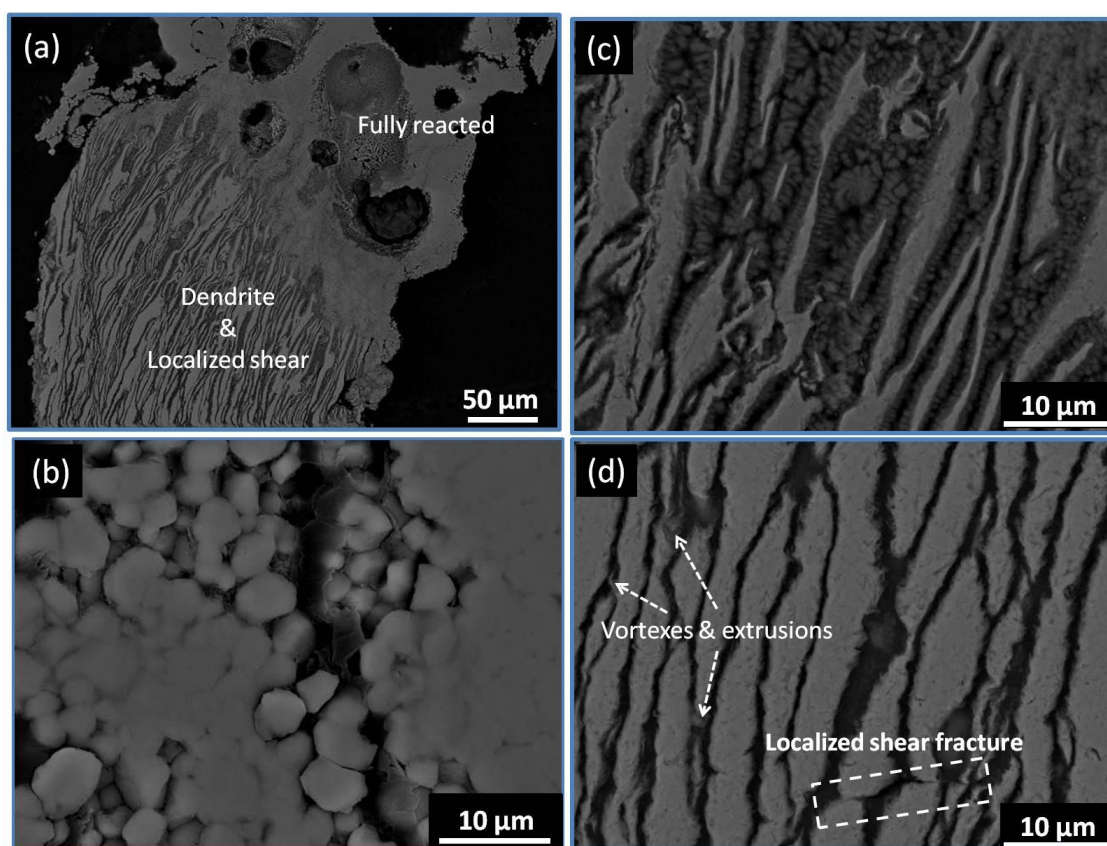
Figure 96: (a) Cross-section of the irradiated mico-laminate from 1305 J laser experiment; (b) fully reacted NiAl intermetallic grains of the sample (a); (c) dendrites of NiAl3 intermetallic phase; (d) intermixed extrusions, vortexes, and localized shear fractures generated by the laser induced shock-less compression.
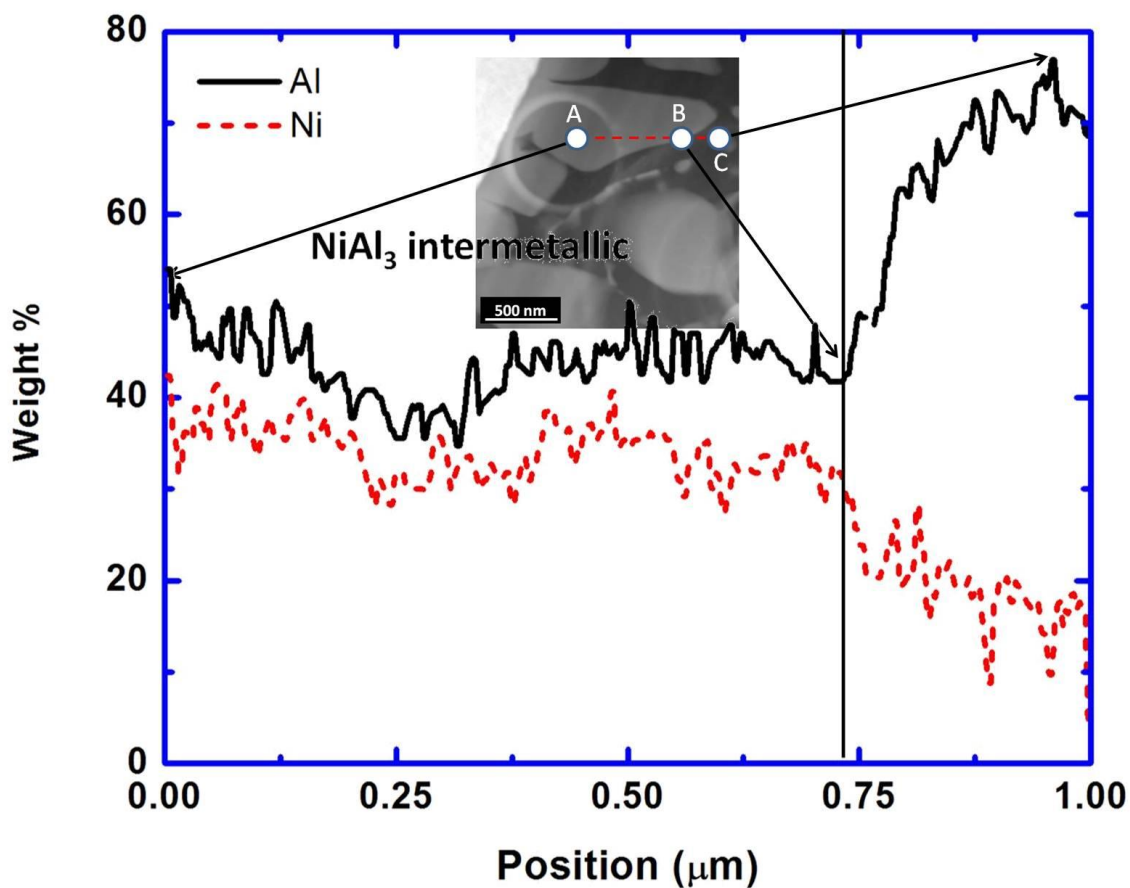
Figure 97: STEM-EDX analysis: the scanning line is shown on the STEM image as the dash line on the micrograph, which crosses the interface between intermetallic and Al phase; the results show that the intermetallic phase is $NiAl_3$ and the compositional distribution in the grain is quit uniform.
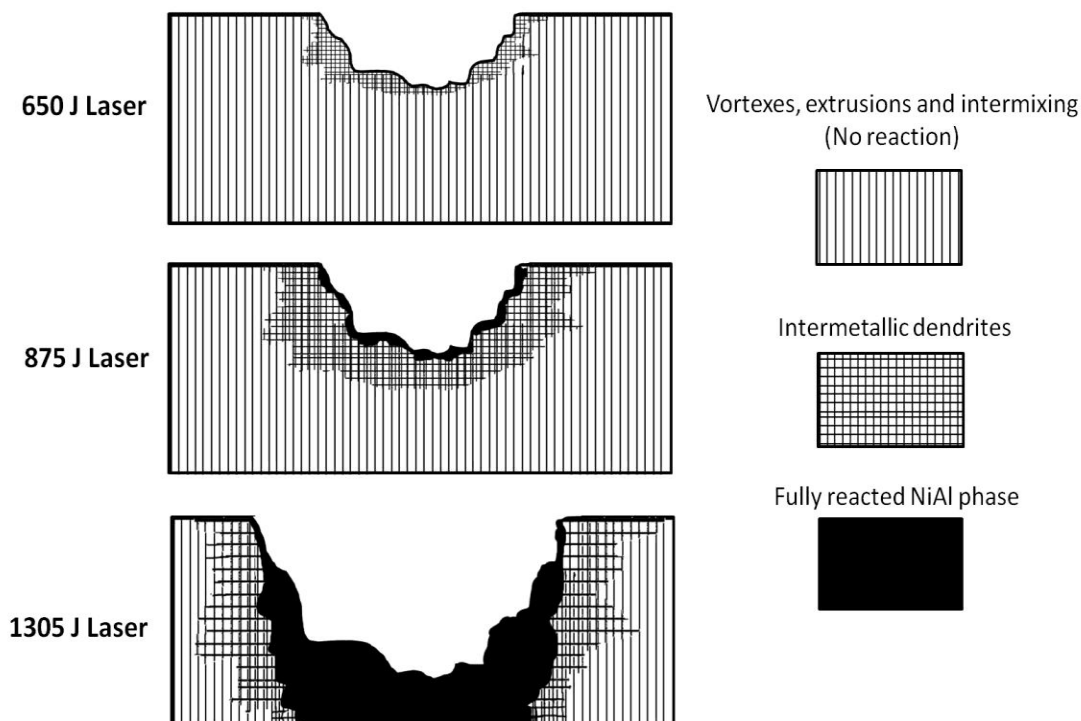
Figure 98: Schematic representation of cross sections of recovered micro-laminates (front samples) with phase distributions.

The distributions of intermetallic phases in the recovered samples of the plasma stagnated micro-laminates corresponding to different laser energies of the laser-driven initially shock-less compression experiments revealed critical features in the reaction stages of the self-sustaining high temperature synthesis (SHS) in Ni/Al laminates. SHS can be ignited in the Ni/Al reactive laminate, especially in the nano-scale Ni/Al reactive laminate, by a simple electrical spark, a flame [16, 17, 55-58], or a laser heating source [1]. Qiu et al. [55-58] defined the Ni/Al reaction in the micro-sacle Ni/Al as two sequential reactions: the first reaction generated $NiAl_3$ intermetallic phase and propagated laterally over the surface of the laminate at a relatively slow rate, and a second reaction consumed the remaining Ni phase and converted the $NiAl_3$ intermetallic into NiAl phase.

The second reaction was of the exothermic chemical reduction process which releases a large quantity of heat and facilitates the further SHS reaction. However, in the current study, the NiAl intermetallic phase was formed in the plasma stagnated crater center in 1305 J laser experiment, and there was no reaction at the edge of the micro-laminate. This suggests the intermetallic reaction did not propagate through the entire sample despite the fact that the final intermetallic phase, NiAl, was detected in the center of the front micro-laminate (Figure 96 (a)). On the other hand, it also suggests that without the continuous heating source such as flame or torch, which contributes a thermal energy for several mini- or micro-seconds [56], the SHS reaction cannot be ignited.

The Ni/Al nano-laminate was converted to a fully-reacted NiAl phase with equiaxed grains, which have grain sizes less than 0.5 µm in all of the laser conditions of this study, as shown in Figure 99 (a, b) for 650 J laser experiment. The fully reacted Ni/Al nano-laminate was produced by the shock-wave loading regardless of the input from external thermal energies. These NiAl intermetallic grains resulted in the undulating features (inset of the Figure 99 (a)), which are characteristic of the self-sustaining reaction in nano-laminates [2]. The self-sustaining reaction of the Ni/Al nano-laminate generated a large amount of heat resulting in melting of the unreacted micro-laminate. Figure 99 (b) shows that the heat from the reaction of the Ni/Al nano-laminate melted the adjacent Ni layer of the micro-laminate, but no intermetallic reaction was found in the back micro-laminate, showing that the reaction did not propagate from the nano-laminate to the micro-laminate.
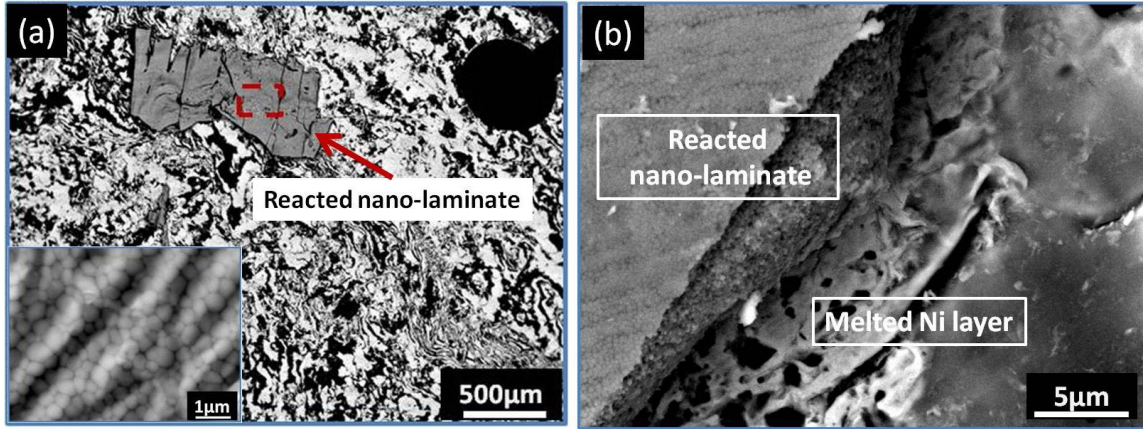
Figure 99: Nano-laminate, 650 J experiment; (a) granular intermetallics in the reacted nano-laminate; (b) melted and resolidified Ni layer underneath areacted nano-laminate intermetallic as a result of heat released from reaction.

4.3.15 Thermodynamic and kinetic analysis

The adiabatically self-sustaining reaction in the nano-scale Ni/Al laminate was driven by the exothermic heat in the reaction front [2, 16, 17, 39, 205, 206], which increased the temperature and produced a propensity for intermetallic reactions. Thermodynamic equations were used to estimate the maximum temperature achieved in each particular exothermic reaction corresponding to specific intermetallics such as NiAl and NiAl$_3$. The following equation was used to estimate the maximum final temperature, T_{max}, in the solid state:

$$\Delta H_{T_0}(Ni_xAl_y) + \int_{T_0}^{T_r} C_p(x \cdot Ni + y \cdot Al)dT = \int_{T_r}^{T_{max}} C_p(Ni_xAl_y)dT \qquad \text{Eqn. (74)}$$

where ΔH_{T0} (Ni_xAl_y) is the heat of formation at T_0 (K) which is *298 K*; C_p(Ni), C_p(Al) and C_p(Ni$_x$Al$_y$) are the specific heat capacities of Ni, Al elemental reactants and Ni$_x$Al$_y$ respectively; T_r is the reaction temperature. The detail of the thermodynamic parameters

is shown in Table 19. The T_r is chosen as 600 K according to [4]. It is found that the estimated final temperature is sufficient to melt the intermetallic phase and the surrounding reactants. For instance, the NiAl adiabatic reaction can reach the $T_{max} = 3774$ *K*. It suggested that the intermetallic and surrounding reactants could be at least partially melted while exothermic reaction is progressing. This facilitates the sequential reactions and results in the self-sustaining high temperature synthesis.

Table 19. Heat of formation and specific heat capacity.

Reactant or intermetallic	ΔH_{298K} (*kJ mol^{-1}*)	Specific heat capacity (J mol^{-1} K^{-1})
Al[a]	---	$=20.108 + 13.166 \times 10^{-3}\, T + 0.033 \times 10^5\, T^{-2}$
Ni[a]	---	$=19.355 + 22.456 \times 10^{-3}\, T + 0.017 \times 10^5\, T^{-2}$
NiAl[b]	-118.407	$=41.925 + 13.6 \times 10^{-3}\, T - 0.033 \times 10^5\, T^{-2} + 0.1 \times 10^{-6}\, T^2$
NiAl$_3$[b]	-150.7	$=43.144 + 138.406 \times 10^{-3}\, T + 14.611 \times 10^5\, T^{-2} - 67.314 \times 10^{-6}\, T^2$

[a] Subtracted from Morsi's work [205].

[b] Subtracted from "Thermochemical Properties of Inorganic Substance" [207].

The intermetallic reactions in the Ni/Al laminates are significantly influenced by the heat dissipation rate, the intermixing of layers [4, 16, 17], and the bilayer thickness [16, 17]. Ma et al. [2] proposed an energy balance model which was used for estimating the maximum bilayer thickness required for the self-sustaining high temperature reaction at ambient temperature. In this approach, the rate of the heat generation rate should be

faster than the sum of the rates of the heat absorption by the materials, $C\dfrac{dT}{dt}$, and the

heat dissipation, $\dfrac{dE}{dt}$, at the reaction front due to the conduction and radiation. The

inequality is:

$$\frac{dH_{To}}{dt} > C\frac{dT}{dt} + \frac{dE}{dt},$$
<div align="right">Eqn. (75)</div>

where H_{To}, C, T, t and E are the generated heat at the ambient temperature, specific heat

capacity, temperature, time and dissipated heat respectively. The heat generation rate can

be re-written as

$$\frac{dH_{To}}{dt} = \left(\frac{\Delta H_{To}}{L}\right)R(T),$$
<div align="right">Eqn. (76)</div>

where ΔH_{To} is the heat formation per unit volume from the exothermic reaction, L is the

bilayer thickness, and the R(T) is the temperature-dependent reaction rate. By

incorporating Eqn. (68) in to Eqn. (67) and considering that in the limit, there is no

sufficient heat generation to increase the surrounding temperature, which means the

temperature increase, dT/dt, can be neglected, Ma et al. [2] obtained the following

inequality:

$$L_{max} = \frac{\Delta H_{To} \times R(T)}{dE/dt} \geq L$$
<div align="right">Eqn. (77)</div>

The inequality represented by Eqn. (77) establishes limits for the maximum thickness of

bilayer for the self-propagating high temperature reaction at the given temperature and reaction rate at the reaction front.

Wang et al. [16, 17] and Gunduz et al. [206] investigated the self-sustaining high temperature synthesis of the NiAl intermetallic. The plot of reaction speeds vs. bilayer thicknesses from Wang et al. [17] and Gunduz et al. [206] is shown in Figure 100. It demonstrates that the increase of the bilayer thickness, L_{max}, resulted in a decrease of the reaction speed, $R(T)$. The increase of the bilayer thickness also corresponded to a slower heat dissipation rate, dE/dt. However, at the reaction front, the heat dissipation rate is the function of the reaction temperature T and the ambient temperature T_0. Ma et al. proposed that without increasing the ambient temperature, T_0, the maximum bilayer thickness for the self-sustaining high temperature synthesis was restrained [2]. The empirical results [2, 16, 17] and the estimation from the plot of Figure 100 show that maximum reaction length of the NiAl self-sustaining high temperature synthesis is less than 100 nm under the ambient temperature (~298 K). This is consistent with the result in this study where the formation of the fully reacted NiAl phase in the Ni/Al micro-laminate did not result in a self-sustaining high temperature synthesis propagating through the entire sample.
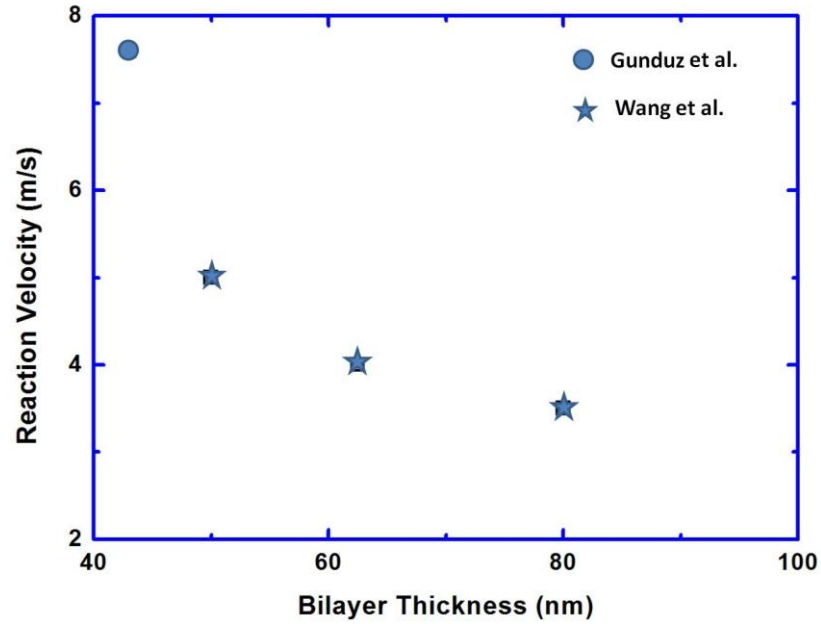
Figure 100: Reaction velocities for self-sustaining high temperature synthesis in nanoscaled Ni-Al laminates as a function of bilayer thicknesses (from Wang et al. [17] and Gunduz et al. [206]).

4.3.16 Morphologies of the nano-scale structure of intermetallics

The fully reacted nano-laminate was found in all the recovered samples at three different laser energies. It exhibited the equiaxed NiAl nano-grains with sizes varying from 200 to 400 nm as shown in Figure 101 (a) (bright field) and (b) (dark field) TEM micrographs. A simple diffusion-controlled grain growth equation can be applied for estimation of the grain growth time of the NiAl nano-grain [208]:

$$t = \lambda^2 / \tilde{D}_{NiAl},$$
Eqn. (78)

where t is the growth time, λ is the average diameter of the NiAl grain which is about 300 nm, and $\tilde{D}_{NiAl}$ is the interdiffusion coefficient of the NiAl intermetallics which can be calculated using the Arrhenius equation:

$$\tilde{D}_{NiAl} = \tilde{D}_{oNiAl} \times \exp(\frac{-\tilde{Q}_{oNiAl}}{RT}),$$

Eqn. (79)

where the pre-exponential factor and the activation energy are obtained from [208], $\tilde{D}_{oNiAl}$ 3.7 × 10^{-2} m²/s and $\tilde{Q}_{oNiAl}$ 358 kJ/mol respectively, and R is the gas constant, and T is the temperature at the reaction front. For the adiabatic reaction of the Ni/Al nano-laminate investigated in this study, the exothermic reaction can increase the temperature to about 1900 K [205] and therefore, the estimated grain growth time, 1.58 × 10^{-2} second, is obtained.

The atomic-resolution TEM micrograph presented in Figure 102 (a) reveals the atomic structure of NiAl (d ~300 nm). The corresponding FFT (fast Fourier transform) image in the inset of Figure 102 (a) shows that a diffraction pattern of the NiAl Pm3m (0 0 1) surface. Lattice defects were seen in the NiAl nano-grains which represented as the randomly distributed shadows in the brighter grains of Figure 101 (b), which had the same zone axis <001> in the dark field images and the corresponding bright field images Figure 101 (a). Figure 102 (b) shows vacancies, partial and complete dislocations in the NiAl nano-grain. It should be noted that clustered areas of point defects were also discovered in the atomic-resolution micrograph and this, as well as vacancies, are commonly found in the materials quenched from near melting temperature [209]. Two different phases of NiAl intermetallic, β-phase in Figure 102 (c) and martensitic phase [210-216] in Figure 102 (d), are both presented in the NiAl intermetalic grains. The identical mesh presenting in Figure 102 (c, d) reveals that the differences of face-center-cubic (fcc) β phase and the body-center-cubic (bcc) martensitic phase in the (0 0 1)

surface orientation. This also is commonly found in the quenched NiAl thin film [210].

The martensitic phase also induced a mismatched plane at the interfaces of the β (B2 phase) and matensitic phases (BCC) which resulted in the partial and complete dislocations as shown in Figure 102 (b). These crystallographic irregularities suggest that the nano-scale laminate is swiftly quenched after reaction. It should be noted that the martensitic transformation in NiAl intermetallic phase can also be produced by external loading as well. Park et al. [216] conducted a molecular dynamics calculation, which predicted that the fcc (B2) phase NiAl intermetallic nano-wires was transformed into bcc martensitic phase by a tensile strain with a strain rate of 10^9 s^{-1}. However in this study, due to the longer grain growth time, which is about 10^{-2} s incorporating the fast compression wave propagation time ($\sim 10^{-6}$ s), it is rational to propose that the martensitic phase was generated by a fast quenching process.
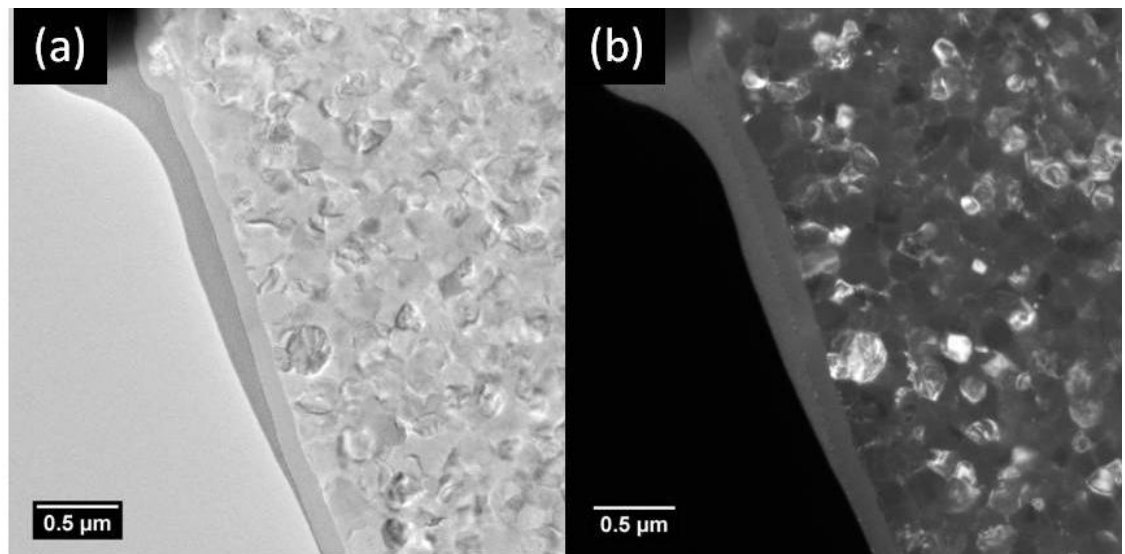
Figure 101: Reacted Ni/Al nano-laminate showing nanoscale grains: (a) bright field image; (b) dark files image.
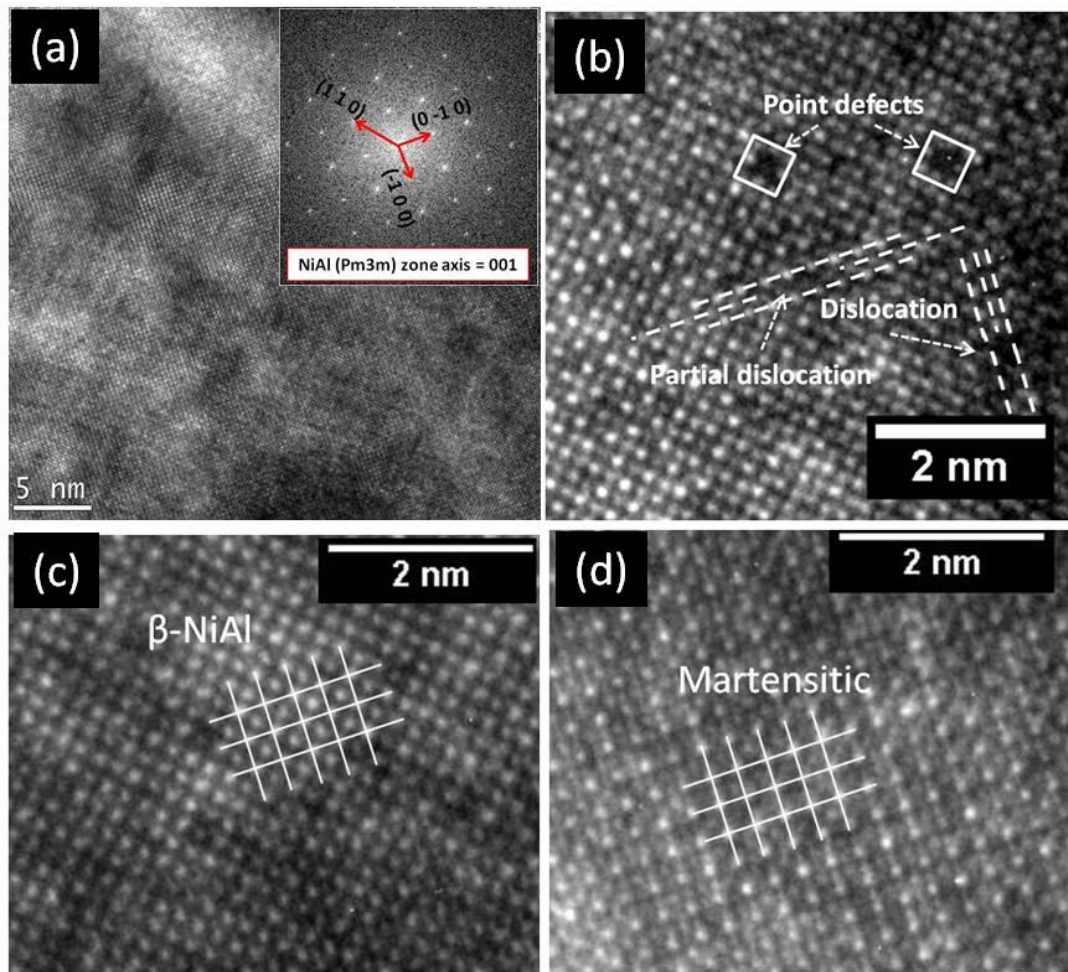
Figure 102: (a)atomic image of the intermetallic single grain with the inset of the FFT image of (a); (b) atomic-micrograph showing lattice defects such as point defects, partial and perfect dislocations in the NiAl intermetallic grain; (c) atomic-micrograph of the β phase NiAl intermetallic; (d) atomic-micrograph of the NiAl martensitic phase.

The $NiAl_3$ phase of the laminates with 5 μm bilayer thickness as shown in Figure 96 (c) was sectioned and trimmed for making a TEM sample using focus ion beam machining. Figure 103 (a, b) show the atomic-scale micrograph from the direct laser shock and the laser-driven plasma generated initially shock-less compression respectively. The $NiAl_3$ phase presented in the NiAl micro-laminates has a grain size over 0.5 μm which can be seen in this study as well as the direct laser shock experiments [82, 94].

However inside the NiAl$_3$ grains, there is a dissimilar atomic structure compared to the crystalline structure of the NiAl intermetallic grains shown in Figure 101. Figure 103 (a) shows the atomic micrograph of the NiAl$_3$ intermetallic induced by the direct laser shock [94]; the size of the mono-crystalline domain is ~7 nm and the multiple sub-grains produces the FFT pattern with rings of bright dots corresponding to the perfect NiAl$_3$ crystallographic surface such as {2 7 0} and {1 7 1} surface group and other diffraction dots. There is a big variety of sub-grain sizes of the NiAl$_3$ produced by laser-driven initially shock-less compression shown in Figure 103 (b). The FFT of Figure 103 (b) shows a few bright dots, such as {1 2 3} phase group, and halo rings which suggests that there is only a scarce amount of areas with the long-range-periodic structure and a large quantity of nano-crystalline intermetallics. These TEM observations prove that the laser-driven initially shock-less compression approach generates a faster quenching process due to the short laser pulse duration [95, 96], hence that the long-range periodic atomic structure is hard to form in the NiAl$_3$ phase.
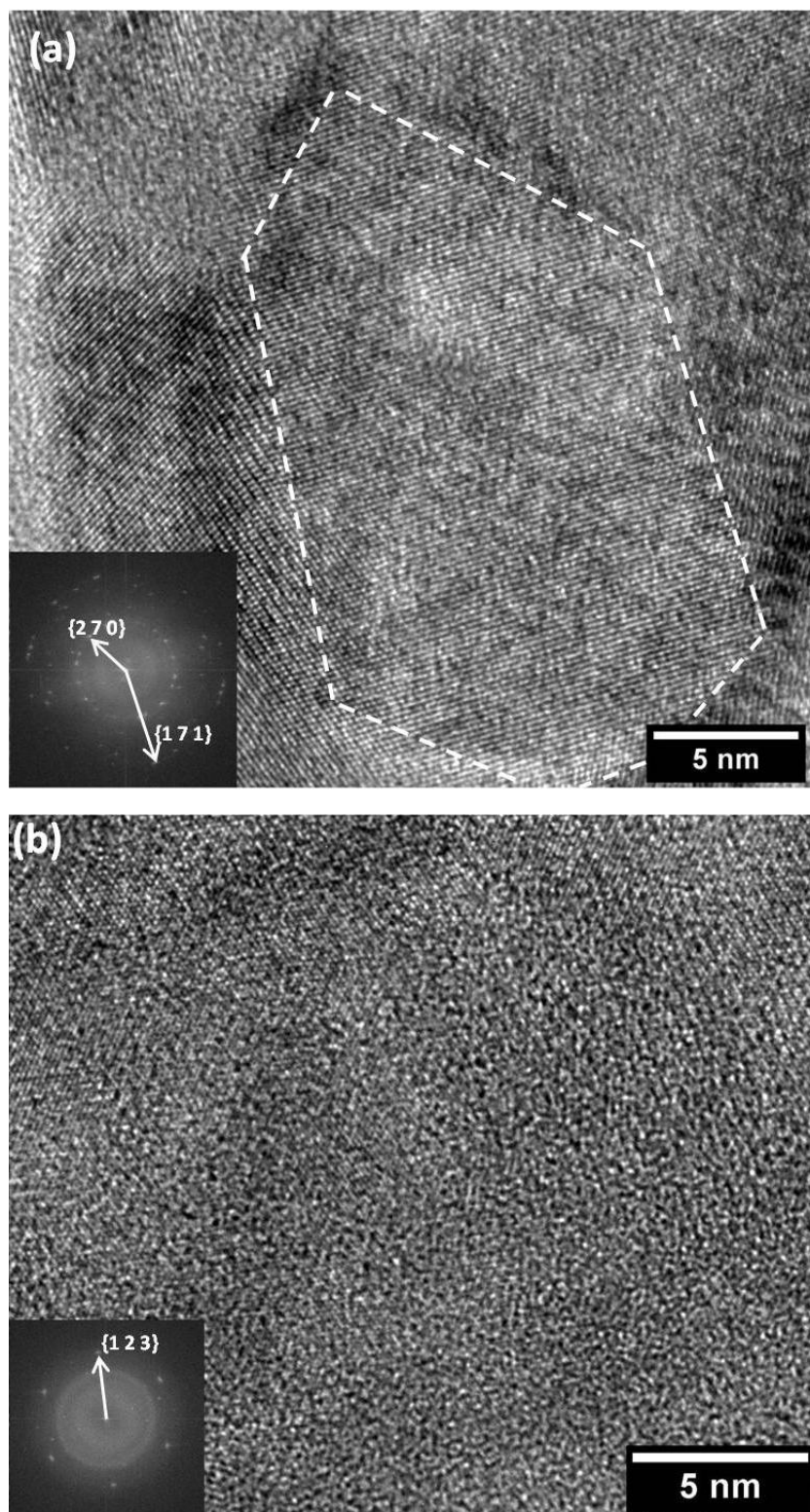
Figure 103: NiAl$_3$ intermetallic dendrites in the micro-laminates: (a) the direct laser irradiated micro-laminate; (b) laser-driven initially shock-less compression experiment.

4.3.17 Conclusions

Ni-Al laminates with three different bilayer thicknesses (5 μm, 30 μm and 54 nm) were tested by laser-driven shock compressions with energies varied from ~24 to ~400 J, and pulse durations 3, 3.7 and 8 ns. Conventional mechanical tests and simulation tools were also used to investigate the mechanical properties and fracture mechanisms of the micro-scale laminates. The following principal conclusions were reached:

1. The laser shock created craters, spall, and also extreme damage in all laminates.

2. The brittle fracture surface shown on the spalls and fragment sizes proved that fracture mechanisms are governed by the pre-existing defects in the cold-rolled laminates. The acquired strain rate for the G-K brittle-ductile transition is higher than ~10^6 s^{-1}.

3. The short pulse laser cannot generate the self-propagating reaction through the entire sample due to the kinetic limitation of the exothermic reaction; however, the shock-induced reaction produced intermetallic reactions that were found in this study.

4. The bilayer thickness is an important geometrical factor for laser shock-induced reaction. Thinner Ni-Al bilayers (5 μm) demonstrate a sub-critical/critical behavior forming molten Al and Ni-Al compounds, whereas thicker bilayers do not exhibit any significant reactions.

5. The laser pulse duration is also an important factor for generating Ni/Al intermetallic reactions in both thinner and thicker bilayer samples under relatively low laser

intensity, which provides a longer thermal heating time from the laser with a longer pulse duration (8 ns).

6. From the RAVEN simulation results, one can conclude that the geometry of the laminate constituents and the interlaminar bonding between Al and Ni played important roles in determining the mechanical responses of the Ni/Al laminates.

7. The laser-driven shock-less compression approach produced strain rates of 10^7 to 10^8 s^{-1} and the propagating shock wave with high amplitudes 30, 75, 118 GPa corresponding to laser energies, 650, 875 and 1305 J respectively. The attenuation of the amplitude of the shock wave propagating in Ni/Al laminates was less than 30%.

8. The intermetallic phases in the recovered samples of the laser-driven shock-less compression experiments varied according to different laser energies. The higher laser energy, 1305 J, produced more intermetallic phase including $NiAl_3$ (dendrites) and NiAl (equiaxed grains).

9. The SHS reaction did not propagate and self-sustain in the Ni/Al micro-laminates. The SHS reaction cannot be ignited in the micro-scale Ni/Al laminate without a sufficient increase of the ambient temperature.

Chapter 4, in part, has been published or is currently being prepared for submissions as the following: Reaction in Ni–Al laminates by Llaser-Shock Compression and Apalling, 2011, C. T. Wei, B. R. Maddox, A. K. Stover, T. P. Weihs, V. F. Nesterenko, M. A. Meyers, Acta Materialia; Laser Shock-Induced Spalling and Fragmentation in Vanadium, 2010, H. Jarmakani, B. Maddox, C. T. Wei, D. Kalantar, M.

A. Meyers, Acta Materialia; Response of Ni/Al Laminates to Laser-Driven Compression, C. T. Wei, V. F. Nesterenko, T. P. Weihs, B. Remington, H. -S. Park, M. A. Meyers, Acta Materialia, to be submitted; Quasi-static and Dynamic Response of Explosively Consolidated Metal-Aluminum Powder Mixtures, C. T. Wei, E. Vitali, D. J. Benson, F. Jiang, K. S. Vecchio, N. N. Thadhani, M. A. Meyers, Acta Materialia, to be submitted. The dissertation author was the primary or co- author of these papers.

Appendix

HYADES CODE

(a)100 J laser shock in vanadium with 61% reflection

```
c
c mesh for Vanadium 250 µm plate
c
mesh 1 201 0. .025
region 1 200 1 6
c velocity 1 1 4.e+6 4.e+6
material 1 v
eos 521 1
c
c Laser source applied on the front surface at mesh 1
c (no fixed boundaries)
c
source laser 0.523 1
tv 0. 0.
tv .1e-10 1.1684e+19
tv 3.e-9 1.1684e+19
tv 3.001e-9 0.
c
c
c Post-processor dumps every 100 ps
c
pparray pres r rcm
parm tstop 4.e-7
parm postdt 1.e-9
parm editdt 1.e-9
parm itmcyc 100
parm nstop 10000
```

(b) 400J laser shock wave in Ni/Al with 48 µm bilayer thickness and 50% laser absorption

mesh 1 20 0. .0024
region 1 19 1 2.7
c
mesh 20 40 .0024 .0048
region 20 39 2 8.908
c
mesh 40 60 .0048 .0072
region 40 59 1 2.7
c
mesh 60 80 .0072 .0096
region 60 79 2 8.908
c
mesh 80 100 .0096 .012
region 80 99 1 2.7
c
mesh 100 120 .012 .0144
region 100 119 2 8.908
c
mesh 120 140 .0144 .0168
region 120 139 1 2.7
c
mesh 140 160 .0168 .0192
region 140 159 2 8.908
c
mesh 160 180 .0192 .0216
region 160 179 1 2.7
c
mesh 180 200 .0216 .024
region 180 199 2 8.908
c
mesh 200 220 .024 .0264
region 200 219 1 2.7
c
mesh 220 240 .0264 .0288
region 220 239 2 8.908
c
mesh 240 260 .0288 .0312
region 240 259 1 2.7
c
mesh 260 280 .0312 .0336
region 260 279 2 8.908
c

```
mesh 280 300 .0336 .036
region 280 299 1 2.7
c
mesh 300 320 .036 .0384
region 300 319 2 8.908
c
mesh 320 340 .0384 .0408
region 320 339 1 2.7
c
mesh 340 360 .0408 .0432
region 340 359 2 8.908
c
mesh 360 380 .0432 .0456
region 360 379 1 2.7
c
mesh 380 400 .0456 .048
region 380 399 2 8.908
c
mesh 400 420 .048 .0504
region 400 419 1 2.7
c
mesh 420 440 .0504 .0528
region 420 439 2 8.908
c
mesh 440 460 .0528 .0552
region 440 459 1 2.7
c
mesh 460 480 .0552 .0576
region 460 479 2 8.908
c
mesh 480 500 .0576 .06
region 480 499 1 2.7
c
mesh 500 520 .06 .0624
region 500 519 2 8.908
c
mesh 520 540 .0624 .0648
region 520 539 1 2.7
c
mesh 540 560 .0648 .0672
region 540 559 2 8.908
c
mesh 560 580 .0672 .0696
region 560 579 1 2.7
c
```

```
mesh 580 600 .0696 .072
region 580 599 2 8.908
c
mesh 600 620 .072 .0744
region 600 619 1 2.7
c
mesh 620 640 .0744 .0768
region 620 639 2 8.908
c
mesh 640 660 .0768 .0792
region 640 659 1 2.7
c
mesh 660 680 .0792 .0816
region 660 679 2 8.908
c
mesh 680 700 .0816 .0840
region 680 699 1 2.7
c
mesh 700 720 .084 .0864
region 700 719 2 8.908
c
mesh 720 740 .0864 .0888
region 720 739 1 2.7
c
mesh 740 760 .0888 .0912
region 740 759 2 8.908
c
mesh 760 780 .0912 .0936
region 760 779 1 2.7
material 1 al
eos 44 1
c
mesh 780 800 .0936 .096
region 780 799 2 8.908
material 2 ni
eos 291 2
c
c
c Velocity source on each boundary
c
source laser 0.523 1
tv 0. 0.
tv .1e-10 .555e+20
tv 3.e-9 .555e+20
tv 3.001e-9 0.
```

```
c
c
c Post-processor dumps every 100 ps
c
pparray pres r rcm deplas xlsint
parm tstop 6.e-6
parm postdt 8.e-9
parm editdt 8.e-9
parm itmcyc 100
parm nstop 10000
```

(c) Laser-driven shock-less compression in Ni/Al micro-laminate with 5um bilayer thickness attached to Ni/Al nano-laminate (54 nm bilayer thickness)

c
c NiAl laminate with 5 um bilayer thickness (total thickness 0.85mm)
c
mesh 1 3 0. .0002
mesh 3 723 0.0002 .085
mesh 723 1224 0.085 .0858
mesh 1224 1230 0.0858 0.15
region 1 3 1 2.7
region 4 6 2 8.908
region 7 9 1 2.7
region 10 12 2 8.908
region 13 15 1 2.7
region 16 18 2 8.908
region 19 21 1 2.7
region 22 24 2 8.908
region 25 27 1 2.7
region 28 30 2 8.908
region 31 33 1 2.7
region 34 36 2 8.908
region 37 39 1 2.7
region 40 42 2 8.908
region 43 45 1 2.7
region 46 48 2 8.908
region 49 51 1 2.7
region 52 54 2 8.908
region 55 57 1 2.7
region 58 60 2 8.908
region 61 63 1 2.7
region 64 66 2 8.908
region 67 69 1 2.7
region 70 72 2 8.908
region 73 75 1 2.7
region 76 78 2 8.908
region 79 81 1 2.7
region 82 84 2 8.908
region 85 87 1 2.7
region 88 90 2 8.908
region 91 93 1 2.7
region 94 96 2 8.908
region 97 99 1 2.7
region 100 102 2 8.908
region 103 105 1 2.7
region 106 108 2 8.908

region 109 111 1 2.7
region 112 114 2 8.908
region 115 117 1 2.7
region 118 120 2 8.908
region 121 123 1 2.7
region 124 126 2 8.908
region 127 129 1 2.7
region 130 132 2 8.908
region 133 135 1 2.7
region 136 138 2 8.908
region 139 141 1 2.7
region 142 144 2 8.908
region 145 147 1 2.7
region 148 150 2 8.908
region 151 153 1 2.7
region 154 156 2 8.908
region 157 159 1 2.7
region 160 162 2 8.908
region 163 165 1 2.7
region 166 168 2 8.908
region 169 171 1 2.7
region 172 174 2 8.908
region 175 177 1 2.7
region 178 180 2 8.908
region 181 183 1 2.7
region 184 186 2 8.908
region 187 189 1 2.7
region 190 192 2 8.908
region 193 195 1 2.7
region 196 198 2 8.908
region 199 201 1 2.7
region 202 204 2 8.908
region 205 207 1 2.7
region 208 210 2 8.908
region 211 213 1 2.7
region 214 216 2 8.908
region 217 219 1 2.7
region 220 222 2 8.908
region 223 225 1 2.7
region 226 228 2 8.908
region 229 231 1 2.7
region 232 234 2 8.908
region 235 237 1 2.7
region 238 240 2 8.908
region 241 243 1 2.7

region 244 246 2 8.908
region 247 249 1 2.7
region 250 252 2 8.908
region 253 255 1 2.7
region 256 258 2 8.908
region 259 261 1 2.7
region 262 264 2 8.908
region 265 267 1 2.7
region 268 270 2 8.908
region 271 273 1 2.7
region 274 276 2 8.908
region 277 279 1 2.7
region 280 282 2 8.908
region 283 285 1 2.7
region 286 288 2 8.908
region 289 291 1 2.7
region 292 294 2 8.908
region 295 297 1 2.7
region 298 300 2 8.908
region 301 303 1 2.7
region 304 306 2 8.908
region 307 309 1 2.7
region 310 312 2 8.908
region 313 315 1 2.7
region 316 318 2 8.908
region 319 321 1 2.7
region 322 324 2 8.908
region 325 327 1 2.7
region 328 330 2 8.908
region 331 333 1 2.7
region 334 336 2 8.908
region 337 339 1 2.7
region 340 342 2 8.908
region 343 345 1 2.7
region 346 348 2 8.908
region 349 351 1 2.7
region 352 354 2 8.908
region 355 357 1 2.7
region 358 360 2 8.908
region 361 363 1 2.7
region 364 366 2 8.908
region 367 369 1 2.7
region 370 372 2 8.908
region 373 375 1 2.7
region 376 378 2 8.908

region 379 381 1 2.7
region 382 384 2 8.908
region 385 387 1 2.7
region 388 390 2 8.908
region 391 393 1 2.7
region 394 396 2 8.908
region 397 399 1 2.7
region 400 402 2 8.908
region 403 405 1 2.7
region 406 408 2 8.908
region 409 411 1 2.7
region 412 414 2 8.908
region 415 417 1 2.7
region 418 420 2 8.908
region 421 423 1 2.7
region 424 426 2 8.908
region 427 429 1 2.7
region 430 432 2 8.908
region 433 435 1 2.7
region 436 438 2 8.908
region 439 441 1 2.7
region 442 444 2 8.908
region 445 447 1 2.7
region 448 450 2 8.908
region 451 453 1 2.7
region 454 456 2 8.908
region 457 459 1 2.7
region 460 462 2 8.908
region 463 465 1 2.7
region 466 468 2 8.908
region 469 471 1 2.7
region 472 474 2 8.908
region 475 477 1 2.7
region 478 480 2 8.908
region 481 483 1 2.7
region 484 486 2 8.908
region 487 489 1 2.7
region 490 492 2 8.908
region 493 495 1 2.7
region 496 498 2 8.908
region 499 501 1 2.7
region 502 504 2 8.908
region 505 507 1 2.7
region 508 510 2 8.908
region 511 513 1 2.7

region 514 516 2 8.908
region 517 519 1 2.7
region 520 522 2 8.908
region 523 525 1 2.7
region 526 528 2 8.908
region 529 531 1 2.7
region 532 534 2 8.908
region 535 537 1 2.7
region 538 540 2 8.908
region 541 543 1 2.7
region 544 546 2 8.908
region 547 549 1 2.7
region 550 552 2 8.908
region 553 555 1 2.7
region 556 558 2 8.908
region 559 561 1 2.7
region 562 564 2 8.908
region 565 567 1 2.7
region 568 570 2 8.908
region 571 573 1 2.7
region 574 576 2 8.908
region 577 579 1 2.7
region 580 582 2 8.908
region 583 585 1 2.7
region 586 588 2 8.908
region 589 591 1 2.7
region 592 594 2 8.908
region 595 597 1 2.7
region 598 600 2 8.908
region 601 603 1 2.7
region 604 606 2 8.908
region 607 609 1 2.7
region 610 612 2 8.908
region 613 615 1 2.7
region 616 618 2 8.908
region 619 621 1 2.7
region 622 624 2 8.908
region 625 627 1 2.7
region 628 630 2 8.908
region 631 633 1 2.7
region 634 636 2 8.908
region 637 639 1 2.7
region 640 642 2 8.908
region 643 645 1 2.7
region 646 648 2 8.908

region 649 651 1 2.7
region 652 654 2 8.908
region 655 657 1 2.7
region 658 660 2 8.908
region 661 663 1 2.7
region 664 666 2 8.908
region 667 669 1 2.7
region 670 672 2 8.908
region 673 675 1 2.7
region 676 678 2 8.908
region 679 681 1 2.7
region 682 684 2 8.908
region 685 687 1 2.7
region 688 690 2 8.908
region 691 693 1 2.7
region 694 696 2 8.908
region 697 699 1 2.7
region 700 702 2 8.908
region 703 705 1 2.7
region 706 708 2 8.908
region 709 711 1 2.7
region 712 714 2 8.908
region 715 717 1 2.7
region 718 720 2 8.908
region 721 723 1 2.7
region 724 726 2 8.908
region 727 729 1 2.7
region 730 732 2 8.908
region 733 735 1 2.7
region 736 738 2 8.908
region 739 741 1 2.7
region 742 744 2 8.908
region 745 747 1 2.7
region 748 750 2 8.908
region 751 753 1 2.7
region 754 756 2 8.908
region 757 759 1 2.7
region 760 762 2 8.908
region 763 765 1 2.7
region 766 768 2 8.908
region 769 771 1 2.7
region 772 774 2 8.908
region 775 777 1 2.7
region 778 780 2 8.908
region 781 783 1 2.7

region 784 786 2 8.908
region 787 789 1 2.7
region 790 792 2 8.908
region 793 795 1 2.7
region 796 798 2 8.908
region 799 801 1 2.7
region 802 804 2 8.908
region 805 807 1 2.7
region 808 810 2 8.908
region 811 813 1 2.7
region 814 816 2 8.908
region 817 819 1 2.7
region 820 822 2 8.908
region 823 825 1 2.7
region 826 828 2 8.908
region 829 831 1 2.7
region 832 834 2 8.908
region 835 837 1 2.7
region 838 840 2 8.908
region 841 843 1 2.7
region 844 846 2 8.908
region 847 849 1 2.7
region 850 852 2 8.908
region 853 855 1 2.7
region 856 858 2 8.908
region 859 861 1 2.7
region 862 864 2 8.908
region 865 867 1 2.7
region 868 870 2 8.908
region 871 873 1 2.7
region 874 876 2 8.908
region 877 879 1 2.7
region 880 882 2 8.908
region 883 885 1 2.7
region 886 888 2 8.908
region 889 891 1 2.7
region 892 894 2 8.908
region 895 897 1 2.7
region 898 900 2 8.908
region 901 903 1 2.7
region 904 906 2 8.908
region 907 909 1 2.7
region 910 912 2 8.908
region 913 915 1 2.7
region 916 918 2 8.908

region 919 921 1 2.7
region 922 924 2 8.908
region 925 927 1 2.7
region 928 930 2 8.908
region 931 933 1 2.7
region 934 936 2 8.908
region 937 939 1 2.7
region 940 942 2 8.908
region 943 945 1 2.7
region 946 948 2 8.908
region 949 951 1 2.7
region 952 954 2 8.908
region 955 957 1 2.7
region 958 960 2 8.908
region 961 963 1 2.7
region 964 966 2 8.908
region 967 969 1 2.7
region 970 972 2 8.908
region 973 975 1 2.7
region 976 978 2 8.908
region 979 981 1 2.7
region 982 984 2 8.908
region 985 987 1 2.7
region 988 990 2 8.908
region 991 993 1 2.7
region 994 996 2 8.908
region 997 999 1 2.7
region 1000 1002 2 8.908
region 1003 1005 1 2.7
region 1006 1008 2 8.908
region 1009 1011 1 2.7
region 1012 1014 2 8.908
region 1015 1017 1 2.7
region 1018 1020 2 8.908
region 1021 1023 1 2.7
region 1024 1026 2 8.908
region 1027 1029 1 2.7
region 1030 1032 2 8.908
region 1033 1035 1 2.7
region 1036 1038 2 8.908
region 1039 1041 1 2.7
region 1042 1044 2 8.908
region 1045 1047 1 2.7
region 1048 1050 2 8.908
region 1051 1053 1 2.7

region 1054 1056 2 8.908
region 1057 1059 1 2.7
region 1060 1062 2 8.908
region 1063 1065 1 2.7
region 1066 1068 2 8.908
region 1069 1071 1 2.7
region 1072 1074 2 8.908
region 1075 1077 1 2.7
region 1078 1080 2 8.908
region 1081 1083 1 2.7
region 1084 1086 2 8.908
region 1087 1089 1 2.7
region 1090 1092 2 8.908
region 1093 1095 1 2.7
region 1096 1098 2 8.908
region 1099 1101 1 2.7
region 1102 1104 2 8.908
region 1105 1107 1 2.7
region 1108 1110 2 8.908
region 1111 1113 1 2.7
region 1114 1116 2 8.908
region 1117 1119 1 2.7
region 1120 1122 2 8.908
region 1123 1125 1 2.7
region 1126 1128 2 8.908
region 1129 1131 1 2.7
region 1132 1134 2 8.908
region 1135 1137 1 2.7
region 1138 1140 2 8.908
region 1141 1143 1 2.7
region 1144 1146 2 8.908
region 1147 1149 1 2.7
region 1150 1152 2 8.908
region 1153 1155 1 2.7
region 1156 1158 2 8.908
region 1159 1161 1 2.7
region 1162 1164 2 8.908
region 1165 1167 1 2.7
region 1168 1170 2 8.908
region 1171 1173 1 2.7
region 1174 1176 2 8.908
region 1177 1179 1 2.7
region 1180 1182 2 8.908
region 1183 1185 1 2.7
region 1186 1188 2 8.908

```
region 1189 1191 1 2.7
region 1192 1194 2 8.908
region 1195 1197 1 2.7
region 1198 1200 2 8.908
region 1201 1203 1 2.7
region 1204 1206 2 8.908
region 1207 1209 1 2.7
region 1210 1212 2 8.908
region 1213 1215 1 2.7
region 1216 1218 2 8.908
region 1219 1221 1 2.7
region 1222 1224 2 8.908
region 1225 1230 1 2.7
c
c materials parameters
c
material 1 al
material 2 ni
eos 44 1
eos 291 2
strength 1 2 3 0
strength 2 2 3 0
data metal 1
data metal 2
c
c shear and yield stress calculated by Steinberg-Guinan model
c
data shear 1 2.76e+11 6.52e-12 7.15e+3
data shear 2 8.55e+11 1.6e-12 3.805e+3
data yield 1 2.9e+9 125. 0. .10 6.8e+9
data yield 2 1.4e+9 46. 0. .53 1.2e+10
data tmelt 1 1.05e-4 1.5 1.97
c
c laser-driven shock-less compression pressure pulse (650J laser)
c
source pres 1 2
tv 0. 7.128e+10
tv 5.42e-9 1.095e+11
tv 7.997e-9 1.342e+11
tv 10.075e-9 1.4438e+11
tv 12.94996e-9 1.3123e+11
tv 15.24827e-9 1.2583e+11
tv 19.847e-9 1.0836e+11
tv 24.013e-9 9.865e+10
tv 27.1e-9 9.331e+10
```

```
tv 29.9e-9 9.018e+10
tv 30e-9 0.
c
c Post-processor dumps every 100 ps
c
pparray pres r rcm strain straind strtot tr rhodr eplast
parm tstop 2.5e-7
parm postdt 5.e-8
parm editdt 5.e-8
change 1.64e-7 postdt 1.e-10
parm iedcyc 100
parm itmcyc 100
parm nstop 160000
```

References

1. J.S. Kim, T. LaGrange, B.W. Reed, M.L. Taheri, M.R. Armstrong, W.E. King, N.D. Browning, G.H. Campbell, Science 321 (2008) 1472.

2. E. Ma, C.V. Thompson, L.A. Clevenger, and K.N. Tu, Appl. Phys. Lett. 57 (1990) 1262.

3. A.J. Gavens, D.V. Heerden, A.B. Mann, M.E. Reiss, and T.P. Weihs, J. Appl. Phys. 87 (2000) 1255.

4. K.J. Blobaum, D.V. Heerden, A.J. Gavens, and T.P.Weihs, Acta Mater. 51 (2003) 3871.

5. E. Ma, C.V. Thompson, L.A. Clevenger, J. Appl. Phys. 69 (1991) 211.

6. M.A. Meyers et. al., Mater. Sci. Eng. A201 (1995) 150.

7. J.C. LaSalvia, An investigation into the synthesis and processing of dense titanium carbide-molybdenum based cermets utilizing combustion synthesis with impact forging, doctoral dissertation, (1994).

8. I. N. Ryabinin, Soviet Phys. Tech. Phys. 1 (1956) 2575.

9. J.C. LaSalvia, D.K. Kim, R.A. Lipsett and M.A. Meyers, Metall. Mater. Trans. A 26A (1995) 3001.

10. J.C. LaSalvia, M.A. Meyers, Metall. Mater. Trans. A 26A (1995) 3011.

11. A.G. Merzhanov and B.I. Khaikin, Prog. Energr. Combust. Sci. 14 (1988) 1.

12. A.G. Merzhanov, J. Mater. Process. Tech. 56 (1996) 222.

13. J.C. LaSalvia, D.K. Kim and M.A. Meyers, Mater. Sci. Eng. A206 (1995) 71.

14. D.A. Hoke, D.K. Kim, J.C. La Salvia, M.A. Meyers, J Am. Ceram. Soc. 79 (1996) 177.

15. D.B. Miracle, Acta Metall. Mater. 41 (1993) 649.

16. J. Wang, E. Besnoin, A. Duckham, S. J. Spey, M. E. Reiss, O. M. Knio, and T. P. Weihs, J. Appl. Phys. 95 (2004) 248.

17. J. Wang, E. Besnoin, O.M. Knio and T.P. Weihs, Acta Mater. 52 (2004) 5265.

18.   A.J. Swiston, T.C. Hufnagel and T.P. Weihs, Scripta Mater. 48 (2003) 1575.

19.   D.E. Eakins and N.N.Thadhani, Intl. Mater. Rev. 54 (2009) 118.

20.   N.N.Thadhani, Progr. Mater. Sci. 37 (1993) 117.

21.   K.S. Vecchio et al., Acta Metall. Mater. 42 (1994) 701.

22.   Wikipedia, Web. " Thermite", (Http://en.wikipedia.org/wiki/Thermite).

23.   P.S. DeCarli, and J.C. Jamieson, Science 134 (1961) 92.

24.   J. Zhang, F.-S. Wu, J. Zou, B. An, H. Liu., ICEPT-HDP (2009).

25.   K.S. Vecchio, J.C. LaSalvia, M.A. Meyers and G.T. Gray III, Metal. Trans. A
       23A (1992) 87.

26.   L. Knapp, "Adding more bang to navy missiles", Web.
       (http://www.wired.com/science/discoveries/news/2002/12/56695), (2002).

27.   Office of naval research, Web. (http://www.onr.navy.mil/Media-Center/Press-
       Releases/2002/Better-Warheads-Through-Plastics.aspx), (2002).

28.   M.A. Meyers, K.K. Chawla, Mechanical Behavior of Materials, Chapter 2,
       (1994).

29.   J.B. Wachtman, Mechanical and Thermal Properties of Ceramics, ed. J.B.
       Wachtman, NBS Special Publication 303, NBS Washington, p. 139, (1963).

30.   J.K. MacKenzie, Proc. Phys. Soc. B63 (1950) 2.

31.   B. Budiansky, R.J. O'connell, Intl. J. Solids Struct. 12 (1976) 81.

32.   F. Zerilli and R.W. Armstrong, J. Appl. Phys. 68 (1990) 1580.

33.   D.S. Gianola, D.H. Warner, J.F. Molinari and K.J. Hermker, Scripta Mater. 55
       (2006) 649.

34.   R. Schwaiger, B. Moser, M. Dao, N. Chollacoop, S. Suresh, Acta Mater. 51,
       (2003) 5159.

35.   Y.M. Wang, E. Ma, Mater. Sci. Eng. A 357 (2004) 46.

36.   D.E. Eakins, and N.N. Thadhani, Appl. Phys. Lett. 92 (2008) 111903.

37. K.M. Lee, J.S. Lee, D.J. Lee, S.S. Kim, I.S. Ahn, M.W. Park, J. Alloy. Compd. 313 (2000)214.

38. O. Kubaschewski and C.B. Alcock, Metallurgical Thermochemistry, Pergamon, Oxford, 267, (1983).

39. A.J. Gavens, D. Van Heerden, A.B. Mann, M.E. Reiss and T.P. Weihs, J. Appl. Phys. 87 (2000) 1255.

40. G.E. Duvall, and R.A. Graham, Rev. Mod. Phys. 49 (1977) 523.

41. M.H. Rice, R.G. McQueen, and J.M. Walsh, Compression of solids by strong shock waves, in Solid State Physics, F. Seitz and D. Turnbull, eds., Academic Press, NY, (1958).

42. M.A. Meyers et al., JOM. 62 (2010) 24.

43. Y. Horie, R.A. Graham, I.K. Simonsen, Mater. Lett. 3 (1985) 354.

44. I.K. Simonsen, Y. Horie, R.A. Graham, M. Carr, Mater. Lett. 5 (1987) 75.

45. S.L. Thompson, "CSQII-An Eulerian Finite Difference Program for Two-Dimensional Material Response-Part I. Material Science," Sandia Laboratories Report No. SAND77-1339, (1984).

46. S.S. Batsanov, Inorg. Mater. 43 (2007) 1070.

47. S.P. Kiselev, Combust. Explo. Shock 31 (1995) 473.

48. K. S. Vecchio et al., Acta Metall. Mater. 42 (1994) 701.

49. M.A. Meyers et al., Acta Mettall. Mater. 42 (1994) 715.

50. M.A. Meyers et al., Mater. Sci. Eng. A201 (1995) 150.

51. W.L. Roberts, Cold Rolling of Steel, Marcel Dekker, Inc., New York, (1978).

52. H. Sierber, J.S. Park, J. Weissmuller and J.H. Perepezko, Acta Mater. 49 (2001) 1139.

53. A. Sagel, H. Siber, H.-J. Fecht and J. H. Perepezko, Acta Mater. 46 (1998) 4233.

54. I.N. Qureshi, S. Rani, F. Yasmin and M. Farooque, Key Eng. Mater. 442 (2010) 268.

55.   X. Qiu, J.H. Graeter, L. Kecskes, and J. Wang, Mater. Res. Soc. Symp. Proc. Vol. 977 (2007).

56.   X. Qiu, J. Graeter, L. Kecskes, J. Wang, J. Mater. Res. 23 (2008) 367.

57.   X. Qiu, R. Liu, S. Guo, J.H. Graeter, L. Kecskes, J. Wang, Metal. Mater. Trans. A 40A (2009) 1541.

58.   X. Qiu and J. Wang, Scripta Mater. 56 (2007) 1055.

59.   L. Battezzati, P. Pappalepore, F. Purbiano and I. Gallino, Acta Mater. 47 (1999) 1901.

60.   T.P. Weihs and M. Reiss: Method of making reactive multilayer foil and resulting product. U.S. Patent No. 6 534 194 (2003).

61.   H. Sieber, J.S. Park, J. Weissmuller, J.H. Perepezko, Acta Mater. 49 (2001) 1139.

62.   N. Tsuji, Y. Saito, S.-H. Lee, and Y. Minamino, Adv. Eng. Mater. 5 (2003) 338.

63.   R.F. Bunshah, Handbook of Deposition Technologies for Films and Coatings- Science, Technology and Applications (2nd Edition), William Andrew Publishing, Noyes, (1994).

64.   D.E. Wolfe, Thesis (Ph.D.), Synthesis and characterization of TiC, TiBCN,TiB2 /TiC and TiC/CrC multilayer coatings by reactive and ion beam assisted, electron beam-physical vapor deposition (EB-PVD), The Pennsylvania State University, (1996).

65.   S.W. Du, B. Aydelotte, D. Fondse, C.T. Wei, F. Jiang, E. Herbold, K. Vecchio, M.A. Meyers, and N.N. Thadhani, Shock Compression of Condensed Matter, AIP Conf. Proc. 1195 (2009) 498.

66.   S.W. Du, and N.N. Thadhani, Shock Compression of Condensed Matter, AIP Conf. Proc. 1195 (2009) 470.

67.   R.Y. Yang, A.B. Yu, S.K. Choi, M.S. Coates, H.K. Chan, Powder Technol. 184 (2008) 122.

68.   M.A. Meyers, and S.L. Wang, Acta Metall. 36 (1988) 925.

69.   R.J. Wright, R.E. Anderson Jr., and Z.R. Waltz, J. Therm. Spray Techn. 3 (1994) 292.

70.   T. George, ASM Handbook, Volume 08- Mechanical Testing and Evaluation, H. Kuhn, D. Medlin editors (2000).

71.   S.K. Vecchio and F.-C. Jiang, Metall. Mater. Trans. A 38A (2007) 2655.

72.   W. Chen, B. Song, D.J. Frew and M.J. Forrestal, Exper. Mech. 43 (2003) 20.

73.   D.J. Parry, A.G. Walker and P.R. Dixon, Measurement Sci. Technol. 6 (1995) 443.

74.   S. Ellwood, L.J. Griffiths and D.J. Parry, J. Phys. E: Sci. Instrum. 15 (1982) 280.

75.   S. Nemat-Nasser et al., J. Eng. Mater. Technol. 127 (2005) 83.

76.   J. Duffy, J.D. Campbell, and R.H. Hawley, J. Appl. Mech. 37 (1971) 83.

77.   G.T. Gray: ASM Handbook, vol. 8, Mechanical Testing and Evaluation, ASM INTERNATIONAL, Materials Park, OH, 462–76, (2000).

78.   C.E. Franz, P.S. Follanbee and W.J. Wright: 8th Int. Conf. on High Energy Rate   Fabrication, Pressure Vessel and Piping Division, San Antonio, TX, 1984, I. Beaman and J.W. Schroeder, eds., ASME, (1984).

79.   P.S. Follanbee, Metals Handbook, vol. 8, Mechanical Testing, 9th ed., ASM, Metals Park, OH, 198–217, (1985).

80.   S. Nemat-Nasser, J.B. Isaacs and J.E. Starrett, Proc. R. Soc. London A 435, (1991) 371.

81.   D.J. Frew, M.J. Forrestal and W. Chen, Exper. Mech. 42 (2002) 93.

82.   C.T. Wei, B.R. Maddox, T.P. Weihs, A.K. Stover, V.F. Nesterenko, and M.A. Meyers, Proc. APS 2009 Conf. Shock Compression of Condensed Matter, API, 305-308, (2010).

83.   M.A. Meyers, H.N. Jarmakani, E.M. Bringa, P. Earhart, B.A. Remington, V. Nhon and Y.M. Wang, Proc. APS 2009 Conf. Shock Compression of Condensed Matter, API, 1051-1056, (2010).

84.   M.A. Meyers, H. Jarmakani, B.Y. Cao, C.T. Wei, B. Kad, B.A. Remington, E.M. Bringa, B. Maddox, D. Kalantar, D. Eder, A. Koniges, Proc DYMAT, (2009).

85.   H. Jarmakani, B.R. Maddox, C.T. Wei, D. Kalantar, A. Koniges, D. Eder, M.A. Meyers, Acta. Mat. 58 (2010) 4604.

86.   G.A. Askarion and E.M. Morez, JETP Lett. 16 (1963) 1638.

87.   J. Lindl, Phys. Plasmas 2 (1995) 3933.

88.   M.S. Schneider, B.K. Kad, F. Gregori, D.H. Kalantar, B.A. Remington and M.A. Meyers, Int. J. Impact Eng. 32 (2005) 473.

89.   G.V. Samsonov, Handbook of the Physicochemical Properties of the Elements. New York: Washington; (1968).

90.   C.G.M. van Kessel and R. Sigel, Phys. Rev. Lett. 33 (1974) 1020.

91.   L. Berthe, R. Fabbro, P. Peyre, L. Tollier and E. Bartnicki, J. Appl. Phys. 82 (1997) 2826.

92.   V. Allmen, Lasaer-beam interaction with materials, Springer-Verlag Berlin, Heidelberg, New York, (1987).

93.   Y. Ping, R. Shepherd, B.F. Lasinski, M. Tabak, H. Chen, K.B. Fournier, S.B. Hansen, A. Kemp, D.A. Liedahl, K. Widmann, S.C. Wilks, W. Rozmus and M. Sherlock, Phys. Rev. Lett. 100 (2008) 085004.

94.   C.T. Wei, B.R. Maddox, A.K. Stover, T.P. Weihs, V.F. Nesterenko, M.A. Meyers, Acta Mater. 59 (2011) 5276.

95.   J. Edwards et al., Phys. Rev. Lett. 92 (2004) 075002.

96.   K.T. Lorenz, M.J. Edwards, A.F. Jankowski, S.M. Pollaine, R.F. Smith, B.A. Remington, High Energy Density Phys. 2 (2006) 113.

97.   Goldstein, D. Newbury, D. Joy, C. Lyman, P. Echlin, E. Lifshin, L. Sawyer, and J. Michael, Scanning Electron Microscopy and X-Ray Microanalysis, third edition, New York, Kluwer Academic/Plenum Publishers, (2003).

98.   I.M. Watt, The principles and practice of electron microscopy, second edition, Cambridge, Cambridge University Press, (1997).

99.   J.S. Kim et al., Science 321 (2008) 1472.

100.   L.-L. Ooi, Principles of x-ray crystallography, Chpater 2, Oxford; New York: Oxford University Press, (2010).

101.   N. Qureshi, S. Rani, F. Yasmin and M. Farooque, Key Eng. Mater. 442 (2010) 268.

102.   I.K. Simonsen, Y. Horie, R.A. Graham and M. Carr, Mater. Lett. 5 (1987) 75.

103.   R. Fitzgerald, K. Keil and K.F.J. Heinrich, Science 159 (1968) 528.

104.   D.A. Wollman, K.D. Irwin, G.C. Hilton, L.L. Dulcie, D.E. Newbury, J.M. Martinis, J. Microsc. 188 (1997) 196.

105.   B.D. Cullity, Elements of X-Ray Diffraction, second edition, Menlo Park, Addison-Wesley Publishing Company, Inc., (1978).

106.   D. Benson, Meth. Appl. M. 99 (1992) 235.

107.   N.C. Woolsey et al., Phys. Rev. E 57 (1998) 4650.

108.   A.M. Rubenchik, M.D. Feit, M.D. Perry, J.T. Larsen, Appl. Surf. Sci. 127-129 (1998) 193.

109.   A. Zhidkov, A. Sasaki, T. Tajima, Phys. Rev. E 61 (2000) 2224.

110.   J.O. Kane et al., Phys. Rev. E 63 (2001) 055401-4.

111.   R.P. Drake, Phys. Plasmas, 9 (2002) 3545.

112.   H.F. Robey et al., Phys. Plasmas, 10 (2003) 614.

113.   D.C. Swift et al., Phys. Rev. E 69 (2004) 036406-9.

114.   D.C. Swift and R.P. Johnson, Phys. Rev. E 71 (2005) 066401-5.

115.   A.D. Edens et al., Phys. Rev. Lett. 95 (2005) 244503-4.

116.   A.R. Reighard et al., Phys. Plasmas, 13 (2006) 082901-5.

117.   L. Tollier, R. Fabbro and E. Bartnicki, J. Appl. Phys. 83 (1998) 1224.

118.   L. Tollier, R. Fabbro and E. Bartnicki, J. Appl. Phys. 83 (1998) 1231.

119.   L.M. Barker, Shock Compression of Condensed Matter, AIP Conf. Proc. 505 (2000) 11.

120.   L.M. Barker, Shock Compression of Condensed Matter, AIP Conf. Proc. 429 (1998) 833.

121.   E. Dunbar, N.N. Thadhani, R.A.Graham, J. Mater. Sci. 28 (1993) 2903.

122.   N. N. Thadhani, S. Work, R. A. Graham and W. F. Hammetter, J. Mater. Res. 7 (1992) 1063.

123. K.A. Philpot, Z.A. Munir and J.B. Holt, J. Mater. Sci. 22 (1987) 159.

124. R.J. Kurtz, M.L. Hamilton, H. Li, J. Nucl. Mater. 1375 (1998) 258.

125. S.J. Zinkle et al., J. Nucl. Mater. 205 (1998) 258.

126. R.J. Kurtz et al., J. Nucl. Mater. 70 (2000) 283.

127. G.V. Samsonov, editor. Handbook of the physicochemical properties of the elements. New York: IFI Plenum; 383, (1968).

128. I. Gilath, L. Davison, D.E. Grady and M. Shahinpoor, Editors, High-pressure shock compression of solids, Springer, New York, 90–120, (1996).

129. M.A. Meyers and C.T. Aimone, Prog. in Mater. Sci. 28 (1983) 1.

130. D.E. Grady, J. Appl. Phys. 53 (1982) 322.

131. M.E. Kipp and D.E. Grady, J. Mech. Phys. Solids 33 (1985) 399.

132. D.E. Grady, J. Mech. Phys. Solids 36 (1988) 353.

133. L.M. Barker, R.E. Hollenbach, J. Appl. Phys. 43 (1972) 4669.

134. M.E. Kipp, D.E. Grady, J.W. Swegle, Int. J. Impact Eng. 14 (1993) 427.

135. D.E. Grady and M.E. Kipp, J. Appl. Phys. 58 (1985) 1210.

136. D.E. Grady, J. Appl. Phys. 68 (1990) 6099.

137. D.E. Grady, M.L. Kipp, High-Pressure Shock Compression of Solids, J.R. Asay, M. Shahinpoor, eds. Springer NY, 265-322 (1993).

138. H. Yoshinaga, K. Toma, K. Abe, S. Morozumi, Phil. Mag. 23 (1971) 1387.

139. Y.V. Batsanov, A.B. Glushak, B.L. Glushak, S.A. Novikov, N.D. Fishman, Combust Explos. Shock Waves 31 (1995) 605.

140. L.C. Chabildas, C.R. Hill, Metallurgical applications of shock wave and high strain-rate phenomena, L.E. Murr, K.P. Staudhammer, M.A. Meyers, editors, New York: Marcel Dekker, 429, (1986).

141. A.M. Lennon, K.T. Ramesh, Int. J. Plast. 14 (1998) 1279.

142. L.A. Glenn, A. Chudnovsky, J. Appl. Phys. 59 (1986) 1379.

143. C. Mariot, V. Michaut, J.F. Molinari, DYMAT 2009, Proceedings of the 9th international conference on the mechanical and physical behavior of materials under dynamic loading, 1523, (2009).

144. F. Zhou, J.F. Molinari, K.T. Ramesh, Comput. Mater. Sci. 37 (2006) 74.

145. M.A. Meyers, B.B. Gupta and L.E. Murr, J. Meter, 33 (1981) 21.

146. H.L. Coker, M.A. Meyers and J.F. Wessels, J. Mater. Sci. 26 (1991) 1277.

147. S.L. Wang, M.A. Meyers and A. Szecket, J. Mater. Sci. 23 (1988) 1786.

148. L.H. Yu, M.A. Meyers and T.C. Peng, Mater. Sci. Eng. A132 (1991) 257.

149. L.H. Yu and M.A. Meyers, J. Mater. Sci. 26 (1991) 601.

150. S. Shang, K. Hokamoto and M.A. Meyers, J. Mater. Sci. 27 (1992) 5470.

151. S.S. Shang and M.A. Meyers, J. Mater. Sci. 31 (1996) 252.

152. K. Hokamoto, S. Tanaka, M. Fujita, S. Itoh, M.A. Meyers, H.-C. Chen, Physica B 239 (1997) 1.

153. L.H. Yu, M.A. Meyers, N.N.Thadhani, J. Mater. Res. 5 (1990) 302.

154. M.M. Meyers, Dynamic behavior of materials, Chapter 4, John Wiley & Sons, Inc., New York, 98-123, (1994).

155. H.M. Ledbetter and S.K. Datta, Mater. Sci. Eng. 67 (1984) 25.

156. H. Liholt, S. Ochiai (Ed.), Mechanical properties of metallic composites, Marcel Dekker, Inc. New York, 389-471, (1993).

157. Z. Hashin, J. Appl. Mech. 29 (1962) 143.

158. E. Arzt, Acta Mater. 46 (1998) 5611.

159. P. Kasiraj, T. Vreeland, Jr. R.B. Schwarz, and T.J. Ahrens, Mechanical properties of a shock consolidated steel powder, Shock Wave in Condense Matter, p. 693, (1983).

160. M. Taya, Meter. T JIM 32 (1991) 1.

161. S.P. Garg, G.B. Kale, R.V. Patil, T. Kundu, Intermetallics 7 (1999) 901.

162. M.M.P. Janssen, G.D. Riecks, Trans. Met. Soc. AIME 239 (1967) 1372.

163. C. Wagner, Acta Metall. 17 (1969) 99.

164. U. Gosele, K.N. Tu, J. App. Phys. 53 (1982) 3252.

165. K.M. Lee, J.S. Lee, D.J. Lee, S.S. Kim, I.S. Ahn, M.W. Park, J. Alloy. Compd. 313 (2000) 214.

166. C.L. Yeh, H.J. Wang, J. Alloy Compd. 485 (2009) 280.

167. J. Cai, F. Jiang, K.S. Vecchio, M.A. Meyers, V.F. Nesterenko, AIP Conf. Proc. 955 (2007) 723.

168. J. Cai, V.F. Nesterenko, K.S. Vecchio, F. Jiang, E.B. Herbold, D.J. Benson, J.W. Addiss, S.M. Walley, W.G. Proud, Appl. Phys. Lett. 92 (2008) 031903.

169. E.B. Herbold, J. Cai, D.J. Benson and V.F. Nesterenko, AIP Conf. Proc. 955 (2007) 785.

170. E.B. Herbold, V.F. Nesterenko, D.J. Benson, J. Cai, K.S. Vecchio, F. Jiang, J.W. Addiss, S.M. Walley, W.G. Proud, J. Appl. Phys. 104 (2008) 103903.

171. E. Vitali, C.T. Wei, D.J. Benson, M.A. Meyers, Acta Mater. 59 (2011) 5869.

172. J. B. Kim, H. Shin, Int. J. Impact Eng. 36 (2009) 746.

173. D. J. Vigueras, A continuous identation test for metals, master's thesis, New Mexico Institute of Mining and Technology, (1983).

174. Y. Chen, High strain, high strain-rate deformation of tantalum, UCSD, (1998).

175. G. R. Johnson, W. H. Cook, Eng. Fract. Mech. 21 (1985) 31.

176. D. J. Steinberg, Equation of state and strength properties of selected materials, Lawrence Livermore National Laboratory, (1996).

177. V.F. Nesterenko, Dynamics of Heterogeneous Materials, New York: Springer-Verlag; (2001).

178. D.J. Benson, Comput. Methods Appl. Mech. Eng. 99 (1992) 235.

179. D.J. Benson, Comput. Mech. 15 (1995) 558.

180. D.J. Benson, Comput. Methods Appl. Mech. Eng. 140 (1997) 59.

181. E. Vitali, D.J. Benson, Int. J. Numer. Methods Eng. 67 (2006) 1420.

182. E. Vitali, D.J. Benson, Int. J. Numer. Methods Eng. 76 (2008) 893.

183. E. Vitali, D.J. Benson, Comput. Mech. 43 (2009) 847.

184. E. Vitali, D.J. Benson, Comput. Mech. in preparation.

185. H. Okamoto, J. Phase Equilib. 14 (1993) 257.

186. G.X. Li, C.S. Liu and Z.G. Zhu, Phy. Rev. Lett. 71 (2005) 094209.

187. L. KoČi, E.M. Bringa, D.S. Ivanov, I. Hawreliak, A. McNaney J. Higginbotham, L.V. Zhigilei, A.B. Belonoshko, B.A. Remington and T. Ahuja, Phys. Rev. B 74 (2006) 012101.

188. R. Boehler, M. Ross, Earth Planet Sc. Lett. 153 (1997) 223.

189. D.E. Eakins, and N.N. Thadhani, Mater. Res. Soc. Symp. Proc. 896, 0896- H06- 04.1, (2006).

190. W. H. Zhu, M. Yoshida, H. Tamura, K. Kondo, S. Tanimura, J. Mater. Sci. Lett. 20 (2001) 961.

191. P. Amendt, R.E. Turner, and O.L. Landen, Phys. Rev. Lett. 89 (2002) 10.1130, 165001.

192. M.S. Schneider, B.K. Kad, F. Gregori, D. Kalantar, B.R. Remington and M.A. Meyers, Metall. Mater. Tran. A 35 (2004) 2633.

193. P. Peralta, S. DiGiacomo, S. Hashemian, S.N. Luo, D. Paisley, R. Dickerson, E. Loomis, D. Byler, and K.J. McClellan, Int. J Damage Mech. 18 (2009) 393.

194. C.H. Lu, B.A. Remington, B.R. Maddox, B. Kad, H.S. Park, S.T. Prisbrey, R. Luo and M.A. Meyers, AIP Conf. Proc. (2011) in press.

195. C.H. Lu, B.R. Maddox, B.A. Remington, E.M. Bringa, M. Kawasaki, T.G. Langdon, H.S. Park, B. Kad, and M.A. Meyers, AIP Conf. Proc. (2011) in press.

196. E. Loomis, P. Peralta, J. Swift, C.H. Lim, R. Dickerson, P. Dickerson, Mater. Sci. Eng. A 437 (2006) 212.

197. E. Loomis, D. Swift, J. McNaney, H. Lorenzana, P. Peralta, Acta Mater. 56 (2008) 3647.

198. T.E. Tierney, D.C. Swift, S.N. Luo, J. Niemczura, J.T. Gammei, P. Peralta, AIP Conf. Proc. 845 (2006) 1425.

199. D.H. Kalantar, G.W. Collins, J.D. Colvin, J.H. Eggert, J. Hawreliak, H.E. Lorezana, M.A. Meyers, R.W. Minich, K. Rosolankova, M.S. Schneider, J.S. Stolken, J.S. Wark, Int. J Impact Eng. 33 (2006) 343.

200. H.N. Jarmakani, E.M. Bringa, P. Earhart, B.A. Remington, V. Nhon and M.A. Meyers, Acta Mater. 56 (2008) 5584.

201. J.R. Asay, Int. J. Impact Engng. 20 (1997) 27.

202. B.A. Remington et al., Metall. Mater. Trans. A 35A (2004) 2587.

203. D.J. Steinberg, S.G. Coshran and M.W. Guinan, J. Appl. Phys., 51 (1980) 1498.

204. T. Sano, K. Kato and H. Takeishi, J. Mater. Process. Tech. 48 (1995) 391.

205. K. Morsi, Mater. Sci. Eng. A 299, (2001) 1.

206. I.E. Gunduz, K. Fadenberger, M. Kokonou, C. Rebholz, and C.C. Doumanidis, Appl. Phys. Lett. 93 (2008) 134101.

207. O. Knacke, O. Kubaschewski, K. Hesselmann (Eds.), Thermochemical properties of inorganic substance, second edition, (1991).

208. R. Nakamura, K. Takasawa, Y. Yamazaki, Y. Iijima, Intermetalics 10 (2002) 195.

209. B.L. Eyre, J. Phys. F: Metal Phys. 3 (1973) 422.

210. Y. Zhang, J.A. Haynes, B.A. Pint, I.G. Wright, W.Y. Lee, Surf. Coat. Tech., 163-164 (2003) 19.

211. D. Farkas, B. Mutasa, C. Vailhe and K. Ternes, Modeling Simul. Mater. Sci. Eng. 3 (1995) 201.

212. A.G. Khachaturyan, S.M. Shapiro and S. Semenovskaya, Phys. Rev. B 43 (1991) 10832.

213. A.S. Murthy and E. Goo, Acta Metall. Mater. 41 (1993) 2135.

214. R.J. Thompson, J.-C. Zhao, K.J. Hemker, Intermetallics 18 (2010) 796.

215. A. Masherghi, M.M. Moshksar, J. Alloy Compd. 482 (2009) 196.

216.   H.S. Park, Nano lett. 6 (2006) 958.